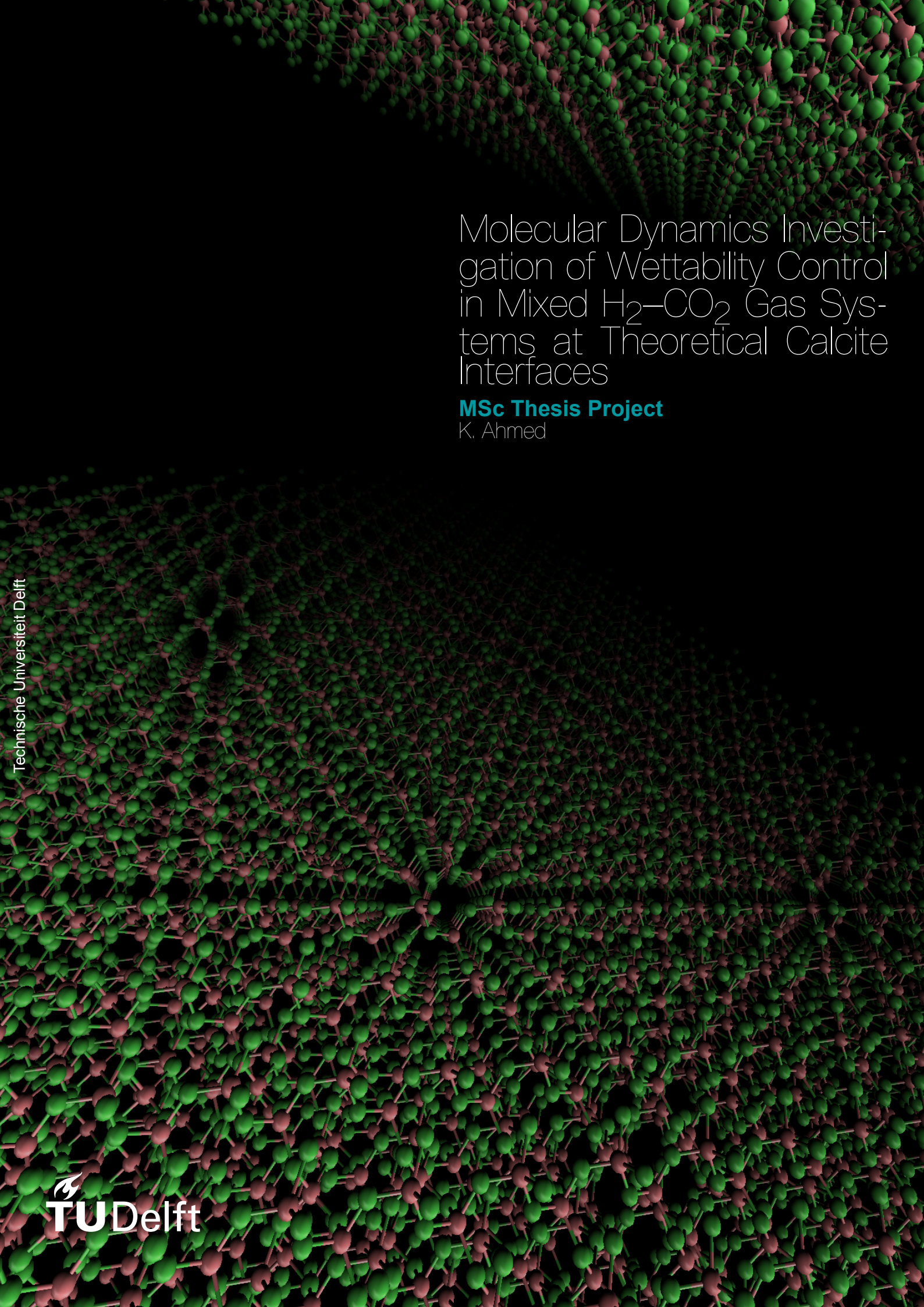

Molecular Dynamics Investigation of Wettability Control in Mixed H_2–CO_2 Gas Systems at Theoretical Calcite Interfaces

MSc Thesis Project

K. Ahmed

Technische Universiteit Delft

TUDelft

Molecular Dynamics Investigation of Wettability Control in Mixed H_2–CO_2 Gas Systems at Theoretical Calcite Interfaces

MSc Thesis Project

by

K. Ahmed

to obtain the degree of Master of Science
at the Delft University of Technology.

Student number:	5088054	
Project duration:	September 8, 2025 – February 30, 2026	
Thesis committee:	Prof. dr. ir. T. J. H. Vlugt,	TU Delft, supervisor
	Dr. ir. T. H. Chakrapani,	The University of Edinsburgh, supervisor
	Prof. dr. ir. H. Hajibeygi,	TU Delft
	Dr. ir. O. Moultos,	TU Delft
	Prof. dr. E. Pidko,	TU Delft

An electronic version of this thesis is available at http://repository.tudelft.nl/.

TU Delft

Preface

I am pleased to present this research project, which was conducted as part of my MSc thesis in Chemical Engineering. The opportunity to work on this study on subsurface hydrogen storage has been highly rewarding, and I have greatly enjoyed the experience and the knowledge gained throughout this project.

The work was carried out during the period 09/2025 – 02/2026 within the Engineering Thermodynamics group of the Faculty of Mechanical Engineering and the Reservoir Engineering group of the Faculty of Geoscience and Civil Engineering. The objective of this study was to investigate changes in hydrogen wettability in underground hydrogen storage environments using molecular dynamics simulations.

First and foremost, I would like to express my sincere gratitude to Thijs Vlugt and Hadi Hajibeygi for providing me with the opportunity to be part of this research and for welcoming me into their groups. Their guidance and support throughout the project have been invaluable, and I am grateful for the opportunity to learn from their expertise.

I extend my sincere appreciation to Thejas Hulikal Chakrapani, my supervisor, for his exceptional mentorship and continuous support. Working alongside him has been an enriching experience, and I am deeply grateful for his guidance, encouragement, and insightful feedback, which have contributed significantly to this research.

I would also like to thank Othon Moultos for his assistance during the project and for his valuable input in several key decisions. His expertise and guidance were instrumental in helping me get started on the right path.

K. Ahmed
Delft, February 2026

Abstract

Understanding wettability in subsurface gas–water–rock systems is essential for applications such as geological hydrogen storage, carbon sequestration, and reactive transport in porous media. In this study, molecular dynamics simulations were performed to investigate the wettability behavior of mixed H_2-CO_2 gas bubbles on a mineral surface under aqueous conditions. The focus was placed on disentangling the roles of gas composition and gas–rock interaction strength in controlling contact angle behavior.

Systematic scaling of gas–solid interaction parameters revealed that wettability can be governed by the adsorption affinity, rather than gas fraction alone. Therefore, by increasing the CO_2–rock interaction, a significant rise in contact angles can be observed, whereas scaling H_2–rock interactions produced weaker effects. These findings indicate that CO_2 acts as the dominant wettability controlling species due to its stronger dispersion interactions and quadrupolar character, which promote preferential adsorption at the mineral interface.

Additionally, simulations varying the CO_2 fraction demonstrated two distinct regimes depending on which gas dominated the interfacial adsorption layer. When CO_2 formed the primary adsorbed layer, increasing its fraction enhanced surface hydrophobicity. In contrast, when H_2 dominated the interface, changes in composition produced a different wettability response. This highlights the importance of interfacial structuring over bulk composition.

The results provide a mechanistic framework for understanding competitive gas adsorption and its influence on wettability in mixed-gas systems. These insights are relevant for predicting multiphase behavior in subsurface energy storage and carbon management applications, where interfacial phenomena critically impact gas trapping, mobility, and long-term stability.

Contents

List of Figures

List of Tables

Nomenclature

AC	Interaction scaling systems (H_2/CO_2)
AF	Composition varied systems (H_2/CO_2)
CA	Contact Angle
CLAYFF	Clay force field (mineral FF)
FF	Force field
GROMACS	GROningen MAchine for Chemical Simulations
LJ	Lennard–Jones potential
MD	Molecular Dynamics
PBC	Periodic Boundary Conditions
PME	Particle Mesh Ewald
RDF	Radial Distribution Function
SPC/E	Simple Point Charge–Extended water model
UHS	Underground Hydrogen Storage
vdW	van der Waals

1 Introduction

1.1. Background and Motivation

Due to an increasing demand for sustainable energy solutions and carbon management strategies, interest in subsurface geological formations for gas storage applications have intensified [58]. Underground hydrogen storage (UHS) is considered a promising option for large scale energy storage, while carbon dioxide sequestration is a key strategy for mitigating greenhouse gas emissions. Long-term efficiency and safety depend strongly on multiphase interactions occurring within the porous rocks under elevated pressure and temperature conditions. [58]

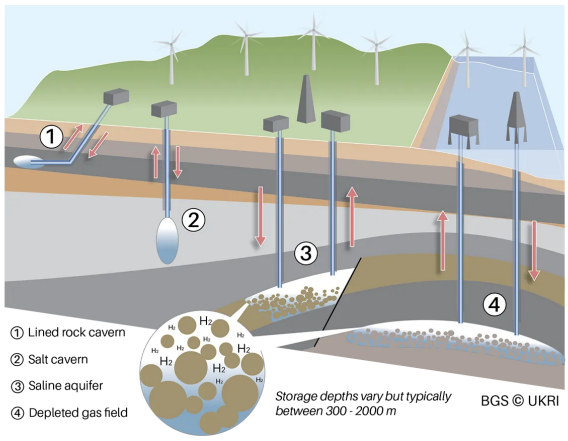

Figure 1.1: Schematic visualizing several different underground hydrogen storage methods, of which (1), (2), (3) and (4) are a lined rock cavern, a salt cavern, a saline aquifer and a depleted gas field respectively [16].

In the subsurface, gas phases exist with brine and mineral surfaces. Therefore forming complex solid-liquid-gas interfaces. Processes such as capillary trapping and wettability are determined by the interplay of these interfaces. In particular, the relative affinity of H_2 and CO_2 towards substrates can influence interfacial stability and displacement mechanisms [12]. Many geological formations contain carbonate minerals such as calcite, therefore understanding gas-water-calcite interactions at the molecular scale is important for storage performance [67].

Experimental investigations under reservoir relevant conditions, which are at hundreds of bar and at elevated temperatures, are challenging. Molecular dynamics (MD) simulations are therefore a complementary approach, providing atomistic insight on adsorption mechanisms and interfacial structures [74].

Numerous single component systems studies have been conducted at the atomic scale, yet combined systems of both H_2 and CO_2 remain much less explored [20][29][66][67]. In particular, most investigated systems are based on the so called sessile drop method, where a water droplet is modeled in a gas environment. Captive bubble methods, where a gas bubble is modeled in a liquid environment are much less investigated.

In this thesis, MD simulations are utilized to investigate the interfacial behavior of H_2-CO_2 bubble mixtures in contact with a calcite surface at 323 K and 200 bar. In order to investigate this, a cylindrical gas bubble is

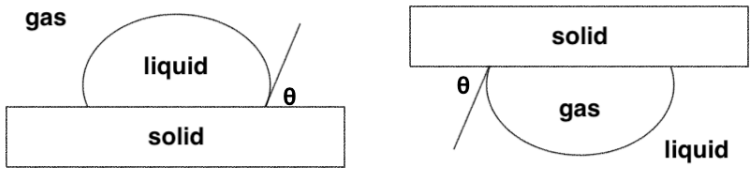

Figure 1.2: Schematic showing the difference between the sessile drop and captive bubble methods. The contact angle θ here is defined as the angle between the solid and the outer angle of the droplet or the bubble.

placed within an aqueous phase on top the calcite substrate, by which adsorption and wettability effects can now be assessed. In order to also understand the sensitivity of interfacial behavior to variations in gas-surface interactions between the different gas species, scaling factors will also be applied to their respective interaction parameters in selected simulations.

Three categories will be considered in the study. Firstly, reference systems are simulated using unmodified interaction parameters. Secondly, interaction scaling systems are constructed in which surface affinity of either H_2 or CO_2 are selectively varied. Lastly, composition varied systems are studied in which the fractions of H_2 and CO_2 within the bubble are varied. This structured approach allows separation of composition effects from interaction strength effects and provides insight into how substrate affinity and gas mixture composition determine interfacial behavior.

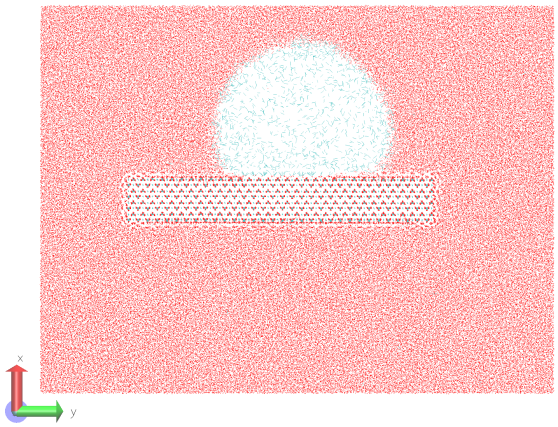

Figure 1.3: Snapshot of a MD simulation of a cylindrical bubble on a calcite substrate. Where the solid slab is the central rectangle in the central of the box, the gas bubble is the green low density region on top of the solid slab, and the rest is the water phase.

Results of this work contribute to a molecular level understanding of gas-water-mineral interactions under high pressure conditions, with such insights being relevant to multiphase behavior and wettability in geological storage environments.

1.2. Research Objectives and Questions

The central questions addressed in this thesis are:

- How does the relative fraction of H_2 and CO_2 influence interfacial structure and adsorption at a calcite surface?
- How does selective scaling of gas–surface interactions modify wettability behavior, and therefore which species is the dominant wettability controlling factor?
- Is wettability primarily governed by bulk gas composition, or by the identity of the gas species forming the adsorbed interfacial layer?

2

Theory

2.1. The Fundamentals of Molecular Dynamics

Molecular Dynamics is a computational technique used in order to study many particle systems over a short time, mostly nanoseconds, by integrating their equations of motion. In classical MD, atoms are treated as point particles and their interactions are described by force fields, which are often empirical potential energy functions. Due to the simulated particle trajectories at atomic scale, MD becomes quite suitable for studying fluids, solids and interfaces.

In this thesis, molecular dynamics simulations are employed to investigate gas–liquid–solid interfacial systems. A clear understanding of the statistical mechanical foundations, boundary conditions, and interatomic interactions underlying MD is therefore essential.

2.1.1. Statistical Mechanics

Classical statistical mechanics is rooted in the theoretical foundation of molecular dynamics, and it therefore provides the framework which links microscopic particle behavior to the thermodynamics [7]. In molecular dynamics the many particle systems are governed by integrating the Newton's equations of motion,

$$m_i \frac{d^2 \mathbf{r_i}}{dt^2} = \mathbf{F_i}. \tag{2.1}$$

The forces on the particles in MD simulations can be derived from the gradient of the system's potential energy,

$$\mathbf{F_i} = -\nabla_i U(\mathbf{r_1}, \mathbf{r_2}, ..., \mathbf{r_n}) \tag{2.2}$$

where U is the potential energy in terms of particle position and ∇_i denotes the particle gradient of that potential energy [7].

By integrating these equations of motion, MD generates trajectories of the system, based on the positions and momenta of all particles [7]. Under the assumption of ergodicity, in which the system explores all of its possible configurations over time, we can average over time in one long simulation to get the ensemble averages. This forms the basis of extracting the thermodynamic properties directly from a single MD trajectory [7].

Newton's equations of motion cannot be solved analytically for many body systems, so they are integrated numerically using finite time steps [7]. In MD simulations, one typically uses time-reversible, symplectic integration algorithms to maintain numerical stability and achieve reliable energy conservation over long simulation durations. One of the most widely used algorithms is the velocity Verlet integrator, which updates particle positions and velocities using forces evaluated at discrete time steps [7]:

$$\mathbf{v}(t + \frac{1}{2}\delta t) = \mathbf{v}(t) + \frac{1}{2}\delta t \mathbf{a}(t) \tag{2.3a}$$

$$\mathbf{r}(t + \delta t) = \mathbf{r}(t) + \delta t \mathbf{v}(t + \frac{1}{2}\delta t) \tag{2.3b}$$

$$\mathbf{v}(t + \delta t) = \mathbf{v}(t + \frac{1}{2}\delta t) + \frac{1}{2}\delta \mathbf{a}(t + \delta t). \tag{2.3c}$$

2.1.2. Micro-Canonical NVE Ensemble

There exist different statistical ensembles which correspond to different physical constraint that act on the system. In the micro-canonical NVE ensemble the number of particles, system volume and total energy are conserved, representing an isolated system [28]. The total energy in classical systems can be given by the Hamiltonian H, which is the sum of the kinetic and potential energy:

$$H = \sum_{i=1}^{n} \frac{\mathbf{p}_i}{2m} + \mathrm{U}(\mathbf{r^N}). \tag{2.4}$$

Where the assumption being made that the potential energy does not depend on the momenta **p** [28]. The classical partition function in the micro canonical NVE ensemble can be obtained by integrating over all points in the phase space with the condition that the Hamiltonian is equal tot the specified energy E. The constraint that system has to be on $H(\mathbf{p}^{\mathrm{N}}, \mathbf{r}^{\mathrm{N}}) = \mathrm{E}$ can be expressed by the Dirac delta function (δ), and therefore for a three-dimensional system the partition function becomes:

$$\Omega_{N,V,E} \equiv \frac{1}{h^{3N}N!} \int d\mathbf{p}^N d\mathbf{r}^N \delta(H(\mathbf{p}^{\mathrm{N}}, \mathbf{r}^{\mathrm{N}}) - \mathrm{E}). \tag{2.5}$$

2.1.3. Canonical NVT Ensemble

The ensemble with constant N, V and T is called the canonical ensemble. Similar to the 2.5, the NVT classical partition function Q can be expressed as:

$$Q_{N,V,T} \equiv \frac{1}{h^{3N}N!} \int d\mathbf{p}^N d\mathbf{r}^N e^{[-\beta H(\mathbf{p}^{\mathrm{N}}, \mathbf{r}^{\mathrm{N}})]}. \tag{2.6}$$

Integration can be done analytically since the potential energy does not depend on the momenta of the system [28], while defining the thermal Broglie wavelength Λ as:

$$\Lambda = \sqrt{\frac{h^2}{2\pi m k_b T}} \tag{2.7}$$

then the canonical partition function can be writen as:

$$Q_{N,V,T} \equiv \frac{1}{\Lambda^{3N}N!} \int d\mathbf{r}^N e^{[-\beta U(\mathbf{r}^{\mathrm{N}})]} \equiv \frac{1}{\Lambda^{3N}N!} Z(N,V,T). \tag{2.8}$$

Therefore the configuration integral is defined as:

$$Z(N,V,T) = \int d\mathbf{r}^N e^{[-\beta U(\mathbf{r}^{\mathrm{N}})]}. \tag{2.9}$$

2.1.4. Isobaric-isothermal NPT Ensemble

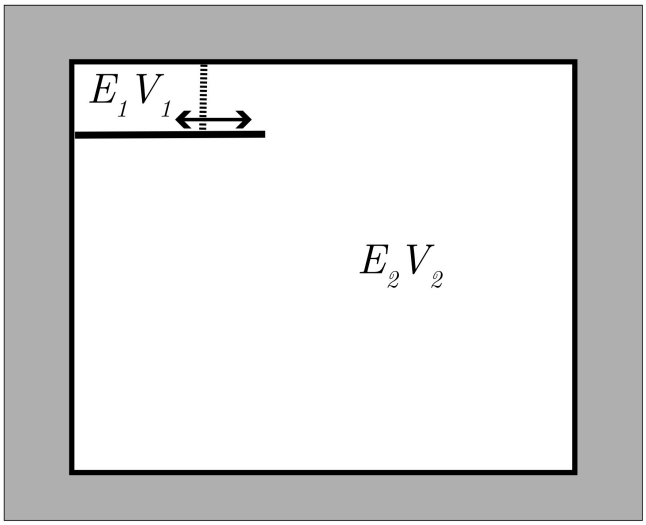

Figure 2.1: Isolated system composed of two subsystems which can change volume and exchange energy while the total volume remains the same. System two is also a lot larger such that it can act as a heat bath and it can exert a constant pressure on system one [28].

Often in experiments it is easier to control the temperature rather than the volume, therefore the NPT ensemble can be of great use [28]. Starting from a quantum expression for the total entropy of a system composed of system 1 and system 2 where system 2 is in contact with system 1 and acts as both a barostat and thermostat and the subsystems can change their volume while the total volume remains the same and they can exchange their energy, as shown in figure 2.1, is equal to [28]:

$$S = S_1 + S_2 = k_b \ln \Omega_1(E_1, V_1, N_1) + k_b \ln \Omega_2(E_2, V_2, N_2). \tag{2.10}$$

System 2 is much larger than system 1, therefore an expansion of Ω around V and E:

$$\begin{aligned} \ln \Omega_2(E_2, V_2, N_2) &= \ln \Omega(E, V, N_2) + \left.\frac{\partial \ln \Omega(E, V, N_2)}{\partial E}\right|_{N,V} (E - E_1) + \left.\frac{\partial \ln \Omega(E, V, N_2)}{\partial V}\right|_{N,E} (V - V_1) + \dots \\ &= \ln \Omega(E, V, N_2) + \frac{E - E_1}{k_B T} + \frac{P(V - V_1)}{k_B T} + \dots \end{aligned} \tag{2.11}$$

While keeping only the first-order terms in this expansion and nothing that the remaining terms are constant with respect to system 1, the probability of observing system 1 with energy E_1 and volume V_1 is proportional to [28]:

$$exp[-\frac{E_1 + PV_1}{k_B T}]. \tag{2.12}$$

Which bring us to the partition function $Q \equiv Q(N, P, T)$, which is an integral over the particle coordinates and over the volume [28]:

$$Q(N, P, T) \equiv \frac{\beta P}{\Lambda^{3N} N!} \int dV exp[-\beta PV] \int d\mathbf{r}^N exp[-\beta U(\mathbf{r}^N)]. \tag{2.13}$$

2.1.5. Temperature and Pressure via Equipartition Theorem and the Virial Expression

The temperature in molecular dynamics is defined through the equipartition theorem, in which the average kinetic energy $\langle K \rangle$ per degree of freedom is computed [28]. For a system with f degrees of freedom the temperature then becomes:

$$k_B T = \frac{\langle 2K \rangle}{f}. \tag{2.14}$$

The number of degrees of freedom of an system with N amount of particles is equal to $Nd - N_c$, where d is the dimensionality and N_c is the number of constraints [28].
In the canonical ensemble, the pressure can be obtained from the derivative of the Helmholtz free energy with respect to volume. Leading to the virial expression:

$$P = \frac{N k_B T}{V} + \frac{1}{3V} \langle \sum_{i=1}^{N} \mathbf{F}_i * \mathbf{r}_i \rangle \tag{2.15}$$

where the first term corresponds to the ideal-gas contribution and the second term accounts for intermolecular interactions [28].

2.1.6. Boundary Conditions

MD simulations are performed on systems which contain a finite number of particles, in order to let the system behave approximately as a macroscopic system and reduce the finite size effects, boundary conditions are imposed. With the most common method being that the system, which can be represented by cubic box, in replicated in the x, y and z directions to form an infinite lattice [7].

Due to the periodic boundary conditions, a particle that leaves the simulation box through once side will re-enter the box through the opposing side. The interactions are then computed as if the particles were surrounded by an infinite amount of periodic images [7].

The interparticle interactions are taken into account using the minimum image convention, whereby each particle interacts with the nearest periodic image of every other particle. Therefore the shortest distance is used for the calculations of the interaction force calculations [7]. The minimum image convention is valid provided that the interaction cutoff radius is less than half the smallest box dimension [7].

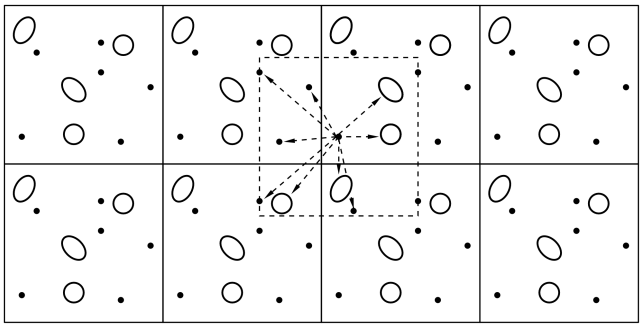

Figure 2.2: Representation of a periodic boundary condition causing an infinite lattice, where the simulation box is replicated in all spatial directions. The minimal image convention is also illustrated by the dashed box, where a particle interacts only with the closest periodic image of a neighboring particle [28]

2.1.7. Interatomic Interactions

Interactions between particles can be described by the classical potential energy function U, which is dependent on the instantaneous position of all atoms in the system. The potential energy can be expressed as the sum of the bonded and nonbonded contributions: [7].

$$U = U_{bonded} + U_{nonbonded} \tag{2.16}$$

where bonded interactions account for the covalent bonds within the molecules and nonbonded interactions for the forces between atoms that are not directly bonden [7].

The bonded interactions are often represented using harmonic or inharmonic potentials to describe the bond stretching and angle bending and torsional motion.

$$U_{bonded} = \sum U_{bond}(r) + \sum U_{angle}(\theta) \sum U_{dihedral}(\phi). \tag{2.17}$$

The molecular structure is maintained by these terms and are short ranged, as they only act between the connected atoms [7].

The nonbonded interactions consist of a short-range of repulsive and attractive contribution, often modeled using a Lennard-Jones 12-6 potential [7].

$$U_{LJ} = 4\epsilon_{ij}[(\frac{\sigma_{ij}}{r_{ij}})^{12} - (\frac{\sigma_{ij}}{r_{ij}})^{6}]. \tag{2.18}$$

Where ϵ is the depth of the potential well, which indicates the attraction between particle i and j and σ_{ij} is the finite distance at which the LJ potential is zero [7].

Another term which takes into account the electrostatic interactions between partial charges is the Coulomb interaction:

$$U_{coulomb}(r_{ij}) = \frac{q_i q_j}{4\pi\epsilon_0 r_{ij}}. \tag{2.19}$$

Where q_i and q_j are the charges and ϵ_0 is the permittivity of free space [7]. The Lennard–Jones potential captures Pauli repulsion at short distances and dispersive attraction at intermediate distances, while electrostatic interactions decay more slowly with distance [7].

In order to reduce computational cost, the nonbonded interactions are truncated to a finite cutoff radius r_c. For short-range interactions this is generally valid provided that the cutoff is chosen to be large enough [7]. As mentioned in subsection 2.1.6 the minimum image convention and periodic boundary conditions require that the cutoff radius to be smaller than half the smallest box dimension [28].

Cutoff methods are suitable for short-range interactions, but electrostatic interactions decay slowly with distance and therefore cannot be accurately simulated. Therefore special methods are required to treat the long-range electrostatics which will be discussed in section 2.3 [7].

2.2. Force Fields

2.2.1. TIP and SPC Water Models

The TIP and SPC models are rigid non-polarizable models that describe water interactions [60]. There are several different types of these models but they can be separated in terms of their amount of sites, which are mostly three-site (TIP3P and SPC/E, four-site (TIP4P and TIP4P/2005) and five-site models (TIP5P) [60].

The water models discussed share the same underlying form for the potential energy, consisting of bonded terms, and nonbonded Lennard-Jones and Coulomb interactions. The primary differences between these models arise from the number and placement of interaction sites, the distribution of partial charges, and the choice of geometric parameters [60].

$$U_{total} = U_{bond} + U_{angle} + U_{LJ} + U_{Coul}. \tag{2.20}$$

The two parameters for the Lennard-Jones interactions of the TIP3P model were chosen to reproduce the density, pressure and vaporization enthalpy at room temperature of water [60]. The second three-site model, the SPC/E model, with its key difference with TIP3P being that the SPC/E model does not use the experimental geometry of the water molecule in the gas phase, it simply uses two simple values for the bond length and bond angle (1 Å instead of the experimental 0.9578 Å for bond the bond length and 109.5 degrees instead of the experimental 105.46 degrees for the bond angle) [60]. Another difference between SPC/E and TIP3P is how the interactions parameters where obtained. While also for the SPC/E model the parameters where obtained by reproducing the density, pressure and vaporization enthalpy at room temperature, the vaporization enthalpy was corrected for the self-polarization, which a not-polarizable model cannot account for, with the self-polarizability being the term that takes into account that the dipole moment of the water molecule is different in the gas phase than from the liquid phase [60]. The correction is given by:

$$\frac{E_{pol}}{N} = \frac{(\mu - \mu_{gas})^2}{2\alpha_p} \tag{2.21}$$

where α_p is the polarizability of the water molecule, μ_{gas} and μ is the dipole moment of the molecule in the gas phase and the model respectively.

For the two four-site models, TIP4P and TIP4p/2005 the positive charges are located on the hydrogen atoms, which is also the case for the SPC/E and TIP3P models, but the negative charge is now not placed on the oxygen atoms but along the HOH bisector [60]. In terms of the used interaction parameters the method of obtaining them are the same for TIP3P and TIP4P. Where for the TIP4P/2005 again the corrected enthalpy of vaporization is used to obtain the interaction parameters. The difference between the TIP4P and the TIP4P/2005 is that the instead of the densty at room temperature, which was used for TIP4P, the isobar densities where used to obtain the interaction parameters for TIP4P/2005 [60].

The final model is the TIP5P model, in which again the positive charges are placed on the hydrogen but there now being placed two negative charges on the position of the lone pair electrons position [60]. While the interactions parameters where obtained in the same manner as the TIP4P model [60].

2.2.2. ClayFF

The ClayFF force field was developed to model hydrated mineral systems, which include clays, oxides and hydroxides, with their interfaces with aqueous solutions [23]. Therefore the ClayFF model provides a general set of simple interatomic potentials that allow investigation into their complex behavior in MD simulations, since traditional characterization and spectroscopic analysis are quite difficult due to the complex chemistry, presence of water and hydroxyls and lack of quality single crystals and other limitations [23].

ClayFF predominantly uses a nonbonded description of interatomic interactions. In contrast to conventional bonded force fields, metal-oxygen interactions are treated using a combination of Coulombic electrostatics and short-range Lennard-Jones interactions rather than explicit covalent bonds [23].

$$U_{total} = U_{Coul} + U_{VDW} + U_{\text{bond stretch}} + U_{\text{bond angle}}. \tag{2.22}$$

The total potential energy in ClayFF can be seen as the sum of the electrostatic, Van der Waals and bonded contributions (bond angles and bond stretch). The Van der Waals contributions are modeled using the Lennard-Jones 12-6 potential, as shown in equation 2.18 [23]. The Coulomb interactions are modeled using the Coulomb potential as shown in equation 2.19. The bonded interactions are then modeled as:

$$U_{\text{bond stretch}} = k_1(r_{ij} - r_0)^2 \tag{2.23a}$$

$$U_{\text{bond angle ijk}} = k_2(\theta_{ijk} - \theta_0)^2. \tag{2.23b}$$

Where k_1 and k_2 are the force constants, and r_0 and θ_0 are the equilibrium bond length and equilibrium bond angle. The bonded interaction terms are included only for water molecules and hydroxyl groups [23].

This model is commonly combined with SPC-based water models and has been shown to reproduce structural and interfacial properties accurately for a wide range of mineral systems [23]

2.2.3. IFF

The Interface Force Field (IFF) is an all-atom parameters force field that have undergone validation to reproduce a variety of bulk and surface properties of inorganic compounds, bio molecules and polymers [32]. Rather than introducing a new functional form, IFF is designed as an extension of widely used harmonic force fields such as AMBER, CHARMM and OPLS-AA, thereby allowing inorganic and organic components to be treated within a single, compatible framework [32].

IFF uses the standard harmonic force field potential, in which the potential energy can be decomposed, similarly to the other force fields mentioned, into bonded and nonbonded contributions [32]:

$$U_{pot} = U_{bonds} + U_{angles} + U_{dihedrals} + U_{impropers} + U_{Coul} + U_{LJ} \tag{2.24}$$

where the first four terms describe bonded interactions, bond stretching, angle bending, dihedral torsions and out-of-plane distortions respectively, and the last terms represents nonbonded Coulombic and Lennard–Jones (LJ) interactions respectively [32].

The principle of how the parameters are obtained for IFF is thermodynamic consistency, which means that the parameters should reproduce both atomic scale and macroscopic experimental observables in two steps. Firstly the atomic charges are assigned to reproduce the experimental electrostatics properties, such as the dipole moments and dielectric constants. Once determined, these charges are kept fixed and are not adjusted to reproduce bulk thermodynamic properties [32]. Secondly, the Lennard-Jones parameters, are the refined to reproduce bulk and interfacial thermodynamic properties, such as density, surface tension and cleavage energy. This sequential parameterization avoids the compensating errors between electrostatic and Van der Waals interactions [32].

2.2.4. Xiao's Force Field

In order to simulate calcite correctly in MD simulations Xiao et al. developed a force field to accurately model the structural and mechanical properties of calcite ($CaCO_3$) crystals, with an emphasis to reproduce their anisotropic elastic behavior at atomic scale [63]. Unlike other calcite force fields that were parameterized reproducing thermodynamic properties, this force field optimizes elastic constants [63].

$CaCO_3$ has both ionic and covalent characteristics. There is the strong covalent bonding withing the carbonate ion and highly charged calcium cations. The interatomic interactions are modeled using a combination of Coulombic electrostatics and Lennard-Jones interactions, while also maintaining the internal geometry of the carbonate ion with bonded interaction terms [63]. The total potential energy is given by:

$$U_{pot} = U_{Coul} + U_{LJ} + U_{angle} + U_{dihedral}. \tag{2.25}$$

Where U_{angle} is defined in equation 2.23b, and $U_{dihedral}$ equates to:

$$U_{dihedral} = k(1 - \cos 2\phi). \tag{2.26}$$

Where here k can be seen as the force constant and ϕ is the out of plane dihedral angle [63]. In the case of the U_{angle}, here the θ_0 is equal to 120 degrees, corresponding to the equilibrium carbonate geometry. The molecule is treated as a rigid molecular unit constraint by angular and dihedral terms and therefore no bond stretching term required [63].

The force field parameters were optimized by fitting experimental unit cell parameters and elastic constant matrices of aragonite, resulting in the force field showing to accurately reproducing elastic moduli, surface energies and lattice energies, while this force field has also been demonstrated to be transferable to other $CaCO_3$ polymorphs such as calcite and vaterite [63].

The cross interaction parameters for the $CaCO_3$-water systems were derived using the three point TIP3P water model. It was done by fitting Lennard–Jones interactions such that molecular dynamics simulations can reproduce the experimentally determined crystal structure of hydrated $CaCO_3$ phases [63].

2.2.5. Hydrogen Models (single,two and three-site models)

Several hydrogen models exist to represent the hydrogen in the MD simulations. The Hirschfelder model treats the hydrogen as a single site, spherically symmetric particle, interacting via a Lennard-Jones 12-6 potential [56]. This model does not take the rotational degrees of freedom and electrostatic multipoles into account making it very computationally efficient and especially suitable for situations where hydrogen behaves approximately as a simple Van der Waals gas. The total potential energy for the Hirschfelder model is given by:

$$U_{\text{pot Hirschfelder}} = U_{LJ}. \tag{2.27}$$

The Buch model was developed to also take the quantum rotational effects of hydrogen into account. Therefore, the hydrogen molecules are treated as quantum rotors and an anisotropic interaction arises from that that quadrupole-quadrupole coupling [17]. The total potential energy can be describes as:

$$U_{\text{pot Buch}} = U_{LJ} + U_{quad}. \tag{2.28}$$

Where $U_quad \propto \frac{Q^2}{r^5}$ with Q being the quadrupole moment [17].

Lastly, the Alavi model is a rigid diatomic hydrogen model which is parameterized to reproduce the adsorption energies and thermodynamics of hydrogen in confinement and at interfaces [3]. It represents the hydrogen using a combination of partial charges placed on the hydrogen atoms and an additional site at the molecular center of mass. The nonbonded interactions are represented using the Coulombic and Lennard-Jones terms:

$$U_{\text{pot Alavi}} = U_{Coul} + U_{LJ}. \tag{2.29}$$

Cross-interaction parameters with water are obtained using standard Lorentz–Berthelot combination rules [3].

2.3. Long range Interactions

Accurate treatment of long-range interactions is essential in molecular dynamics simulations, particularly for systems containing charged species and extended interfaces. Electrostatic interactions decay slowly with distance and cannot be truncated without introducing significant artifacts, while long-range dispersion interactions also contribute to the total energy and pressure of the system [28].

2.3.1. Ewald Summation

In MD simulations, where periodic boundary conditions are present, each charged particle not only interacts with all other particles in the simulation box but also with their infinite set of images [7]. This results in electrostatic energy that involves an infinite sum over Coulomb sum over interactions which, as shown in equation 2.19, decays very slowly as $\frac{1}{r}$. Truncating the interaction at a finite cutoff leads to great artifacts, also taking into account the uphysical shape of the simulation cell which is simulated as a box instead of a sphere [7].

Using the Ewald summation method an efficient way of evaluating this infinite sum by rewriting the Coulomb interactions as the sum of two converging contributions. This is done by adding and subtracting the same smooth charge distributions around each point charge, in which the total charge density remains unchanged while still allowing the electrostatic interactions to be separated into short and long-ranged components [7].

The Ewald construction is built of surrounding a diffuse Gaussian charge cloud of equal magnitude and opposite sign around each point charge, with this Gaussian charge cloud acting as a screening charge, transforming the interactions between neighboring charges into a short-ranged, rapidly decaying potential [7]. The electrostatic interaction between the screened charges can therefore be evaluated efficiently in real space with the finite cutoff:

$$\frac{1}{r} \rightarrow \frac{\operatorname{erfc}(\alpha r)}{r}, \tag{2.30}$$

where $\operatorname{erfc}(x)$ is the complementary error function and α is a screening parameter that controls the spatial extent of the Gaussian charge distribution. The complementary error function approaches 1 at short distances and decays rapidly to zero at large distances, ensuring that the real-space interaction is short-ranged [7].

But due to the introduction of the screening charge clouds the original charge distribution is changed. In order to restore that a compensating Gaussian charge distribution of the same shape and sign is added back, with this compensating charge density being smooth and periodic and its electrostatic energy being evaluated in the Fourier space (reciprocal) [7]. Therefore the long ranged contributions are computed from the Fourier transform of the charge density [7]. Combining these two contributions, the Coulomb interaction is exactly decomposed as:

$$\frac{1}{r} = \frac{\operatorname{erfc}(\alpha r)}{r} + \frac{\operatorname{erf}(\alpha r)}{r}, \tag{2.31}$$

where $\operatorname{erf}(x)$ is the error function. The first term represents the short-ranged, screened interaction evaluated in real space, while the second term contains the smooth long-ranged contribution treated in reciprocal space [7].

A correction is also required in order to remove the interaction of each point charge with its own screening cloud, this self interaction term is independent of the particle positions and can be subtracted directly from the total electrostatic energy [7]. A surface term is also required due the nonzero net dipole moment which is caused by the truncation of the infinite lattice which gives rise to a depolarizing electric field at the boundary [7]. In practice, MD simulations typically assume conducting 'tin-foil' boundary conditions, which corresponds to an external dielectric constant $\epsilon_s \to \infty$. Under these conditions, the surface term vanishes, and the Ewald summation yields a meaningful electrostatic energy for a periodic system [7].

Therefore the total electrostatic energy of a periodically replicated system of point charges can be written as:

$$\begin{aligned} U_{Coul} = & \frac{1}{2}\sum_{i\neq j}\sum_{\mathbf{m}} \frac{q_i q_j \operatorname{erfc}\left(\alpha\left|\mathbf{r}_{ij}+\mathbf{m}L\right|\right)}{\left|\mathbf{r}_{ij}+\mathbf{m}L\right|} \\ & + \frac{1}{2V}\sum_{\mathbf{k}\neq 0}\frac{4\pi}{k^2}\exp\left(-\frac{k^2}{4\alpha^2}\right)\left|\sum_{j=1}^{N} q_j e^{i\mathbf{k}\cdot\mathbf{r}_j}\right|^2 \\ & - \frac{\alpha}{\sqrt{\pi}}\sum_{i=1}^{N} q_i^2 \; + \; \frac{2\pi}{3V}\left(\sum_{i=1}^{N} q_i \mathbf{r}_i\right)^2 . \end{aligned} \tag{2.32}$$

where, q_i and $\mathbf{r}_i$ denote the charge and position of particle i, $\mathbf{r}_{ij} = \mathbf{r}_i - \mathbf{r}_j$, L is the box length, V is the simulation cell volume, and $\mathbf{m}$ runs over all lattice vectors of the periodic images. The parameter α controls the width of the Gaussian screening charge distribution and determines the relative weight of the real and reciprocal space contributions. The reciprocal space sum runs over all nonzero wave vectors $\mathbf{k} = 2\pi\mathbf{n}/L$, with $\mathbf{n} \in \mathbb{Z}^3$ [7].

2.3.2. Particle Mesh Ewald (PME)

Conventional Ewald summation provides an accurate description of the electrostatics, although its computational cost scales heavily with system size [28]. To make the computation more efficient, the Particle Mesh Ewald method can be applied, which increases the computational efficiency of the reciprocal space contribution [28]. This is done by the fact that the Poisson equation can be solved more efficiently if a mesh is used and the charges are distributed with fixed spacing. Fast Fourier Transforms (FFT) can be used to compute the Fourier components of the charge density due to applying a mesh, which lowers the computational cost [28].

This method reduces the computational complexity of the reciprocal space calculation from $\mathcal{O}(N^{3/2})$ to $\mathcal{O}(N \log N)$, where N is the number of particles. The accuracy of PME is controlled by the grid spacing, interpolation order, and the Ewald screening parameter [28]. PME has become the standard method for treating long-range electrostatics in MD simulations due to its balance between accuracy and efficiency [28].

2.3.3. Slab and Vacuum Corrections

General Ewald summation and PME methods assume three-dimensional periodicity of the simulation box, which is an appropriate assumption for bulk systems [28]. But there could be the case that one's systems that is finite in one dimension and infinite in the other two dimensions, then special techniques should be applied in order to compute long-range interactions of such inhomogeneous systems [28].

In these systems where one dimension is finite, a net dipole moment develops perpendicular to the interface due to the asymmetric distribution of charges [28]. Under the three-dimensional periodic boundary conditions,

these dipole moment will interact with its own periodic images and will therefore give cause to a electric field across the slab, with this artificial field possibly significantly affecting electrostatic energies and thermodynamic behavior [28].

In order to eliminate these artifacts, an electrostatic correction needs to be applied, with one of the most common ones being the Yeh-Berkowitz correction [28]. This correction removes the contributions of the dipole-dipole correction along the non periodic direction by modifying the reciprocal space contribution of the Ewald sum, the corrections can be written as:

$$U_{\text{corr}} = \frac{2\pi}{V} M_z^2, \tag{2.33}$$

where V is the simulation cell volume and M_z is the total dipole moment of the system along the non periodic direction. This correction effectively enforces two-dimensional periodicity while retaining the accuracy of the Ewald or PME method in the periodic directions [28]. Practically, this correction is combined with a sufficiently large vacuum region to minimize residual interactions between periodic images [28].

2.3.4. Long Range Dispersion Corrections

Van der Waals interactions described by the Lennard-Jones potential are often truncated beyond a finite cutoff radius to reduce computational cost. However, truncation neglects the long-range attractive tail of the r^{-6} dispersion interaction, which contributes to the total potential energy and pressure of the system.

To account for this missing contribution, analytical long-range dispersion corrections are applied to the energy and pressure, assuming a homogeneous bulk system beyond the cutoff, with these corrections improving the accuracy of the thermodynamic quantities. The analytical correction to the Lennard-Jones energy can be written as:

$$U_{\text{disp}} = N \frac{8\pi\rho}{3} \varepsilon\sigma^6 \left[\frac{1}{3} \left(\frac{\sigma}{r_c} \right)^9 - \left(\frac{\sigma}{r_c} \right)^6 \right]. \tag{2.34}$$

For interfacial systems or slab systems however, the assumption of a homogeneous density distribution is incorrect and can therefore result the long range dispersion corrections may no longer be valid and can introduce systematic errors. In those cases the correction could be neglected [28].

2.4. Surface and Interfacial Thermodynamics

2.4.1. Surface Tension

In the interface between two phases, molecules experience an asymmetric environment due to the absence of neighboring particles on one side of the interface. Due to this imbalance, an excess free energy associated with one interface exists, which is commonly referred to as the surface tension. This surface tension, γ, can be defined as the change in free energy at constant N, V and T of an area of a flat unstructured surface or interface [28]. Starting from the Helmholtz free energy (F) of a single component system surface area A, N, V and T:

$$dF = -SdT - PdV + \mu dN + \gamma dA. \tag{2.35}$$

Which becomes:

$$\gamma = \left(\frac{\partial F}{\partial A} \right)_{N,V,T}. \tag{2.36}$$

For a liquid-vapor interface, surface tensions represents the energetic cost of increasing the surface area by one unit and it usually being expressed in force per unit length (N/m) or energy per unit area (J/m^2) [46].

In MD simulations, surface tension is often described using the mechanically derivation from the anisotropy of the pressure tensor. For a planar interface which is oriented perpendicular to the z direction, the surface tension can be described as:

$$\gamma = \frac{L_z}{2} \left(P_N + P_T \right) \tag{2.37}$$

where $P_N = P_{zz}$ and $P_T = \frac{1}{2}(P_{xx} + P_{yy})$ are equal to are the diagonal components of the pressure tensor and L_z is the box dimension normal to the interface [7]. In which the microscopic pressure tension arises from the intermolecular forces and can be defined by the viral expression:

$$P_{\alpha\beta}(z) = \rho(z)k_B T\delta_{\alpha\beta} + \frac{1}{V}\langle \sum_{i=1}^{N-1}\sum_{j>i}^{N}(\mathbf{r}_{ij})_\alpha(\mathbf{f}_{ij})_\beta \frac{1}{|z_{ij}|}\Theta\left(\frac{z_i - z}{z_{ij}}\right)\Theta\left(\frac{z - z_j}{z_{ij}}\right)\rangle \tag{2.38}$$

where α and β are the Cartesian components, z the spatial coordinate perpendicular to the interface and Θ the unit step function [7].

For curved interfaces, surface tension gives rise to a pressure difference between the two phases [72]. For a cylindrical interface of radius R, the Laplace pressure is given by:

$$\Delta P = \frac{\gamma}{R} \tag{2.39}$$

indicating that smaller bubbles require higher internal pressures for mechanical stability [72].

2.4.2. Contact Angle and Young's Equation

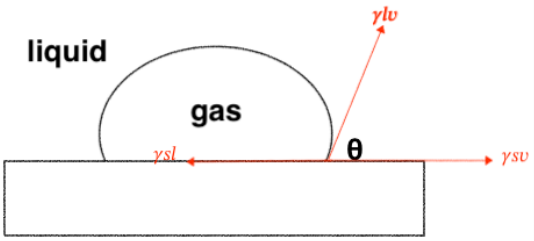

Figure 2.3: Schematic showing the force balance between at the three phase contact line. The contact angle θ here is defined as the angle between the solid and the outer angle of the droplet or the bubble, with the three line tensions shown in red.

When a liquid comes into contact with solid surface in the presence of a gas phase, a three phase contact line is formed. The shape of this liquid droplet or gas bubble can be characterized by a contact angle θ. This angle is characterizes the tangent between the liquid and gas interface with the solid surface [54]. By the measurement of these contact angles, great insight into the material properties and liquid/gas-solid interactions can be extracted [54]. The contact angle is determined by a balance of interfacial tension acting at the three phase contact line as shown in figure 2.3 [40]. This balance is described by the Young's equation:

$$\gamma_{sv} - \gamma_{sl} = \gamma_{lv}cos(\theta_y) \tag{2.40}$$

where γ_{sv}, γ_{sl} and γ_{lv} denote the solid–vapor, solid–liquid, and liquid–vapor interfacial tensions, respectively. Young's equation assumes an idealized system consisting of a rigid, chemically homogeneous, and perfectly smooth surface. Under these assumptions, the contact angle provides a macroscopic measure of the relative affinity of a surface for the liquid phase [40].

In MD simulations, contact angles are often extracted from the equilibrium shape of the droplets or bubbles by fitting an interface geometry to a density profile. This provides an indirect but practical way to characterize solid-fluid-gas interactions where direct calculation of the interfacial tensions is challenging [54].

2.4.3. Line tension and nanoscale effects

The Young's equation accurately describes the wetting behavior at macroscopic scales, but deviations arise when the dimensions of the system approach the nanometer scale [72]. In such cases, contributions of the line tension effects τ, which is the excess free energy per unit length of the three phase contact line can become quite significant [72]. The Young's equation can therefore be modified by which the line tension effects are also included into the equation, which represent the nanoscale behavior [72]:

$$cos(\theta) = cos(\theta_y) - \frac{\tau}{\gamma_{lv}r} \tag{2.41}$$

where θ_y is the Young's contact angle, which can be seen as the macroscopic contact angle, θ the apparent contact angle and R the radius of the curvature.

For nanoscale droplets or bubbles which are the encountered scales in MD simulations, the radius of the curvature becomes small enough that the ratio between the radius and line tension becomes very large and therefore the line tension effects become very apparent, which therefore significantly affects the contact angle. [72].

2.4.4. Wettability and Adhesion Energy

Another approach which can describe the wetting behavior is provided by the concept of wettability, which reflects the tendency of a liquid to spread over a solid surface. Wettability can be quantified through the work of adhesion, defined as the reversible work required to separate a unit area of solid-liquid interface into solid-vapor and liquid-vapor interfaces. This can behavior can be described by the Young-Dupré equation, where the work of adhesion W_A is given by:

$$W_A = \gamma_{LV}(1 + \cos(\theta)) \tag{2.42}$$

This expression directly links the contact angle to an energetic measure of solid–liquid affinity.

2.5. Crystallography

Crystallography describes the ordered arrangement of atoms in solids. In crystalline materials, atoms are arranged in periodic arrays, whereas in amorphous materials, atoms are not arranged [9]. Atomic order has significant influence on the material properties, as can be seen with by the different carbon polymorphs such as diamond and graphene, which consist of the same element but exhibit different properties [9].

In order to determine crystal structures, techniques such as X-ray and neutron diffraction are applied [9]. With these techniques the lattice parameters and atomic positions can be extracted [9].

2.5.1. Motifs and Lattices

A crystal structure can be described as the combination of a lattice and a motif [9]. The lattice is a periodic array of points in space with identical surroundings, where lattice points do not necessarily correspond to atomic positions, but rather define symmetry [9]. In three dimensions the lattice points are generated by combinations of lattice vectors:

$$\mathbf{r} = u\mathbf{a} + v\mathbf{b} + w\mathbf{c} \tag{2.43}$$

where u, v and w are integers and a, b and c are the lattice vectors [9].

The motif consists of one or more atoms associated with each lattice point. When the motif is placed on every lattice point, the full crystal structure is obtained, as shown in figure 2.4 [9].

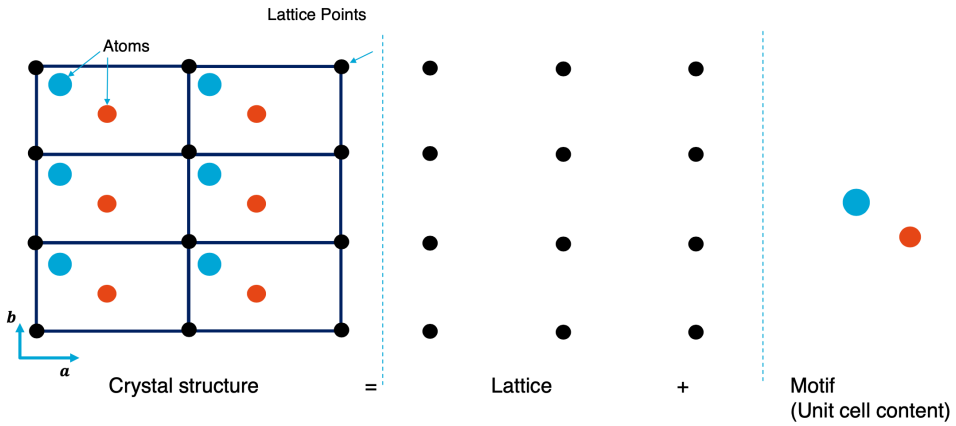

Figure 2.4: Schematic on how the crystal is constructed of the motifs and lattice. Where the crystal structure is composed of the lattice and the motif [9].

The unit cell can be seen as a repeating unit defined by the lattice vectors that span the crystal. The smallest possible unit cell is called the primitive unit cell [9].

In three dimensions the lattices are classified into 14 different Bravais lattices, which are built of combining the 7 crystal classes with the four centering types, namely, the primitive (P), body centered (I), face centered (F) and base centered (C). The seven crystal classes, namely, triclinic, monoclinic, orthorhombic, tetragonal, cubic, hexagonal, and rhombohedral are defined by the lattice parameters, a, b and c and interaxial angles α, β and γ [9].

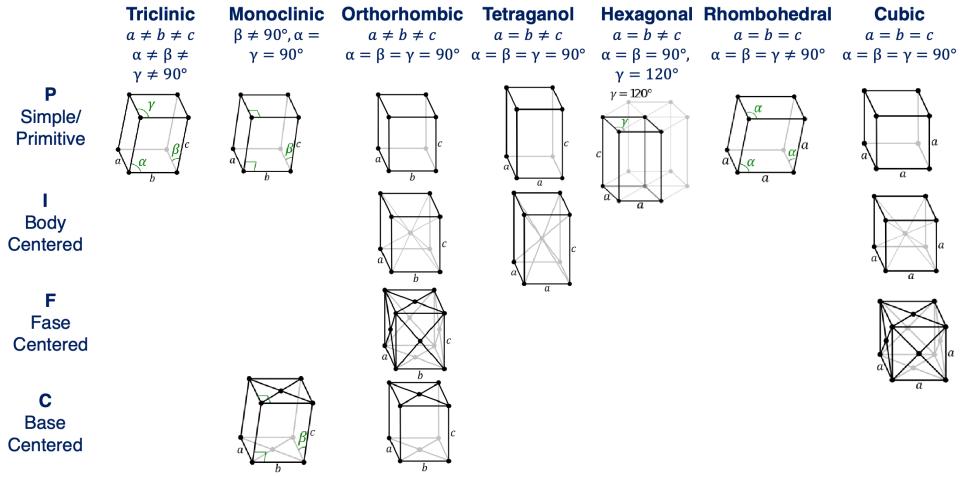

Figure 2.5: Diagram with the 14 different Bravais lattices. The first row of the diagrams shows the crystal classes, and the first column the four different centering types [9].

2.5.2. Miller Indices

Miller indices provide a concise notation to describe orientations of crystallographic planes and directions. Given a set of lattice vectors defining a crystal unit cell, a plane can be defined by three integers $(h\,k\,l)$, where each index is inversely proportional to the intercept of the plane with the corresponding axis [9].

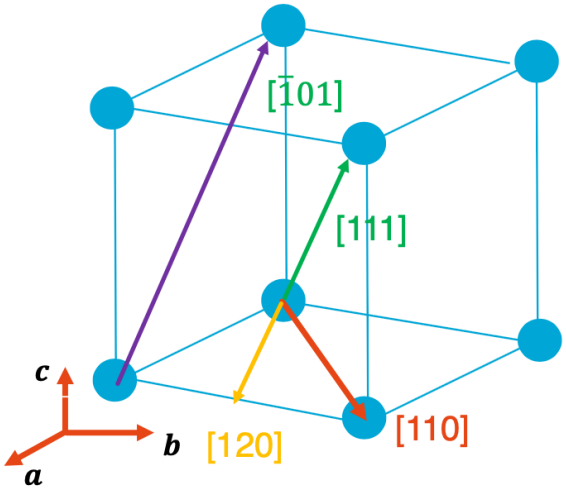

Figure 2.6: Schematic with example Miller indices. The [111], [110], and [120] directions represent regular lattice vectors, while the [$\bar{1}$01] direction illustrates a vector with a negative Miller index [9].

3

Literature Review

3.1. State-of-the-art Description

For Underground Hydrogen Storage (UHS), wettability and transport control the trapping and mobility of stored hydrogen gas. Under nanoconfinement, many interfacial properties (such as viscosity, diffusion and interfacial tension) and apparent contact angle deviate from the bulk behavior [4].

In order to study wettability of hydrogen bubbles the contact angles are assessed, this is usually be done by a sessile drop method or captive bubble method, either a gas bubble or a liquid droplet respectively [25]. In Molecular Dynamics simulations most contact angle studies use quasi-2D bubbles rather than fully 3D spherical bubbles due to the nanoscale line tension biases on the apparent contact angle. In Equation 3.1 and Equation 3.2 you see the general Young's equation and modified Young's equation [36]. Where γ_{sl}, γ_{sv} and γ_{lv} are the the solid-liquid, solid-vapor and liquid-vapor interfacial tensions respectfully. and with θ_y, θ, τ and r being the Young's contact angle and apparent contact angle, line tension and bubble radius respectfully. The reason the bubble is extended in the one of the axes making it an cylindrical slab (and therefore a quasi-2D bubble) is due Equation 3.2 where r becomes infinite ($r \to \infty$) and therefore the third term (line tension including) in the equation tending to zero, causing the apparent angle and the Young's angle to become the same and experimental validation being possible.

$$\gamma_{sv} - \gamma_{sl} = \gamma_{lv} cos(\theta_y) \tag{3.1}$$

$$cos(\theta) = cos(\theta_y) - \frac{\tau}{\gamma_{lv} r}. \tag{3.2}$$

Secondly, while contact angles are well studied in MD, there are few to none MD studies on flow driven bubble transport dynamics in nanopores. There is a significant gap for UHS how velocity profiles affect hydrogen bubbles detachment of the surface, transport and shape.

Finally, micriobial activty (biofilms/EPS layers) is experimentally known to reduce hydrogen contact angles on smooth quartz surfaces and the surface therefore becoming more water-wat [13]. However, Molecular Dynamics simulations involving biofilm-like wettability studies remain scarce, and should be explored further.

3.2. Context regarding Force Fields and Substrate Choice

3.2.1. Force Field - H_2O

There exist many different water models that work well for predicting the bulk water properties in bulk water, with them mainly being split up in three-, four- an five-point and polarizable models [39]. With the models that are mainly used in literature for the properties of this study being the, TIP3P, SPC/E, TIP4P/2005 and TIP5P. Where TIP3P and SPC/E are three-point models, TIP4P/2005 is a model built on TIP4P and a four-point model and lastly TIP5P is a five-point model [60]. The main difference between the different models in terms of amount of points lies in how the partial charges are distributed withing the molecule [60].

Surface Tension

Vega et al. investigated the different water models on their surface tension validity and found that most models do not reproduce quantitatively the experimental data of the surface tension of water. The models that provide

more accurate results of the water surface tension are models that provide a better description of the vapor-liquid coexistence curve. They concluded that SPC/E and TIP4P/2005 gave the best results for the surface tension, with TIP4P/2005 giving being able to accurately describe the surface tension, while SPC/E are found to be in reasonably good agreement with the experimental data as seen by figure 3.1 [59].

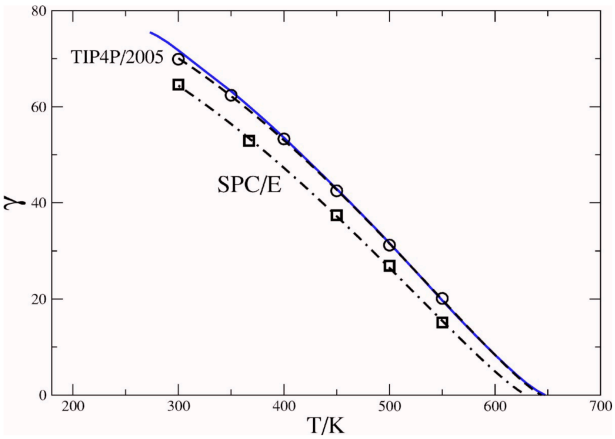

Figure 3.1: Values of surface tension, with solid line being the experimental data, SPC/E being the dotted line with open squares and TIP4P/2005 being the dotted line with open circles. The surface tension is given in mJ/m^2 [59]

The reason for the differing quality on surface tension of the many different models seems to lie in how the target property is defined for the models [60]. With for TIP3P, TIP4P and TIP5P one of the target properties to validate the models being the vaporisation enthalpy (ΔH_v). Models matching the ΔH_v result in rather poor predictions of the surface tension, with the surface tension being predicted too low. The vaporisation enthalpy was not a target property for both SPC/E and TIP4P/2005 and and overestimate the ΔH_v, but therefore yield much better predictions for the surface tension [60]. TIP4P/2005 performes best due to where the negative charge is H – O – H, with the negative charge bing on the bisector for TIP4P/2005 and on the oxygen for SPC/E [60].

Interfacial Tension

In order to validate the water model it is not only important to look at the quality of surface tension results but also the quality of interfacial tension results. Omrani et al. and Adam et al. both investigated the interfacial tension between water and hydrogen using SPC/E and TIP4P/2005 as the water models, which were the best performing models for predicting the surface tension [59], and different hydrogen models [49][1].

Adam et al. conducted experiments comparing SPC/E and TIP4P/2005 by using a two-site hydrogen model. In figure 3.2 the results of the study are shown. It was found that TIP4P/2005 performed very good across different pressures with a discrepancy of around 3-4 mN/m while SPC/E performed quite a bit worse with a discrepancy of roughly 15 mN/m. SPC/E therefore had a absolute relative deviation (ARD) of about 22%, while TIP4P/2005 had an ADR of about 6%.

Omrani et al. did not only compare SPC/E and TIP4P/2005 but also other models such as TIP5Pe and TIP4P OPLS/AA models. Although it became quite clear that TIP5Pe and TIP4P OPLS/AA did not result in very good results, resulting IFTs with an ADR between 25.36% and 36.29% [49]. Comparing SPC/E and TIP4P/2005 at the same temperature and pressure and using a single-site model hydrogen model (Cracknell) in combination with SPC/E and a two/three-site model with TIP4P/2005, it became clear that TIP4P/2005 performed best at providing the IFT's. With TIP4P/2005 having an ADR of 5.43% and SPC/E having an ADR of 21.76% [49]. The discrepancy can be seen as a direct effect of the water model and not necessarily of the hydrogen model, as will be explained in the hydrogen chapter shortly. This results is also comparable to the results retrieved from Adam et al. indicating that in terms of IFT's TIP4P/2005 is superior to SPC/E [49][1].

Choice of Force Field - H_2O

The choice depends on if the data obtained by this research is more used qualitatively and if a discrepancy on IFT data of over 20% justifies the use on a qualitative basis when using SPC/E, or if the choice is made to result in obtaining data that is also quantitatively viable. Of course, SPC/E is less computationally expensive due to it having less interaction sites [60] and therefore, in terms of efficiency, that model is preferred. Discussions will be had what will be the best course of action after review of this research.

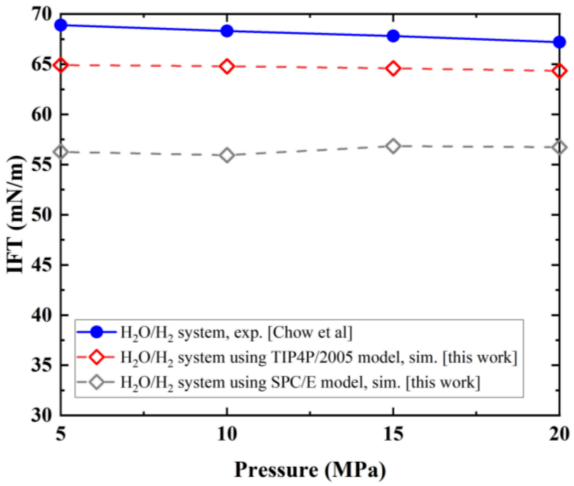

Figure 3.2: Comparison between SPC/E and TIP4P/2005 IFT data of H_2O/H_2 system. With the experimental data used from Chow et al. [22] and temperature of the experiment being 323.15 K [1].

3.2.2. Force Field - H_2

Similarly to the choice of the water model, here we would also prefer to use the least computationally expensive model for the sake of efficiency, which still results in viable physical result. There exist many hydrogen models, such as single-, two and three-site models and more expensive models such as IFF [5][34][34].

Ali et al. looked at different hydrogen models to investigate the wettability of a clay/hydrogen/brine system, with the the clay modeled as a Kaolinite [5]. Before committing to a choice of hydrogen model they first did preliminary testing between a Buch model and Marx model which are a one-site and three-site models respectively. After obtaining the contact angle from both models and them being very similar, $96.6°$ and $96.8°$ for Buch and Marx respectively [5]. They also included IFT and density as compared parameters between the models and came to the conclusion to continue using the Buch model for rest of their paper due to the contact angels being very comparable and the computed density of hydrogen being closer to the experimental value when using the Buch model [5].

Yang et al. compared different hydrogen models such as the Hirschfelder, Alavi and IFF models, which are a one-site, tho/three-site and a general model respectively, together with TIP4P/2005 [64]. The variations due to the different hydrogen models where found to be less significant with an ADR of about 6.4% and 5.5% using Hirschfelder and IFF respectively, as can be seen from figure 3.3 [64]. This highlights the importance of choosing an appropriate water model rather than a hydrogen model.

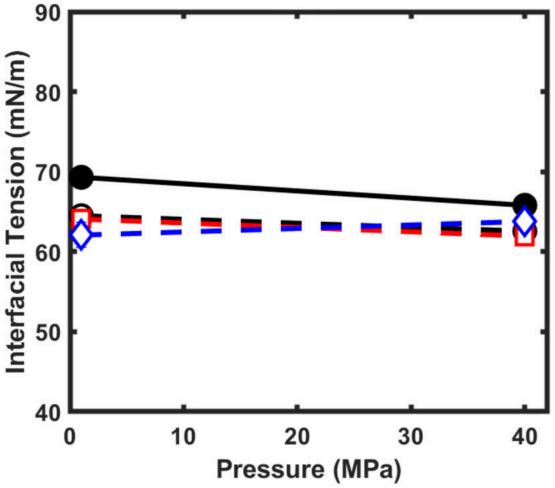

Figure 3.3: IFT values of the different models at 323 K. Where the solid circle is the experimental data from chow et al. [22]. Hirschelder, Alavi and IFF are shown as open circle, square and diamond symbols respectively [64].

3.2.3. Substrate

In the subsurface there are two main substrate type relevant to UHS (Underground Hydrogen Storage). First, caprocks, which act as seals or barriers, are often composed of clay minerals (such as kaolinite and montmorillonite) and evaporates (such as halite). Clay minerals, are common sealing phases due to their low permeability under fluid exposure [26]. Second, reservoir rock, which are often sandstones dominated by quartz or carbonate rocks (such as calcite and dolomite). These reservoir substrates host the storage volume and permeability to successfully allow hydrogen movement and storage [62][48].

Real reservoir and caprocks are heterogeneous which complicates their accurate reproduction in experiments or simulations [52]. The rocks are often simplified to their main constituents, such as quartz or kaolinite [10][66]. As a carbonate rock calcite could be chosen, calcite exhibits hydrophilic behavior due to the presence of Ca^{2+} and $CO_3{}^{2-}$ surface groups [42]. The surface chemistry can become quite complicated due terminations of the surface groups and surface charge possibly effecting wettability [2].
Kaolinite exhibits both extreme hydrophilic and moderately hydrophilic behavior depending on the surface site, with them being Gibbsite (Al – OH)and Siloxane (Si – O) respectively [38]. Kaolinite is therefore inherently water-wet, therefore a kaolinite slit pore tends to saturate with water under subsurface conditions, gas molecules such as CH_4 and by analogy also H2 tend to form clusters/nanobubbles inside of the water phase [81].

The hydraulic conductivity in kaolinite nanpores are nonzero and in order of 10^{-11} nm [75]. This is of course very small and will not be visible when converted to MD scale simulations. By imposing a larger velocity profile of several orders of magnitude larger than natural profiles while the system remains within linear respose regime, the timeframe can be shortened to something visible in MD making a simulation useful [19].

3.3. Hydrogen Bubble Dynamics

There have not been MD nanoscale hydrogen bubble dynamics studies, so some relevant insights from some microscale studies will be discussed.

Boon et al. investigated multiphase flow hydrogen/brine through a Berrea sandstone core under a medical X-ray CT scanner [12][14]. This made it possible to directly image the complex behavior of the H_2 during imbibition and drainage and no-flow periods. Showing that dissolution of hydrogen can significantly influence gas redistribution via Oswald ripening during no flow periods. Where Oswald ripening is the process where smaller hydrogen clusters shrink by dissolution due to their high internal gas pressure and therefore high chemical potential, and re-precipitate at the bigger hydrogen clusters which have a lower chemical potential [12][14].

Song et al. also studied the hydrogen transport through a core, using a 3D printed core and a natural sandstone sample from the underground gas storage (UGS) in China [57]. Multiple cycling injections and extractions were done of hydrogen and nitrogen in the water saturated core samples. The seepage was visualized with a micro-CT and a self developed core holder [57]. Their results showed that there occurs significant redistribution of hydrogen after 12 hours of storage in a natural sandstone sample, where again Oswald ripening is occurring with an increase of both number and size of larger bubbles, which did not occur for nitrogen in their experiments [57].

Salehpour et al. performed a ultra-high-resolution microfluidic experiment that captured the transport of trapped hydrogen ganglia in realistic pore geometries over several weeks [55]. They developed a coupled microscale capillary pressure–saturation ($P_c - S$) relationship using the pore-morphology method (PMM), calibrated against publicly available core-flood datasets. To describe the diffusion driven redistribution of hydrogen they expressed the evolution equation for S_g as [55]:

$$\frac{\partial S_g}{\partial t} = D_{eff} \frac{\partial^2 S_g}{\partial x^2}. \tag{3.3}$$

Where D_{eff} is the effective diffusivity of the hydrogen through the water filled pore space. With the analytical solution of this equation predicting an exponential decay of saturation variations with a characteristic equilibration time [55]:

$$t_{eq} = \frac{\lambda^2}{4\pi^2 D_{eff}}. \tag{3.4}$$

Where λ represents the characteristic spatial length scale of heterogeneity. When extending the model to reservoir scales, the authors computed that the characteristic timescale of ripening is comparable to the seasonal injection - withdrawal cycles typical of underground hydrogen storage [55].

3.4. 3D vs quasi-3D Bubble

Similarly to what is stated in Section 3.1 it remains unclear if the Young's equation is valid on 3D nano bubbles, with there being evidence that the contact angle of nanodroplets and nanobubbles could deviate significantly from the angle predicted from the Young's equation due to the line tensions involved at nanoscale, where the line tension is defined as the excess free energy per unit length of the three phase contact line [73]. To take into account the line tension effects the modified Young's equation has been developed in Equation 3.5:

$$cos(\theta) = \frac{\gamma_{sv} - \gamma_{sl}}{\gamma_{lv}} - \frac{\tau}{\gamma_{lv} r} = cos(\theta_y) - \frac{\tau}{\gamma_{lv} r}. \tag{3.5}$$

Where γ_{sl}, γ_{sv} and γ_{lv} are the the solid-liquid, solid-vapor and liquid-vapor interfacial tensions respectfully. and with θ_y, θ, τ and r being the Young's contact angle and apparent contact angle, line tension and bubble radius respectfully.

Line tensions are not a new subject, although its sign and significance are still unclear. Theoretical analysis of line tensions has been done by for example using density functional theory, yet these studies indicate that the magnitude of the line tension is very small, from 10^{-12} to 10^{-10} J/m. Experimental measurements are very difficult due to these small magnitudes.

MD has often been applied in order to assess the wettability of of nanodroplets and nanobubbles on a surface, as well as line tension behavior. In MD the surface can be modeled as a completely smooth and homogeneous surface. An often used method to measure the line tension in MD is to make a linear fit of the relationship between the cosine of the apparent contact angle to the radius of the contact line.

Zhang et al. states that there is a large variability in MD results for the line tensions, even if the problem setup is the same. While the magnitude is indeed of the order 10^{-11}, the signs are reported to be either positive or negative. The variability in the MD line tension results are a consequence of the definition of the line tension, where the line tension in Equation 5 is not the "pure" line tension but the apparent line tension that combines the effect of the Tolman length and stiffness coefficient of the contact line. Where the Tolman length, denoted as δ, measures how the surface tension changes for very small droplets and bubbles compared to a planar surface [11], and the stiffness coefficients refer to how the line tension depends on the contact angle and contact radius [73]. Therefore at nanoscale, the MD data fitted to the modified Young's equation are apparent line tensions and Tolman lengths and stiffness coefficients might affect those [75].

Zhang et al. utilized MD to simulate 3D nanodroplets on a platinum-type surface for both hydrophilic and hydrophobic cases. They then obtain the apparent line tensions and the effects of the Tolman length and position of the solid-liquid dividing interface were then investigated. The authors demonstrate that the modified Young's equation is useful for predicting the macroscopic contact angle, with the fitting of measured contact angles. While the effect of the solid-liquid dividing interface has an effect on the result [73].

3.4.1. Measurement of the Young's Contact Angle and Apparent Line Tension

The way to measure the apparent line tension is to show the relationship between the cosine of the contact angle and the curvature of the contact line. Once that is done you have a linear equation such as $y = ax + b$ where y is $cos(\theta)$, x is $\frac{1}{a}$, a is $\frac{\tau}{\gamma_{lv}}$ and b is $cos(\theta_y)$. Therefore the intercept is the Young's contact angle and is the contact angle obtained from macroscopic bubbles, and the apparent line tension can be obtained by the slope if the solid-vapor surface tension is known [73].

3.4.2. Tolman Length Effects

The curvature-dependent surface tension can be written as follows:

$$\gamma_{lv}^*(R) = \gamma_{lv}(1 - \frac{2\delta^T}{R}). \tag{3.6}$$

Where R is the droplet radius, γ_{lv} is the liquid-vapor surface tension and $\gamma_{lv}^*(R)$ is the curvature dependent liquid-vapor surface tension. By replacing the γ_{lv} in Equation 3.5 by the $\gamma_{lv}^*(R)$ of Equation 3.6 Equation 3.7 is obtained.

$$cos(\theta) = cos(\theta_y) - \frac{1}{\gamma_{lv} r}(\tau^* - \delta^T \gamma_{lv} sin(2\theta_Y). \tag{3.7}$$

Using Equation 3.7, a linear fit can still be achieved with the slope being $\frac{\tau^* - \delta^T \gamma_{lv} sin(2\theta_Y)}{\gamma_{lv}}$. Where τ^* can be seen as the modified line tension, where Tolman length effects are excluded and curvature dependence is

removed from the line tension, and δ^T being the Tolman length. Therefore the relationship between apparent and modified line tensions is:

$$\tau^* = \tau + \delta^T \gamma_{lv} sin(2\theta_Y). \tag{3.8}$$

When the experimental value of the Tolman length is known and the liquid-vapor surface tension the modified line tension can also be computed. Till thus far there is no computed value for the Tolman length for a hydrogen-water interface, this could be part of the research question. Zhang et al. found that the effect of the Tolman length mattered for extremely hydrophilic and extremely hydrophobic surfaces and the difference between apparent and modified line tensions being negligible close to 90°. The authors also specified that there was no clear relationship found between the Young's contact angle and the line tensions, therefore other properties, besides Tolman length, effect the system [73]. Lastly the authors state the importance of clearly specifying the solid-liquid dividing interface, in order to get valuable and reproduce able results since small shifts in the z-direction can impact the obtained apparent line tension significantly, while the Young's contact angle is impacted [73].

3.5. Size Dependence of bubble and droplet wetting

Zhang et al. investigated the relationship of size dependence on the wetting behavior of both droplets and bubbles [72]. Using both free energetics analysis and MD simulations their study showed a significant difference in bubble wetting and droplet wetting for bubbles with a size smaller than 10 micrometers [72].

In Equation 3.1, Young's Equation is shown with the angle θ_y being the angle for a bubble system. In Equation 3.9, Young's Equation is shown for a droplet system with θ_d being the Young's contact angle. The two Young's contact angles of the droplet and the bubble can be related by the interfacial tensions as shown in Equation 3.10 and 3.11 [72].

$$\gamma_{sl} - \gamma_{sv} = \gamma_{lv} \cos(\theta_b) \tag{3.9}$$

$$\cos(\theta_b) = -\cos(\theta_d) \tag{3.10}$$

$$\theta_b = \pi - \theta_d. \tag{3.11}$$

3.5.1. Theoretical Break Down

Starting from a bubble on a substrate with the volume of the bubble being V^b and its liquid/vapor and solid/vapor interfacial area being A_{lv} and A_{sv}. They can be written as:

$$V^b = \frac{1}{3}\pi R^3 (1 - \cos(\theta_b))^2 (2 + \cos(\theta_b)) \tag{3.12}$$

$$2\pi R^2 (1 - \cos(\theta_b)) \tag{3.13}$$

$$\pi R^2 \sin^2(\theta_b). \tag{3.14}$$

With the assumption that the volume of liquid solution surrounding the formed bubble is large enough so that pressure and temperature changes due to the formation of the bubble can be neglected [72]. The change in Helmholtz energy can be written as shown in Equation 3.15, where P^{in} and P^{out} are the pressure inside and outside of the bubble. $\gamma_{sv} - \gamma_{sl}$ can be replaces by $\gamma_{lv}\cos(\theta_d)$. The effect of line tension is neglected due to it being very small [73]. Also since the gas is insoluble and the solvent is involatile the chemical potential is also neglected [72].

$$\Delta F = -(P^{in} - P^{out})V^b + \gamma_{lv} A_{lv} + (\gamma_{sv} - \gamma_{sl}) A_{sv}. \tag{3.15}$$

The Helmholtz free energy then becomes Equation 3.16 at equilibrium states. The assumption is made that the insoluble gas acts ideally and therefore the state equation of the ideal gas can be applied $NK_bT = (\Delta + P^{out})V^b$ in which ΔP is the Laplace pressure, $\Delta P = 2\gamma_{lv}/R$ [72]. Using the ideal gas constraint Equation 3.17 can be obtained.

$$\begin{aligned} d\left(\frac{\Delta F}{\gamma_{lv}}\right) = \pi R\left[4(1-\cos\theta_b) + 2\cos\theta_d \sin^2\theta_b - \frac{4}{3}\left(2 - 3\cos\theta_b + \cos^3\theta_b\right)\right] dR \\ + \pi R^2\left[2\sin\theta_b(1 + \cos\theta_d\cos\theta_b) - 2\sin\theta_b(1 - \cos^2\theta_b)\right] d\theta_b = 0 \end{aligned} \tag{3.16}$$

$$d\left(\frac{NK_BT}{\gamma_{lv}}\right) = \pi R\left[\left(\frac{4}{3}+\frac{RP'}{\gamma_{lv}}\right)\left(2-3\cos\theta_b+\cos^3\theta_b\right)\right]dR$$
$$+\pi R^2\left[\left(2+\frac{RP'}{\gamma_{lv}}\right)\sin\theta_b\left(1-\cos^2\theta_b\right)\right]d\theta_b = 0. \tag{3.17}$$

Combining Equations 3.16 and 3.17, a relation between θ_b, θ_d and R can be obtained [72].

$$\left[4+2\cos\theta_d(1+\cos\theta_b)+\frac{RP'}{\gamma_{lv}}\left(2-\cos\theta_b-\cos^2\theta_b\right)\right](1+\cos\theta_b)\left(2+\frac{RP'}{\gamma_{lv}}\right)$$
$$=\left[2+2\cos\theta_d\cos\theta_b+\frac{RP'}{\gamma_{lv}}\left(1-\cos^2\theta_b\right)\right](2+\cos\theta_b)\left(\frac{4}{3}+\frac{RP'}{\gamma_{lv}}\right). \tag{3.18}$$

If R is large enough $\frac{RP^{out}}{\gamma_{lv}}$ dominates in Equation 3.18, and it therefore simplifies to Equation 3.10. However, when R is very small, then $\Delta P >> P^{out}$ (since $\Delta P = \frac{2\gamma_{lv}}{R}$). Therefore the pressure inside the bubble is much greater that the external pressure of the liquid, with $\Delta P = \frac{2\gamma_{lv}}{R} \rightarrow 0$ and Equation 3.18 can be simplified to Equation 3.19 [72].

$$\cos\theta_b = \frac{-2-\cos\theta_d+\sqrt{4+2\cos\theta_d-2\cos^2\theta_d}}{\cos\theta_d}. \tag{3.19}$$

3.5.2. Differences from 'Realistic' Simulations

Zhang et al. mentioned in their studies several points that can be discussed on where their research differs from more realistic systems. With the main points being that the gas is insoluble and the liquid being involatile [72]. Therefore across the gas-liquid interface there will occur no mass transfer:

$$\frac{dN_{liquid}}{dt} = 0 \qquad \frac{dN_{gas}}{dt} = 0. \tag{3.20}$$

Due to there being no mass transfer across the bubble interface, the ideal gas law is being applied on Equation 3.15 [72]. What is important to note, is that therefore only mechanical equilibrium is taken into account in the system. Realistic gases are soluble and realistic liquids are volatile, and therefore the use case of the ideal gas law would fail. Also chemical equilibrium should be obtained in a realistic system, therefore the chemical potential terms should be present in Equation 3.15 [71]. In Equation 3.21 the free energy for a realistic system is shown where the chemical potential components are also included. Where B and ΔB are the free energy and the change in free energy of the system, G^L, F^L, F^{LG}, F^{LG}, F^{LG}, P^L and V^b are the Gibbs, Helmholtz function together with the liquid pressure and bubble volume respectively, with the subscripts L, G, LG, SG and SL representing liquid, gas, liquid-gas, solid-gas and solid liquid respectively [71].

$$B = G^L + F^G + F^{LG} + F^{SL} + F^{SG} + P^L V^b. \tag{3.21}$$

When then considering system as a two component system in a closed environment Equation 3.21 then can be derived to Equation 3.22

$$\begin{aligned} B = {} & (\mu_1^L n_1^L + \mu_2^L n_2^L) + (\mu_1^G n_1^G + \mu_2^G n_2^G - P^G V^b) \\ & + (\mu_1^{LG} n_1^{LG} + \mu_2^{LG} n_2^{LG} + \gamma^{LG} A^{LG}) \\ & + (\mu_1^{SL} n_1^{SL} + \mu_2^{SL} n_2^{SL} + \gamma^{SL} A^{SL}) \\ & + (\mu_1^{SG} n_1^{SG} + \mu_2^{SG} n_2^{SG} + \gamma^{SG} A^{SG}) + (P^L V^G) \end{aligned} \tag{3.22}$$

Where μ is the chemical potential, n is the molar number, γ is the interfacial tension and A is the interface area. The change in the free energy can be defined when a reference state is taken into account, meaning when the system is not in equilibrium and the bubble still needs to completely form, as shown in Equation 3.23 [71].

$$\begin{aligned} \Delta B = {} & \gamma^{LG} A^{LG} - A^{SG}\cos\theta - (P^G - P^L)V^b \\ & + N_1\left(\mu_1^L - \mu_1^0\right) + N_2\left(\mu_2^L - \mu_2^0\right) \\ & + \left(n_2^G + n_2^{LG} + n_2^{SG}\right)\left(\mu_2^G - \mu_2^L\right) \end{aligned} \tag{3.23}$$

In Equation 3.23 you see an similar to Equation 3.15, although now the chemical potential terms are also included in the equation and therefore is not only mechanically correct but also chemically complete. It can be understood that it becomes much more difficult to obtain a relation between the bubble contact angle, droplet contact angle and radius [72]. Although a similar breakdown such as Zhang et al. is to be expected, with a shift due to system specific chemical effects.

3.5.3. MD simulation Break Down

Zhang et al. continued to investigate MD simulation to see if they would behave similar as the theoretical behavior explained in subsection 3.5.1. LAMMPS is used in this study where firstly a droplet of a linear chain solvent molecules in contact with a flat substrate is studies and afterwards a gas bubble surrounded by the same solvent on the same flat surface [72]. Simulations were done on the NVT ensemble where the liquid, gas and solid where represented by a truncated 12-6 Lennard-Jones (LJ) potential with a 3.2σ cutoff distance. The gas molecules are simulated as singe LJ beads, while the solvent molecules contain four LJ atoms and are connected by the finite extensible nonlinear elastic potential (FENE), with the maximum bond length being 1.5σ and the spring constant being $20\varepsilon\sigma^2$ [72].

The size of the boxes was chosen to be 30σx30σx40σ and 35σx35σx30σ, while applying boundary conditions on all three directions. During the simulation the substrates were fixed, frozen to the top and bottom of the box [72]. In order to generate different surface wettability the interaction parameter is adjusted between the solid and the solvent atoms from 0.35ε to 0.8ε, while the interaction between the gas-liquid and gas-solid was fixed to 0.3162ε and 0.25ε respectively. To convert the reduced units to real units the LJ parameters of argon should be used [72].
The contact angles were obtained by counting the heights and radius and averaging them over 50 ns. The contact angle can then be obtained using the geometry of the spherical cap, as shown in Equation 3.24. Where r is the base radius and h is the cap height from the top of substrate [72].

$$\cos(\theta) = \frac{r^2 - h^2}{r^2 + h^2}. \tag{3.24}$$

In figure 3.4 the graph is shown where both Equations 3.11 and 3.19 are plotted together with the MD contact angle data. The figure shows that Equation 3.19 captures the general trend of the MD data points and that the generally implied Equation 3.11 fails at nano scale. Therefore, when bubble sizes are decreased to nano scale, there is a large difference between the bubble contact angle and the droplet contact angle. It is therefore important to not ignore either phase which would cause in over- or underestimation of the contact angles [72].

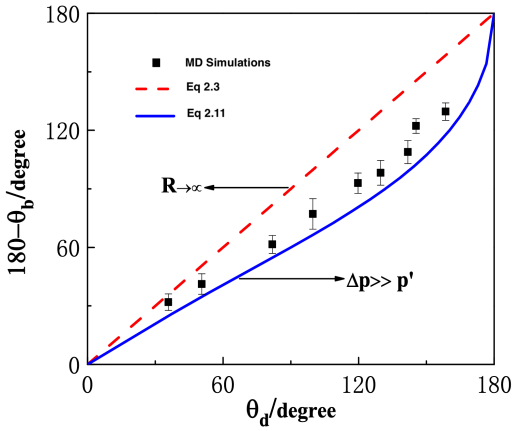

Figure 3.4: Comparison between the different bubble and droplet contact angle relationships supported with MD contact angle data. A clear deviation is shown of the MD simulation contact angles with the expected linear behavior of the contact angles at macroscale between bubbles and droplets [72].

3.5.4. Need for Bubble Studies

From the perspective of underground gas storage and specifically underground hydrogen storage, multiple experimental pore-scale imaging studies indicate that hydrogen is present as gas bubbles or ganglia trapped in water/brine saturated porous media [47][69]. The gas then occupies the pore centers with the wetting phase coating the mineral surface, resulting in a discontinuous capillary trapped hydrogen phase. There exist little evidence for there being liquid droplets surrounded by a hydrogen gas phase in underground reservoir conditions. This reinforces that bubble wetting is physically the most relevant system for UHS.

3.6. Review of UHS Wettability Studies

In this section a literature study of the UHS wettabilitty studies will be done. A lot of different wettability studies with many different substrates and gas compositions have been done in recent years relevant to UHS. Tables 3.1 and 3.2 give a good overview of the different studies that have been done in this field. These studies span across different substrates such as quartz, carbonate and several clays under a wide range of pressures, temperatures and salinities. Most studies utilized a sessile droplets or captive bubbles geometry to obtain the contact angles, with sessile droplets being utilized the most. Many different variations were also used in terms of force fields for the gases and brines, while for the substrates often CLAYFF was employed.

Table 3.1: Simulation system setup overview of molecular dynamics studies investigating H_2/H_2 and mixed-gas systems on mineral surfaces.

Reference	Substrate / Termination	Gas Composition	Fluid Phases	Geometry	Force Fields (solid / water / gas / ions)	P (MPa)	T (K)	Sim. Time (ns)	Notes
Al-Yaseri et al. (2023) [67]	Quartz (001) (Q2), Calcite	H_2O	H_2O/Brine	Droplet	CLAYFF / SPC/E / IFF / (Aqvist + Chandrashekhar)	5–20	300–323	11	
Al-Yaseri et al. (2023b) [68]	Quartz-Q2 (+humic acid)	H_2	H_2O /Brine [0.5M]	Bubble	CLAYFF / SPC/E / OPLS–AA / IFF / (Aqvist + Chandrashekhar	Ambient	300	100	Humic acid reduces hydrophilicity
Ali et al. (2024) [6]	Kaolinite (001) Al–OH / Si–O	H_2, H_2+CO_2, H_2+CH_4	Brine (10 wt% NaCl)	Droplet + bubble	CLAYFF / SPC/E / EPM2–CO_2 / Buch/Marx/ TraPPE–UA	5–40	323	5	Dual component gas bubbles were studied, floating due to hydrophilic rock
Zheng et al. (2024) [80]	Quartz (Q2,Q4)	H_2, CH_4	H_2O/Brine	Droplet	CLAYFF / SPC/E / Three-stie/ OPLS–AA	1–30	338	-	Methylation decreases and salinity (methylated surface increases hydrophilicity
Chen & Xia (2024) [20]	Quartz (Q2,Q4)	H_2, CH_4, CO_2	H_2O	Droplet	IFF / TIP4P / TraPPE, OPLS–AA/ IFF	1–60	320	6	Multi-gas comparison
Huang et al. (2024) [34]	Quartz (Q2)	H_2, CH_4, CO_2	Brine (1.5–3 M NaCl)	Droplet	CLAYFF / OPC4 / TraPPE– UA , Aimei , Yagasaki	20	333	15	$\mathrm{CO_2} > \mathrm{CH_4} > \mathrm{H_2}$ contact angle trend
Ghafari et al. (2024) [29]	Quartz (101 and 001), β – Cristobalite (101 and 111)	H_2, CH_4, CO_2, N_2	H_2O	Droplet	IFF / SPC/E / IFF, Cygan, TraPPE / (Smith and Dang)	10–30	333–413	10	pH, surface charge effects
Chen et al. (2023) [21]	Quartz (Q2)	CO_2-H_2 mixtures (0–30 mol% H_2)	Brine	Bubble	IFF / TIP4P-2005 / TraPPE, IFF / Madrid-2019 ions	10	300–400	-	Temperature increase causes contact angle decrease
Yu et al. (2025) [70]	Graphene	H_2, CH_4, CO_2	H_2O	droplet	CVFF / SPC/E / IFF, CVFF, CVFF	5–40	292–343	5	contact angle decreases with T , and increases with P; $\mathrm{CO_2} > \mathrm{CH_4}$
Phan et al. (2025) [51]	Talc, Kaolinite	H_2, +CO_2/CH_4 (0–40 %)	Brine (20 wt% NaCl + 1 wt% KCl)	droplet	CLAYFF / SPC/E / three-site / EPM2 / TraPPE-UA	15	333	50	Talc hydrophobic, kaoOH hydrophilic
Zheng et al. (2024b) [78]	Quartz (Q2,Q4) with varied roughness and methylation	H_2, CH_4	brine (NaCl 0–0.5 M)	Droplet	IFF / TIP4P-2005 / IFF, OPLS–AA	0–30	300–338	15–20	Pressure and surface chemistry strongly affect contact angle
Yang et al. (2024) [65]	Quartz (Q2) and kerogen slabs	H_2	H_2O	Droplet	IFF / TIP4P-2005 / IFF	1–160	298–523	10	Compared three H_2 models, weak contact angle variation with P,T, validation of FF choice
Yao et al. (2025) [66]	Quartz (Q3,Q4)	H_2	Brine (NaCl,KCl,$CaCl_2$ 0–5.4 mol kg^{-1})	Droplet	INTERFACE / TIP4P-2005 / IFF	14–150	323–423	9-12	Assessed salinity, temperature and FF effects
Zhang et al. (2025) [74]	Quartz, Calcite, Halite, Na-Montmorillonite	H_2	Brine (NaCl 0–1 $molL^{-1}$)	Droplet	CLAYFF / SPC/E / IFF	5–20	300–400	10	Multi-mineral comparison, water-wetness maintained, mineral order in terms of water wetness $MMT > calcite > quartz > halite$

Table 3.2: Summary of contact-angle determination methods and key wettability findings from molecular dynamics studies.

Reference	Method for θ	Wetting Character	Gas Dependence	Main Observations	Relevance for UHS
Al-Yaseri et al. (2023) [67]	2D density mapping	Strongly hydrophilic	H_2	No P–T dependence on θ	Confirms H_2 non-wetting behavior
Al-Yaseri et al. (2023b) [68]	2D density mapping	hydrophilic to hydrophobic	H_2	Organic acids reduce θ	Models aged reservoirs
Ali et al. (2024) [6]	2D density mapping	Siloxane: Intermediate to hydrophobic Gibbsite: hydrophilic	H_2, CH_4, CO_2	Cushion gases lower IFT therefore increase in contact angle	
Zheng et al. (2024) [80]	2D density mapping	Hydrophilic to hydrophobic	H_2, CH_4	Methylation increases contact angle and salinity decreases contact angle	
Chen & Xia (2024) [20]	2D density mapping	Hydrophilic	H_2, CH_4, CO_2	The interaction of H_2 with H_2O/silica is much weaker than that of CH_4 and CO_2.	Explains gas affinity hierarchy
Huang et al. (2024) [34]	2D density mapping	Hydrophilic	$CO_2 > CH_4 > H_2$ contact angle trend	Salinity increases contact angle; gas–solid forces dominate	Caprock wetting order validated
Ghafari et al. (2024) [29]	2D density mapping	Hydrophilic	$CO_2 > CH_4 > N_2 > H_2$ contact angle trend	Increased pH causes decreased contact angle	Multi-gas effects on silica
Chen et al. (2023) [21]	2D density mapping	CO_2-wet, H_2-wet contrast	CO_2 dominant	contact angle decreases with with T; CO_2 strong adsorption	Mixture & T effects quantified
Yu et al. (2025) [70]	2D density mapping	Intermediate to gas-wet	H_2<CH_4<CO_2	contact angle decreaes with T, and increases with P	Organic shale caprock behavior
Phan et al. (2025) [51]	2D density mapping	Talc hydrophobic, kaoOH hydrophilic	CO_2/CH_4 on Talc	CO_2/CH_4 increases contact angle on talc, not on kaoOH	Cushion gas effects on clay faces
Zheng et al. (2024b) [78]	2D density mapping	Hydrophilic to hydrophobic	H_2, CH_4	increased contact angle wiht methylation, decreased with salinity	
Yang et al. (2024) [65]	2D density mapping	Hydrophilic	H_2	contact angle nearly constant with P,T	Provides FF benchmark for H_2/H_2O interfaces
Yao et al. (2025) [66]	2D density mapping	Hydrophilic	H_2	Salinity and T affect contact angle, $CaCl_2$ most hydrophobic system	Quantifies salt-type dependence and confirms silica remains water-wet
Zhang et al. (2025) [74]	2D density mapping	Hydrophilic	H_2	contact angle stable with P,T	Cross-mineral wettability trend

Quartz based substrates [67][79][34][20] remain the most studies systems, often serving as a representation of sandstone reservoirs. The studies consistently report hydrophilic behavior for hydroxylated surfaces, which are the Q2 or Q3 surfaces, and weakly hydrophobic behavior for the dehydroxylated surfaces, which are the Q4 surfaces. Recently, more studies also focussed on different substrates such as kaolinite, montmorillonite and talc, which extends the studied minerals also to the caprocks [51][4][74]. Where Zhang et al performed a multi-mineral comparison showing that the mineral order of decreasing hydrophilicity was $MMT > Calcite > Quartz > Halite$ [74].

Most studies studied H_2 as the sole gas in the system or discussed cusion gas affects. This was done by simulating the gases separately [34][20] or as a mixture of gases [51][70][4]. With all studies using binary gas mixtures with hydrogen. Expect for Ali et al. the studies that looked at binary gas mixtures applied the sessile droplet system, where Ali et al also looked at a binary mixture bubble [4]. From the studies a consistent trend emerges, wettability decreases in the order $CO_2 > CH_4 > H_2$. While temperature and pressure effects are generally minor compared to surface chemistry and ionic composition.

3.6.1. Physical and Chemical Roughness

Physical roughness can be seen as topography roughness, meaning different geometric features in the surface. These features can be expressed as steps, kinks grooves or pits, therefore these features can be seen as the deviations in height and shape from a perfectly flat plane [15]. Chemical roughness can be seen as the heterogeneity of the surface. Therefore can be explained as the spatial variation of surface chemistry at nanometer scale, e.g. patches with different functional groups. These could be silanol or methyl for groups for Quartz or different degrees or hydroxylation or different mixtures of termimations for clays. Cassie's law , as shown in Equation 3.25, formalizes how mixed chemistries average to an apparent contact angle. Where f_1 and f_2 are the area fractions of the surface components and θ_1 and θ_2 are the Young's contact angles for perfect smooth patches of that chemistry. In MD this is often done changing densities of the functional groups/charges on the lattice site or by building patchy patterns [61].

$$\cos(\theta_c) = f_1 \cos(\theta_1) + f_2 \cos(\theta_2) \tag{3.25}$$

There have been studies that looked at the roughness of a substrate and included a wettability study [78][77]. Where for on study the quartz was used as the substrate and a roughness factor of 2.1 was applied, where the roughness factor can be seen as the value of the rough surface area divided by the smooth surface area [78]. Another study used a similar roughness that was obtained after having applied an Atomic Force Microscopy at nanoscale on a Ketton rock (carbonite rock), where then the surface roughness was remodelled and can be seen in figure 3.5. Afterwards Fourier Transforms were computed to obtain the most prominent frequent oscillation period. These resulted in figure 3.6 and were then analyzed in terms of wettability of H_2O droplet [77].

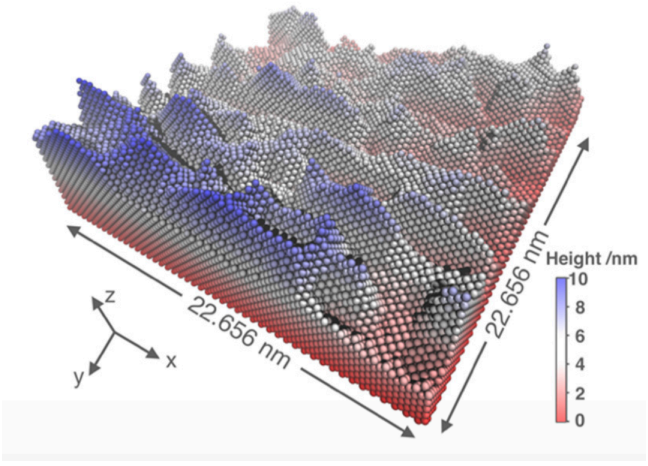

Figure 3.5: Visualization of a reconstruction of a Keton surface at nano scale [77].

3.6.2. Reactive Molecular Dynamics

A topic that also could be explored is reactive MD. Nonreactive 'classical' MD can already capture static wettability trends for many different systems, using the nonreactive force fields such as IFF, CLAYFF as shown in

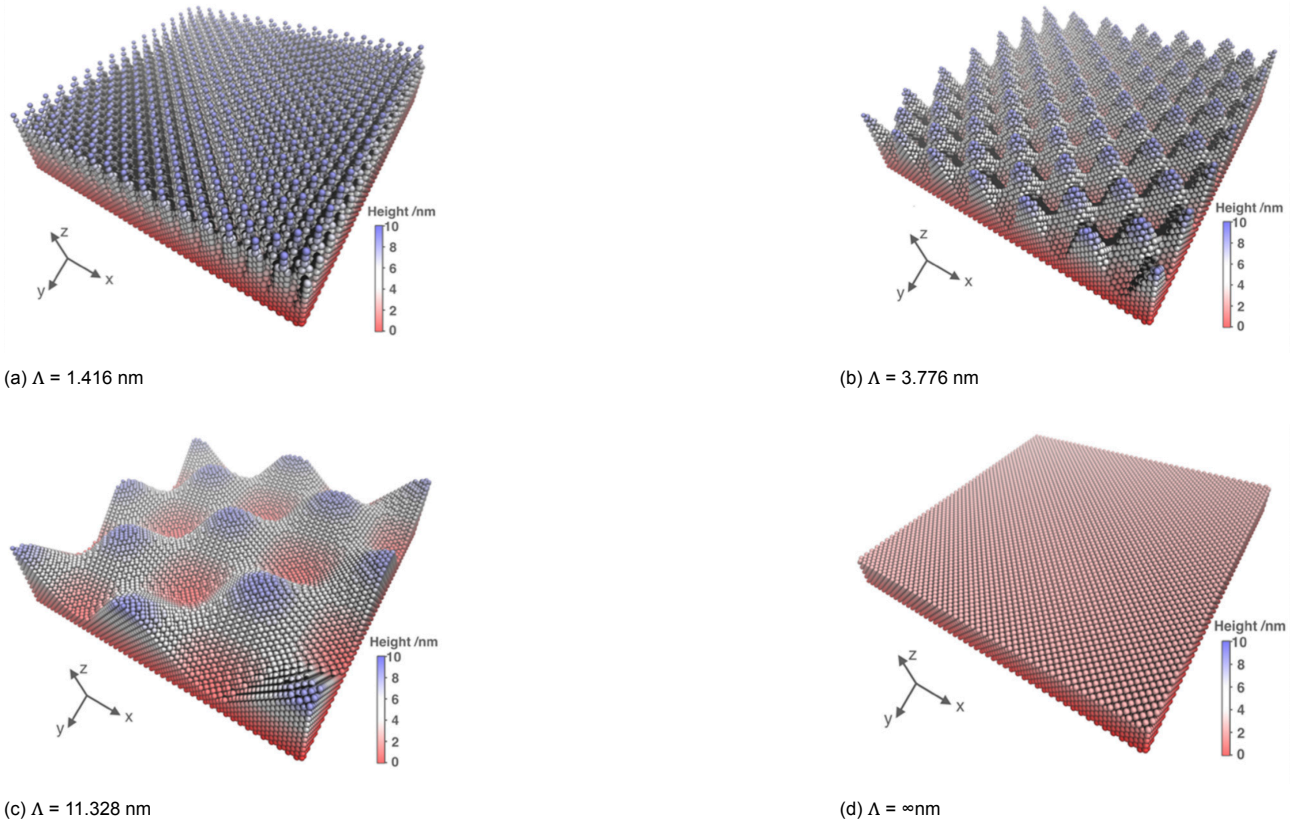

(a) Λ = 1.416 nm

(b) Λ = 3.776 nm

(c) Λ = 11.328 nm

(d) Λ = ∞nm

Figure 3.6: 4 sinusoidal surfaces with a 4 nm amplitude and different wavelengths, characterized by the usage of Fourier transform [77].

Tables 3.1 and 3.2. Reactive MD would be able to capture dissociating of CO_2, calcite precipitation or surface hydroxylation/dehydroxylation. Also, the pH evolution would not be fixed anymore and could also change over time. Chemical aging of the surface could become apparent. Question that could be answered would be if alternating H_2/CO_2 injection chemically ages a caprock surface at nano-scale [24][43].

There are several main issues about reactive MD, with the main one being simulation time. Due to the usage of the reactive force field ReactFF, many more calculation are made in terms of bond-order evaluation and charge equilibration. Therefore the time steps used are also much shorter in reactive simulations and the real time total simulation duration can amount to 15-20x the time of a classical MD run [45]. Another issue is finding a correct parameter element set for the ReactFF system that is validated. There are some parameter sets for certain combinations of elements but not necessarily specified for UHS systems. For instance, the silica-water ReaxFF sets can reproduce hydroxylatiom/dehydroxylation on quartz surfaces but do not include ions, and other gases out of the box [27]. So in practice, for UHS, studies must find a validated parameter set that reproduce that subsystem and stay within its element set.

3.6.3. Research Gaps

Most pressure and temperature effects have already been extensively studied, so in terms of research gaps, the main possibilities lie in the substrate choice and system configuration. As mentioned before, many studies looked at binary gas systems, although all but one applied it on a droplet system. In subsection 3.5.4, it was discussed that bubble measurements are very important for UHS wettability studies and that droplet and bubble measurements can't be easily translated back and forth at nano scale as is possible in the macro scale. Therefore studying bubble systems with different gas compositions seems to be a prominent research gap. In addition to this, it is known that CO_2 can decompose into HCO_3^- and CO_3^{2-}, and is often neglected in the simulation [70]. Therefore another possible option is to look into the effects of the decomposed CO_2 gases on the contact angle. Lastly, roughness is a property which is also often neglected and in its place a smooth surface is modeled. Although it remains unclear if true roughness is present at nano scale, there is roughness present at microscale with a root-mean-square of 0.8-10 nn [25]. Zheng et al. included a roughness factor of 2.1 to a quartz surface and also changed the degree of methylation, where it is mentioned that at higher pressures the roughness can induce pinning effects and therefore affect the contact angle. Zheng et al. does state that both pinning effects and H_2-quartz interaction mechanisms influence the contact angle, but to ascertain which mechanism is dominant, more studies should be done [78].

4

Methods and System Design

4.1. Simulation Objectives and Design Rationale

The objectives of the research are already specified in the form of research questions in Section 1.2, but they do need some more clarification of specific choices that have to be made to attain the research goals. These specific system and design choices will be delved into in this chapter.

Therefore, the objectives of the research is to assess the wettability of a bubble composed of both hydrogen and carbon dioxide when in contact with a calcite slab. This slab will also be altered in order to asses the wettability effects by the gases by altering the interactions parameter.

4.2. Substrate Construction

The substrate studied in this research consists of crystalline calcite, $CaCO_3$, representing a carbonate reservoir mineral, which widespread occurrence in the subsurface [42]. A calcite crystal is a trigonal crystal system with space group $R\bar{3}c$, with its experimental lattice parameters being approximately $a = 4.99$ Å, $b = 4.99$ Åand $c = 17.06$ Åat ambient conditions [35]. The structure consists of 30 atoms per unit cell, with $Z = 6$ formula units [8]. These parameters were used as the basis for constructing the bulk cell as shown in figure 4.1a.

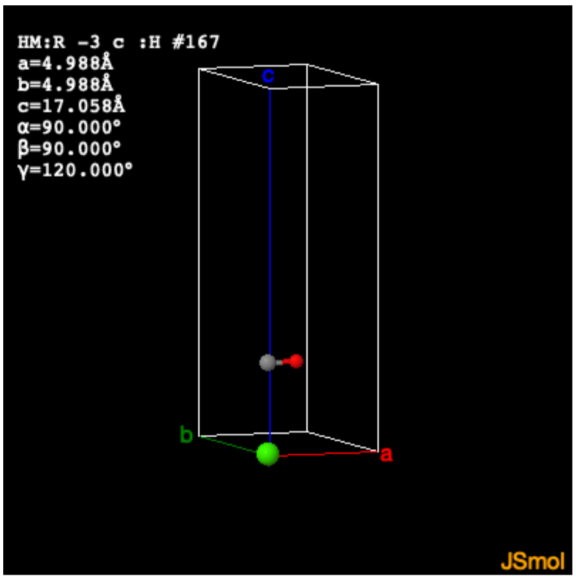

(a) Visualization of the calcite unit cell [35]

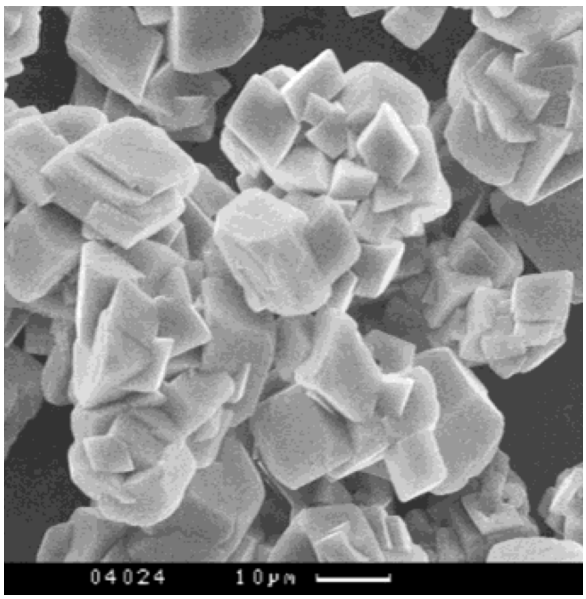

(b) SEM image of a calcite crystal at μm scale [31]

Figure 4.1: A calcite crystal unit cell (a) and a calcite SEM image (b)

4.2.1. Surface Orientation and Cleavage Plane

The calcite slab was cleaved along the thermodynamically stable (104) plane, whereas the (104) plane is the most stable and commonly exposed calcite surface under geological conditions. It has also been extensively characterized experimentally and computationally [35]. Due to its stability and relevance to interfacial studies,

it makes the (104) plane the appropriate surface for wettability studies [35]. The slab was then constructed in such a way the (104) surface was oriented parallel to the xy-plane of the simulation box, with its normal aligned along the z direction.

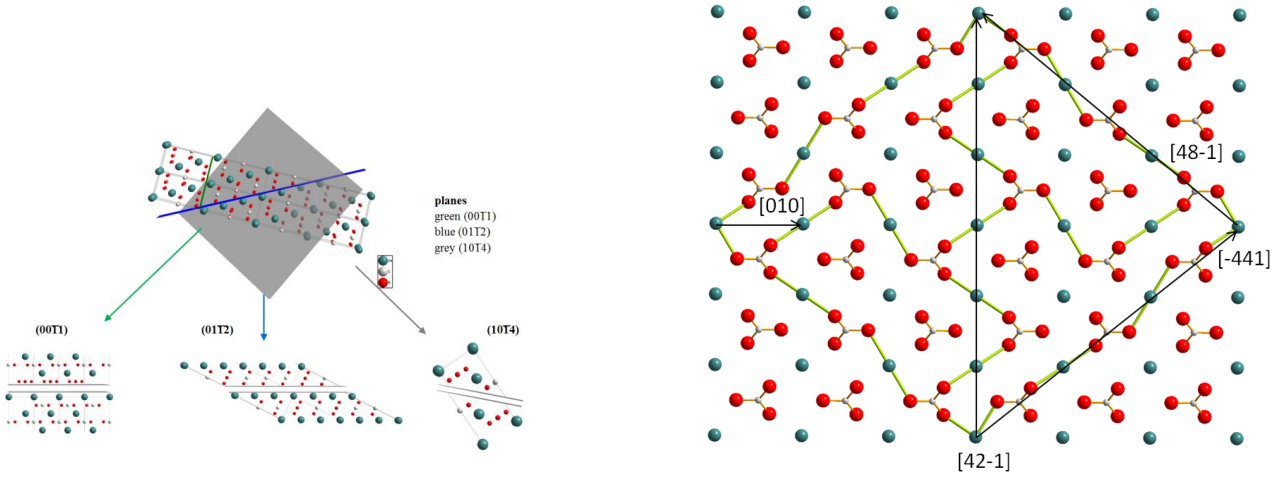

(a) Schematic showing the different possible calcite planes, namely the (010), (012) and (104) planes [41].

(b) Schematic of the molecular structure of the (104) plane of calcite, with lattice vectors and periodic bond chains indicated [31].

Figure 4.2: Illustrations of calcite crystal faces and the (104) surface structure.

4.2.2. Surface Termination

The cleaved surface was constructed in the (104) plane, which can be seen as a charge-neutral configuration. As shown in figure 4.2a, the (104) plane has an alternating CO_3^{2-} and Ca^{2+} which causes the surface to be charge neutral. Therefore the surface will not have additional protonation or hydration layers. The neutral termination ensures electrostatic stability under the periodic boundary conditions and avoids artificial surface dipoles [35].

4.2.3. Slab Thickness and Layer Convergence

The substrate is constructed using eight atomic layers of calcite. This thickness ensures bulk like structural behavior while maintaining computational efficiency, with previous studies showing that a slab thickness of at least 6 layers are sufficient to achieve bulk like properties at the center of the slab and obtain a careful description of the surface [76]. To reduce artificial deformation the whole slab was put under a harmonic position restraint. In this approach, each atom of the slab was restrained to its initial reference position using a harmonic potential of the form:

$$V_{pr} = \frac{1}{2} k_{pr} |\mathbf{r}_i - \mathbf{R}_i|^2 \tag{4.1}$$

with $\mathbf{r}_i$ and $\mathbf{R}_i$ being the reference and instantaneous coordinates of atom i and k_{pr} being the restrain force constant, in this case being equal to 5000 $kJmol^{-1}nm^{-2}$.

4.2.4. Supercell Construction

In order to achieve the sufficiently large surface area, the primitive unit cell was first converted in a unit cell representing the (104) plane, which could later be supercelled in order to achieve the complete slab. By the usage of several transformation matrices a cell of the (104) plane obtained and a representing unit cell could be cleaved from that in the correct configuration. The four matrices used in order to get the (104) unit cell where as follows:

$$\text{(a)} \begin{bmatrix} 2 & 1 & 0 \\ 1 & 1 & 0 \\ 0 & 0 & 1 \end{bmatrix} \quad \text{(b)} \begin{bmatrix} 1 & -1 & 0 \\ 0 & 2 & 0 \\ 0 & 0 & 1 \end{bmatrix} \quad \text{(c)} \begin{bmatrix} 2 & 0 & 0 \\ 0 & 1 & 0 \\ 0 & 0 & 1 \end{bmatrix} \quad \text{(d)} \begin{bmatrix} 0.707 & 0 & 0.707 \\ 0 & 1 & 0 \\ -0.707 & 0 & 0.707 \end{bmatrix}$$

where first the (104) plane is cleaved using the matrix a, afterwards the a direction another cleave was done using matrix b in order to make the cell orthorhombic. Matrix c then doubles the cell in the a direction by which then matrix d rotates the cell around the b axis by 45 degrees in order to expose the (104) plane normal to c and the unit cell. The smallest unit cell can then be extracted from this cell, which can be used to make the supercell representing the calcite slab.

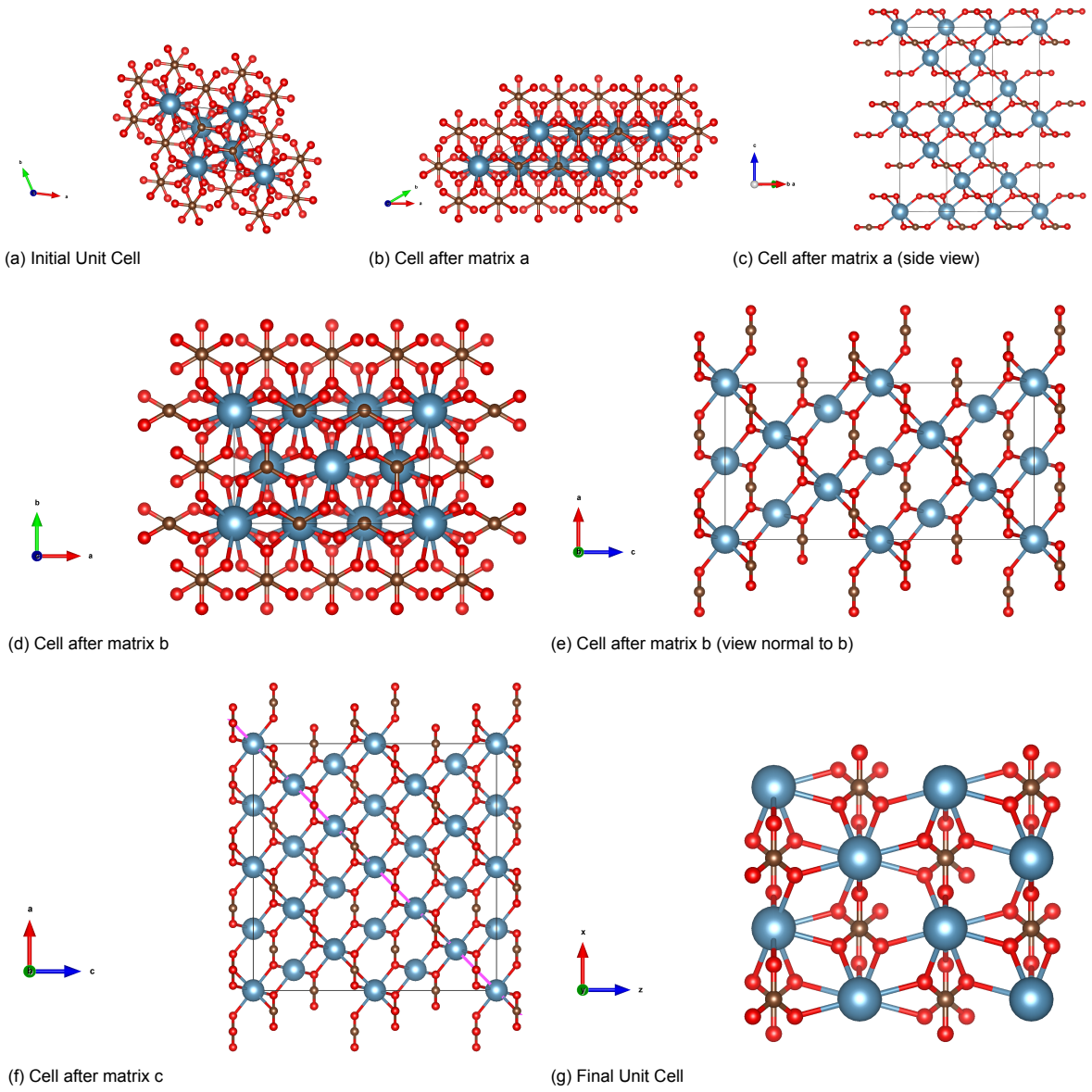

(a) Initial Unit Cell (b) Cell after matrix a (c) Cell after matrix a (side view)

(d) Cell after matrix b (e) Cell after matrix b (view normal to b)

(f) Cell after matrix c (g) Final Unit Cell

Figure 4.3: Cell transformation leading to the final unit cell, where the blue, brown and red particles are Ca, C and O respectively.

The unit cell has dimensions $Lx = 12.13928$ Å, $Ly = 5.03748$ Å, and $Lz = 12.13927$ Å. In order to obtain the calcite slab which will be simulated an matrix d can be applied in order to supercell the unit cell in x, y and z directions:

$$\begin{bmatrix} 13 & 0 & 0 \\ 0 & 32 & 0 \\ 0 & 0 & 2 \end{bmatrix}$$

where the final slab dimension are equal to $Lx = 15.781064$ nm, $Ly = 16.1199936$ nm and $Lz = 2.427854$ nm, as shown in figure 4.4.

4.3. Fluid and Gas Phase

In this study, the liquid phase surrounding the calcite slab consists of water into which a gas bubble of H_2 and CO_2 molecules are introduced. Water was chosen as the solvent to represent reservoir water, of which reservoir brine is the dominant aqueous phase in subsurface systems, but due to time constraints, water has been used as the solvent [33]. H_2 and CO_2 have been employed to represent the gas component, in order to assess the wettability with varying compositions to investigate the influence of the gas mixture on the interfacial phenomena.

Water was modeled using the SPC/E model, which as explained in section 2.2.1, is a rigid non-polarizable three site model. H_2 has been modeled using a single site model defined by Hirschefelder, as explained in section 2.2.5, which is computationally less expensive than the two or three site H_2 models. In section 3.2.2, it

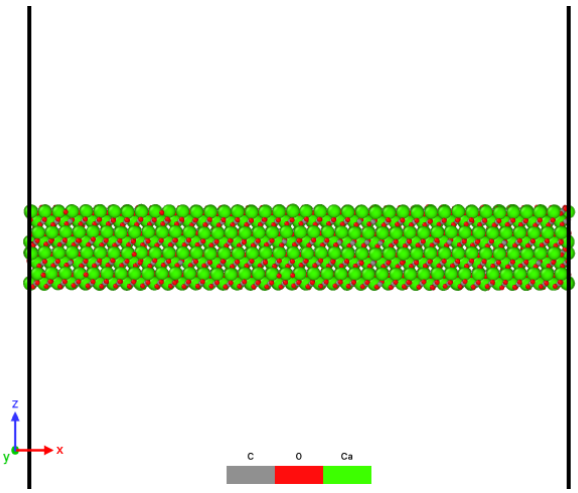

Figure 4.4: Final slab configuration which will be used in the simulations, where the green, gray and red particles are Ca, C and O respectively.

was shown that hydrogen models variations are less significant for the interfacial tensions and rather the water model should carefully be chosen. The CO_2 is modeled using the TraPPE (Transferable Potentials for Phase Equilibria) forcefield, which was developed to describe the thermophysical behavior of small linear molecules [53]. CO_2 is treated as a rigid linear triatomic molecule with LJ interaction sites on each atom and fixed partial charges that reproduce its quadrupolar electrostric character [53]. CO_2 molecules were constrained using the LINCS algorithm to maintain rigidity during the dynamics.

The bubble of gas is modeled as half a cylinder directly on top of the slab with 2 Åof spacing. The reason for modeling the gas bubble as a cylinder was due to the nanoscale line tension effects, as shown in Equation 4.2,

$$cos(\theta) = cos(\theta_y) - \frac{\tau}{\gamma_{lv} r}. \tag{4.2}$$

.
Where the θ, θ_y, τ, r and γ_{lv} are the apparent contact angle, the Young's contact angle, the line tension, the bubble radius and the liquid-vapor surface tension respectively. Equation 4.2 is the modified Young's equation and the line tension parameter is integrated due to it having an affect at nanoscales. The curvature of the three-phase line can be seen as $\kappa = \frac{1}{r}$, where r is the bubble radius and at a large radius the curvature is tending to zero. Therefore, at macroscopic radii the apparent and Young's contant angles are the same due to the third term tending to zero, but at nanoscale that third term cannot be disregarded. Therefore to circumvent this problem, a cylindrical bubble can be utilized, where the bubble is continuous in one of the axes, causing the curvature of the contact line, κ tending to 0, and therefore $r \to \infty$, which causes the third term to again be tend to zero and the measured contact angle behaving the same as it would have at macroscopic scales.

The radius of the cylinder is chosen to be 3 nm. The gas bubble was constructed using the Packmol software, in which both H_2 and CO_2 could be placed in the cylindrical volume with differing mol fractions. Afterwards the cavity was carved out of the water slab in which the gas cylinder could be placed.

4.4. Simulation Box and Geometry

The simulation box dimensions were $L_x = 15.781$ nm, $L_y = 25.0$ nm and $L_z = 20.0$ nm. Periodic boundary conditions were applied in all three spatial directions (x, y, and z). The box length in the x direction matches the lateral dimension of the calcite slab, ensuring continuity in the periodic images.

The system was constructed by combining three components: a calcite slab, a water phase, and a cylindrical gas bubble. The calcite slab spans the entire x direction and has a thickness of approximately 2.43 nm in the z direction. It is positioned in the middle of the simulation box. The reason for it not also being continues in the y direction was to be able to let the water move freely in the simulation box and therefore keep the chemical potential, μ of all systems the same, namely the chemical potential of bulk water.

Around the mineral surface, the remaining volume was filled with liquid water. The water phase surrounds the solid slab to avoid truncation of the water region at the nano scale and to maintain a consistent chemical po-

tential across all simulations. Because water molecules can move freely across the periodic boundaries in all directions, the system effectively maintains the chemical potential of bulk water. A cylindrical cavity was carved out of the water phase to introduce the gas bubble. The bubble extends continuously along the x direction and, due to periodic boundary conditions, forms an effectively infinite cylindrical gas domain. The cylinder has a radius of 3 nm and is centered at [12.5, 16.2] in the x–z plane.

Sufficient clearance between each gas cylinder and other components was applied of 2 Å. In order to not have self interactions between bubbles across periodic images the z and y direction of the simulation box was chosen to be at least twice the diameter of the cylinder.

Due to the slab not being continuous in the y direction, the planes normal to the x vectors are exposed. These are not low energy planes, and therefore when kept as is, the plane will disintegrate, as shown in figure 4.5. In order to solve this problem, 1 nm of each side was frozen in place. In this way, the sides do not disintegrate and the slab does not shift its position in the simulation box.

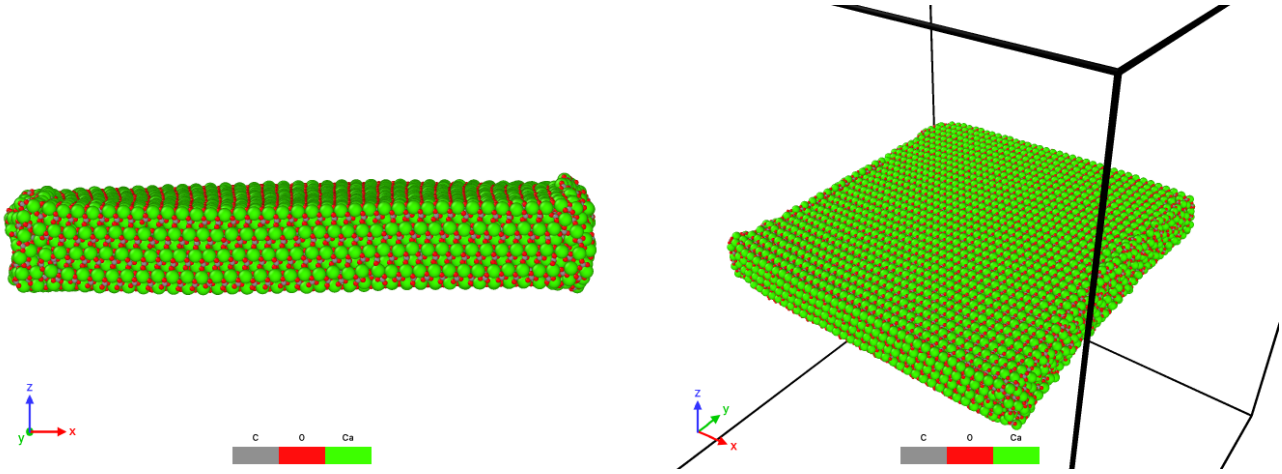

Figure 4.5: Calcite slab snapshots of disintegration of unstable planes. With the unstable planes being the planes with a vector normal the the x and y directions due to the only stable plane being the [104] plane.

An overview of the system construction is shown in figure 4.6. First, the water slab was generated with the slab and bubble volumes removed (figure 4.6a). The calcite slab was subsequently inserted into its carved position (figure 4.6b). Finally, the gas molecules were placed inside the cylindrical cavity, resulting in the complete system (figure 4.6c). A side view illustrating the continuity of the cylindrical bubble along the y direction is provided in figure 4.6d.

4.5. System Variants

The prepared systems were designed to address three distinct research objectives. The first group comprises the reference systems (R), in which realistic interaction parameters were used without modification. These systems serve as the baseline for comparison.

The second group consists of parameter scaling systems (AC), in which the gas–surface interaction strength of either H_2 or CO_2 was systematically modified. The AC systems are further subdivided into ACH and ACC. The third letter indicates which gas species was scaled. In the ACH systems the H_2 interaction parameter was varied while the CO_2 interaction remained unchanged, whereas in the ACC systems the CO_2 interaction parameter was varied while the H_2 interaction remained fixed.

The third group contains the composition variation systems (AF), where the molar fraction of H_2 and CO_2 within the bubble was systematically altered. These systems are subdivided into AFH and AFC. In the AFH systems, H_2 forms the preferentially adsorbed layer at the surface, while in the AFC systems CO_2 forms the preferentially adsorbed layer. This distinction allows investigation of how different substrate affinities influence interfacial behavior and wettability.

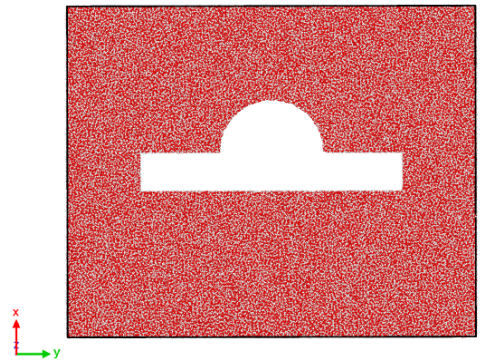

(a) Water slab with slab and bubble positions carved out.

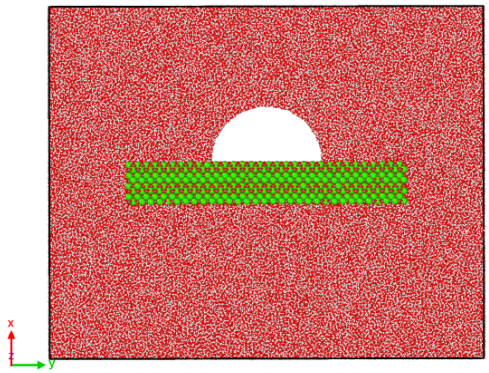

(b) Water slab with slab placed in its carved position.

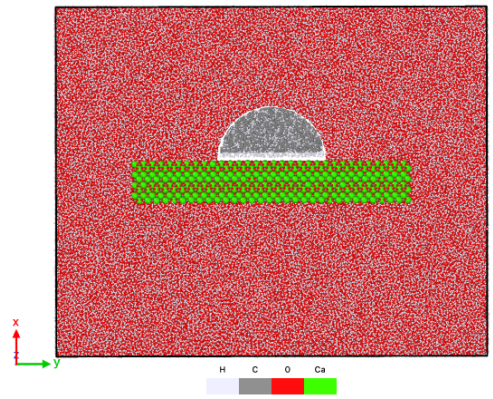

(c) Full system including the bubble (front view).

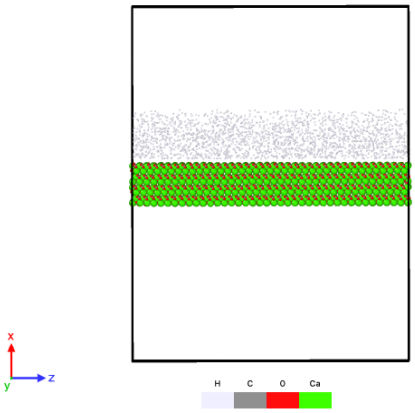

(d) Side view (no water), showing the continuity of the cylinder bubble.

Figure 4.6: Overview of system configuration. Different sub steps of the configurations are shown in (a), (b), (c) and (d).

4.6. Force Fields and Interactions

All components of the system were described using classical force fields with Lennard Jones (LJ) and Coulombic interactions. Long-range electrostatics were treated using the Particle Mesh Ewald (PME) method, while van der Waals interactions were truncated at a cutoff distance of 1.2 nm. Table 4.3 shows the atom type parameters used in the simulations, where the interactions are defined using the C_6 and C_{12} coefficients.

The calcite slab was modeled using the forcefield defined by Xiao et al [63]. Which has been validated for reproducing the structural and interfacial properties of calcite crystals. The slab atoms were harmonically restrained to their position and partial charges were assigned according to the original parameterization. Water was modeled using the SPC/E model. This model reproduces the density and phase behavior of water well under ambient and moderately elevated pressures [60]. Hydrogen (H_2) and carbon dioxide (CO_2) were modeled using Hirschefelder and TraPPE forcefields.

4.6.1. Cross Interactions and Interaction Scaling

Cross interactions between unlike atom types were computed using the Lorentz–Berthelot mixing rules:

$$\sigma_{ij} = \frac{\sigma_i + \sigma_j}{2} \tag{4.3}$$

$$\epsilon_{ij} = \sqrt{\epsilon_i \epsilon_j}. \tag{4.4}$$

The Lennard Jones interaction was implemented in the equivalent C_6–C_{12} form:

$$U_{ij}(r) = \frac{C_{12,ij}}{r^{12}} - \frac{C_{6,ij}}{r^6} \tag{4.5}$$

where the coefficients are related to the ϵ–σ representation via

Table 4.1: Overview of simulated systems. λ_{H_2} and λ_{CO_2} denote the Lennard Jones interaction scaling factors applied to gas-surface interactions. All simulations were performed at 323 K and 200 bar using semi-isotropic pressure coupling (y and z directions).

System ID	Substrate Layers	Radius (nm)	N_{H_2}	N_{CO_2}	H_2 (%)	CO_2 (%)	λ_{H_2}	λ_{CO_2}	T (K)	P (bar, yz)	av. box dim. x (nm)	av. box dim. y (nm)	av. box dim. z (nm)
R0	8	3	3000	0	100	0	1.0	1.0	323	200	20.6552	23.9437	15.7811
R10	8	3	2700	300	90	10	1.0	1.0	323	200	20.8345	23.7819	15.7811
R20	8	3	2400	600	80	20	1.0	1.0	323	200	20.6456	23.9979	15.7811
R30	8	3	2100	900	70	30	1.0	1.0	323	200	20.6673	24.0125	15.7811
R40	8	3	1800	1200	60	40	1.0	1.0	323	200	20.6534	23.9456	15.7811
R50	8	3	1500	1500	50	50	1.0	1.0	323	200	20.6909	23.8549	15.7811
R60	8	3	1200	1800	40	60	1.0	1.0	323	200	20.6476	23.9858	15.7811
R70	8	3	900	2100	30	70	1.0	1.0	323	200	20.6753	23.9036	15.7811
R80	8	3	600	2400	20	80	1.0	1.0	323	200	20.4179	24.1507	15.7811
R90	8	3	300	2700	10	90	1.0	1.0	323	200	20.4204	24.1715	15.7811
R100	8	3	0	3000	0	100	1.0	1.0	323	200	20.5355	23.9847	15.7811
ACH2	8	3	1500	1500	50	50	2.0	1.0	323	200	20.0871	26.8462	15.7811
ACH3	8	3	1500	1500	50	50	3.0	1.0	323	200	20.0014	26.9794	15.7811
ACH4	8	3	1500	1500	50	50	4.0	1.0	323	200	20.2917	26.7927	15.7811
ACH5	8	3	1500	1500	50	50	5.0	1.0	323	200	20.1407	26.6732	15.7811
ACH6	8	3	1500	1500	50	50	6.0	1.0	323	200	19.7962	26.7179	15.7811
ACH7	8	3	1500	1500	50	50	7.0	1.0	323	200	19.8609	26.6183	15.7811
ACH8	8	3	1500	1500	50	50	8.0	1.0	323	200	20.0575	26.591	15.7811
ACC2	8	3	1500	1500	50	50	1.0	2.0	323	200	20.267	26.6601	15.7811
ACC3	8	3	1500	1500	50	50	1.0	3.0	323	200	20.1937	26.964	15.7811
ACC4	8	3	1500	1500	50	50	1.0	4.0	323	200	20.1045	26.6739	15.7811
ACC5	8	3	1500	1500	50	50	1.0	5.0	323	200	20.0664	26.5648	15.7811
ACC6	8	3	1500	1500	50	50	1.0	6.0	323	200	20.7967	26.7287	15.7811
ACC7	8	3	1500	1500	50	50	1.0	7.0	323	200	21.1966	26.7636	15.7811
ACC8	8	3	1500	1500	50	50	1.0	8.0	323	200	20.397	26.4965	15.7811
AFH0	8	3	3000	0	100	0	8.0	2.0	323	200	19.6337	26.5156	15.7811
AFH10	8	3	2700	300	90	10	8.0	2.0	323	200	19.6457	26.566	15.7811
AFH20	8	3	2400	600	80	20	8.0	2.0	323	200	20.0143	26.497	15.7811
AFH30	8	3	2100	900	70	30	8.0	2.0	323	200	20.0262	26.5246	15.7811
AFH40	8	3	1800	1200	60	40	8.0	2.0	323	200	20.0573	26.6154	15.7811
AFH50	8	3	1500	1500	50	50	8.0	2.0	323	200	20.1435	26.4194	15.7811
AFH60	8	3	1200	1800	40	60	8.0	2.0	323	200	19.7531	26.4434	15.7811
AFH70	8	3	900	2100	30	70	8.0	2.0	323	200	19.555	26.6086	15.7811
AFH80	8	3	600	2400	20	80	8.0	2.0	323	200	19.8253	26.4832	15.7811
AFH90	8	3	300	2700	10	90	8.0	2.0	323	200	19.7462	26.4435	15.7811
AFH100	8	3	0	3000	0	100	8.0	2.0	323	200	19.779	26.488	15.7811
AFC0	8	3	3000	0	100	0	8.0	4.0	323	200	19.9902	26.4206	15.7811
AFC10	8	3	2700	300	90	10	8.0	4.0	323	200	19.749	26.9197	15.7811
AFC20	8	3	2400	600	80	20	8.0	4.0	323	200	19.864	26.6045	15.7811
AFC30	8	3	2100	900	70	30	8.0	4.0	323	200	19.8877	26.8124	15.7811
AFC40	8	3	1800	1200	60	40	8.0	4.0	323	200	20.1559	26.4371	15.7811
AFC50	8	3	1500	1500	50	50	8.0	4.0	323	200	20.1411	26.58	15.7811
AFC60	8	3	1200	1800	40	60	8.0	4.0	323	200	19.7346	26.5091	15.7811
AFC70	8	3	900	2100	30	70	8.0	4.0	323	200	19.3938	26.6001	15.7811
AFC80	8	3	600	2400	20	80	8.0	4.0	323	200	19.8044	26.7014	15.7811
AFC90	8	3	300	2700	10	90	8.0	4.0	323	200	19.6269	26.673	15.7811
AFC100	8	3	0	3000	0	100	8.0	4.0	323	200	19.5385	26.6413	15.7811

Table 4.2: Force fields and molecular models used for each system component.

Component	Force Field / Model	Notes
Calcite substrate	[Xiao et al. Forcefield [63]]	Flexible slab, partial charges included
Water	[SPC/E]	Rigid geometry
Hydrogen (H_2)	[Hirschfelder et al Forcefield [56]]	[Single-site LJ]
Carbon dioxide (CO_2)	[TraPPE]	[Three-site linear model]

Table 4.3: Atom type parameters used in the simulations. Lennard–Jones interactions are defined via C_6 and C_{12} coefficients.

Atom Type	Mass (g mol^{-1})	Charge (e)	C_6	C_{12}
Ca	40.0780	1.6680	1.42E-03	2.52E-07
CO	12.0107	0.9990	4.61E-03	1.44E-05
OC	15.9994	-0.8890	2.03E-03	1.77E-06
H2	2.0160	0.0000	7.7538E-04	4.88589E-07
OW	15.9994	-0.8476	2.6184E-03	2.63696E-06
HW1	1.0080	0.4238	0	0
HW2	1.0080	0.4238	0	0
CO2_C	12.0107	0.7000	4.33E-04	2.08523E-07
CO2_O	15.9994	-0.3500	2.12E-03	1.70262E-06

$$C_{12,ij} = 4\epsilon_{ij}\sigma_{ij}^{12} \tag{4.6}$$

$$C_{6,ij} = 4\epsilon_{ij}\sigma_{ij}^{6}. \tag{4.7}$$

For the AC and AF systems, the gas–surface Lennard Jones interaction strength was modified by introducing

a scaling factor λ. The scaling was applied to the dispersion interaction strength, such that

$$C_{6,ij}^{\text{scaled}} = \lambda\, C_{6,ij} \tag{4.8}$$

and consistently

$$C_{12,ij}^{\text{scaled}} = \lambda\, C_{12,ij} \tag{4.9}$$

which is equivalent to scaling the ϵ_{ij} parameter while keeping σ_{ij} unchanged.

The gas–surface interactions were scaled. Gas–gas and gas–water interactions remained unchanged in order to preserve bulk thermodynamic properties. The water–surface Lennard Jones interaction strength was scaled using a fixed factor of $\lambda = 0.125$ for all systems, with the exception of the reference (R) simulations, where unmodified interaction parameters were used. This controlled modification enables systematic investigation of adsorption strength and wettability effects without altering intrinsic fluid behavior.

4.6.2. Non-Bonded Interaction Treatment

Electrostatic interactions were calculated using the Particle Mesh Ewald (PME) method with a real-space cutoff of 1.0 nm. The Verlet cutoff scheme was employed with a neighbor-list cutoff of 1.2 nm. Van der Waals interactions were treated using a cut-off scheme with a truncation distance of 1.0 nm. Analytical long-range dispersion corrections were not applied due to the heterogeneous slab geometry.

Table 4.4: Non-bonded interaction settings used in all simulations.

Parameter	Value
Electrostatics	PME
Real-space cutoff	[1.0 nm]
LJ cutoff	[1.0 nm]
Neighbor-list cutoff	[1.2 nm]
Dispersion correction	[**OFF**]

4.7. Initial Minimization, Equilibration and Productions runs

All simulations were performed using GROMACS. The simulation protocol consisted of three sequential stages, namely, energy minimization, equilibration, and production runs. An overview of the simulation workflow is provided in table 4.5.

Table 4.5: Simulation workflow for all systems.

Stage	Ensemble	Duration	Purpose
Energy minimization	—	up to 50 000 steps	Remove clashes
NVT equilibration	NVT	[200 ps]	Temperature stabilization
NPT equilibration	NPT	[2 ns]	Pressure and volume relaxation
Production run	NPT	[3 ns]	Data collection

4.7.1. Energy Minimization

Prior to dynamical simulations, all systems were subjected to energy minimization using the steepest descent algorithm. A maximum of 50 000 steps was allowed, with a convergence criterion of 700-1000 kJ mol^{-1} nm^{-1} on the maximum force. This can be seen as quite a high maximum force which is done due to the slab being frozon on the edges up to 1 nm as explained in 4.4.

During minimization, positional restraints were applied to the substrate atoms Ca and CO_3. Periodic boundary conditions were applied in all directions.

4.7.2. Equilibration Simulations

Following minimization, systems were equilibrated in two stages.

The systems were first equilibrated in the NVT ensemble to stabilize the temperature at 323 K. Temperature coupling was achieved using the V-rescale thermostat with a coupling constant of 0.1 ps for the fluid and gas

species.

Subsequently, pressure equilibration was done using an semi-isotropic pressure coupling, where the Berendsen barostat was employed. The reference pressure was set at 200 bar in the z and y direction, while the x direction the pressure was set to 0. The compressibility was set to 1.41×10^{-6} bar^{-1} in the pressurized directions and zero in the frozen direction. The pressure coupling time constant was 1.0 ps.

4.7.3. Production Simulations

Production simulations were performed in the NPT ensemble using a time step of 2 fs. All bonds were constrained using the LINCS algorithm.

Electrostatic interactions were treated using the Particle Mesh Ewald method with a real-space cutoff of 1.0 nm, while van der Waals interactions were truncated at 1.0 nm. The Verlet cutoff scheme with a neighbor list update every 20 steps was employed. Each production run consisted of 1,500,000 integration steps, corresponding to 3 ns of simulation time. The pressure coupling was achieved using the C-rescale barostat with coupling constant between 5.0 ps to 10.0 ps, with again the same compressibilities employed during equilibration.

4.7.4. Equilibration Criteria

Equilibration was assessed by monitoring:

- Stabilization of total potential energy,
- Convergence of system temperature around 323 K,
- Pressure fluctuations around the target value of 200 bar,
- Stability of system volume.

Table 4.6: Molecular dynamics parameters used during NVT equilibration, NPT equilibration, and production simulations.

Parameter	NVT Equilibration	NPT Equilibration	NPT Production
Integrator	md	md	md
Time step	1 fs	2 fs	2 fs
Duration	200 ps	2 ns	3 ns
Thermostat	V-rescale	Nosé–Hoover	Nosé–Hoover
τ_T (substrate)	1000 ps	1000 ps	0.1 ps
τ_T (fluids)	1.0 ps	0.1 ps	0.1 ps
Barostat	—	Berendsen	C-rescale
Pressure coupling	—	Semi-isotropic	Semi-isotropic
τ_P	—	1.0 ps	5.0-10.0 ps
Reference pressure	—	200 / 0 bar	200 / 0 bar
Electrostatics	PME	PME	PME
Coulomb cutoff	1.0 nm	1.0 nm	1.0 nm
LJ cutoff	1.0 nm	1.0 nm	1.0 nm
Neighbor list cutoff	1.2 nm	1.2 nm	1.2 nm
Constraints	All bonds (LINCS)	All bonds (LINCS)	All bonds (LINCS)
Frozen group	EDGE (Y Y Y)	EDGE (Y Y Y)	EDGE (Y Y Y)
Position restraints	Ca, CO_3	Ca, CO_3	Ca, CO_3
PBC	xyz	xyz	xyz

4.8. Validation of Bulk Properties

In order to demonstrate that the MD simulation parameters and forcefield models produce meaningful results for the systems, several validation checks were performed under conditions representative of production simulations.

4.8.1. Bulk Water Properties

Independent MD simulations were done on pure water at 323 K and 200 bar was performed to pre-equilibrate it before the full system was constructed. Resulting in an average density of 984 kg m^{-3}, which agrees within

1.3% of experimental data. Similar quantitative deviations of SPC/E density from experimental data have been reported in systematic studies of SPC/E thermophysical properties over wide temperature and pressure ranges [37]. In figure 4.7 the convergence of several key validation criteria are shown.

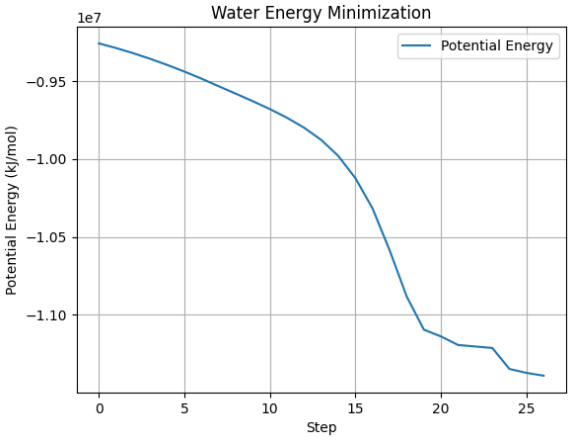

(a) Energy minimization showing convergence for bulk water.

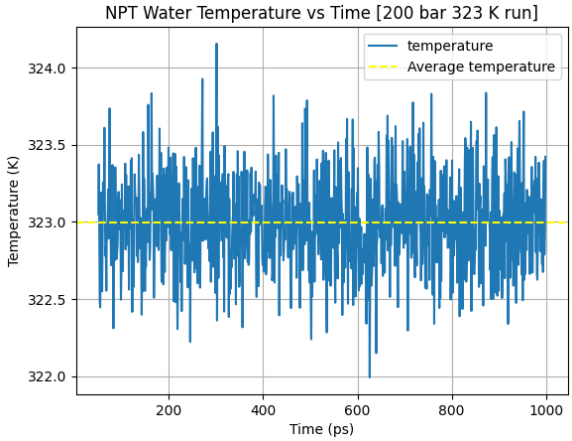

(b) Temperature trace during NPT equilibration illustrating stable approach to 323 K.

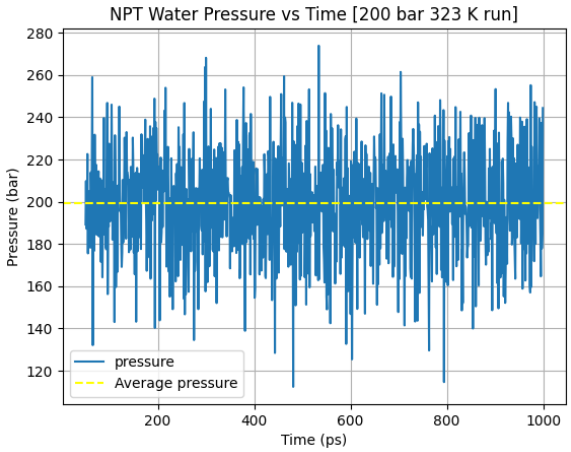

(c) Pressure evolution during NPT equilibration showing convergence toward 200 bar.

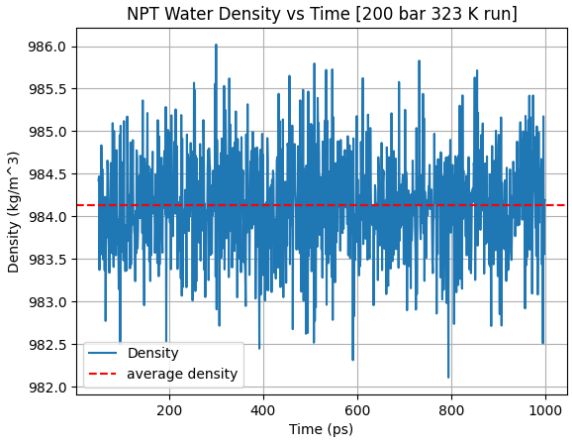

(d) Density evolution in NPT equilibration demonstrating stabilization near the expected bulk value.

Figure 4.7: Validation of the bulk water equilibration: (a) energy minimization shows relaxation of potential energy, (b) temperature converges and remains stable at 323 K, (c) pressure equilibrates near the target of 200 bar, and (d) density reaches a stable value consistent with the expected bulk density for SPC/E water.

4.8.2. Calcite Slab Stability

Structural stability and density was assessed as well of the calcite slab at ambient conditions. No significant drift or lattice distortions were found during equilibration. The resulting density became 2.72 kg m^{-3}, which is under a percent lower than experimental data [30]. In figure 4.8 the convergence of several key validation criteria are shown.

4.8.3. Production System Stability

A representative system (ACC50) was analyzed to verify ensemble stability. The total potential energy and temperature stabilized and remained constant thereafter. The density map normal to the bubble surface area exhibited clear phase separation between solid, liquid, and gas regions without artificial mixing. In figure 4.9 the convergence of several key validation criteria are shown.

4.9. Contact Angle Extraction Methodology

In MD simulations, contact angle measurements are often obtained by identifying the equilibrium shape of the gas interface and fitting a geometric model to the interface profile. Of course, due to atomistic fluctuations in MD simulations, time-averaged 2D density maps are used to define the liquid-vapor interface and calculate the contact angle [20].

4.9.1. Density Map Generation

For each production trajectory, 2D density maps were generated using the built in tools in GROMACS. Water was chosen as the analyzed group for the density maps, with the maps being projected on the x-z plane and averaged over y.

To locate the gas interface within the 2D density map, a percentile based thresholding method was used. Because the density map is generated solely from water molecules, the liquid and gas phases are distinguished based on the statistical distribution of water number density. The bulk liquid density ρ_{liq} was taken as the 95$^{\text{th}}$ percentile of the density values, while the gas phase reference ρ_{gas} was taken as the 5$^{\text{th}}$ percentile.

An interfacial density threshold was then defined as:

$$\rho_{\text{interface}} = 0.2\,(\rho_{\text{liq}} + \rho_{\text{gas}}). \tag{4.10}$$

The value of $\rho_{\text{interface}}$ is then used to extract the contour representing the liquid–vapor boundary from the time-averaged density map and subsequently passed to the geometric fitting routine for contact angle computation.

4.9.2. Contact Angle Extraction

With the obtained time-averaged density map, the contact angles can be extracted using a customized code developed as part of this thesis based on the code made by Pham et al [50]. The customized code that has been used can be found in Appendix A. A circular geometry is fitted to the interface profile to determine the radius of curvature R and center (x_c, z_c) of the liquid–vapor interface. Once the circle parameters are obtained, the contact point where the interface meets the solid surface (at height h) is located using the relations:

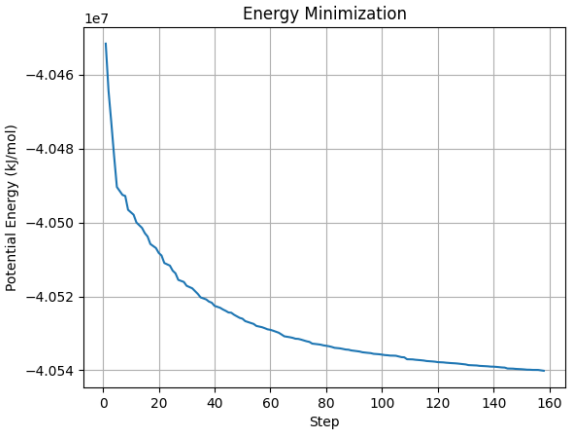

(a) Energy minimization showing convergence for bulk calcite.

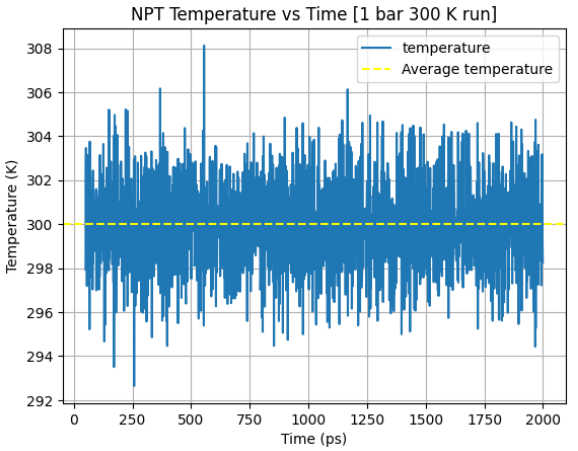

(b) Temperature evolution during NPT equilibration showing stable approach to 300 K.

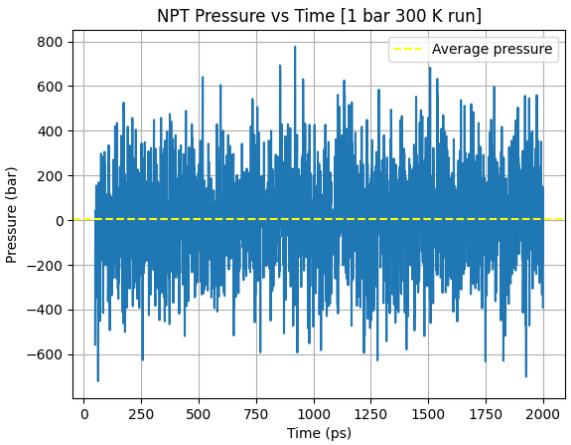

(c) Pressure evolution during NPT equilibration demonstrating convergence toward 1 bar.

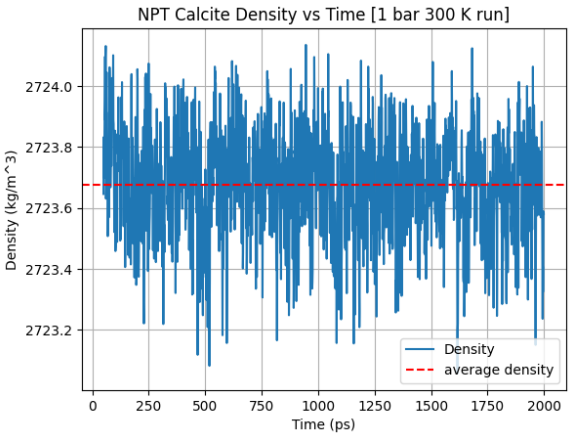

(d) Density evolution in NPT equilibration demonstrating stabilization near the expected bulk value.

Figure 4.8: Validation of the bulk calcite equilibration: (a) energy minimization shows relaxation of forces, (b) temperature converges and remains steady at 323 K, (c) pressure equilibrates near the setpoint of 1 bar, and (d) density stabilizes at an appropriate calcite value.

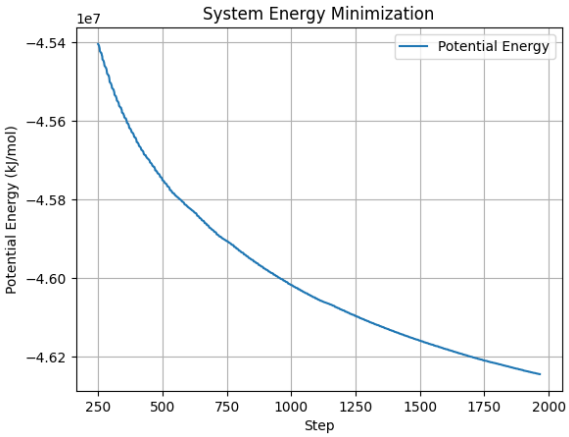

(a) Energy minimization showing convergence for the system.

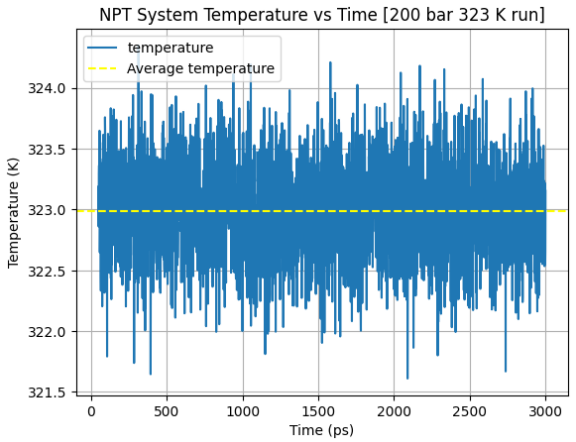

(b) Temperature evolution during NPT equilibration showing stable approach to 323 K.

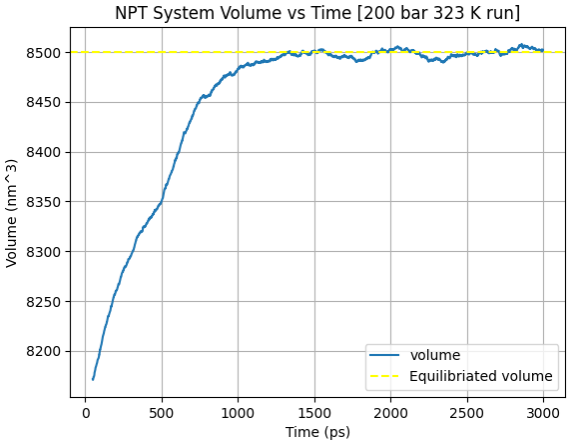

(c) Volume evolution during NPT equilibration demonstrating convergence.

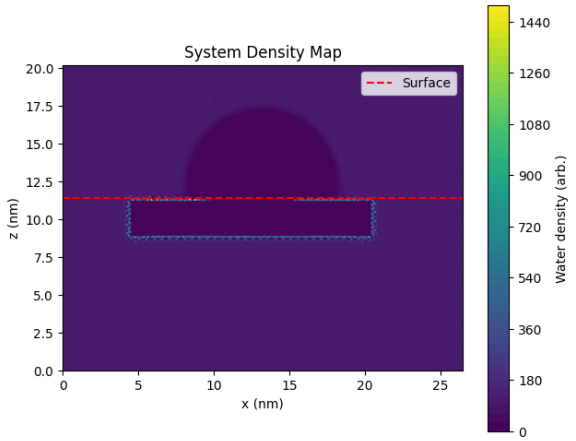

(d) Density map of the full system after equilibration showing phase distribution (slab, water, and gas regions).

Figure 4.9: Validation of the system equilibration: (a) energy minimization shows relaxation of forces, (b) temperature converges and remains steady at 323 K, (c) pressure equilibrates near the setpoint of 200 bar, and (d) the equilibrium density map illustrates a consistent phase distribution of the calcite slab, water phase, and gas bubble, indicating overall structural and thermodynamic stability.

$$d_z = h - z_c, \tag{4.11}$$

$$d_x = \sqrt{R^2 - d_z^2}, \tag{4.12}$$

$$x_{\text{contact}} = x_c + d_x. \tag{4.13}$$

At the contact point, the slope m of the tangent to the fitted circle is given by:

$$m = -\frac{x_{\text{contact}} - x_c}{h - z_c}, \tag{4.14}$$

and the contact angle θ is computed as:

$$\theta_{\text{liquid}} = \arctan\left(|m|\right). \tag{4.15}$$

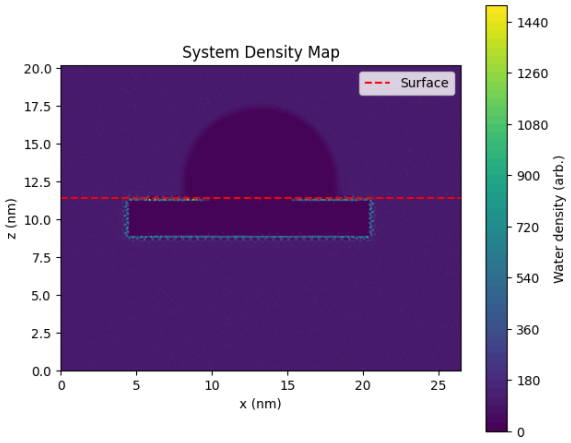

(a) Time-averaged 2D density map of the equilibrated system, showing the calcite surface, water phase, and gas bubble.

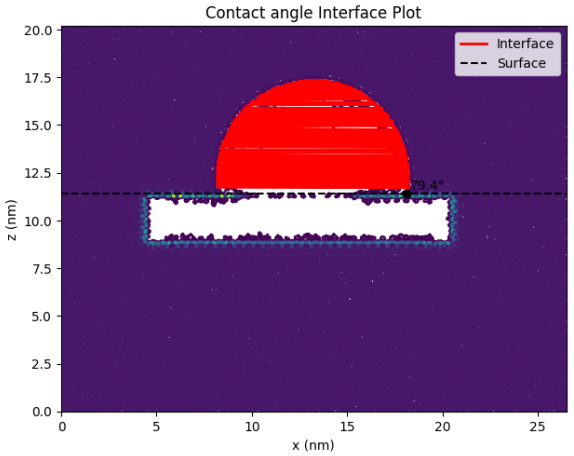

(b) Extracted liquid–vapor interface contour from the density map used for geometric fitting.

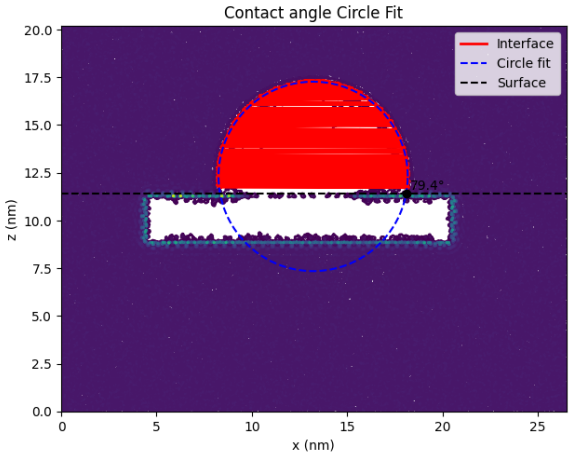

(c) Circle fit applied to the interface contour to determine the local curvature of the bubble surface.

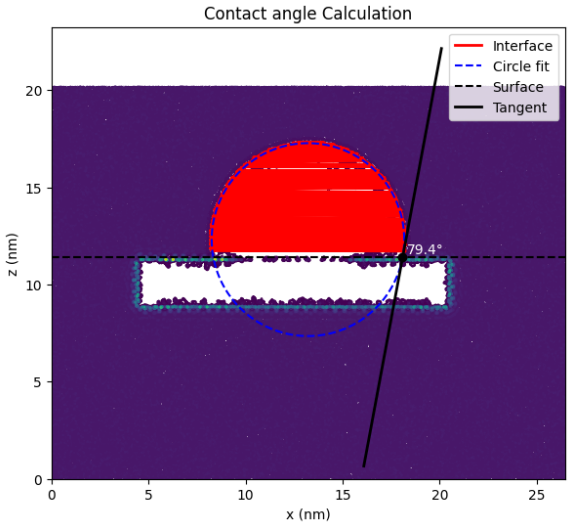

(d) Tangent line drawn at the interface–surface contact point used to calculate the contact angle.

Figure 4.10: Stepwise visualization of the contact angle extraction procedure: (a) the 2D density map of the equilibrated bubble–water–surface system, (b) the extracted interface contour, (c) the circular geometric fit to the interface profile, and (d) the tangent line at the contact point used to compute the contact angle.

5 Results

As explained in the previous sections, three distinct sets of simulations are conducted in this study. In section 5.1, the reference system will be discussed, where unscaled interaction parameters will be used to model the system. In order to assess these systems the fraction of CO_2 will be altered in the bubble, and due to dissolution of the bubble, a bubble fraction correction will be applied.

Secondly, the second set of simulations will be done to assess which interactions, either CO_2 or H_2, controls wettability. This will be done by scaling one of CO_2 or H_2 interactions with the solid slab, while keeping the other constant at its unscaled value. The contact angles are then assessed to see which species control wettability by looking at which contact angles changes the most with scaling the interaction parameter.

Lastly, the third set of simulation will be done on the final system, where the interaction parameters between the slab and the gases are altered in such a way that the slab has become hydrophobic. Due to this the contact angles can be extracted and compared between different gas fraction combinations. Due to the bubble being a mixture of gases, two distinct systems can be defined within the set of simulations. Either a system where there is more hydrogen wetting or more CO_2 wetting. Due to that possibility, both situations are assessed.

5.1. Reference System

5.1.1. Pure H_2

Initially, a pure system of H_2 will be assessed. The unaltered interaction parameters for the whole system can be found in Table 4.3, 5.1 and 5.2. The cross LJ interaction parameters are combined using the Lorentz–Berthelot mixing rules, except for the slab-water interactions, where that follows how the forcefield is parameterized [63].

Figure 5.1 shows a representative equilibrated configuration together with the corresponding time-averaged two-dimensional water density map. As observed in the snapshot, the hydrogen bubble does not establish direct contact with the calcite surface. Instead, a continuous water layer remains between the gas phase and the solid substrate. This behavior is consistent with the hydrophilic character of calcite [6], in which the preferred adsorbed species to the surface is water.
The extracted contact angle for pure H_2 was therefore found to be over 180 degrees, which means it completely detaches from the surface.

Thermodynamic equilibration was also validated by stable temperature and potential energy profiles (see Appendix B). A small fraction of hydrogen was observed to dissolve into the bulk water phase, however, the dissolution does not significantly alter the overall wetting behavior due to the low solubility. Although the solubility itself has not been assessed due to small volume scale and short timescales of the simulations.

5.1.2. Pure CO_2

Pure CO_2 was also investigated, using the same unscaled interaction parameters as defined in Tables 4.3, 5.1, and 5.2.

Figure 5.2 shows the equilibrated configuration together with a time-averaged two-dimensional water density map. Again, as for the pure H_2 bubble, the bubble does not form a stable three phase contact line with the

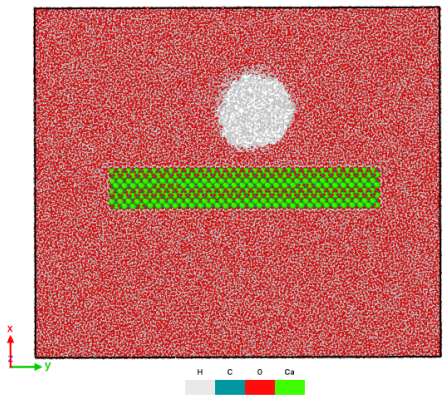

(a) Representative simulation snapshot obtained from the .gro structure file. The rock slab is positioned at the center of the simulation box. Hydrogen molecules are shown in white, CO_2 molecules in blue, and water molecules with oxygen atoms in red and hydrogen atoms in white.

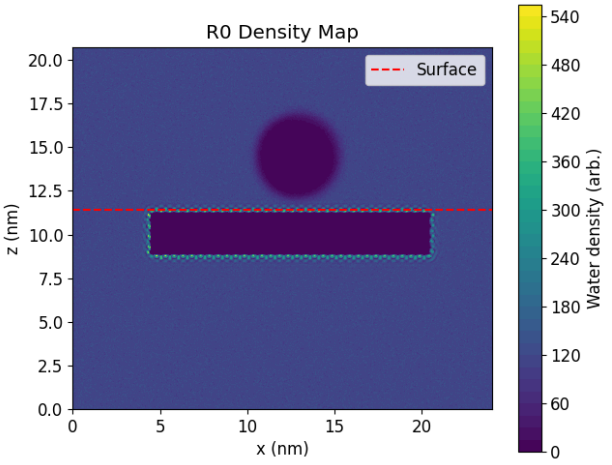

(b) Two-dimensional water density map in the x–z plane used for interface identification.

Figure 5.1: Comparison between the atomistic configuration and a corresponding spatial density field. (a) Snapshot of the equilibrated simulation system. (b) Time-averaged two-dimensional water density distribution.

Table 5.1: Explicit non-bonded Lennard–Jones cross interaction parameters.

Atom i	Atom j	C_6	C_{12}
CO	CO	1.43E-02	4.61E-06
OC	OC	5.21E-05	5.94E-07
Ca	OC	0.00E+00	9.49E-07
CO	OC	3.08E-04	9.04E-10
Ca	Ca	1.42E-03	2.52E-07

Table 5.2: Reference (unscaled) cross Lennard–Jones parameters defined via C_6 and C_{12}.

Atom i	Atom j	C_6	C_{12}
Ca	OW	2.00E-03	8.85E-07
CO	OW	3.39E-03	5.91E-06
OC	OW	2.25E-03	2.07E-06
OC	HW1	9.65E-07	7.98E-09
OC	HW2	9.65E-07	7.98E-09
H2	OW	1.43E-03	1.1455E-06
H2	Ca	1.084E-03	3.75115E-07
H2	CO	1.2574E-03	9.34117E-07
H2	OC	1.99393E-03	2.95022E-06
CO2_C	Ca	3.077E-04	9.188E-08
CO2_C	OC	7.684E-04	5.018E-07
CO2_C	CO	1.726E-03	2.277E-06
CO2_C	OW	8.391E-04	5.912E-07
CO2_C	H2	6.321E-04	3.488E-07
CO2_O	Ca	4.263E-04	1.690E-07
CO2_O	OC	1.029E-03	8.623E-07
CO2_O	CO	2.250E-03	3.707E-06
CO2_O	OW	1.120E-03	1.010E-06
CO2_O	H2	1.282E-03	9.144E-07

calcite surface and instead completely detaches from the surface.

Since the bubble is completely detached, the contact angle can again be seen as 180 degrees. Here also thermodynamic equilibration was confirmed (see Appendix B).

5.1.3. Mixed Bubble Systems

Mixed gas bubbles containing varying fractions of H_2 and CO_2 were also investigated, again using the unscaled interaction parameters. With the purpose of these simulations being to assess whether compositional variation within the bubble influences the wettability.

Across all investigated gas fractions, with the investigated gas fraction spanning from 0.1 to 0.9 mol fraction of

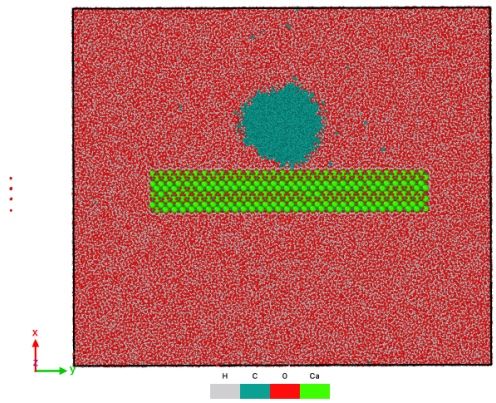

(a) Representative CO_2 bubble configuration obtained from the .gro file.The rock slab is positioned at the centre of the simulation box. Hydrogen molecules are shown in white, CO_2 molecules in blue, and water molecules with oxygen atoms in red and hydrogen atoms in white.

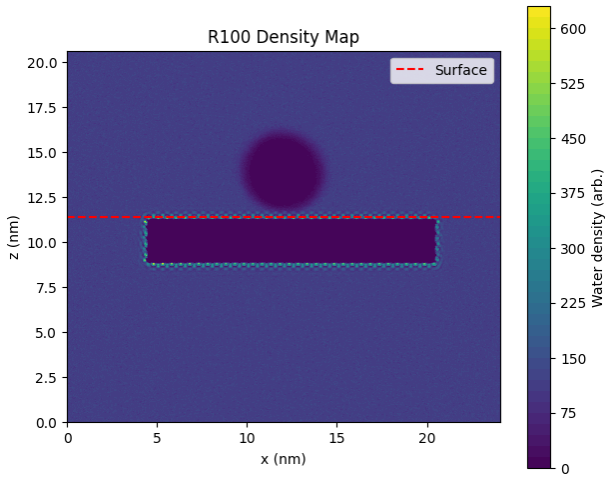

(b) Time-averaged two-dimensional water density map for the pure CO_2 system.

Figure 5.2: Comparison between the atomistic configuration and a corresponding spatial density field. (a) Snapshot of the equilibrated simulation system. (b) Time-averaged two-dimensional water density distribution.

CO_2 in the bubble, the bubble completely detaches from the surface. Therefore no stable three phase line is observed in any configuration and the contact angle consistently exceeds $180°$.

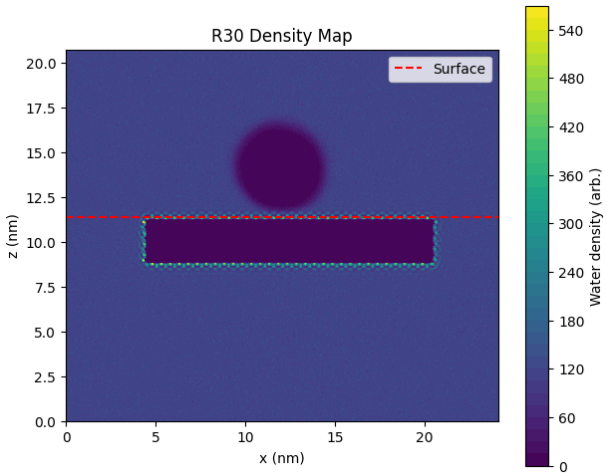

(a) 0.2 CO_2 fraction

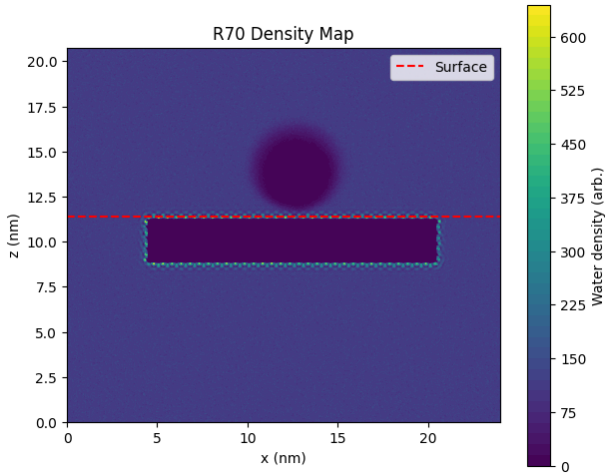

(b) 0.7 CO_2 fraction

Figure 5.3: Representative mixed bubble systems. Independent of composition, the bubble remains detached from the calcite surface, corresponding to a contact angles exceeding $180°$.

Figure 5.3 illustrates two representative configurations for selected mixture ratios, namely [0.3:0.7] and a [0.7:0.3] ratio for [H_2:CO_2]. The corresponding water density maps again show that the bubble completely detaches from the bubble, although as shown in figure 5.4, the continuous water layer separating the gas from the surface does become slightly smaller, with increased CO_2 fraction.

5.1.4. Fraction Correction due to Dissolution

Of course, due to dissolution, part of the gases get dissolved in the bulk water phase. Therefore the mol fractions of each respective gas must be corrected for this loss to make sure the simulated systems appear as they seem. The way this correction was done was by the usage of the contact angle calculation code (see Appendix C), where the central points and the radius of each bubble is extracted, then the number density of

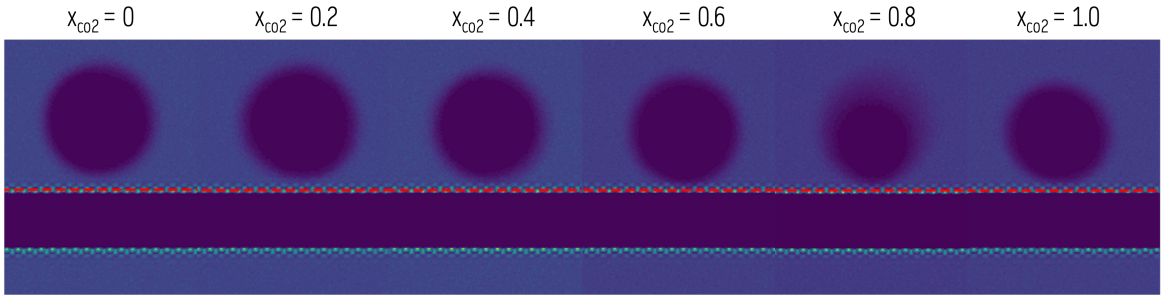

Figure 5.4: An overview of starting from the right pure H_2 bubble is shown and with increment of 0.2 the mole fraction of CO_2 is increased until it reaches a pure CO_2 bubble.

each species in the bubble can be defined and the fractions can therefore be corrected.

The corrections for the systems in this subsection can be found in table 5.4, and the fitted circle parameters can be found in table 5.3

Table 5.3: Parameters of the fitted bubble (centre coordinates and radius).

System	x_c	z_c	R
R0	12.86	14.46	2.30
R10	12.41	14.44	2.41
R20	12.28	14.35	2.35
R30	11.93	14.14	2.37
R40	12.42	14.21	2.25
R50	12.44	13.99	2.24
R60	12.41	13.98	2.25
R70	12.68	13.90	2.10
R80	12.36	13.73	1.84
R90	12.10	13.82	1.94
R100	11.99	13.87	2.07

Table 5.4: Corrected gas fractions and molecule counts within the bubble.

System	$x(H_2)$	$x(CO_2)$	$N(H_2)$	$N(CO_2)$
R0	1.000	0.000	2250	0
R10	0.901	0.099	2066	227
R20	0.803	0.197	1804	443
R30	0.695	0.305	1621	712
R40	0.597	0.403	1350	913
R50	0.481	0.519	1131	1222
R60	0.382	0.618	898	1453
R70	0.276	0.724	605	1591
R80	0.165	0.835	317	1604
R90	0.079	0.921	171	2003
R100	0.000	1.000	0	2471

5.2. Effect of Modified Interaction Parameters

In the next set of simulations, the species which controls wettability will be investigated. Which can be either CO_2 or H_2. This is done in systems where the mol fraction is constant and equal to [0.5:0.5] ([H_2:CO_2]). In order to assess which species controls the contact angle, the interaction parameter of either H_2 and CO_2 with the surface will be altered, while the other will be kept unscaled. In all simulations the interactions parameter of the solid-water will also be altered and kept constant. Therefore the single degree of freedom in these simulations will be the altered interactions parameters of either gas species.

The scaling factor, from here on out called λ, will vary between 2 to 8 for both species, as shown in table 4.1. Due the large amount of systems studied in this report, different systems can be identified by their system name. Which, in these set of simulations, can be recognized by the AC systems.

In table 5.5 and 5.6, the altered interaction parameters are shown for each different scaling factor, therefore these only apply for the set of simulations where H_2-rock or CO_2-rock interactions will be scaled.

5.2.1. Scaling of CO_2 surface interactions

In figure 5.8, representative two-dimensional density maps and their circular contact angle fits are shown for three CO_2-surface scaling factors, namely $\lambda = 2$, 5 and 8 (all intermediate cases are provided in Appendix B).

As can be seen in the figure 5.8, at low scaling, the bubble has lower contact angles indicating that the bubble is less affinate to the water, although is has not fully detached, with a contact angle of roughly 25 degrees. While at higher scaling factors, the bubble is wetting the surface more, which can be seen in the density map and contact angle fit where at $\lambda = 8$ the contact angle has been increased significantly from the initial $\lambda = 2$ now at roughly 96 degrees.

Table 5.5: Scaled Lennard-Jones cross interaction parameters for hydrogen-rock interactions. The scaling factor λ multiplies the reference (REAL) C_6 and C_{12} values for H_2-rock pairs, while other interactions are kept fixed.

Pair	Parameter	Scaling factor λ						
		2	3	4	5	6	7	8
H_2-Ca	C_6	2.1680E-03	3.2520E-03	4.3360E-03	5.4200E-03	6.5040E-03	7.5880E-03	8.6720E-03
	C_{12}	7.50230E-07	1.125345E-06	1.50046E-06	1.875575E-06	2.25069E-06	2.625805E-06	3.00092E-06
H_2-CO	C_6	2.51480E-03	3.77220E-03	5.02960E-03	6.28700E-03	7.54440E-03	8.80180E-03	1.00592E-02
	C_{12}	1.868235E-06	2.8023525E-06	3.73647E-06	4.6705875E-06	5.604705E-06	6.5388225E-06	7.47294E-06
H_2-OC	C_6	3.98786E-03	5.98179E-03	7.97572E-03	9.96965E-03	1.196358E-02	1.395751E-02	1.595144E-02
	C_{12}	5.90044E-06	8.85066E-06	1.180088E-05	1.47511E-05	1.770132E-05	2.065154E-05	2.360176E-05

Table 5.6: Scaled Lennard-Jones cross interaction parameters for CO_2-rock interactions. The scaling factor λ multiplies the reference (REAL) C_6 and C_{12} values for CO_2-rock pairs (CO_2_C and CO_2_O), while H_2-rock interactions are kept at their unscaled (REAL) values.

Pair	Parameter	Scaling factor λ						
		2	3	4	5	6	7	8
CO_2_C-Ca	C_6	6.154E-04	9.231E-04	1.2308E-03	1.5385E-03	1.8462E-03	2.1539E-03	2.4616E-03
	C_{12}	1.8376E-07	2.7564E-07	3.6752E-07	4.5940E-07	5.5128E-07	6.4316E-07	7.3504E-07
CO_2_C-OC	C_6	1.5368E-03	2.3052E-03	3.0736E-03	3.8420E-03	4.6104E-03	5.3788E-03	6.1472E-03
	C_{12}	1.0036E-06	1.5054E-06	2.0072E-06	2.5090E-06	3.0108E-06	3.5126E-06	4.0144E-06
CO_2_C-CO	C_6	3.452E-03	5.178E-03	6.9040E-03	8.6300E-03	1.0356E-02	1.2082E-02	1.3808E-02
	C_{12}	4.554E-06	6.831E-06	9.1080E-06	1.1385E-05	1.3662E-05	1.5939E-05	1.8216E-05
CO_2_O-Ca	C_6	8.526E-04	1.2789E-03	1.7052E-03	2.1315E-03	2.5578E-03	2.9841E-03	3.4104E-03
	C_{12}	3.380E-07	5.070E-07	6.7600E-07	8.4500E-07	1.0140E-06	1.1830E-06	1.3520E-06
CO_2_O-OC	C_6	2.058E-03	3.087E-03	4.1160E-03	5.1450E-03	6.1740E-03	7.2030E-03	8.2320E-03
	C_{12}	1.7246E-06	2.5869E-06	3.4492E-06	4.3115E-06	5.1738E-06	6.0361E-06	6.8984E-06
CO_2_O-CO	C_6	4.500E-03	6.750E-03	9.0000E-03	1.1250E-02	1.3500E-02	1.5750E-02	1.8000E-02
	C_{12}	7.414E-06	1.1121E-05	1.4828E-05	1.8535E-05	2.2242E-05	2.5949E-05	2.9656E-05

The extracted contact angles as a function of scaling factor are shown in figure 5.5. A clear trend is observed, with the contact angle rising from roughly 25 degrees at $\lambda = 2$ to 96 degrees at $\lambda = 8$. The error bars represent one standard deviation, reflecting the sensitivity to the definition of the interface.

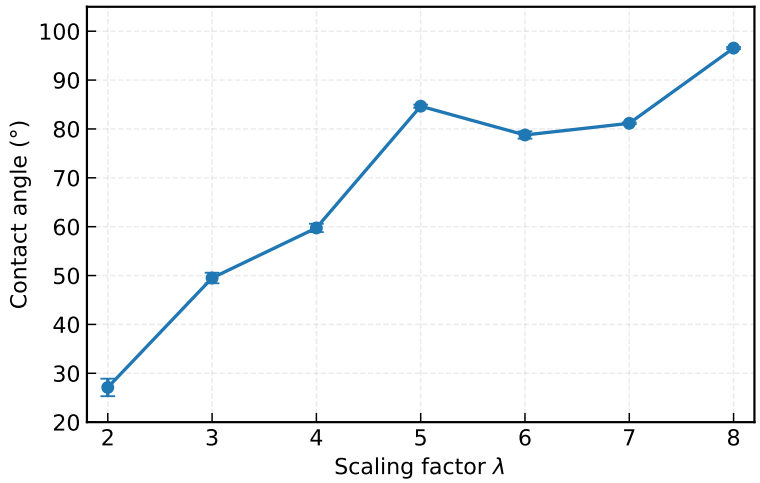

Figure 5.5: Contact Angles vs Interactions scaling for scaling the CO_2-rock interactions parameters

5.2.2. Scaling of H_2 surface interactions

In figure 5.9, representative two-dimensional density maps and their circular contact angle fits are shown for three hydrogen-surface scaling factors, namely $\lambda = 2$, 5 and 8 (all intermediate cases are provided in Appendix B).

As shown in figure 5.9, where, similarly as in the case where the CO_2 interactions were scaled, the bubble has

lower contact angles at low scaling indicating a lower affinity to the surface, although again not fully detached. At the higher scaling factors the bubble wets the surface more, as shown in the density map and contact angle fit, which increased at $\lambda = 8$ to roughly 62 degrees. This increase is significantly lower than the increase when the CO_2 interaction parameters were scaled.

The extracted contact angles as a function of scaling factor are shown in figure 5.6. A clear trend is observed, with the contact angle rising from roughly 25 degrees at $\lambda = 2$ to 96 degrees at $\lambda = 8$. The error bars represent one standard deviation, based on how the interface is defined.

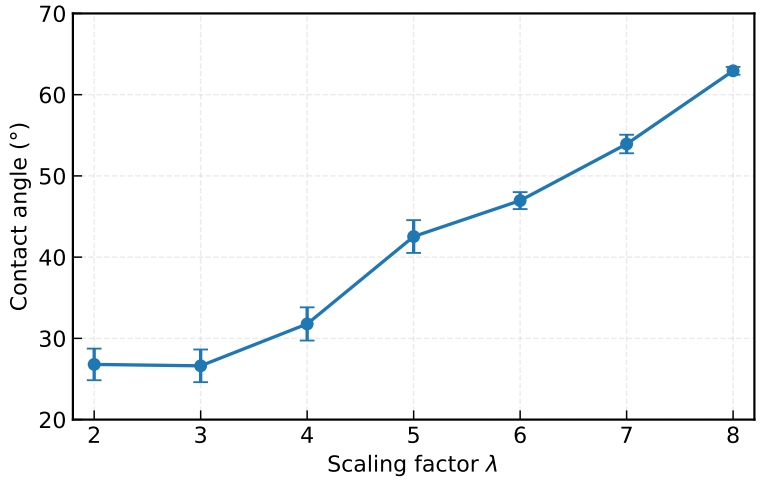

Figure 5.6: Contact Angles vs Interactions scaling for scaling the H_2-rock interactions parameters

5.2.3. Wettability Controlling Interaction

In order to determine which gas species controls the wettability, the contact angle trends obtained from scaling the H_2 and CO_2 is shown in both figures 5.6 and 5.5. These trends can therefore be directly compared in figure 5.7.

For scaling the hydrogen interactions, the angle increases gradually from approximately 25 degrees to 62 degrees. A clear monotonic increase is observed, with the overall change remaining moderate.

In contrast to this, by scaling the CO_2 interaction parameters results in significantly stronger responses. The contact angle increases more rapidly and reaches a much higher value exceeding 90 degrees at $\lambda = 8$. The increase is both steeper and larger in magnitude compared to the H_2 scaling.

This comparison demonstrates that the wettability of the system is considerably more sensitive to variations in the CO_2-surface interaction than to changes in the H_2-surface interaction strength.

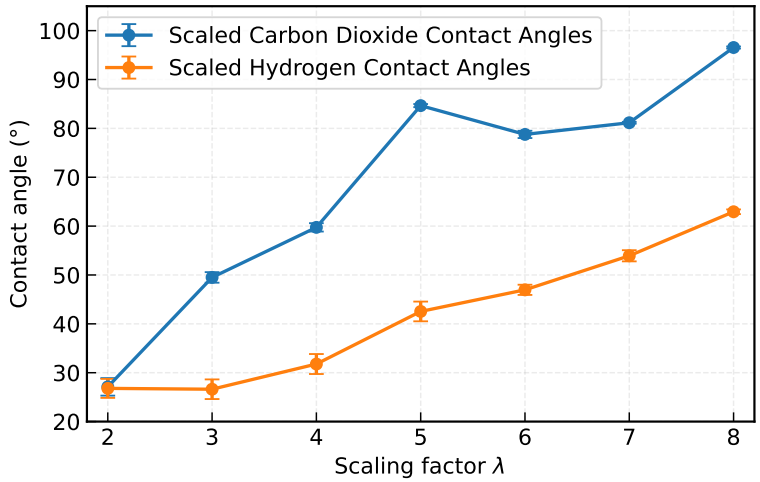

Figure 5.7: Contact Angles vs Interactions scaling for scaling both the H_2-rock and CO_2-rock interactions parameters in the same graph.

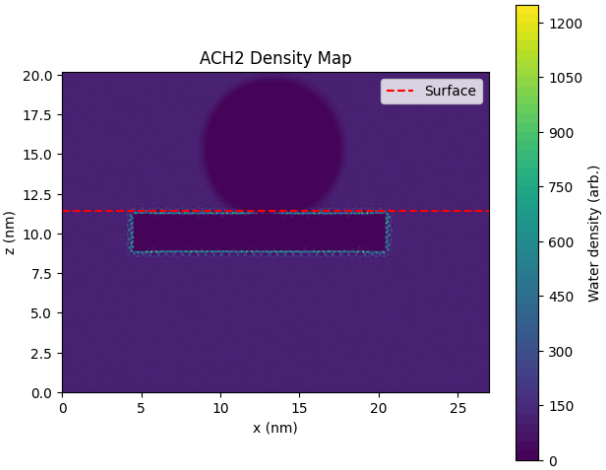

(a) Density map, $\lambda = 2$

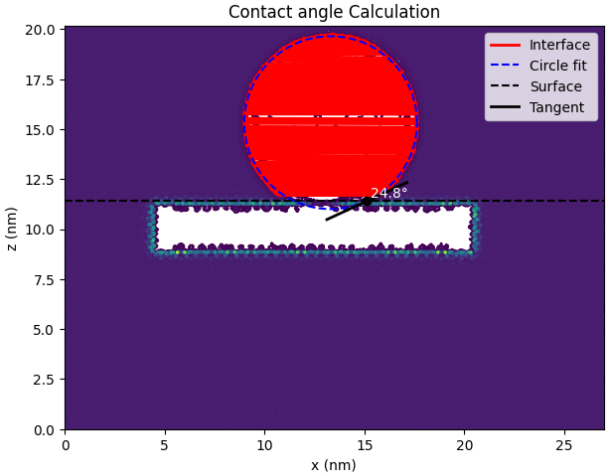

(b) Contact angle fit, $\lambda = 2$

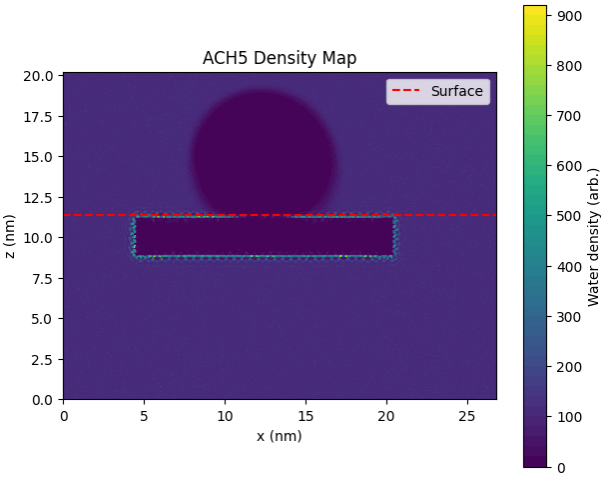

(c) Density map, $\lambda = 5$

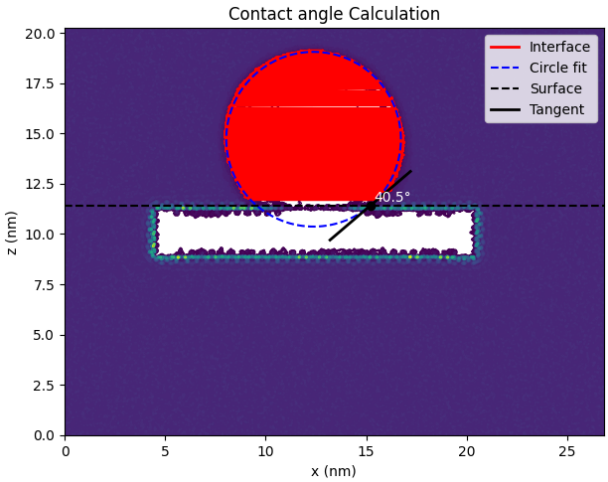

(d) Contact angle fit, $\lambda = 5$

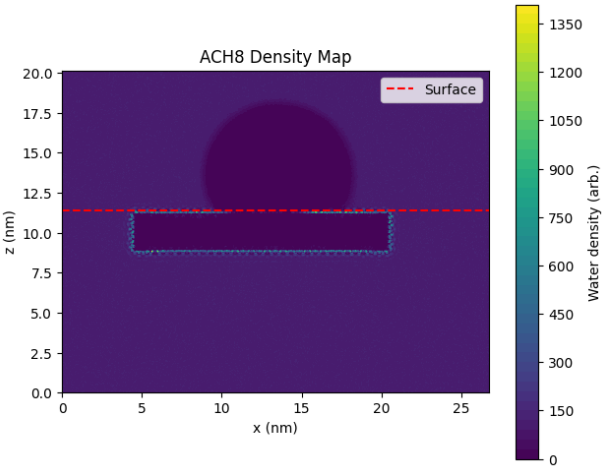

(e) Density map, $\lambda = 8$

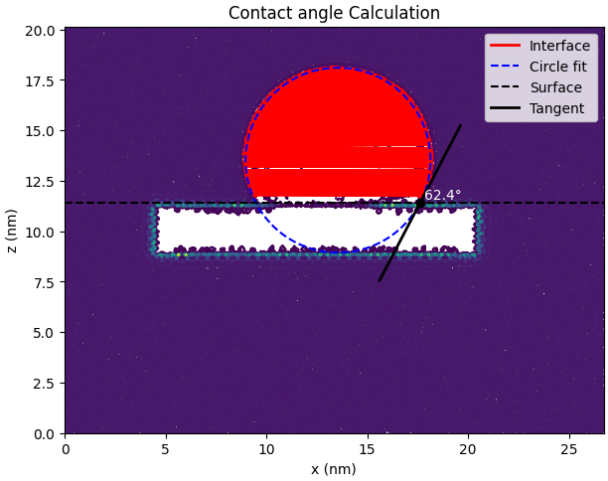

(f) Contact angle fit, $\lambda = 8$

Figure 5.8: Representative systems for three CO_2-surface scaling factors. Left column: time-averaged two-dimensional density maps used for interface identification. Right column: corresponding circular fits and tangent construction used to determine the contact angle. From top to bottom, the scaling factor increases from $\lambda = 2$ to $\lambda = 8$, illustrating the transition in wettability behavior with increasing gas-surface interaction strength.

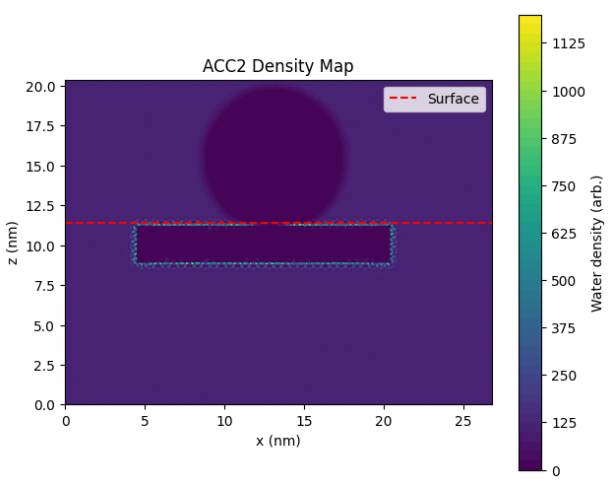

(a) Density map, $\lambda = 2$

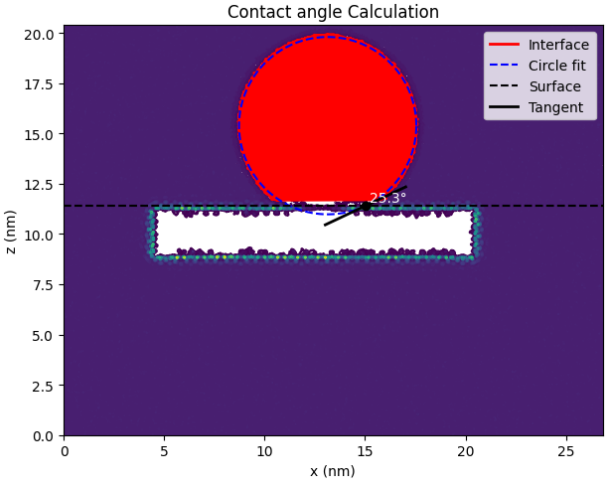

(b) Contact angle fit, $\lambda = 2$

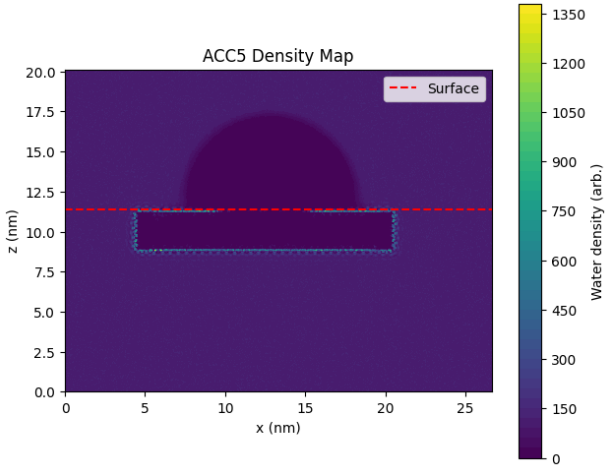

(c) Density map, $\lambda = 5$

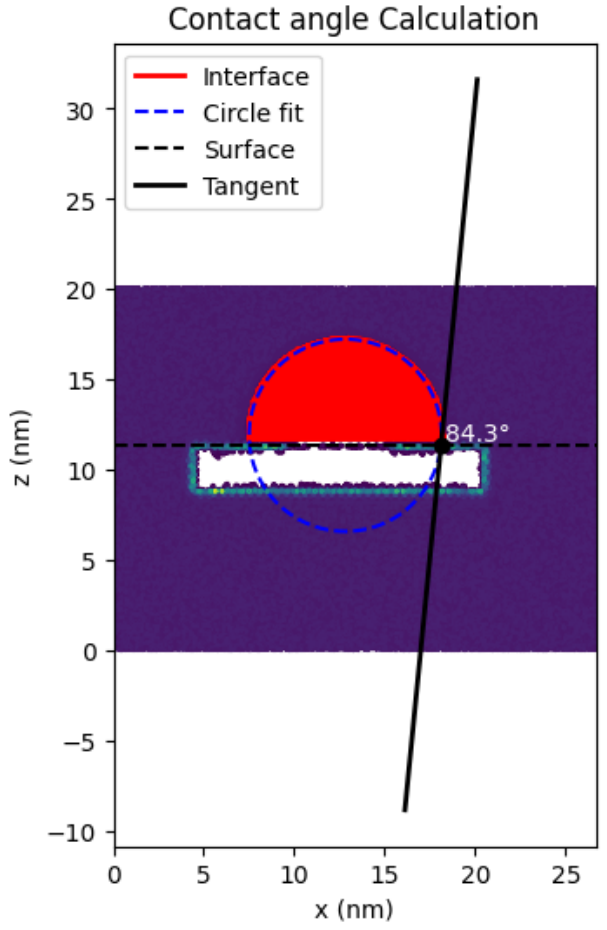

(d) Contact angle fit, $\lambda = 5$

Figure 5.9: Representative systems for three hydrogen-surface scaling factors. Left column: time-averaged two-dimensional density maps used for interface identification. Right column: corresponding circular fits and tangent construction used to determine the contact angle. From top to bottom, the scaling factor increases from $\lambda = 2$ to $\lambda = 8$, illustrating the transition in wettability behavior with increasing gas-surface interaction strength.

5.3. Effect of CO_2 fraction on Contact Angle

In the final set of simulations, the gas-rock interaction parameters were modified such that the surface exhibits hydrophobic behavior, the set of interactions parameters are shown in table 5.7. The gas–rock interactions are modified by scaling the H_2–rock interactions to $\lambda = 8$ in all simulations, while the CO_2–rock interactions are scaled to either $\lambda = 2$ or $\lambda = 4$.

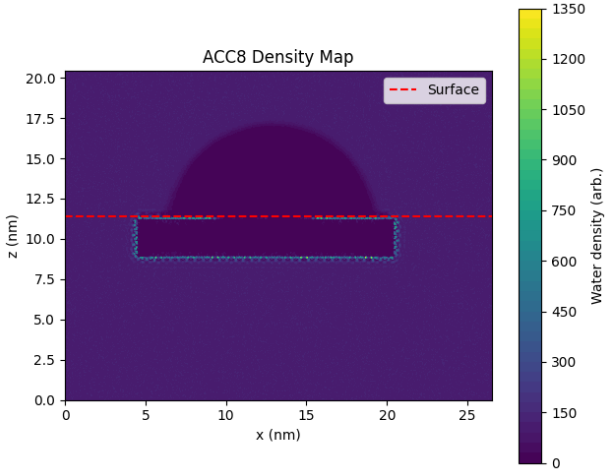

(e) Density map, $\lambda = 8$

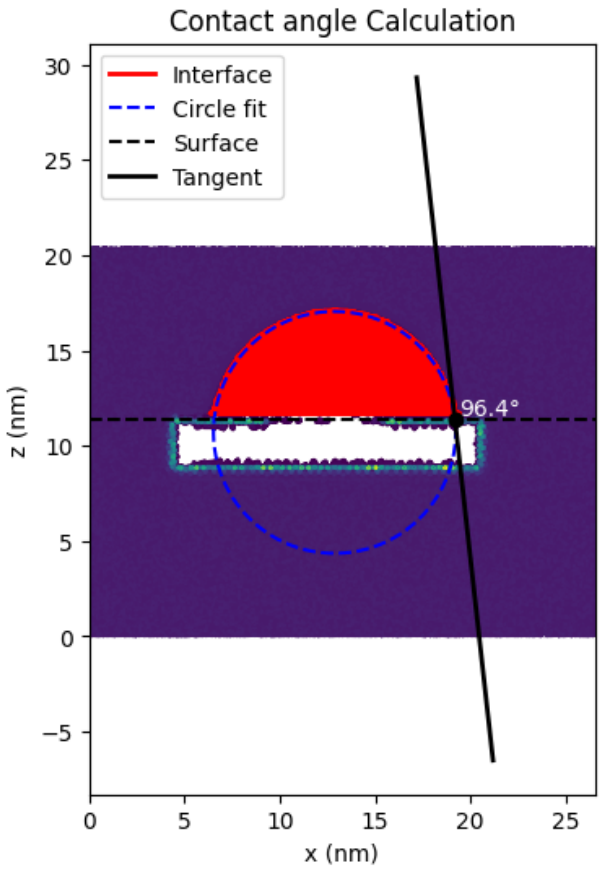

(f) Contact angle fit, $\lambda = 8$

Because the bubble consists of a binary mixture of H_2 and CO_2, competitive adsorption at the rock surface may occur. Depending on the relative surface affinity of each species, either hydrogen or CO_2 can preferentially accumulate near the interface, thereby modifying the effective gas-rock interfacial energy. To investigate this behavior, systems exhibiting dominant CO_2 adsorption and systems exhibiting dominant H_2 adsorption are considered separately.

5.3.1. CO_2 Adsorbed Layer

In the systems where the CO_2-rock interaction dominates, a clear enrichment of CO_2 molecules at the solid interface is observed, as shown in figure 5.10. Figure 5.12 shows the two-dimensional density map of both CO_2 and H_2. In this figure there is a clear layer of higher density CO_2 present at the gas-rock interface.

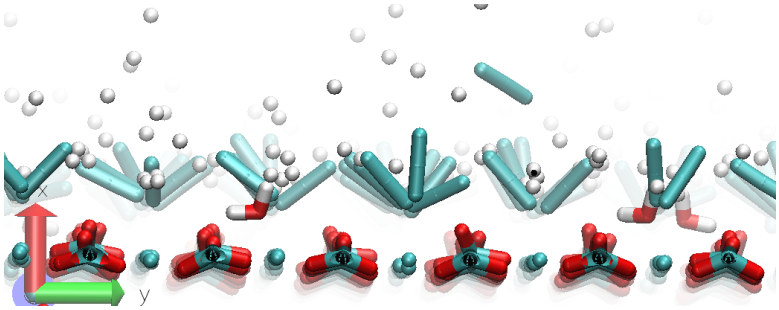

Figure 5.10: Zoomed in snapshot showing the gas-rock interface, where the bottom half represents the solid, and the white and blue particles are H_2 and CO_2 respectively.

As the CO_2 fraction in the bubble increases, the contact angle slightly tends to increase although with some variability. By which increasing the CO_2 content enhances the effective gas-rock affinity of the bubble, leading to an increase in contact angle. This trend is shown in figure 5.11.

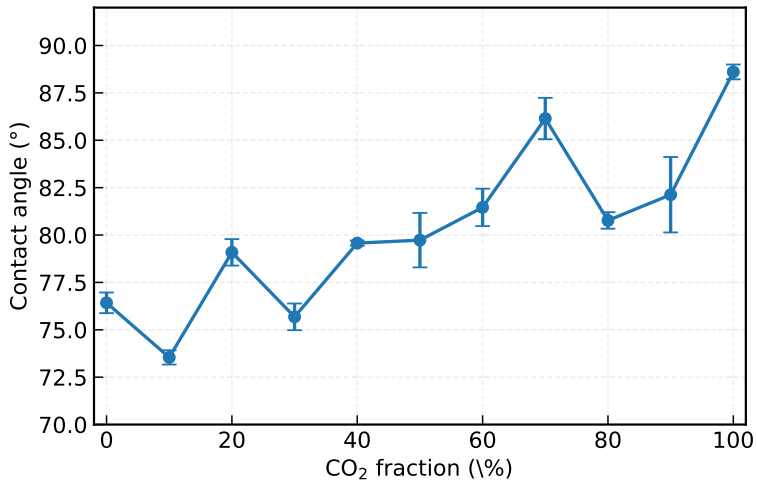

Figure 5.11: Contact Angles vs CO_2 fraction the system with $\lambda_{CO_2} = 4$

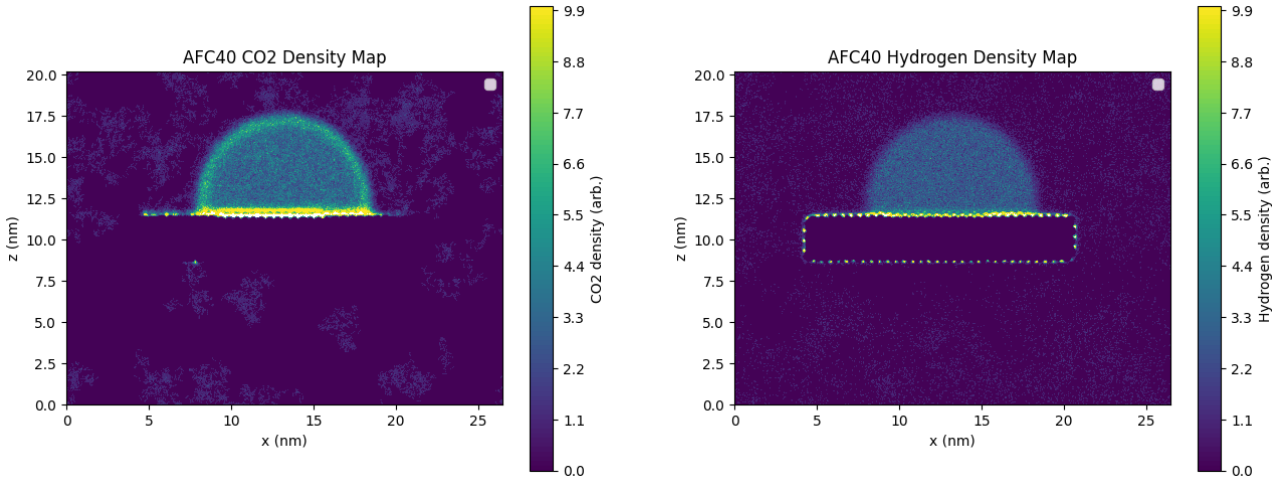

(a) CO_2 density distribution near the surface.

(b) H_2 density distribution near the surface.

Figure 5.12: Two-dimensional density maps illustrating the interfacial distributions of CO_2 (left) and H_2 (right) for the AFC40 system (where $\lambda_{CO_2} = 4$ and the $x_{CO_2} = 0.4$). The density profiles highlight the preferential adsorption behavior at the solid surface.

Table 5.7: Scaled Lennard–Jones cross interaction parameters for mixed systems with $\lambda_{H_2} = 8$ and $\lambda_{CO_2} = 4$ (left) or $\lambda_{CO_2} = 2$ (right). Rock–water interactions are reduced to $1/8$ of the unscaled values. All other interactions remain unscaled.

$\lambda_{H_2} = 8, \lambda_{CO_2} = 4$			
Pair		C_6	C_{12}
H_2–rock			
H_2	Ca	8.672E-03	3.00092E-06
H_2	CO	1.00592E-02	7.47294E-06
H_2	OC	1.595144E-02	2.360176E-05
CO_2–rock			
CO_2C	Ca	1.2308E-03	3.6752E-07
CO_2C	OC	3.0736E-03	2.0072E-06
CO_2C	CO	6.9040E-03	9.1080E-06
CO_2O	Ca	1.7052E-03	6.7600E-07
CO_2O	OC	4.1160E-03	3.4492E-06
CO_2O	CO	9.0000E-03	1.4828E-05

$\lambda_{H_2} = 8, \lambda_{CO_2} = 2$			
Pair		C_6	C_{12}
H_2–rock			
H_2	Ca	8.672E-03	3.00092E-06
H_2	CO	1.00592E-02	7.47294E-06
H_2	OC	1.595144E-02	2.360176E-05
CO_2–rock			
CO_2C	Ca	6.154E-04	1.8376E-07
CO_2C	OC	1.5368E-03	1.0036E-06
CO_2C	CO	3.452E-03	4.554E-06
CO_2O	Ca	8.526E-04	3.380E-07
CO_2O	OC	2.058E-03	1.7246E-06
CO_2O	CO	4.500E-03	7.414E-06

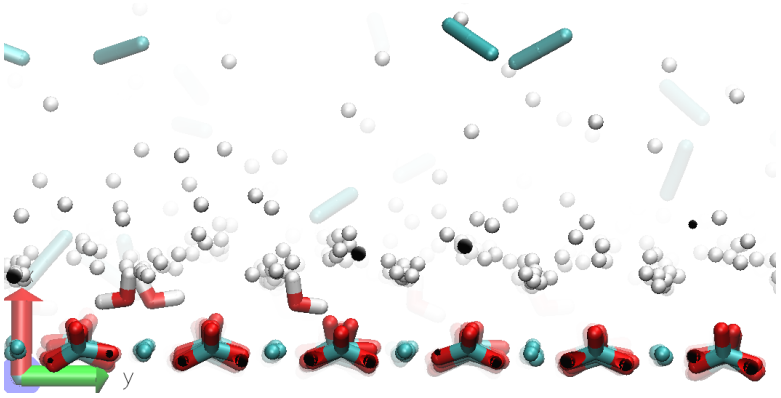

Figure 5.13: Zoomed in snapshot showing the gas-rock interface, where the bottom half represents the solid, and the white and blue particles are H_2 and CO_2 respectively.

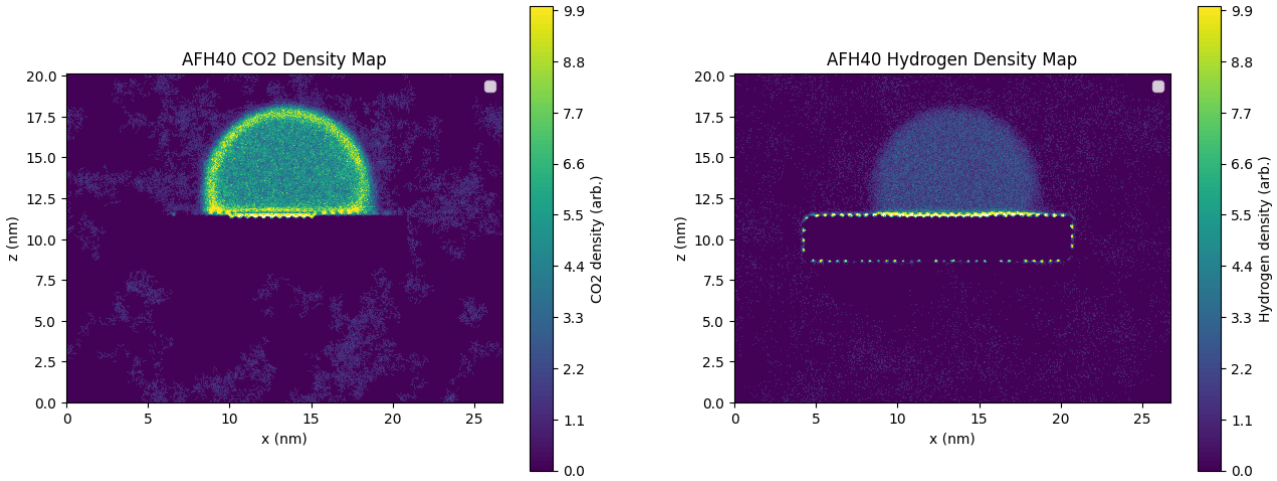

(a) CO_2 density distribution near the surface.

(b) H_2 density distribution near the surface.

Figure 5.14: Two-dimensional density maps illustrating the interfacial distributions of CO_2 (left) and H_2 (right) for the AFH40 system (where $\lambda_{CO_2} = 2$ and the $x_{CO_2} = 0.4$. The density profiles highlight the preferential adsorption behavior at the solid surface.

5.3.2. H_2 Adsorbed Layer

In contrast to the previous system where CO_2-rock interaction dominates, now H_2-rock interaction dominates. This is also clear from figure 5.6, where the H_2 atoms are in much higher quantity when close to the gas-rock interface. Figure 5.14 shows the two-dimensional density map of both CO_2 and H_2. In this figure there is a clear layer of higher density H_2 present at the gas-rock interface, while the CO_2 density is more uniform throughout the bubble.

As the CO_2 fraction in the bubble increases, the contact angle tends to strongly decrease. By which increasing the CO_2 content decreases the effective gas-rock affinity of the bubble, leading to an decrease in contact angle. This trend is shown in figure 5.15.

5.3.3. Affects of Gas Affinity Differences

Figures 5.11 and 5.15 present the contact angle as a function of CO_2 fraction for systems in which either H_2 or CO_2 preferentially adsorbs at the surface. The results demonstrate that differences in gas-surface affinity significantly influence the wettability of the slab.

In the CO_2-adsorbed regime, where CO_2 has a higher surface affinity and forms the dominant interfacial layer, the contact angle increases with increasing CO_2 fraction. In contrast, in the H_2-adsorbed regime, where hydrogen dominates the interfacial region, the contact angle decreases with increasing CO_2 fraction. The introduction of CO_2 in this case reduces the hydrogen coverage at the interface, leading to a measurable change in wettability in the opposite direction.

These opposing trends highlight the critical role of preferential adsorption in determining macroscopic wetting behavior.

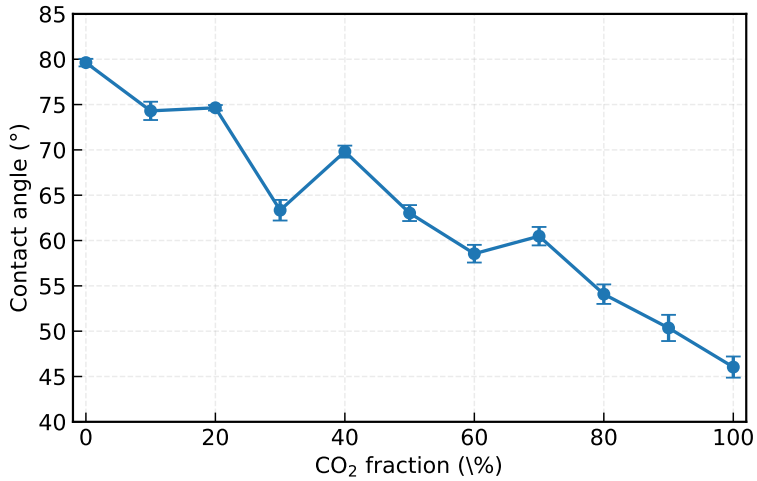

Figure 5.15: Contact Angles vs CO_2 fraction the system with $\lambda_{CO_2} = 2$.

5.3.4. Fraction Correction due to Dissolution

In these systems, part of the gases dissolved as well into the bulk water phase. Therefore a correction of the respective mol fraction of each system should be accounting for this loss. These corrections can be found in table 5.8, with the respective fitted circle parameters in table 5.9.

Table 5.8: Corrected gas fractions and molecule counts for altered fraction (AF) systems. Left: hydrogen-adsorbed regime. Right: CO_2-adsorbed regime.

H_2-Adsorbed Systems					**CO_2-Adsorbed Systems**				
System	$x(H_2)$	$x(CO_2)$	$N_{corr}(H_2)$	$N_{corr}(CO_2)$	System	$x(H_2)$	$x(CO_2)$	$N_{corr}(H_2)$	$N_{corr}(CO_2)$
H0AF	1.000	0.000	2271	0	C0AF	1.000	0.000	2054	0
H10AF	0.889	0.111	1994	249	C10AF	0.876	0.124	2039	288
H20AF	0.789	0.211	1730	463	C20AF	0.759	0.241	1749	554
H30AF	0.697	0.303	1531	665	C30AF	0.660	0.340	1570	808
H40AF	0.574	0.426	1456	1081	C40AF	0.554	0.446	1328	1068
H50AF	0.465	0.535	1108	1273	C50AF	0.454	0.546	1105	1328
H60AF	0.357	0.643	849	1527	C60AF	0.348	0.652	871	1633
H70AF	0.258	0.742	628	1810	C70AF	0.233	0.767	577	1895
H80AF	0.159	0.841	392	2080	C80AF	0.159	0.841	416	2200
H90AF	0.074	0.926	184	2313	C90AF	0.075	0.925	197	2437
H100AF	0.000	1.000	0	2591	C100AF	0.000	1.000	0	2636

Table 5.9: Fitted bubble centre coordinates (x_c, z_c) and radius (R) for altered fraction (AF) systems. Left: H_2-adsorbed regime. Right: CO_2-adsorbed regime.

H_2-Adsorbed Systems			
System	x_c	z_c	R
H0AF	13.32	12.22	4.37
H10AF	13.07	12.60	4.20
H20AF	12.54	13.53	4.57
H30AF	13.51	13.09	4.76
H40AF	13.52	13.05	4.95
H50AF	12.55	13.44	4.37
H60AF	12.54	13.60	4.08
H70AF	12.71	13.45	4.03
H80AF	12.55	13.87	4.11
H90AF	11.98	13.99	3.94
H100AF	13.07	14.23	3.98

CO_2-Adsorbed Systems			
System	x_c	z_c	R
C0AF	13.54	12.58	4.85
C10AF	13.37	12.83	4.95
C20AF	13.18	12.36	4.76
C30AF	13.08	12.66	4.86
C40AF	13.21	12.31	4.96
C50AF	12.17	12.43	5.04
C60AF	12.79	12.06	5.00
C70AF	12.94	11.62	4.59
C80AF	12.78	12.21	5.27
C90AF	12.78	11.94	5.09
C100AF	13.22	11.55	5.02

6

Discussion

6.1. Reference Systems and Baseline Wettability

The reference simulations, performed using unscaled interaction parameters, provide the baseline for interpreting the modified systems. In all reference cases, the gas bubble completely detached from the surface, corresponding to an contact angle of 180°. This indicates that under the original parameterization the surface behaves strongly hydrophilic with respect to the surrounding water phase, preventing stable gas adhesion at the solid interface.
The absence of stable gas attachment in the reference systems highlights that the intrinsic gas–rock interactions are insufficient to overcome the solid–water interfacial affinity.

This baseline is essential for interpreting the subsequent scaling results. Since the initial state corresponds to complete detachment, the contact angle variations observed upon scaling the interaction parameters reflect the ability of gas adsorption to compete with the strong solid–water affinity. The magnitude contact angle increase therefore provide a quantitative measure of the effectiveness of each gas species in modifying the interfacial energy balance.

6.2. Wettability Mechanism and Gas Affinity

The results demonstrate that wettability in the studied systems is primarily governed by the relative gas-rock interaction strength, instead of the gas fraction alone. When the CO_2-rock interactions are scaled, the contact angle increases rapidly and more significantly compared to when the H_2-rock interactions are scaled. Therefore indicating that CO_2 has a much stronger influence on the surface wetting behavior.

This behavior can be explained due to the molecular structure and interaction strength. Where CO_2 possesses a quadrupole moment and stronger dispersion interactions compared to H_2, resulting in a higher affinity for the surface when interaction parameters are increased [44]. Consequentially, CO_2 adsorbs stronger at the solid interface and modifies the contact angle more strongly than H_2. Therefore, CO_2 is the dominant wettability-controlling species, which is consistent with previous studies reporting that CO_2 has a stronger influence on surface wettability than H_2 [4].

6.3. Role of CO_2 Fraction in Mixed Systems

In the altered fraction simulations, the behavior depends strongly on which gas forms the adsorbed layer at the surface. Two distinct regimes are observed.

When CO_2 dominates the adsorbed layer, increasing the CO_2 fraction leads to an increase in contact angle. Suggesting that an increased fraction of CO_2, enhances the hydrophobicity of the surface.

In contrast, when H_2 dominates the adsorbed layer, increasing the CO_2 fraction causes the contact angle to significantly decrease, in the opposite direction of when CO_2 was dominating as the adsorbed layer. Therefore in this situation, the introduction of CO_2 modifies the interfacial balance differently, leading to gas adsorption and lower hydrophobicity.

Although CO_2 usually dominates adsorption at mineral surfaces, hydrogen rich interfacial layers may become relevant in environments where hydrogen consuming microorganisms form biofilms. Biofilms can modify surface chemistry and create local hydrogen gradients, potentially increasing hydrogen affinity at the interface

[18]. In the present simulations, this effect is represented by tuning the interaction parameters, providing a mechanistic model for how microbial activity could influence wettability in subsurface gas systems.

These findings demonstrate that wettability in mixed gas systems cannot be predicted solely from bulk composition. Instead, the surface affinity hierarchy between gases determines the interfacial structure and subsequently the contact angle.

Specifically, systems where CO_2 has stronger surface affinity may experience enhanced adsorption and increased contact angles, potentially influencing trapping and migration processes. Conversely, surfaces favoring H_2 adsorption exhibit different characteristics.

6.4. Limitations and Methodological Considerations

Although the simulations provide clear trends, several limitations should be acknowledged. Firstly, interaction parameters were modified via scaling factors rather than being re-parameterised from first principles. While this approach isolates interaction effects, it may not fully capture realistic chemical behavior.
Secondly, contact angles were extracted from two-dimensional density maps, and uncertainty depends on the chosen interface definition. Although standard deviations were included, systematic uncertainties may remain.
Finally, the simulations were performed at a single thermodynamic condition and system size. Variations in pressure, temperature, or surface morphology could influence adsorption behavior and should be explored in future work.

7

Conclusion

In this work, molecular dynamics simulations were performed to investigate the wettability of a calcite surface in the presence of hydrogen and carbon dioxide gas bubbles. The study focused on three main aspects:

1. the behavior of the unscaled reference system
2. the effect of selectively scaling gas-rock interaction parameters
3. the influence of gas composition in mixed bubble systems under hydrophobic surface conditions

In the reference systems, the gas bubble fully detached from the surface for all gas compositions, therefore resulting in a contact angle of $180°$. Confirming the strongly hydrophilic behavior of the calcite under unmodified interaction parameters, and that neither pure H_2, pure CO_2, nor mixed bubbles exhibit any wetting.

In the simulations where the gas-rock interactions where selectively scaled, a clear difference between hydrogen and carbon dioxide observed. Where increasing the CO_2–rock interaction strength led to a significantly stronger and more rapid increase in contact angle compared to scaling the H_2–rock interactions. Indicating that CO_2 has a stronger affinity for the surface and plays a dominant role in controlling wettability.

Lastly, in the mixed gas systems where the surface was tuned to behave hydrophobic, two different regimes were identified. When CO_2 formed the dominant adsorbed layer at the interface, increasing the CO_2 fraction resulted in an increase in contact angle. On the contrary, when H_2 was the adsorbed species, increasing the CO_2 fraction led to a decrease in contact angle. These results demonstrate that wettability in multi component gas systems is not governed solely by bulk bubble composition, but also by the hierarchy of the gas-surface affinities.

7.1. Recommendations for Future Work

Future work may extend this approach by incorporating pressure and temperature variations, surface roughness effects, or more chemically detailed interaction models. By including these factors, more comprehensive studies can be conducted, thereby improving the predictive capabilities of the simulations.

In addition to this, the present study may be expanded by investigating the effects of salinity and pH on the contact angles, together with the influence of an adsorbed hydrophobic hydrocarbon layer on the surface. Such investigations could provide further insight into how realistic reservoir or environmental conditions affect wetting behavior and interfacial properties.

Furthermore, future work could explore different mineral surfaces or crystal orientations to assess how surface chemistry and structure influence the observed behavior. Comparing simulation results with experimental measurements would also be valuable for validating the modeling approach and improving the reliability of the predicted contact angles.

A

Appendix-A

A.1. Hydrogen and Carbon Dioxide Densities - AF Systems

A.1.1. CO_2 Adsorbed Layer

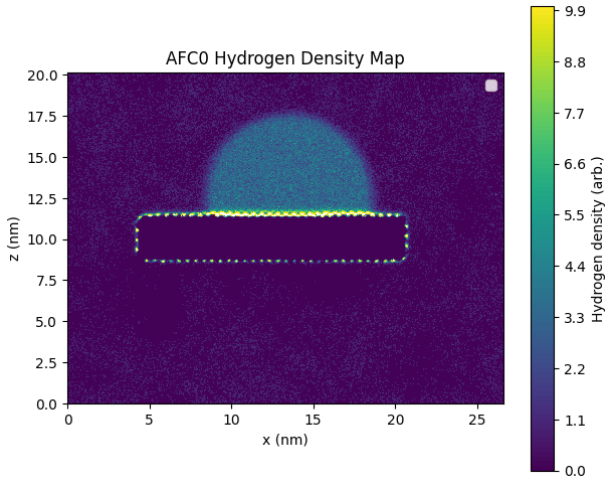

(a) Two-dimensional density map of H_2.

Figure A.1: Time-averaged two-dimensional number density maps of H_2

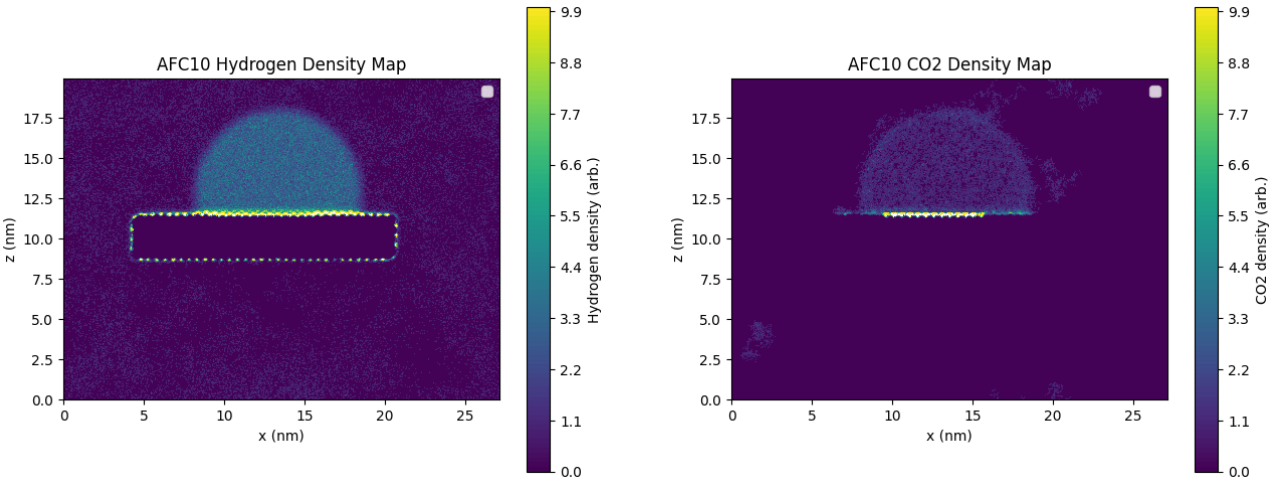

(a) Two-dimensional density map of H_2.

(b) Two-dimensional density map of CO_2.

Figure A.2: Time-averaged two-dimensional number density maps of (a) H_2 and (b) CO_2 in the simulation box

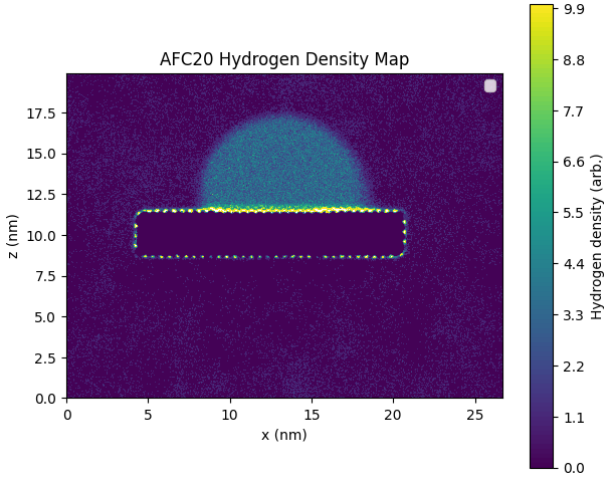

(a) Two-dimensional density map of H_2.

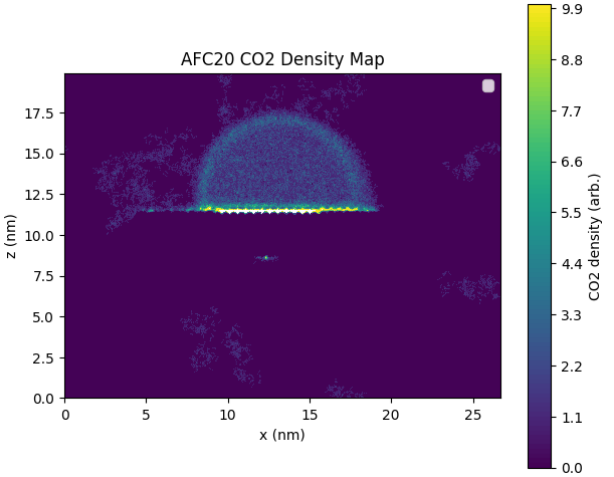

(b) Two-dimensional density map of CO_2.

Figure A.3: Time-averaged two-dimensional number density maps of (a) H_2 and (b) CO_2 in the simulation box

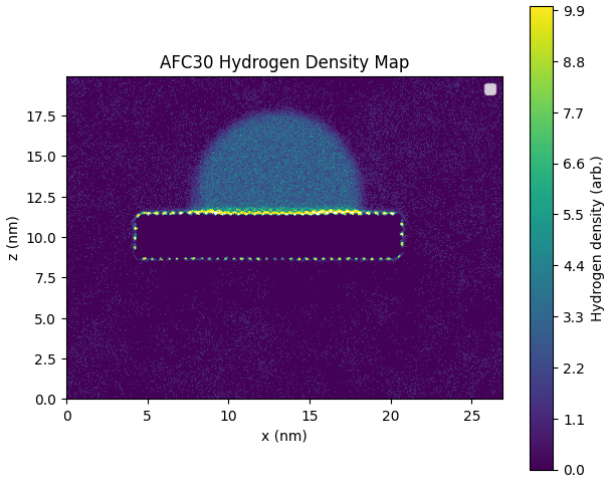

(a) Two-dimensional density map of H_2.

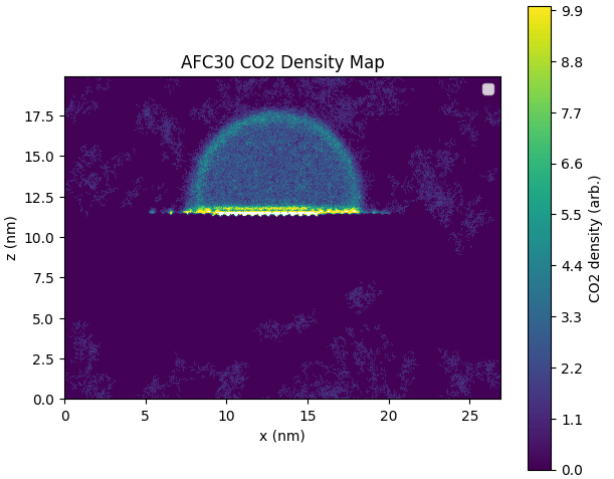

(b) Two-dimensional density map of CO_2.

Figure A.4: Time-averaged two-dimensional number density maps of (a) H_2 and (b) CO_2 in the simulation box

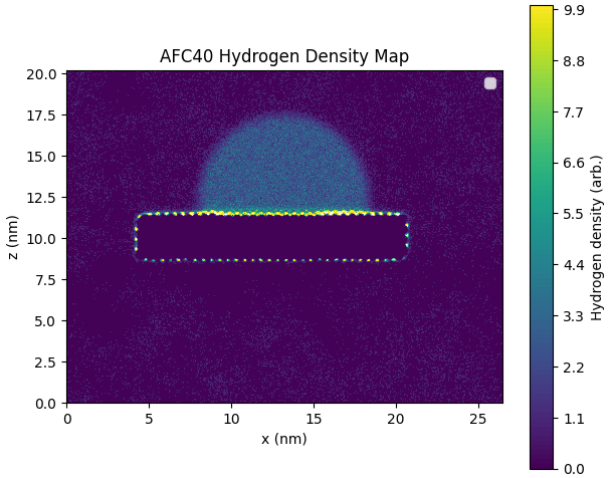

(a) Two-dimensional density map of H_2.

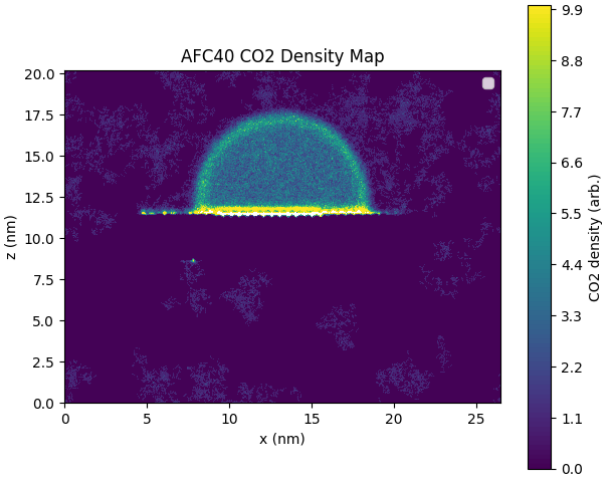

(b) Two-dimensional density map of CO_2.

Figure A.5: Time-averaged two-dimensional number density maps of (a) H_2 and (b) CO_2 in the simulation box

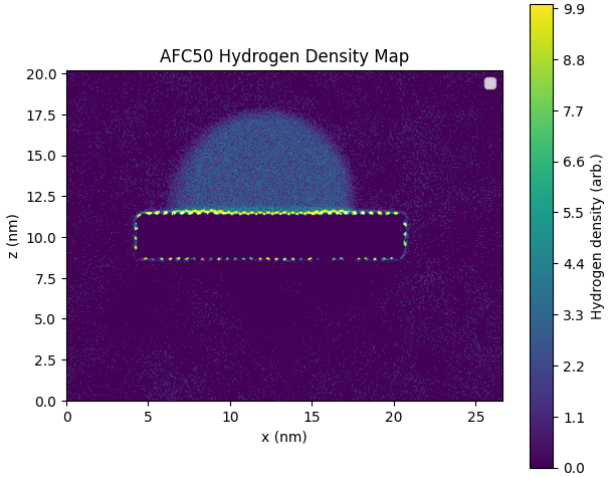

(a) Two-dimensional density map of H_2.

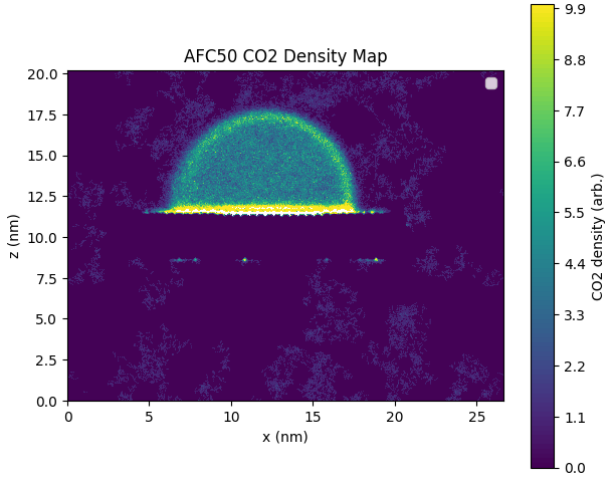

(b) Two-dimensional density map of CO_2.

Figure A.6: Time-averaged two-dimensional number density maps of (a) H_2 and (b) CO_2 in the simulation box

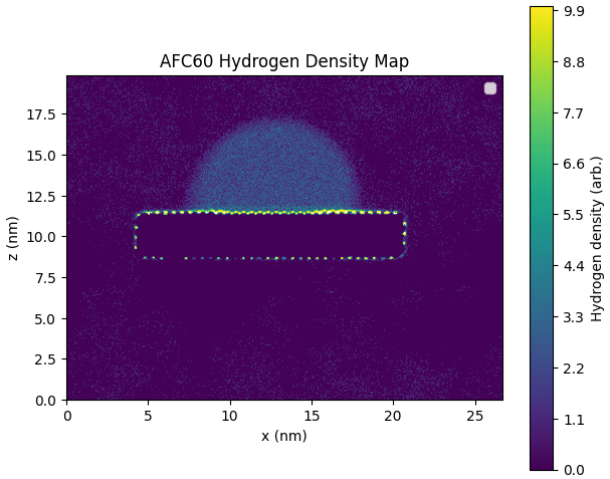

(a) Two-dimensional density map of H_2.

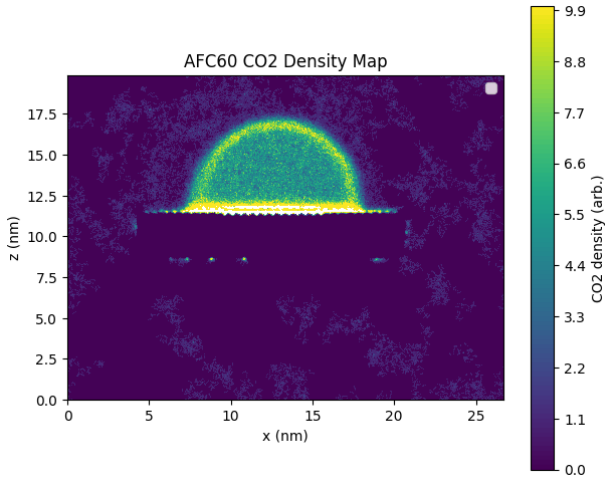

(b) Two-dimensional density map of CO_2.

Figure A.7: Time-averaged two-dimensional number density maps of (a) H_2 and (b) CO_2 in the simulation box

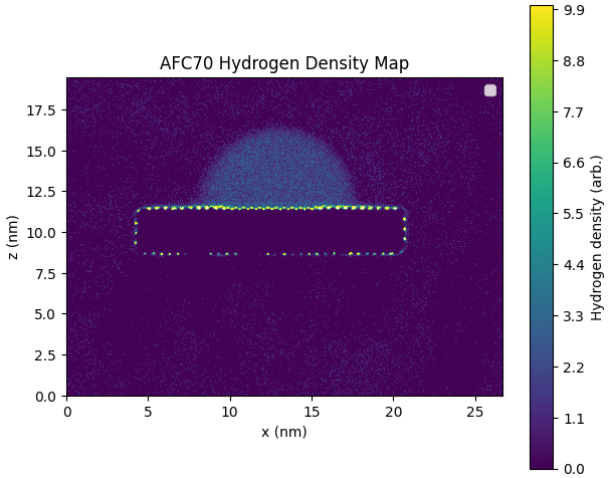

(a) Two-dimensional density map of H_2.

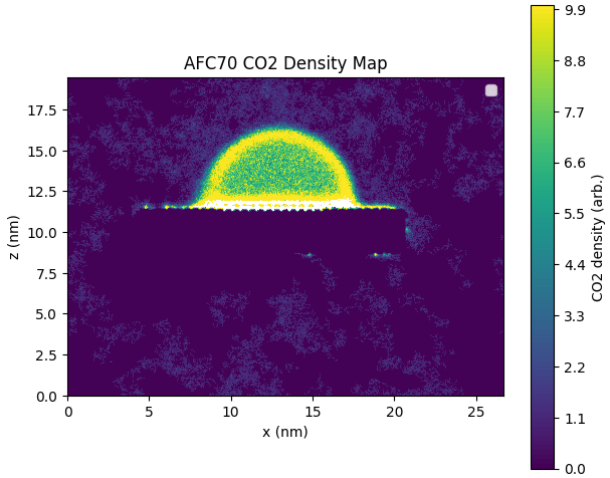

(b) Two-dimensional density map of CO_2.

Figure A.8: Time-averaged two-dimensional number density maps of (a) H_2 and (b) CO_2 in the simulation box

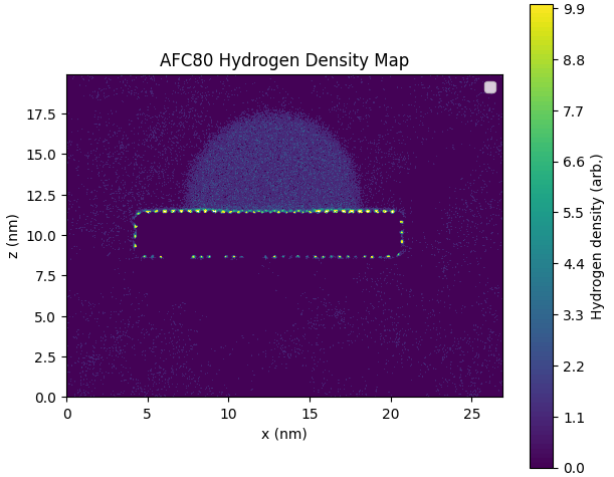

(a) Two-dimensional density map of H_2.

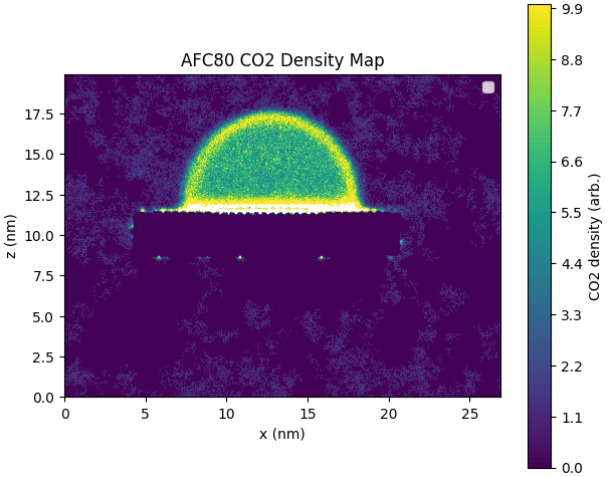

(b) Two-dimensional density map of CO_2.

Figure A.9: Time-averaged two-dimensional number density maps of (a) H_2 and (b) CO_2 in the simulation box

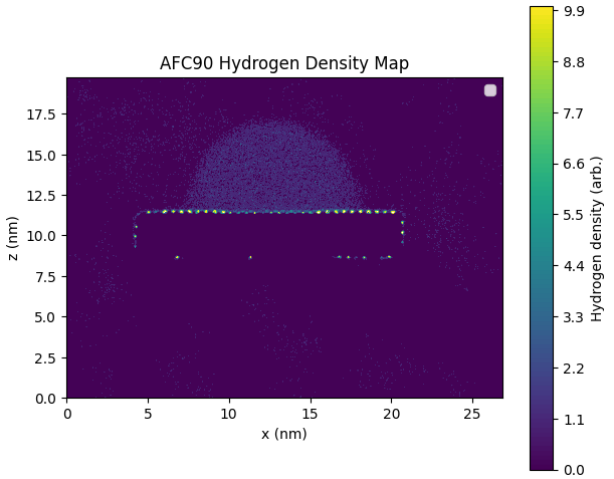

(a) Two-dimensional density map of H_2.

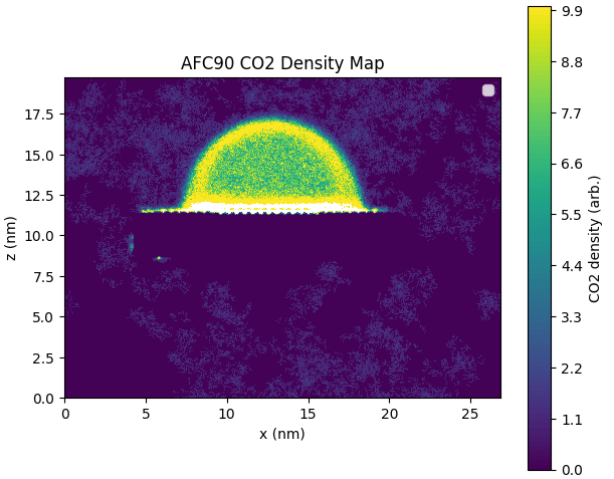

(b) Two-dimensional density map of CO_2.

Figure A.10: Time-averaged two-dimensional number density maps of (a) H_2 and (b) CO_2 in the simulation box

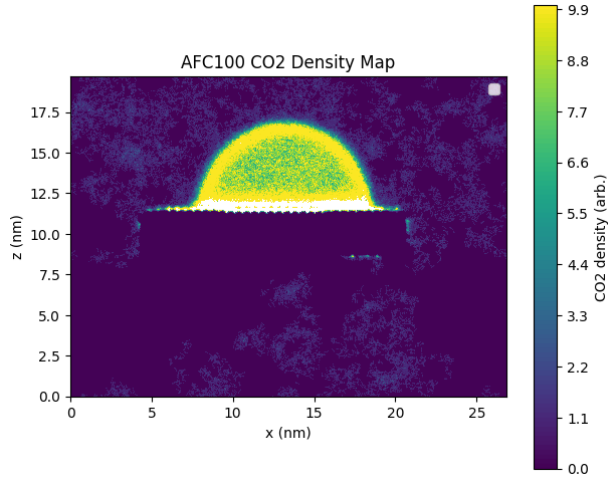

(a) Two-dimensional density map of CO_2.

Figure A.11: Time-averaged two-dimensional number density map CO_2 in the simulation box

A.1.2. H_2 Adsorbed Layer

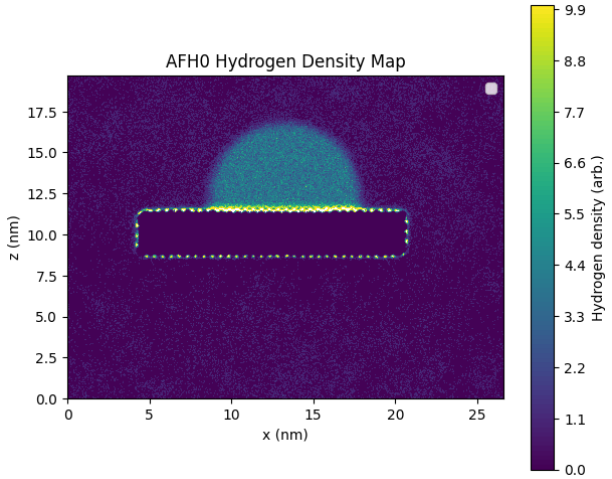

(a) Two-dimensional density map of H_2.

Figure A.12: Time-averaged two-dimensional number density map H_2 in the simulation box

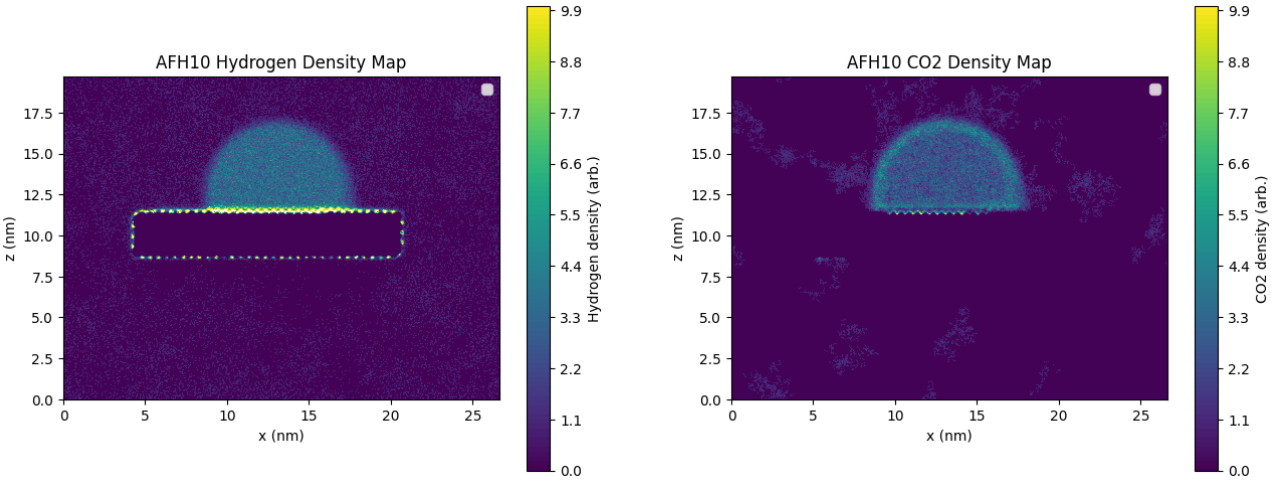

(a) Two-dimensional density map of H_2.

(b) Two-dimensional density map of CO_2.

Figure A.13: Time-averaged two-dimensional number density maps of (a) H_2 and (b) CO_2 in the simulation box

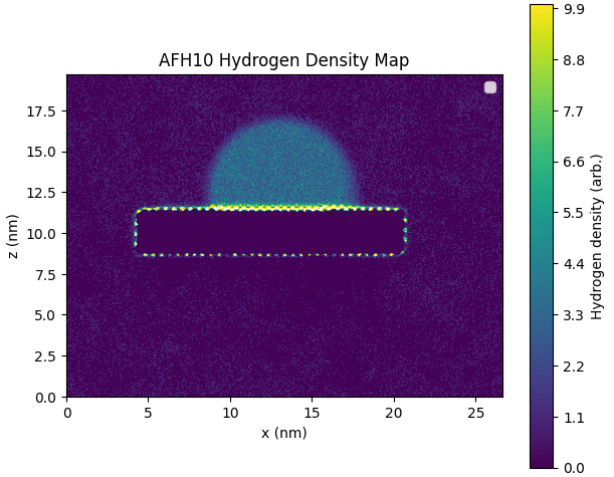

(a) Two-dimensional density map of H_2.

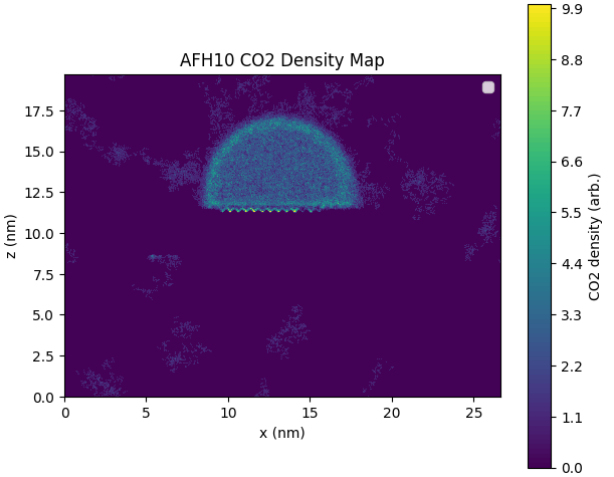

(b) Two-dimensional density map of CO_2.

Figure A.14: Time-averaged two-dimensional number density maps of (a) H_2 and (b) CO_2 in the simulation box

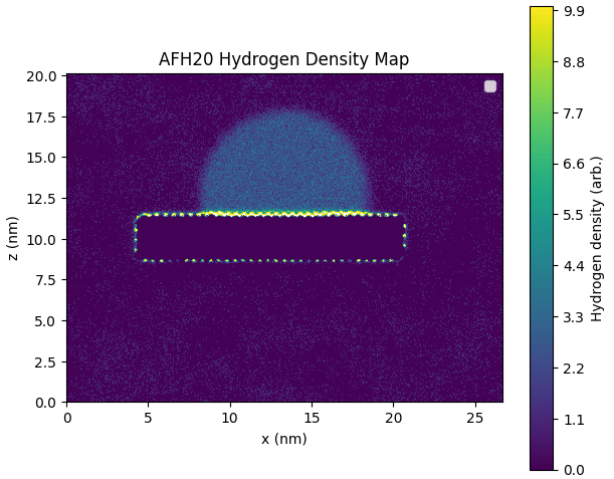

(a) Two-dimensional density map of H_2.

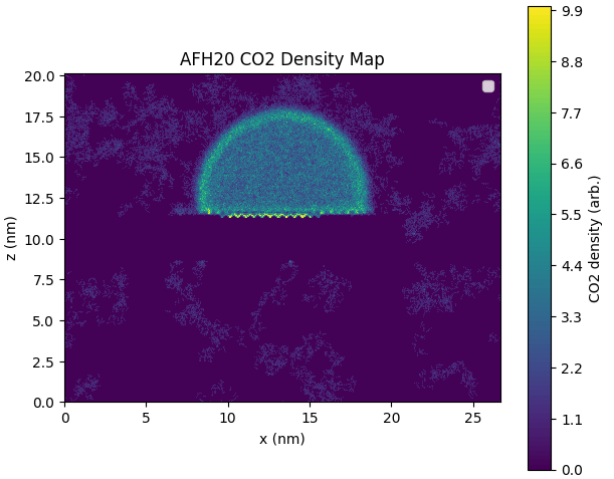

(b) Two-dimensional density map of CO_2.

Figure A.15: Time-averaged two-dimensional number density maps of (a) H_2 and (b) CO_2 in the simulation box

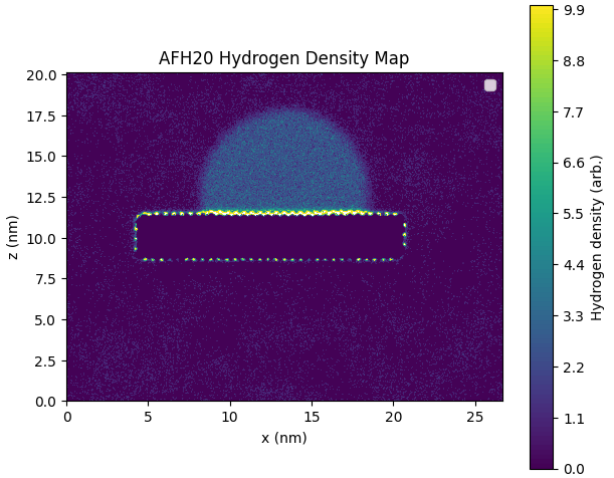

(a) Two-dimensional density map of H_2.

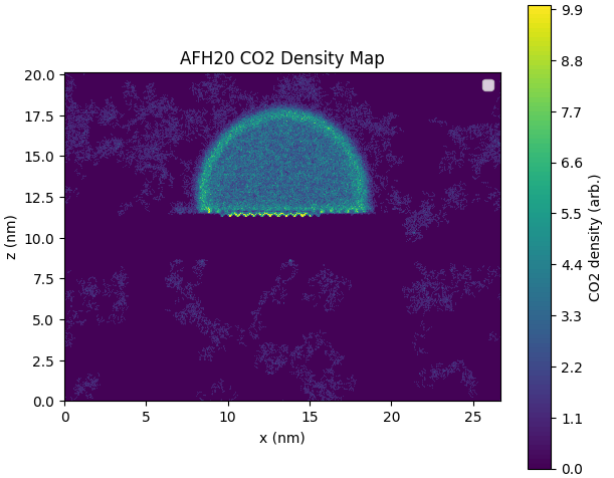

(b) Two-dimensional density map of CO_2.

Figure A.16: Time-averaged two-dimensional number density maps of (a) H_2 and (b) CO_2 in the simulation box

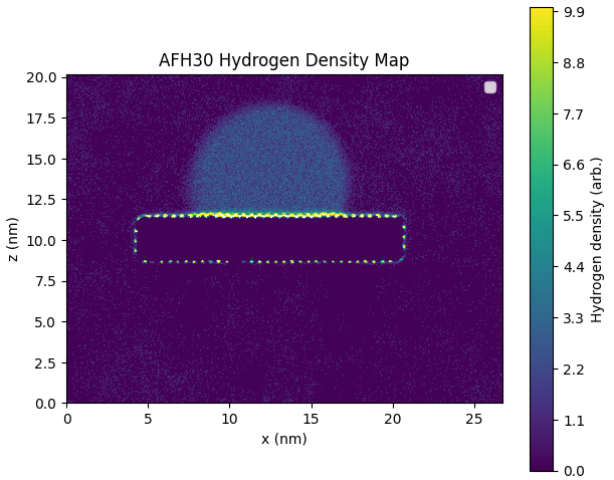

(a) Two-dimensional density map of H_2.

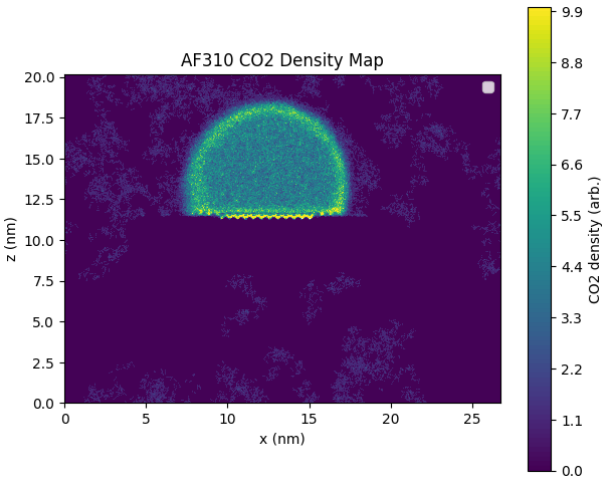

(b) Two-dimensional density map of CO_2.

Figure A.17: Time-averaged two-dimensional number density maps of (a) H_2 and (b) CO_2 in the simulation box

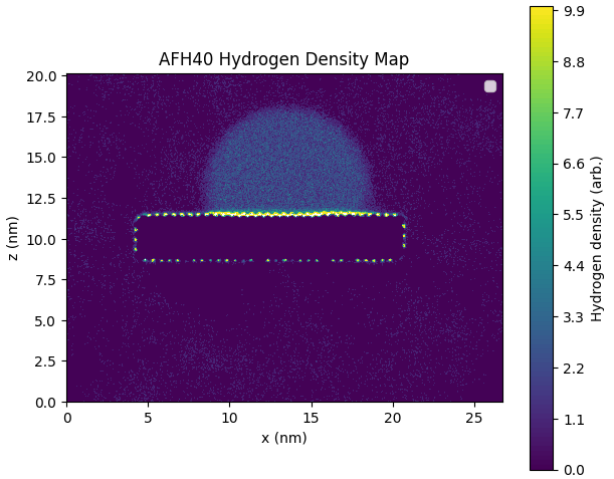

(a) Two-dimensional density map of H_2.

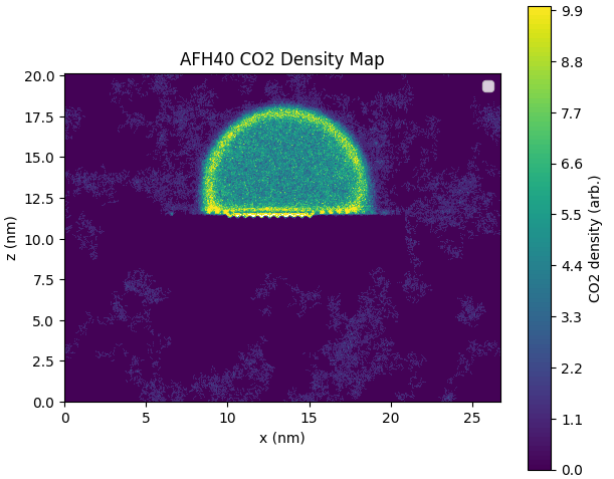

(b) Two-dimensional density map of CO_2.

Figure A.18: Time-averaged two-dimensional number density maps of (a) H_2 and (b) CO_2 in the simulation box

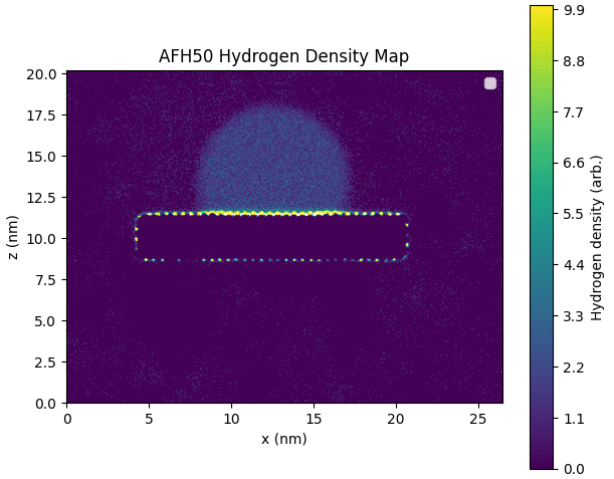

(a) Two-dimensional density map of H_2.

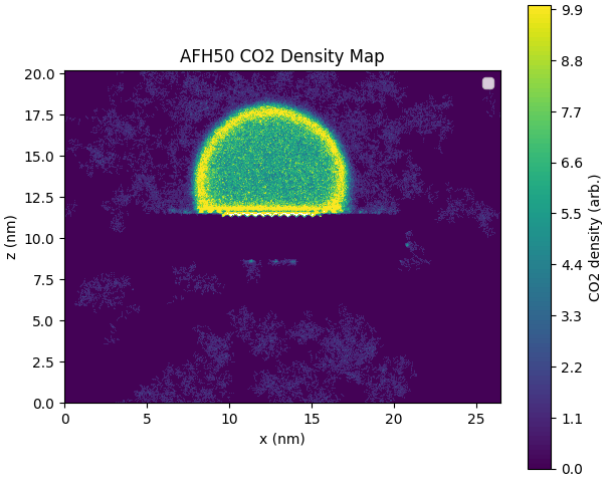

(b) Two-dimensional density map of CO_2.

Figure A.19: Time-averaged two-dimensional number density maps of (a) H_2 and (b) CO_2 in the simulation box

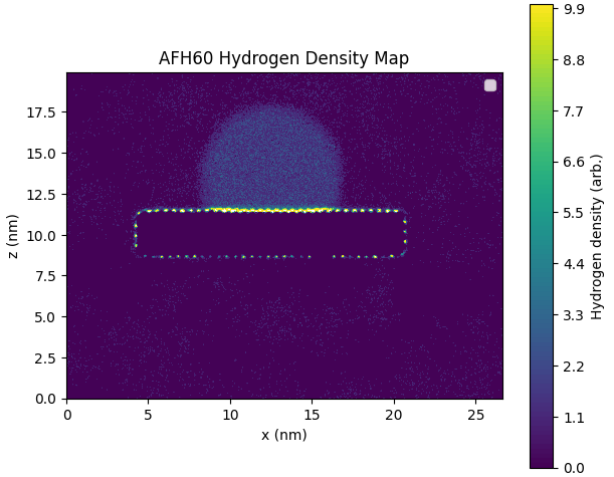

(a) Two-dimensional density map of H_2.

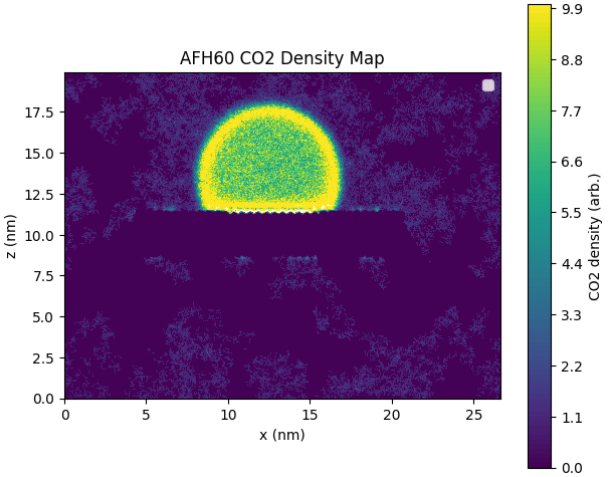

(b) Two-dimensional density map of CO_2.

Figure A.20: Time-averaged two-dimensional number density maps of (a) H_2 and (b) CO_2 in the simulation box

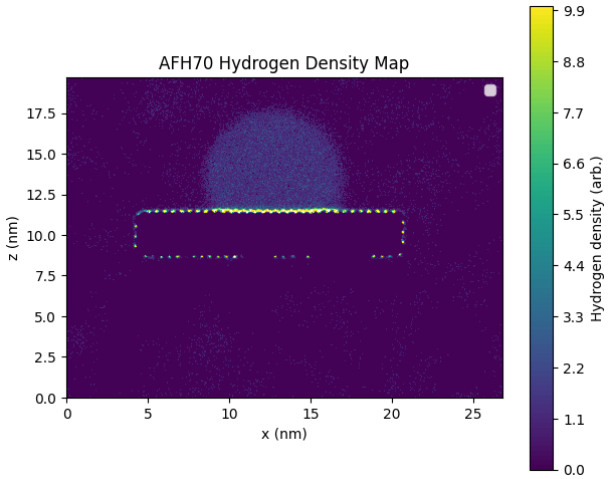

(a) Two-dimensional density map of H_2.

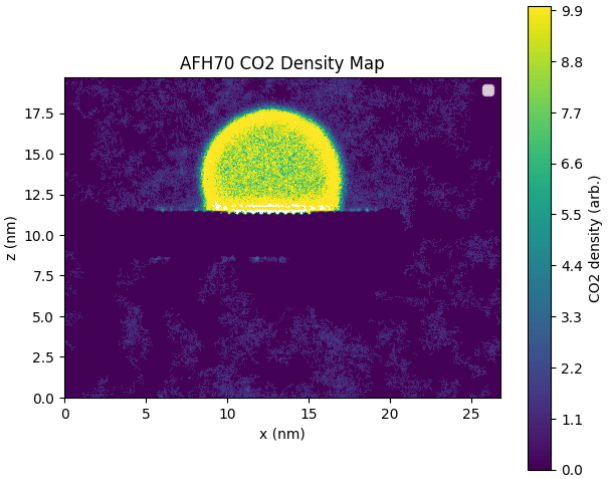

(b) Two-dimensional density map of CO_2.

Figure A.21: Time-averaged two-dimensional number density maps of (a) H_2 and (b) CO_2 in the simulation box

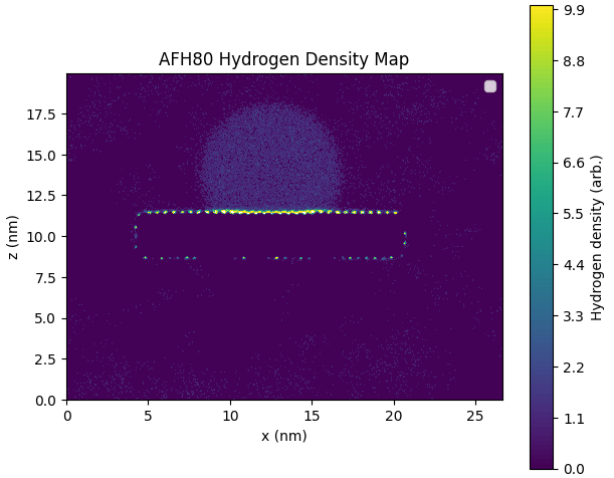

(a) Two-dimensional density map of H_2.

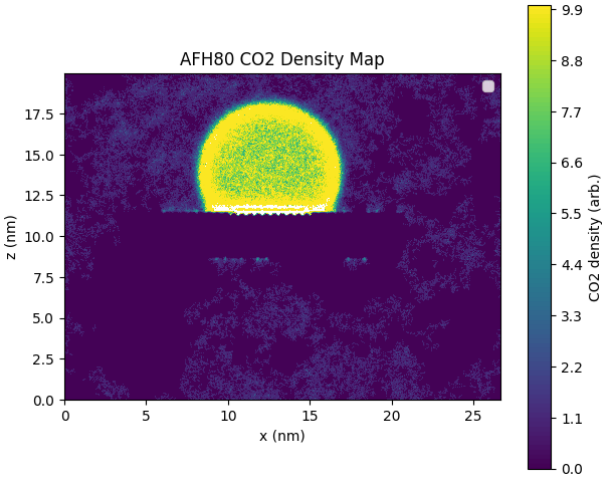

(b) Two-dimensional density map of CO_2.

Figure A.22: Time-averaged two-dimensional number density maps of (a) H_2 and (b) CO_2 in the simulation box

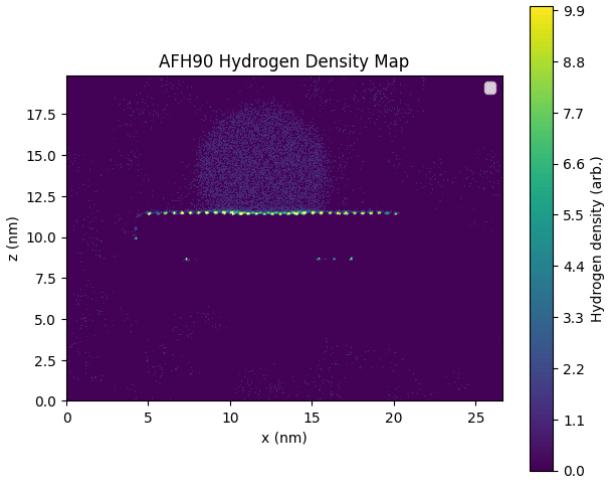

(a) Two-dimensional density map of H_2.

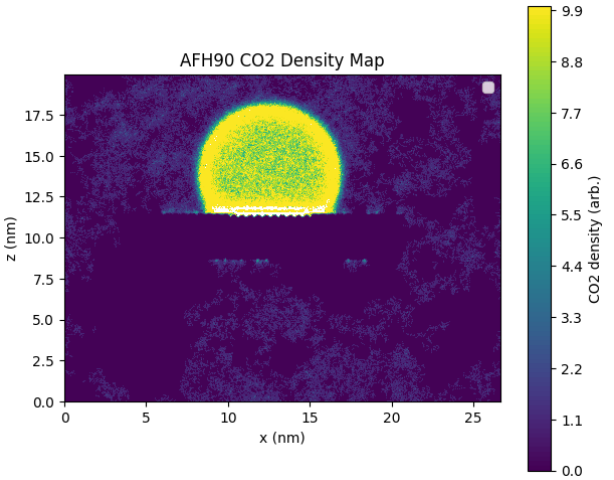

(b) Two-dimensional density map of CO_2.

Figure A.23: Time-averaged two-dimensional number density maps of (a) H_2 and (b) CO_2 in the simulation box

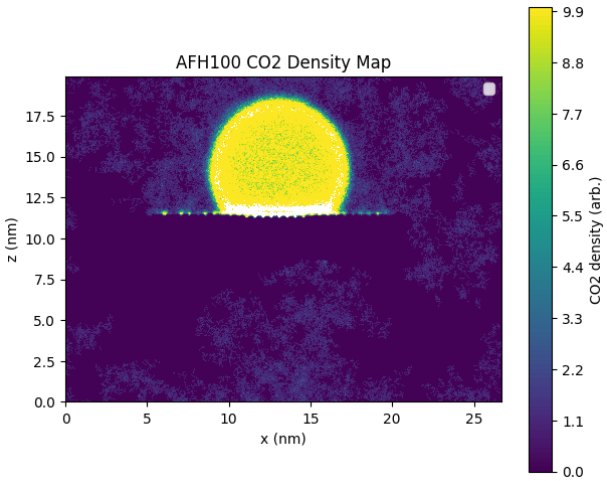

(a) Two-dimensional density map of CO_2.

Figure A.24: Time-averaged two-dimensional number density map CO_2 in the simulation box

B

Appendix-B

B.1. Validation and Equilibration Plots

B.1.1. Reference Systems

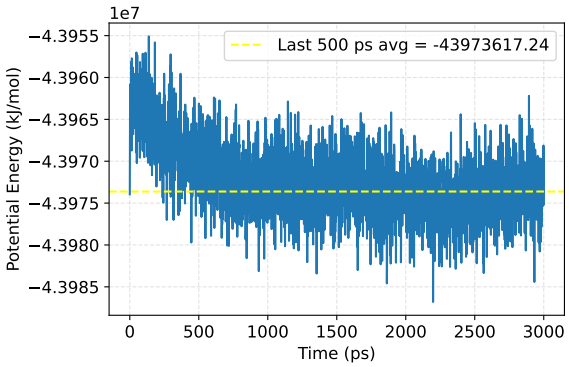

(a) Potential energy

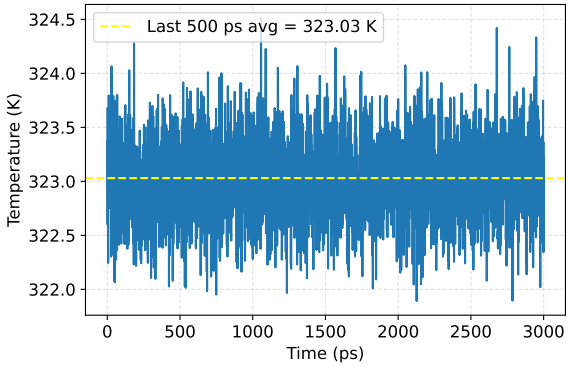

(b) Temperature

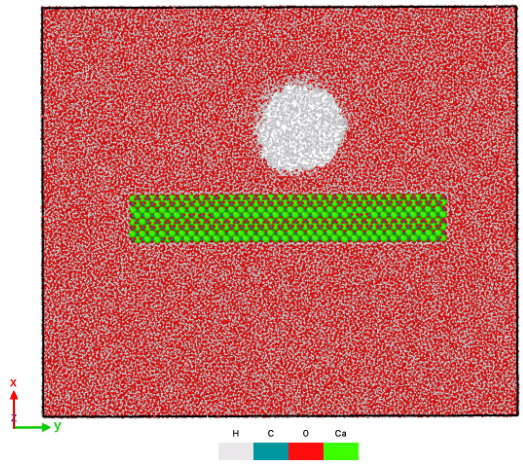

(c) System snapshot (.gro)

Figure B.1: Validation of the equilibrated R0 system. The potential energy (left) and temperature (right) are shown as a function of time; the dashed horizontal lines indicate the mean value over the final 500 ps of the trajectory, used as an equilibrium indicator. The bottom panel shows a representative configuration of the system rendered from the corresponding .gro structure file.

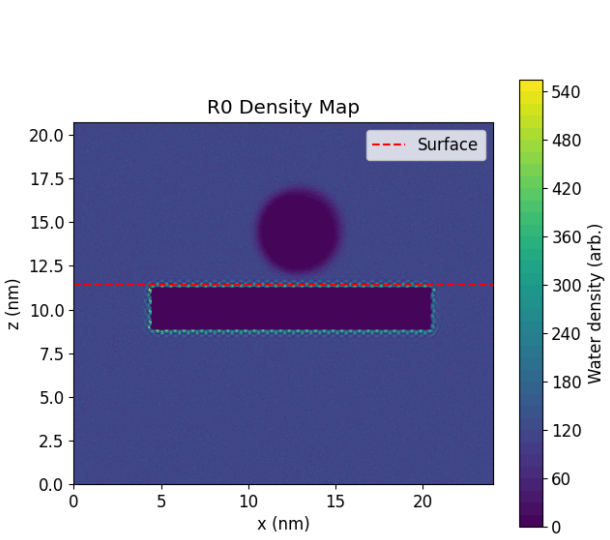

(a) Two-dimensional water density map used to determine the liquid-vapor interface. The dashed line indicates the solid surface position.

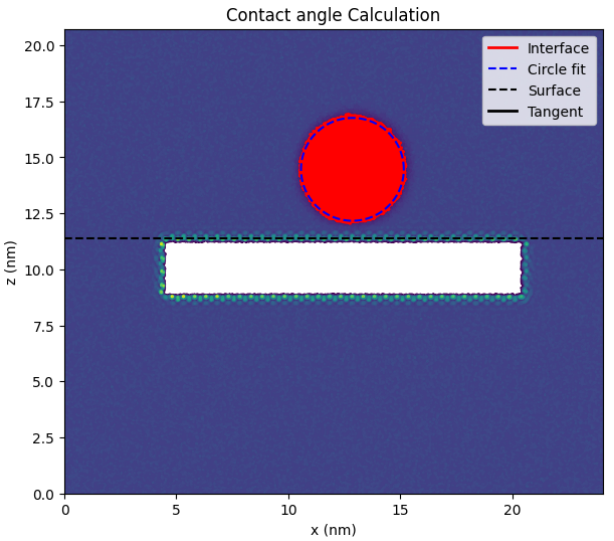

(b) Construction of the contact angle. A circular fit is applied to the detected interface points, and the tangent at the three phase contact line is used to compute the contact angle.

Figure B.2: Illustration of the contact angle determination procedure. (a) The liquid-vapor interface is extracted from the time-averaged density field using a threshold criterion. (b) A circle is fitted to the interface contour, and the contact angle is obtained from the tangent at the intersection between the fitted circle and the solid surface.

B.1.2. AC Systems

Scaled CO_2

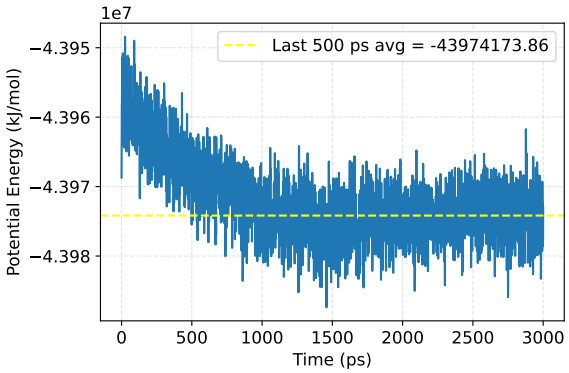

(a) Potential energy

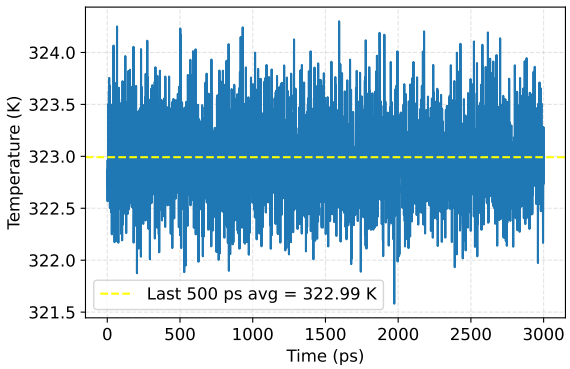

(b) Temperature

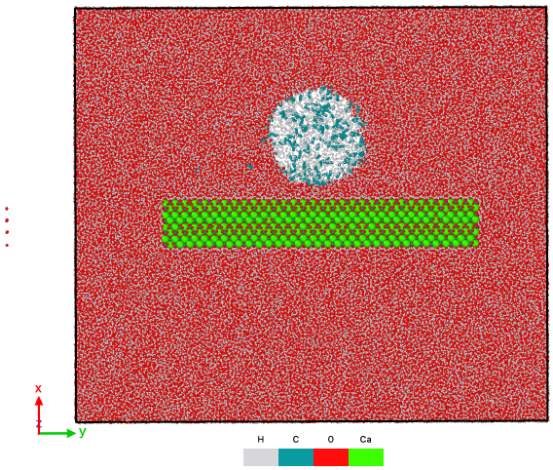

(c) System snapshot (.gro)

Figure B.3: Validation of the equilibrated R10 system. The potential energy (left) and temperature (right) are shown as a function of time; the dashed horizontal lines indicate the mean value over the final 500 ps of the trajectory, used as an equilibrium indicator. The bottom panel shows a representative configuration of the system rendered from the corresponding .gro structure file.

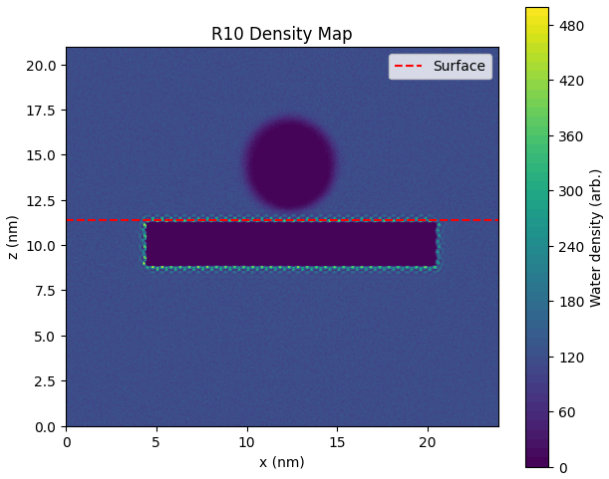

(a) Two-dimensional water density map used to determine the liquid-vapor interface. The dashed line indicates the solid surface position.

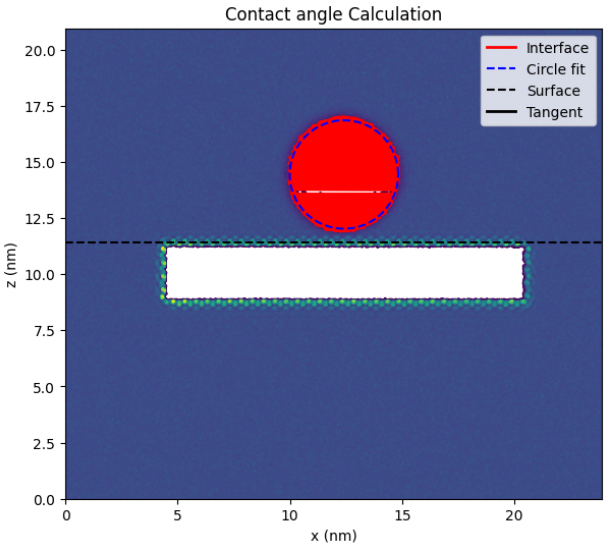

(b) Construction of the contact angle. A circular fit is applied to the detected interface points, and the tangent at the three phase contact line is used to compute the contact angle.

Figure B.4: Illustration of the contact angle determination procedure. (a) The liquid-vapor interface is extracted from the time-averaged density field using a threshold criterion. (b) A circle is fitted to the interface contour, and the contact angle is obtained from the tangent at the intersection between the fitted circle and the solid surface.

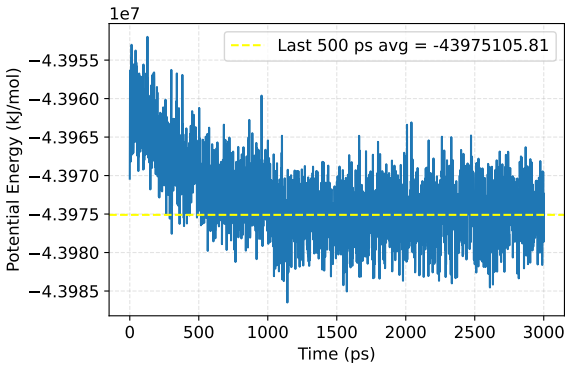

(a) Potential energy

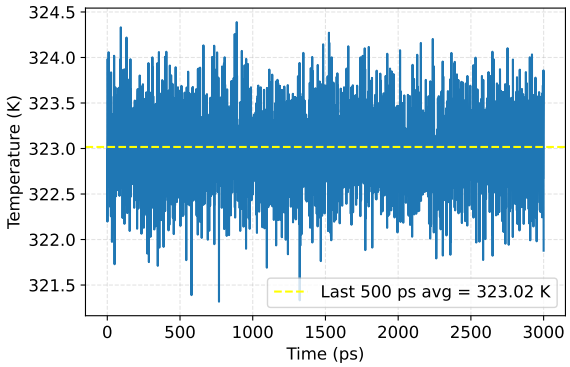

(b) Temperature

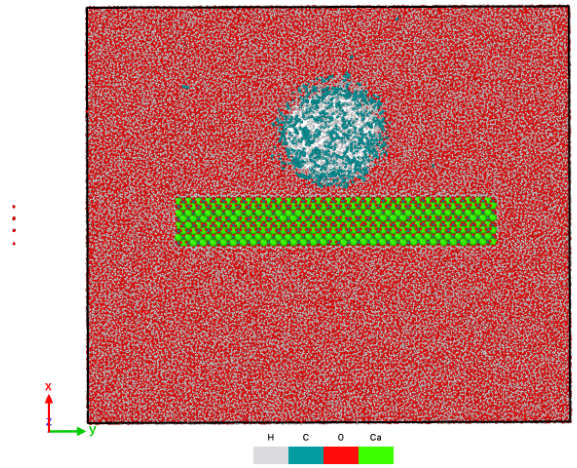

(c) System snapshot (.gro)

Figure B.5: Validation of the equilibrated R20 system. The potential energy (left) and temperature (right) are shown as a function of time; the dashed horizontal lines indicate the mean value over the final 500 ps of the trajectory, used as an equilibrium indicator. The bottom panel shows a representative configuration of the system rendered from the corresponding .gro structure file.

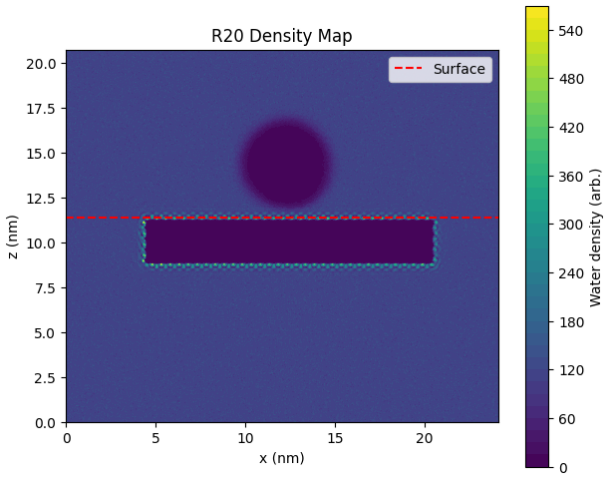

(a) Two-dimensional water density map used to determine the liquid-vapor interface. The dashed line indicates the solid surface position.

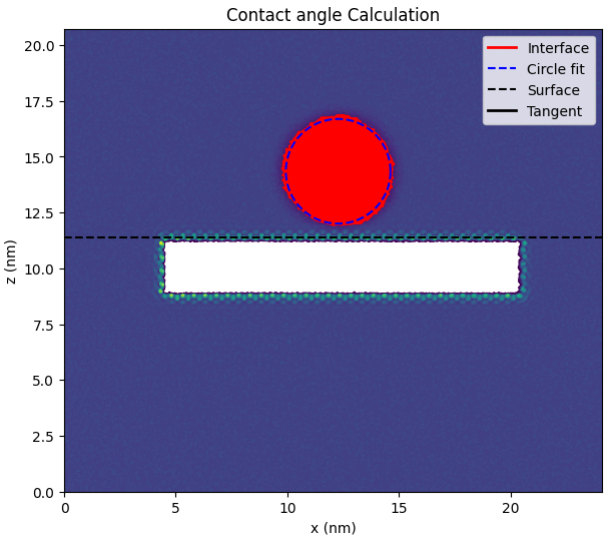

(b) Construction of the contact angle. A circular fit is applied to the detected interface points, and the tangent at the three phase contact line is used to compute the contact angle.

Figure B.6: Illustration of the contact angle determination procedure. (a) The liquid-vapor interface is extracted from the time-averaged density field using a threshold criterion. (b) A circle is fitted to the interface contour, and the contact angle is obtained from the tangent at the intersection between the fitted circle and the solid surface.

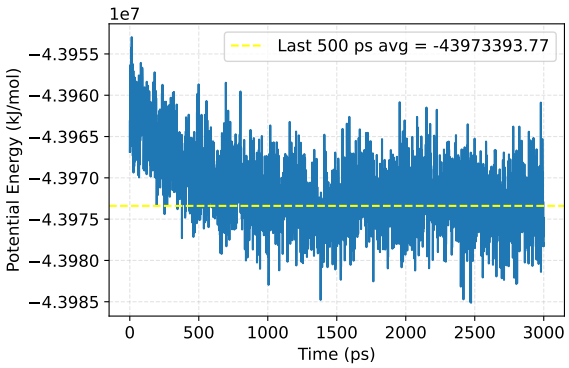

(a) Potential energy

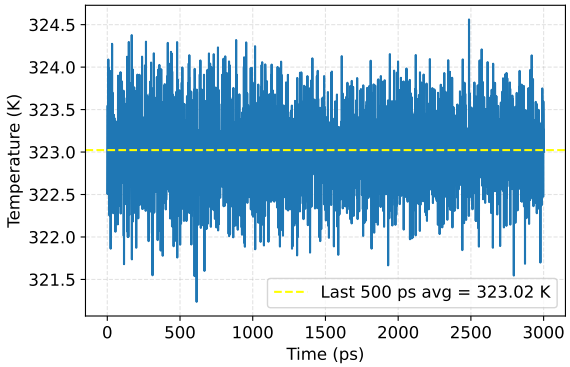

(b) Temperature

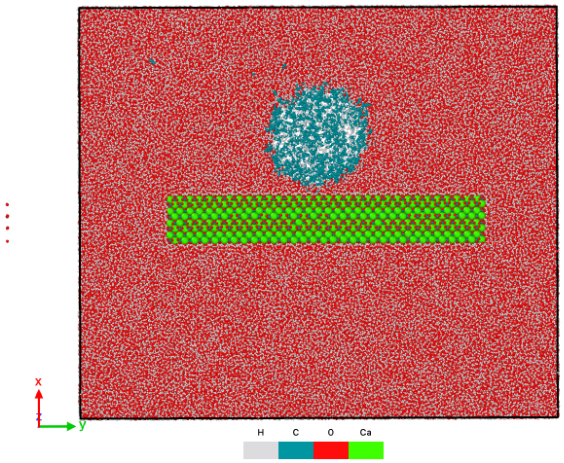

(c) System snapshot (.gro)

Figure B.7: Validation of the equilibrated R30 system. The potential energy (left) and temperature (right) are shown as a function of time; the dashed horizontal lines indicate the mean value over the final 500 ps of the trajectory, used as an equilibrium indicator. The bottom panel shows a representative configuration of the system rendered from the corresponding .gro structure file.

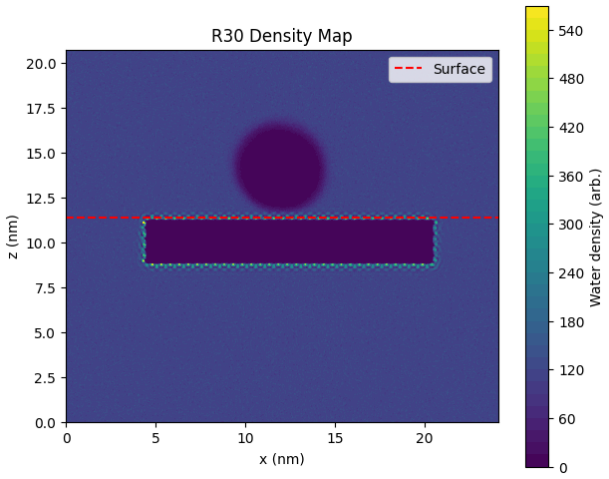

(a) Two-dimensional water density map used to determine the liquid-vapor interface. The dashed line indicates the solid surface position.

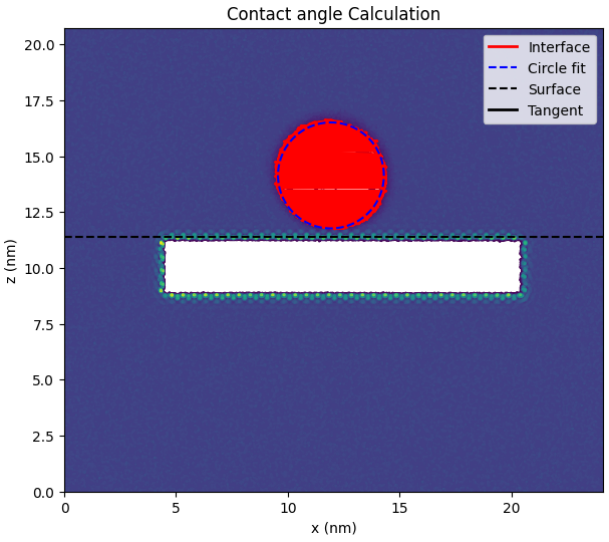

(b) Construction of the contact angle. A circular fit is applied to the detected interface points, and the tangent at the three phase contact line is used to compute the contact angle.

Figure B.8: Illustration of the contact angle determination procedure. (a) The liquid-vapor interface is extracted from the time-averaged density field using a threshold criterion. (b) A circle is fitted to the interface contour, and the contact angle is obtained from the tangent at the intersection between the fitted circle and the solid surface.

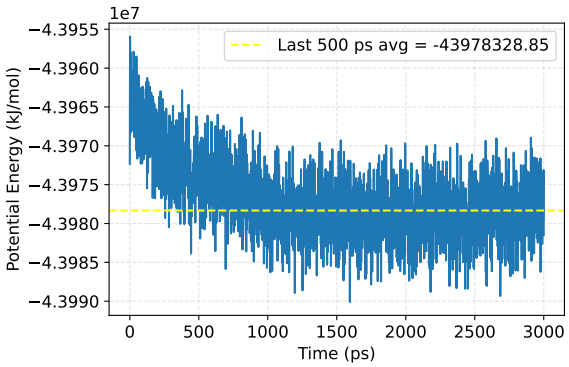

(a) Potential energy

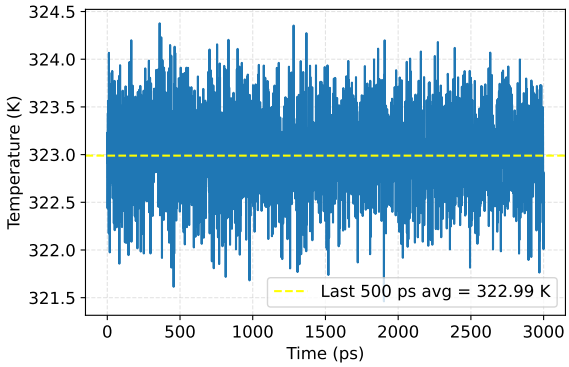

(b) Temperature

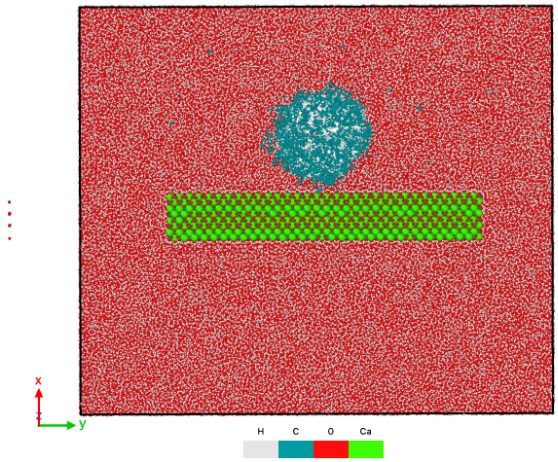

(c) System snapshot (.gro)

Figure B.9: Validation of the equilibrated R40 system. The potential energy (left) and temperature (right) are shown as a function of time; the dashed horizontal lines indicate the mean value over the final 500 ps of the trajectory, used as an equilibrium indicator. The bottom panel shows a representative configuration of the system rendered from the corresponding .gro structure file.

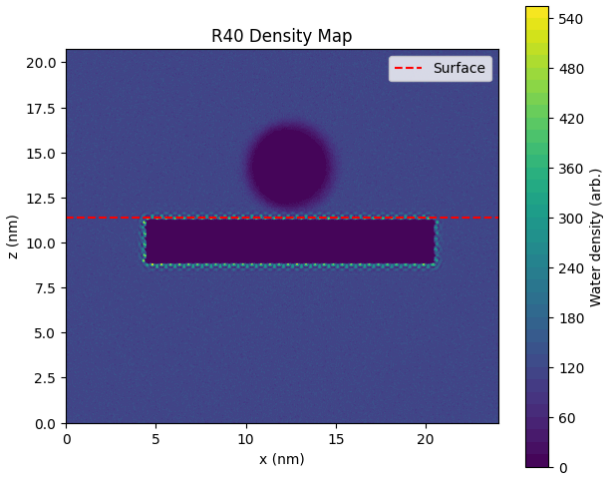

(a) Two-dimensional water density map used to determine the liquid-vapor interface. The dashed line indicates the solid surface position.

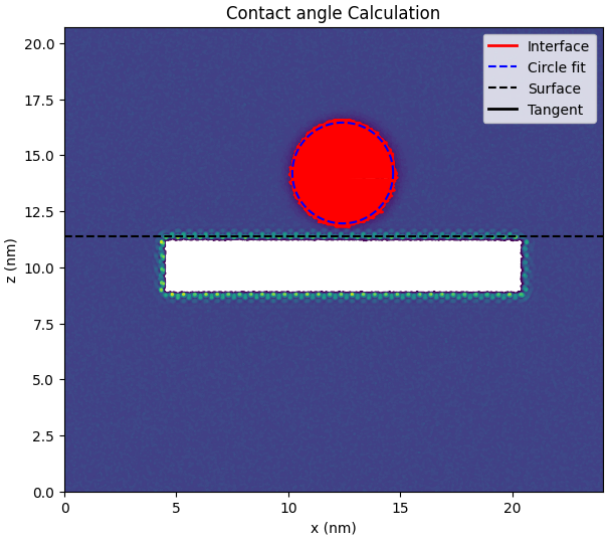

(b) Construction of the contact angle. A circular fit is applied to the detected interface points, and the tangent at the three phase contact line is used to compute the contact angle.

Figure B.10: Illustration of the contact angle determination procedure. (a) The liquid-vapor interface is extracted from the time-averaged density field using a threshold criterion. (b) A circle is fitted to the interface contour, and the contact angle is obtained from the tangent at the intersection between the fitted circle and the solid surface.

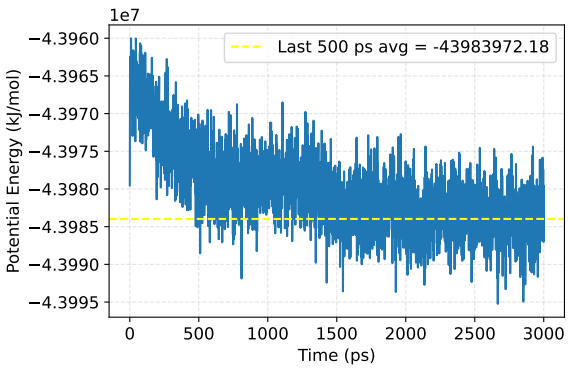

(a) Potential energy

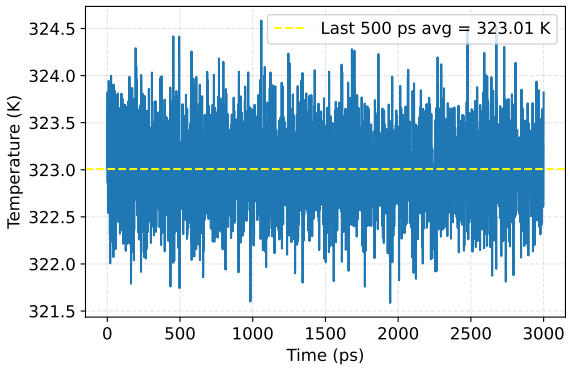

(b) Temperature

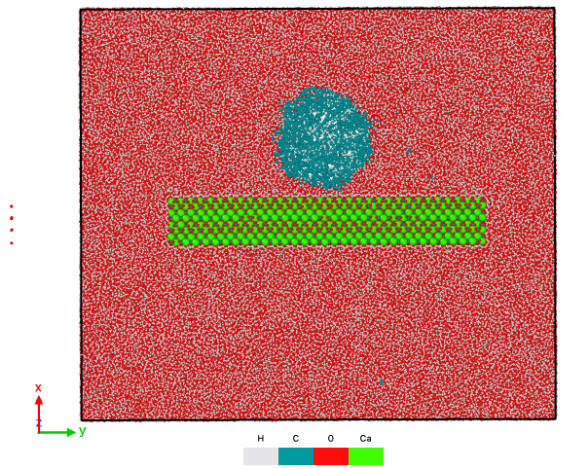

(c) System snapshot (.gro)

Figure B.11: Validation of the equilibrated R50 system. The potential energy (left) and temperature (right) are shown as a function of time; the dashed horizontal lines indicate the mean value over the final 500 ps of the trajectory, used as an equilibrium indicator. The bottom panel shows a representative configuration of the system rendered from the corresponding .gro structure file.

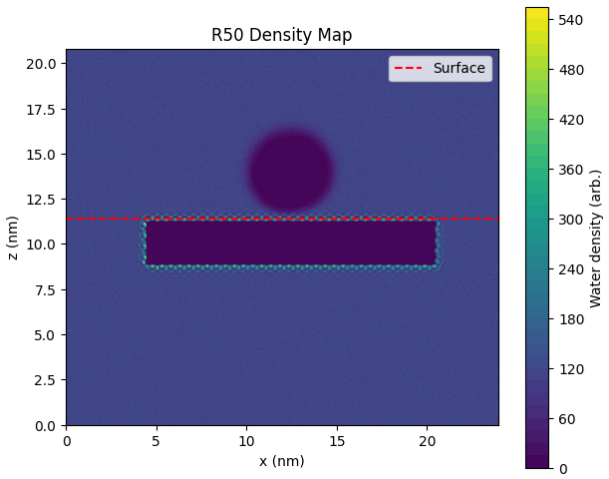

(a) Two-dimensional water density map used to determine the liquid-vapor interface. The dashed line indicates the solid surface position.

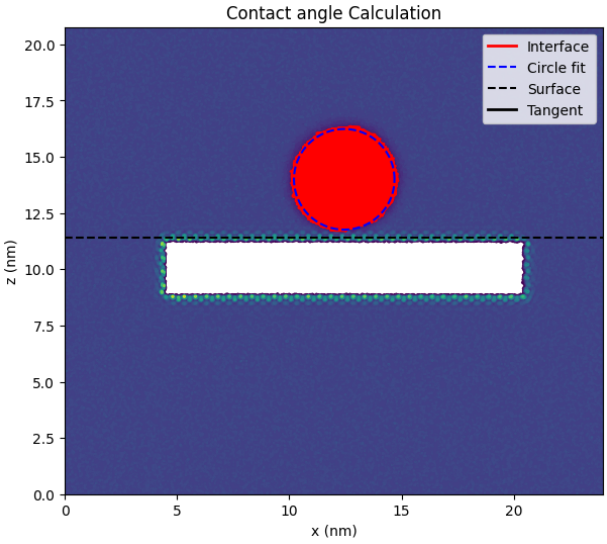

(b) Construction of the contact angle. A circular fit is applied to the detected interface points, and the tangent at the three phase contact line is used to compute the contact angle.

Figure B.12: Illustration of the contact angle determination procedure. (a) The liquid-vapor interface is extracted from the time-averaged density field using a threshold criterion. (b) A circle is fitted to the interface contour, and the contact angle is obtained from the tangent at the intersection between the fitted circle and the solid surface.

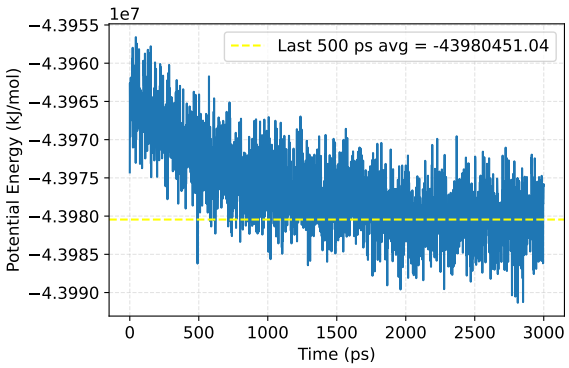

(a) Potential energy

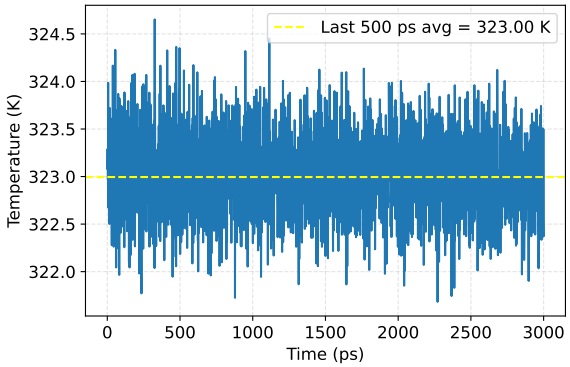

(b) Temperature

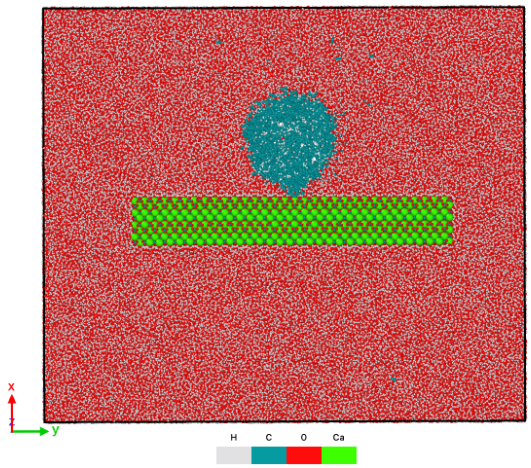

(c) System snapshot (.gro)

Figure B.13: Validation of the equilibrated R60 system. The potential energy (left) and temperature (right) are shown as a function of time; the dashed horizontal lines indicate the mean value over the final 500 ps of the trajectory, used as an equilibrium indicator. The bottom panel shows a representative configuration of the system rendered from the corresponding .gro structure file.

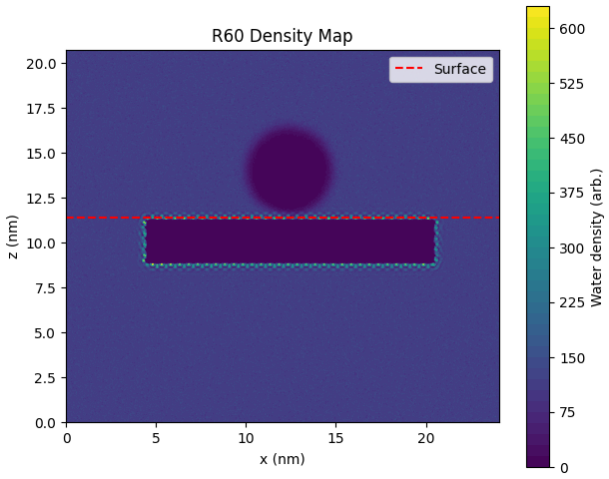

(a) Two-dimensional water density map used to determine the liquid-vapor interface. The dashed line indicates the solid surface position.

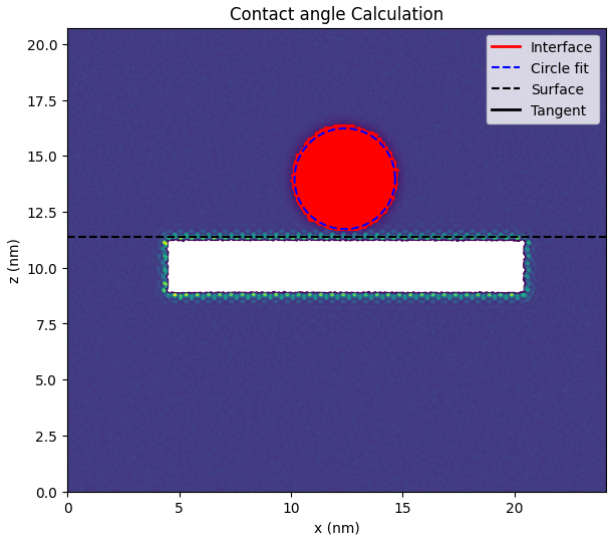

(b) Construction of the contact angle. A circular fit is applied to the detected interface points, and the tangent at the three phase contact line is used to compute the contact angle.

Figure B.14: Illustration of the contact angle determination procedure. (a) The liquid-vapor interface is extracted from the time-averaged density field using a threshold criterion. (b) A circle is fitted to the interface contour, and the contact angle is obtained from the tangent at the intersection between the fitted circle and the solid surface.

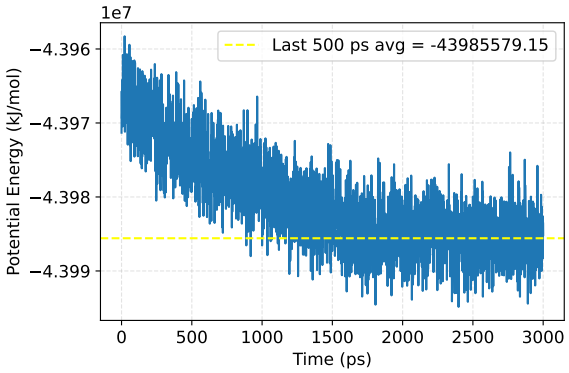

(a) Potential energy

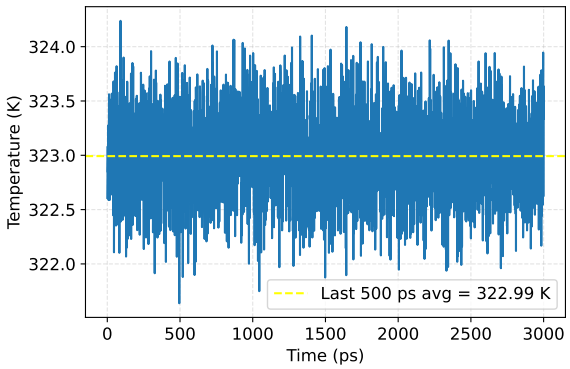

(b) Temperature

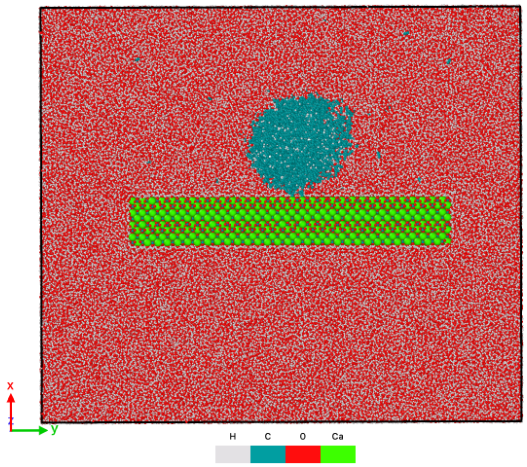

(c) System snapshot (.gro)

Figure B.15: Validation of the equilibrated R70 system. The potential energy (left) and temperature (right) are shown as a function of time; the dashed horizontal lines indicate the mean value over the final 500 ps of the trajectory, used as an equilibrium indicator. The bottom panel shows a representative configuration of the system rendered from the corresponding .gro structure file.

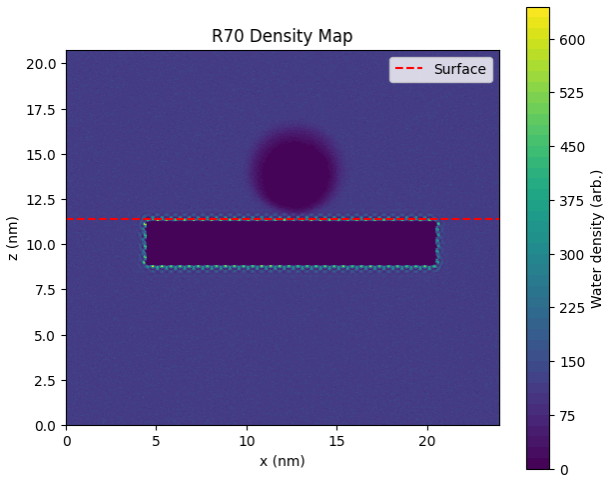

(a) Two-dimensional water density map used to determine the liquid-vapor interface. The dashed line indicates the solid surface position.

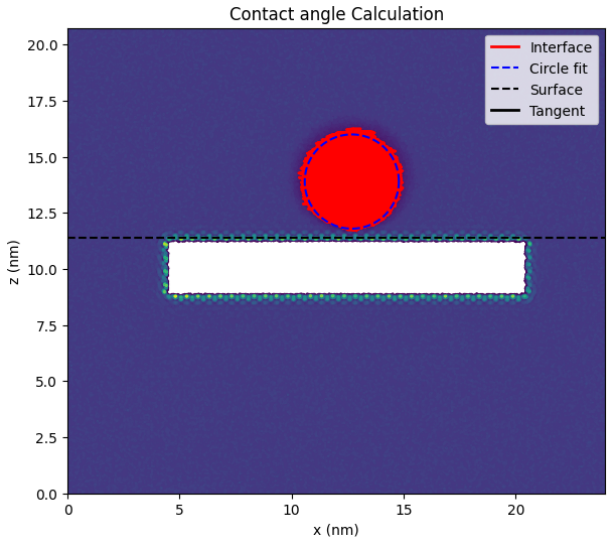

(b) Construction of the contact angle. A circular fit is applied to the detected interface points, and the tangent at the three phase contact line is used to compute the contact angle.

Figure B.16: Illustration of the contact angle determination procedure. (a) The liquid-vapor interface is extracted from the time-averaged density field using a threshold criterion. (b) A circle is fitted to the interface contour, and the contact angle is obtained from the tangent at the intersection between the fitted circle and the solid surface.

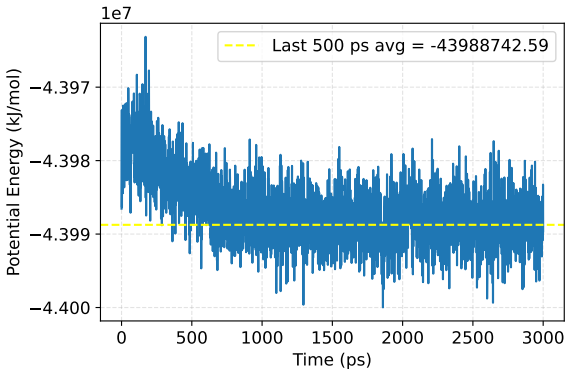

(a) Potential energy

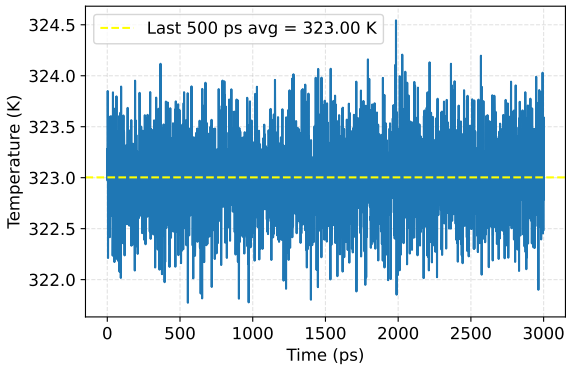

(b) Temperature

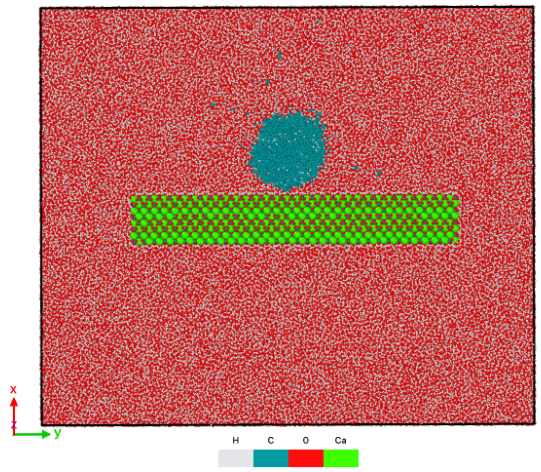

(c) System snapshot (.gro)

Figure B.17: Validation of the equilibrated R80 system. The potential energy (left) and temperature (right) are shown as a function of time; the dashed horizontal lines indicate the mean value over the final 500 ps of the trajectory, used as an equilibrium indicator. The bottom panel shows a representative configuration of the system rendered from the corresponding .gro structure file.

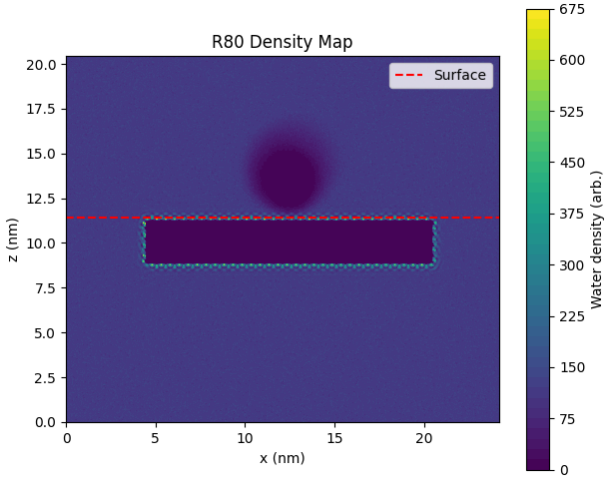

(a) Two-dimensional water density map used to determine the liquid-vapor interface. The dashed line indicates the solid surface position.

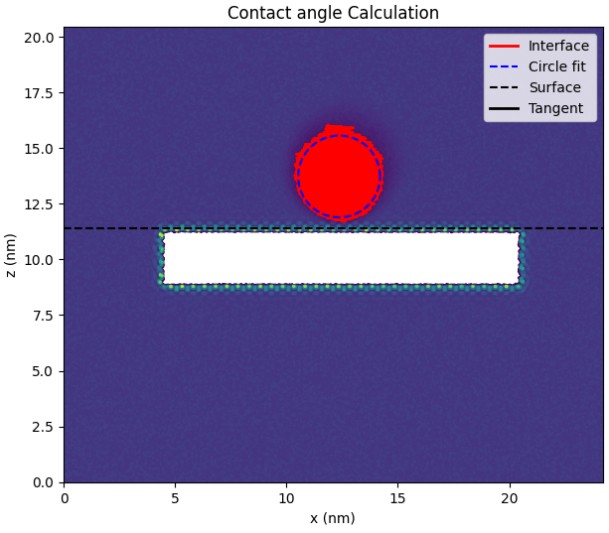

(b) Construction of the contact angle. A circular fit is applied to the detected interface points, and the tangent at the three phase contact line is used to compute the contact angle.

Figure B.18: Illustration of the contact angle determination procedure. (a) The liquid-vapor interface is extracted from the time-averaged density field using a threshold criterion. (b) A circle is fitted to the interface contour, and the contact angle is obtained from the tangent at the intersection between the fitted circle and the solid surface.

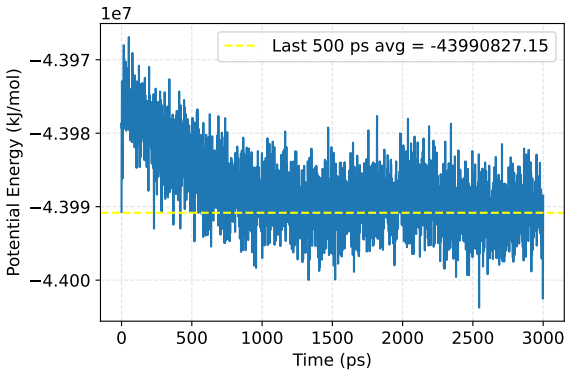

(a) Potential energy

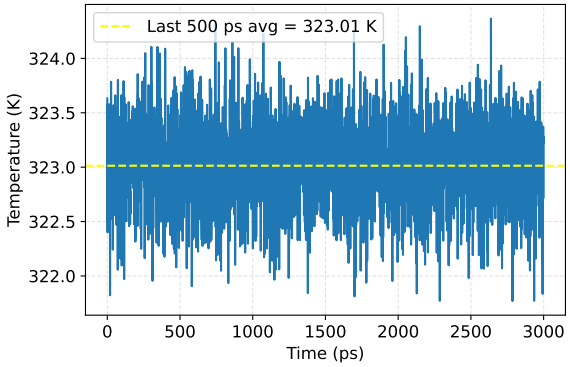

(b) Temperature

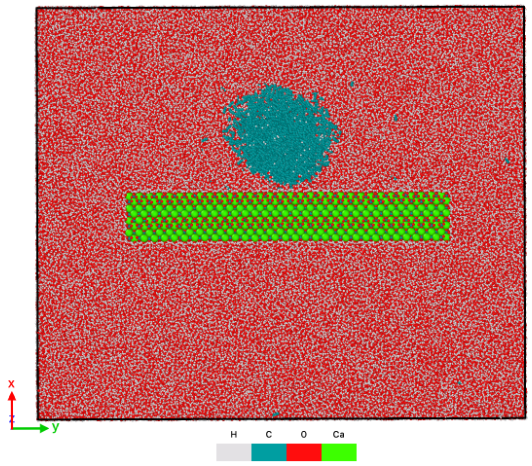

(c) System snapshot (.gro)

Figure B.19: Validation of the equilibrated R90 system. The potential energy (left) and temperature (right) are shown as a function of time; the dashed horizontal lines indicate the mean value over the final 500 ps of the trajectory, used as an equilibrium indicator. The bottom panel shows a representative configuration of the system rendered from the corresponding .gro structure file.

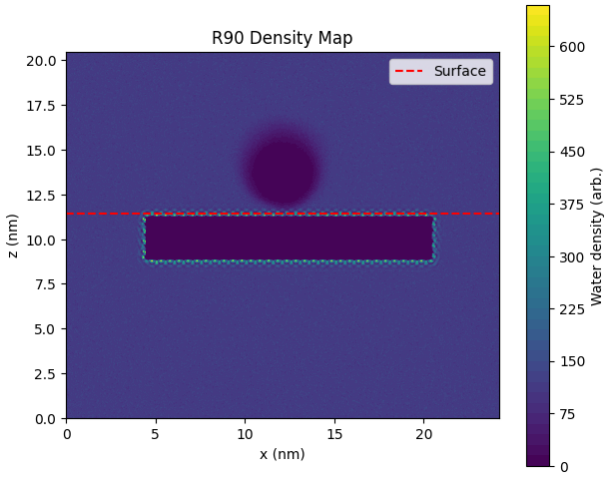

(a) Two-dimensional water density map used to determine the liquid-vapor interface. The dashed line indicates the solid surface position.

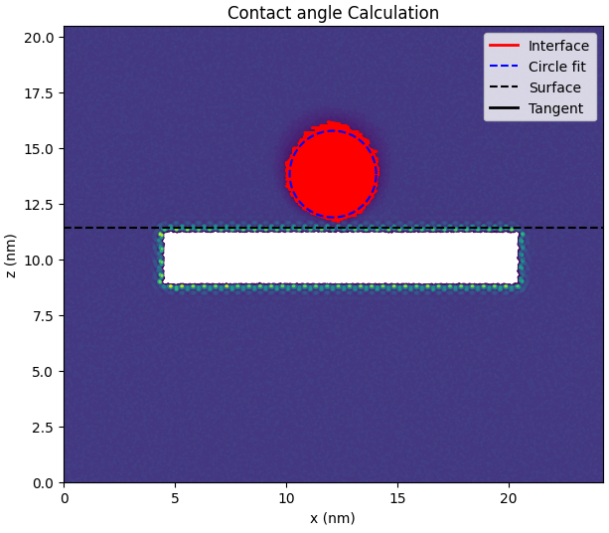

(b) Construction of the contact angle. A circular fit is applied to the detected interface points, and the tangent at the three phase contact line is used to compute the contact angle.

Figure B.20: Illustration of the contact angle determination procedure. (a) The liquid-vapor interface is extracted from the time-averaged density field using a threshold criterion. (b) A circle is fitted to the interface contour, and the contact angle is obtained from the tangent at the intersection between the fitted circle and the solid surface.

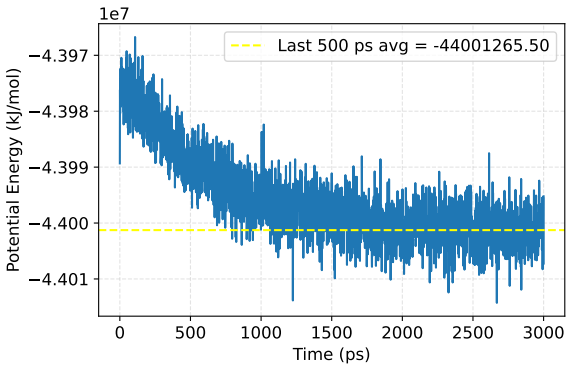

(a) Potential energy

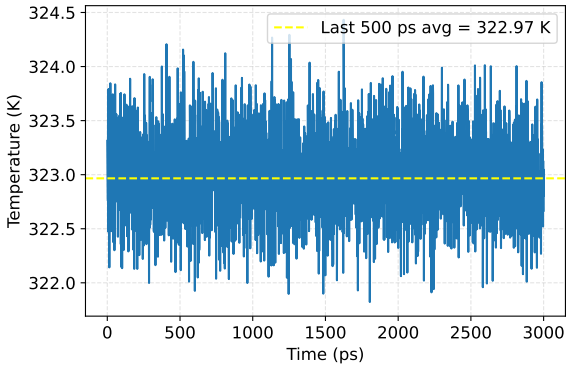

(b) Temperature

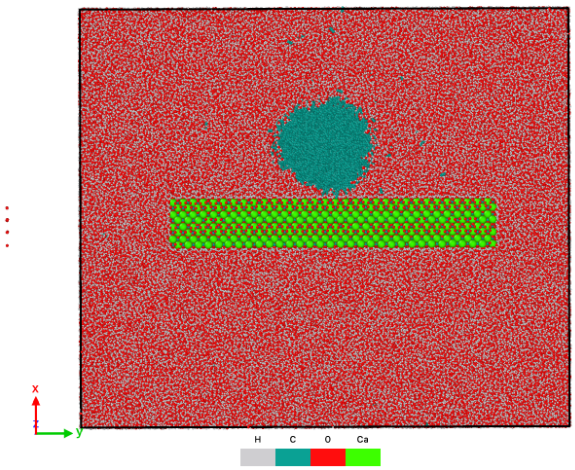

(c) System snapshot (.gro)

Figure B.21: Validation of the equilibrated R100 system. The potential energy (left) and temperature (right) are shown as a function of time; the dashed horizontal lines indicate the mean value over the final 500 ps of the trajectory, used as an equilibrium indicator. The bottom panel shows a representative configuration of the system rendered from the corresponding .gro structure file.

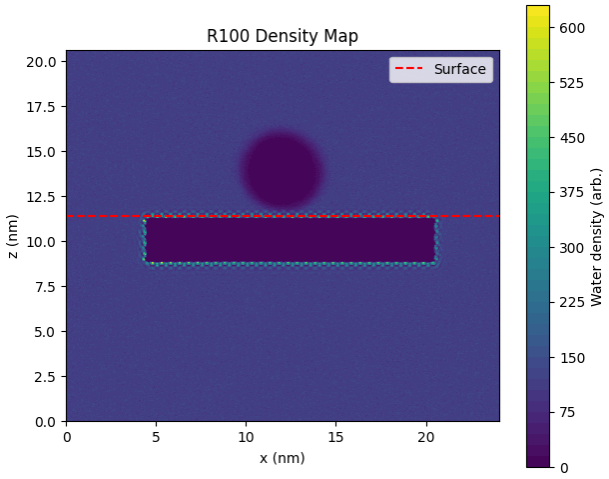

(a) Two-dimensional water density map used to determine the liquid-vapor interface. The dashed line indicates the solid surface position.

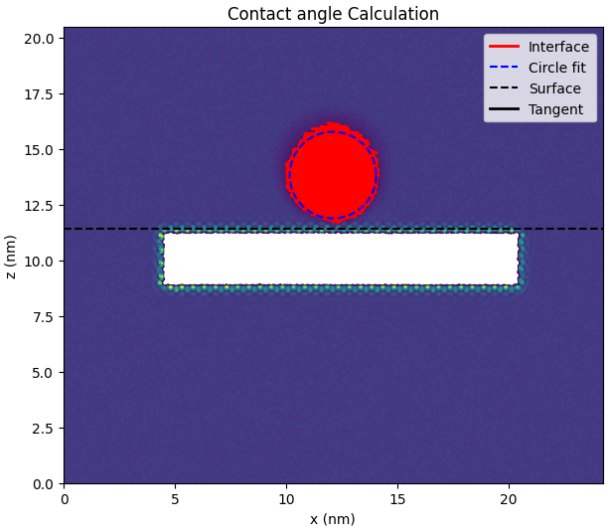

(b) Construction of the contact angle. A circular fit is applied to the detected interface points, and the tangent at the three phase contact line is used to compute the contact angle.

Figure B.22: Illustration of the contact angle determination procedure. (a) The liquid-vapor interface is extracted from the time-averaged density field using a threshold criterion. (b) A circle is fitted to the interface contour, and the contact angle is obtained from the tangent at the intersection between the fitted circle and the solid surface.

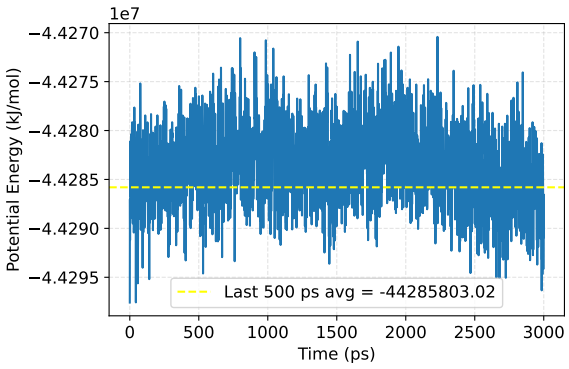

(a) Potential energy

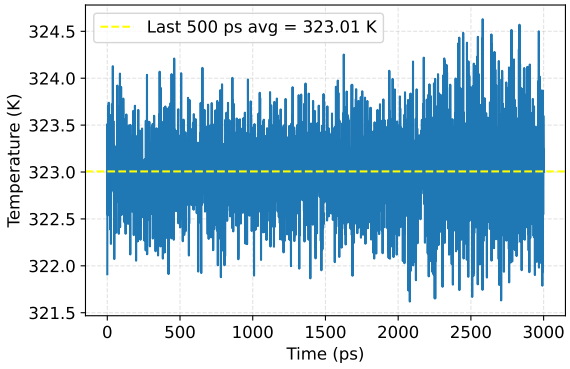

(b) Temperature

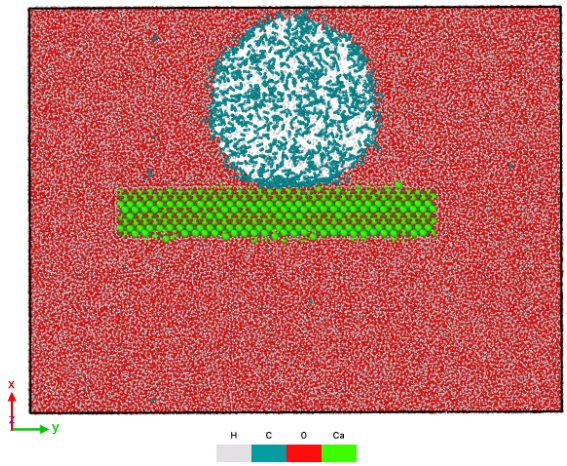

(c) System snapshot (.gro)

Figure B.23: Validation of the equilibrated ACC2 system. The potential energy (left) and temperature (right) are shown as a function of time; the dashed horizontal lines indicate the mean value over the final 500 ps of the trajectory, used as an equilibrium indicator. The bottom panel shows a representative configuration of the system rendered from the corresponding .gro structure file.

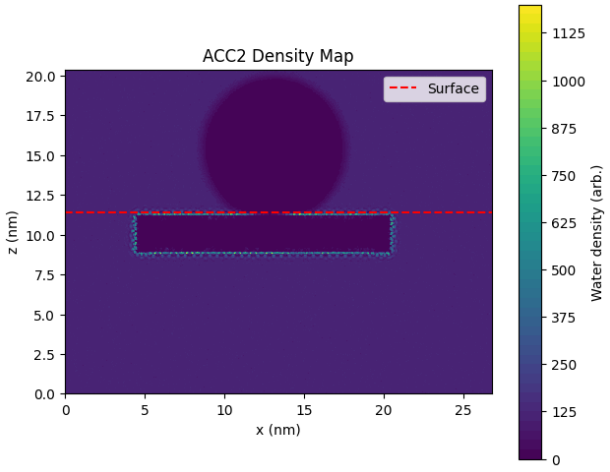

(a) Two-dimensional water density map used to determine the liquid-vapor interface. The dashed line indicates the solid surface position.

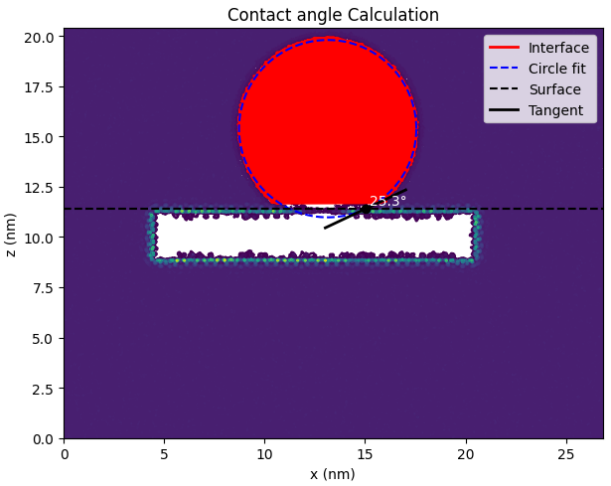

(b) Construction of the contact angle. A circular fit is applied to the detected interface points, and the tangent at the three phase contact line is used to compute the contact angle.

Figure B.24: Illustration of the contact angle determination procedure. (a) The liquid-vapor interface is extracted from the time-averaged density field using a threshold criterion. (b) A circle is fitted to the interface contour, and the contact angle is obtained from the tangent at the intersection between the fitted circle and the solid surface.

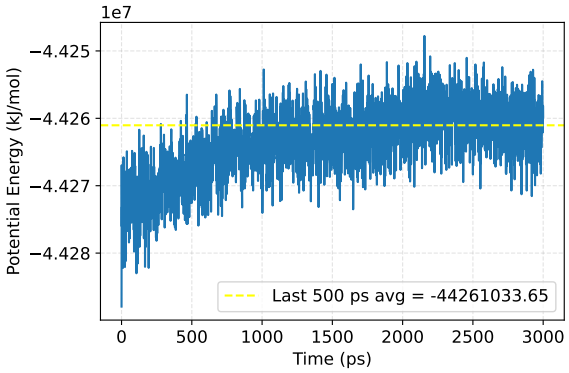

(a) Potential energy

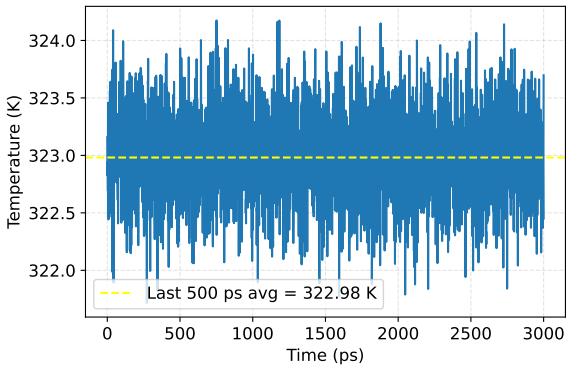

(b) Temperature

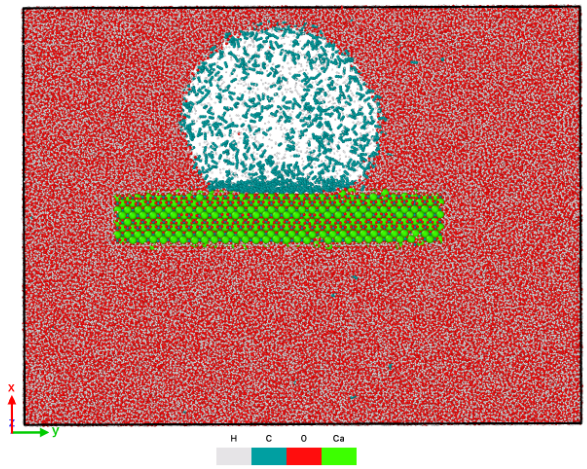

(c) System snapshot (.gro)

Figure B.25: Validation of the equilibrated ACC3 system. The potential energy (left) and temperature (right) are shown as a function of time; the dashed horizontal lines indicate the mean value over the final 500 ps of the trajectory, used as an equilibrium indicator. The bottom panel shows a representative configuration of the system rendered from the corresponding .gro structure file.

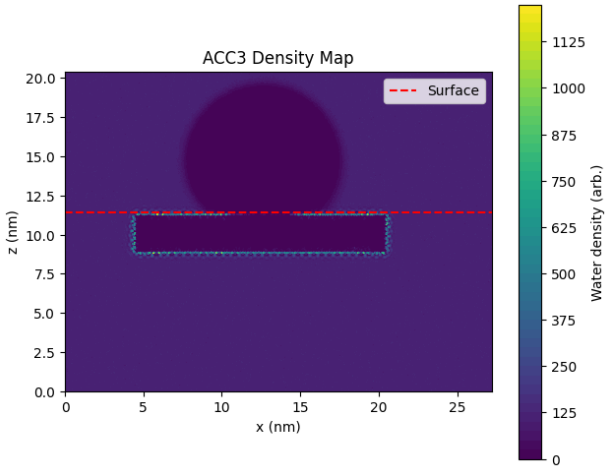

(a) Two-dimensional water density map used to determine the liquid-vapor interface. The dashed line indicates the solid surface position.

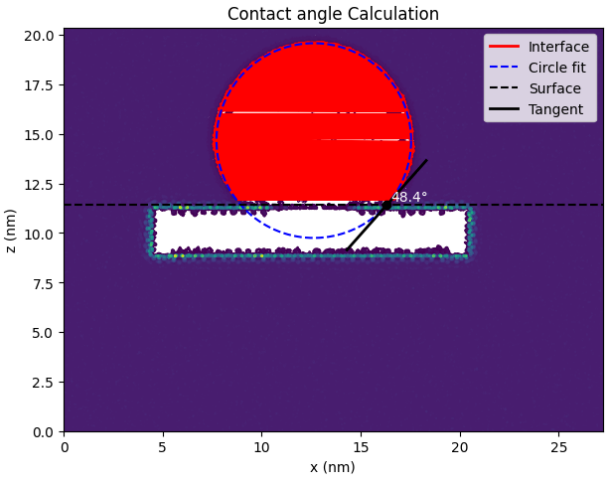

(b) Construction of the contact angle. A circular fit is applied to the detected interface points, and the tangent at the three phase contact line is used to compute the contact angle.

Figure B.26: Illustration of the contact angle determination procedure. (a) The liquid-vapor interface is extracted from the time-averaged density field using a threshold criterion. (b) A circle is fitted to the interface contour, and the contact angle is obtained from the tangent at the intersection between the fitted circle and the solid surface.

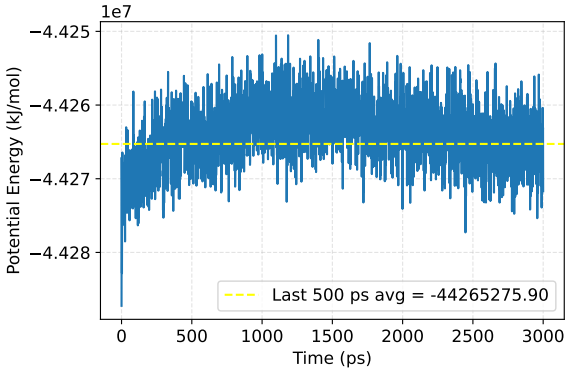

(a) Potential energy

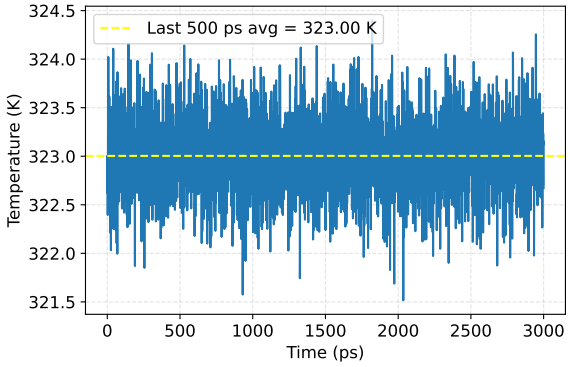

(b) Temperature

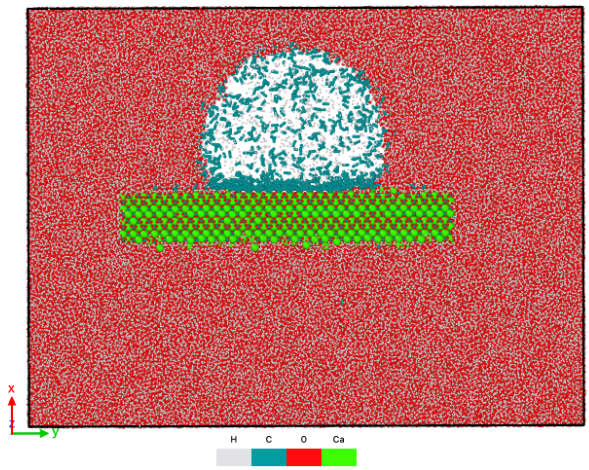

(c) System snapshot (.gro)

Figure B.27: Validation of the equilibrated ACC4 system. The potential energy (left) and temperature (right) are shown as a function of time; the dashed horizontal lines indicate the mean value over the final 500 ps of the trajectory, used as an equilibrium indicator. The bottom panel shows a representative configuration of the system rendered from the corresponding .gro structure file.

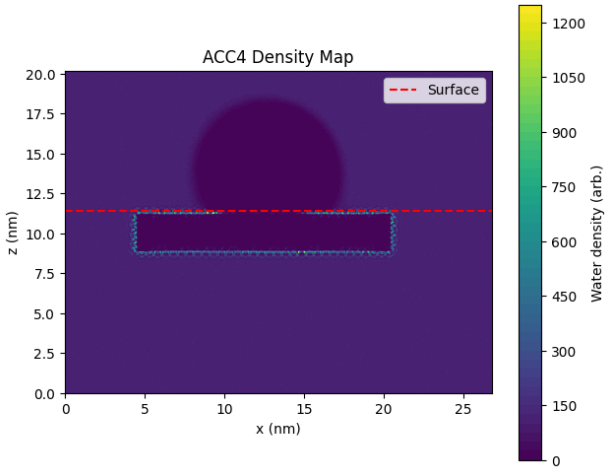

(a) Two-dimensional water density map used to determine the liquid-vapor interface. The dashed line indicates the solid surface position.

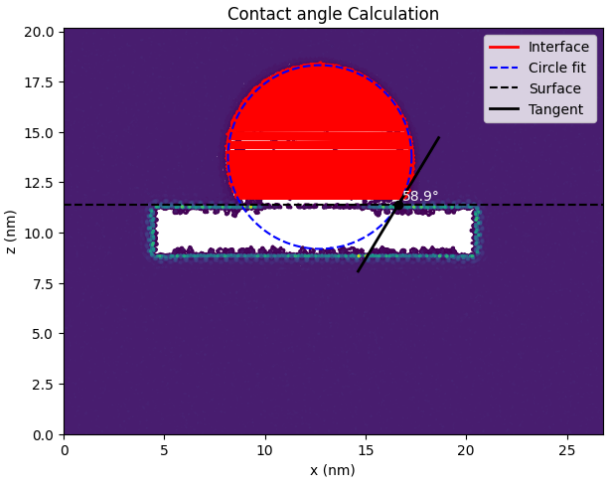

(b) Construction of the contact angle. A circle fit is applied to the detected interface points, and the tangent at the three phase contact line is used to compute the contact angle.

Figure B.28: Illustration of the contact angle determination procedure. (a) The liquid-vapor interface is extracted from the time-averaged density field using a threshold criterion. (b) A circle is fitted to the interface contour, and the contact angle is obtained from the tangent at the intersection between the fitted circle and the solid surface.

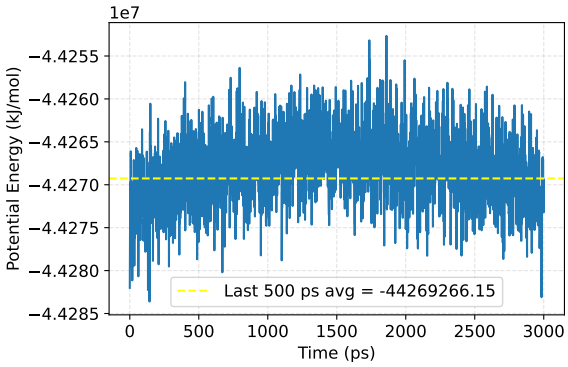

(a) Potential energy

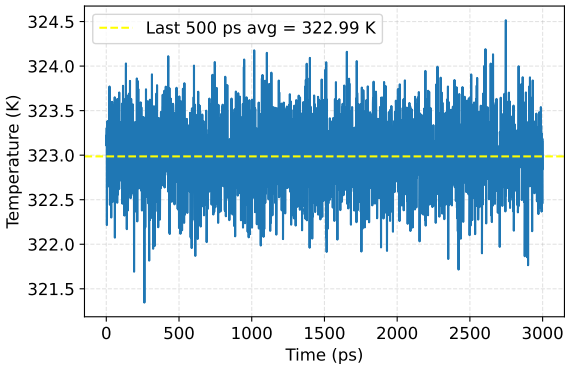

(b) Temperature

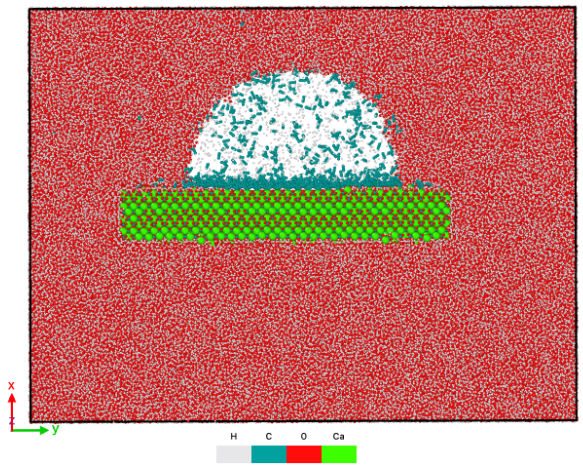

(c) System snapshot (.gro)

Figure B.29: Validation of the equilibrated ACC5 system. The potential energy (left) and temperature (right) are shown as a function of time; the dashed horizontal lines indicate the mean value over the final 500 ps of the trajectory, used as an equilibrium indicator. The bottom panel shows a representative configuration of the system rendered from the corresponding .gro structure file.

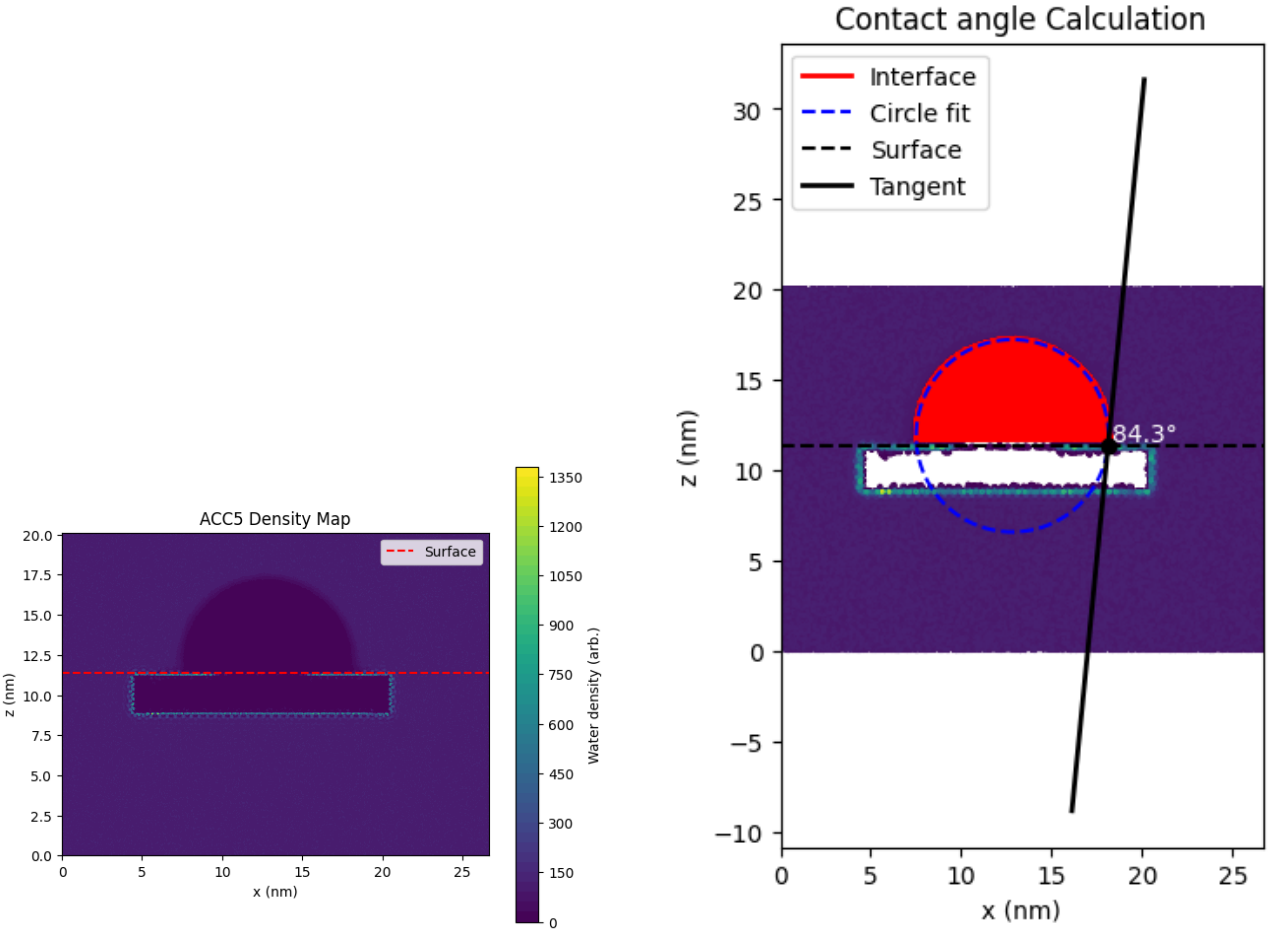

(a) Two-dimensional water density map used to determine the liquid-vapor interface. The dashed line indicates the solid surface position.

(b) Construction of the contact angle. A circular fit is applied to the detected interface points, and the tangent at the three phase contact line is used to compute the contact angle.

Figure B.30: Illustration of the contact angle determination procedure. (a) The liquid-vapor interface is extracted from the time-averaged density field using a threshold criterion. (b) A circle is fitted to the interface contour, and the contact angle is obtained from the tangent at the intersection between the fitted circle and the solid surface.

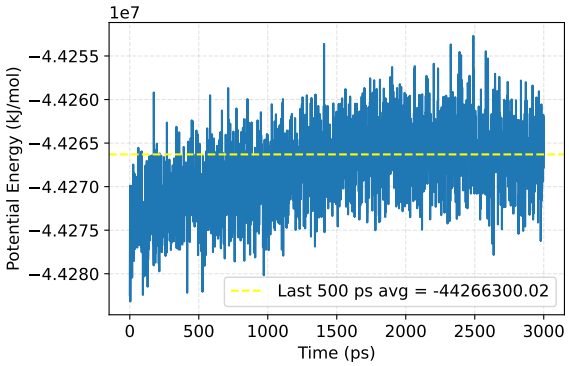

(a) Potential energy

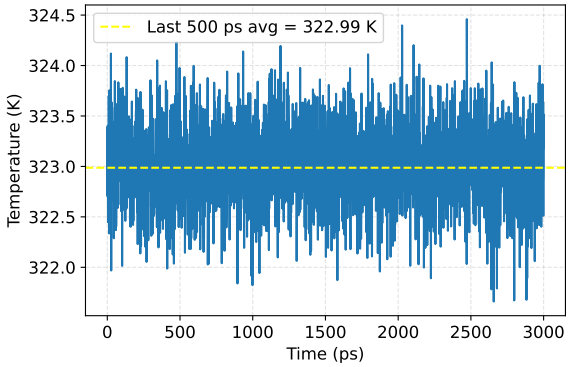

(b) Temperature

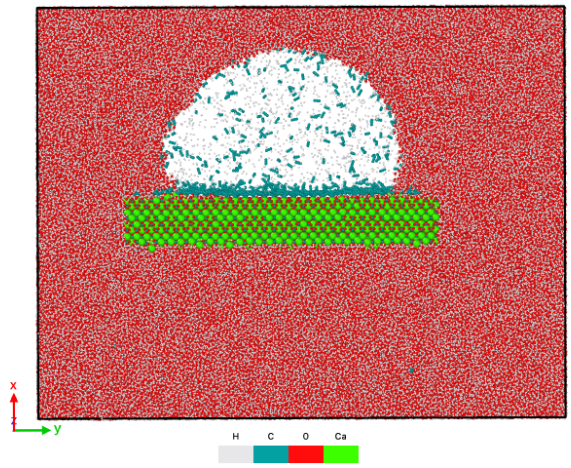

(c) System snapshot (.gro)

Figure B.31: Validation of the equilibrated ACC6 system. The potential energy (left) and temperature (right) are shown as a function of time; the dashed horizontal lines indicate the mean value over the final 500 ps of the trajectory, used as an equilibrium indicator. The bottom panel shows a representative configuration of the system rendered from the corresponding .gro structure file.

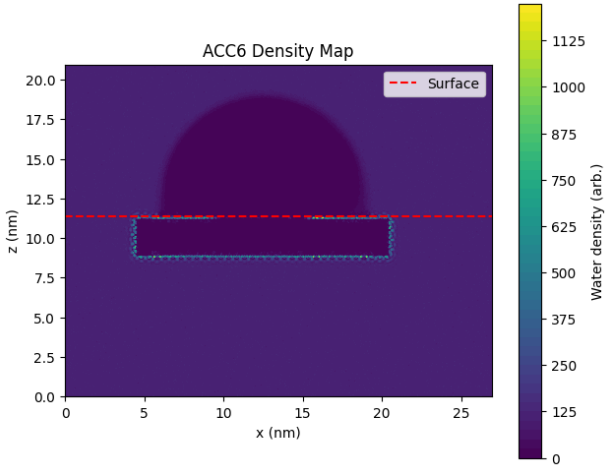

(a) Two-dimensional water density map used to determine the liquid-vapor interface. The dashed line indicates the solid surface position.

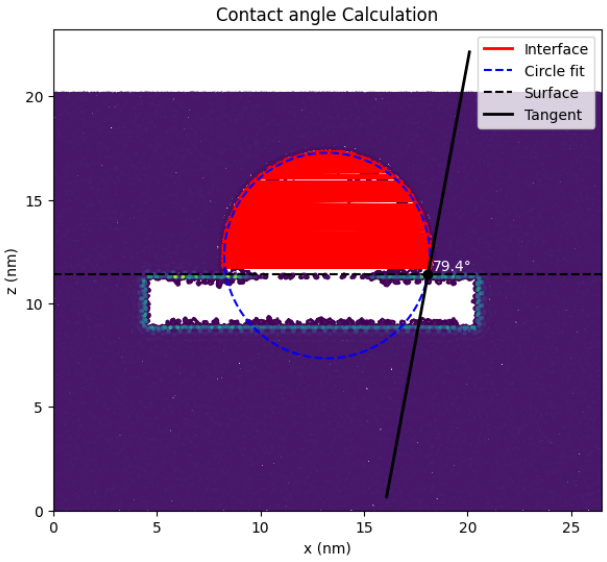

(b) Construction of the contact angle. A circular fit is applied to the detected interface points, and the tangent at the three phase contact line is used to compute the contact angle.

Figure B.32: Illustration of the contact angle determination procedure. (a) The liquid-vapor interface is extracted from the time-averaged density field using a threshold criterion. (b) A circle is fitted to the interface contour, and the contact angle is obtained from the tangent at the intersection between the fitted circle and the solid surface.

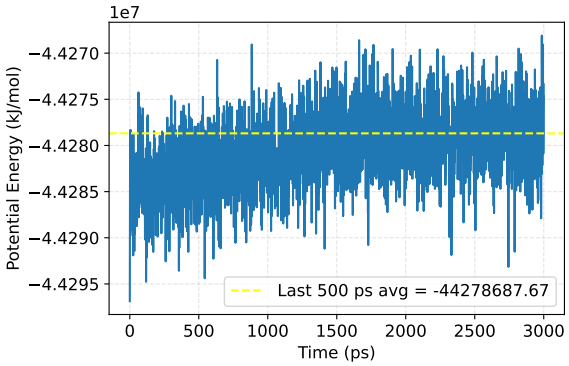

(a) Potential energy

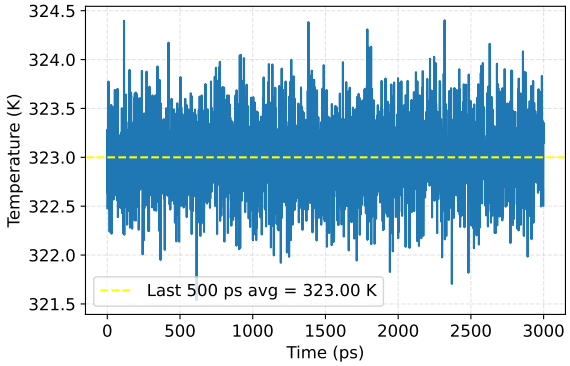

(b) Temperature

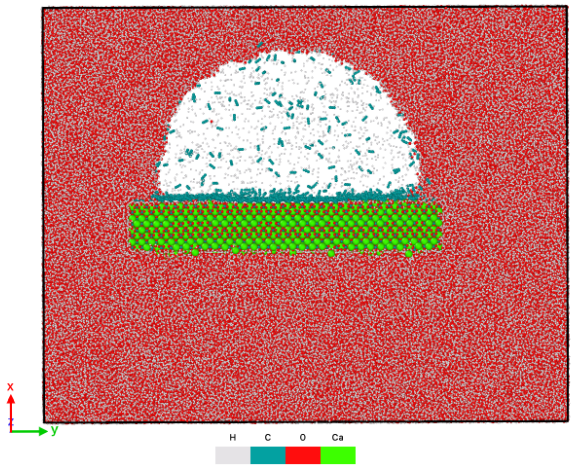

(c) System snapshot (.gro)

Figure B.33: Validation of the equilibrated ACC7 system. The potential energy (left) and temperature (right) are shown as a function of time; the dashed horizontal lines indicate the mean value over the final 500 ps of the trajectory, used as an equilibrium indicator. The bottom panel shows a representative configuration of the system rendered from the corresponding .gro structure file.

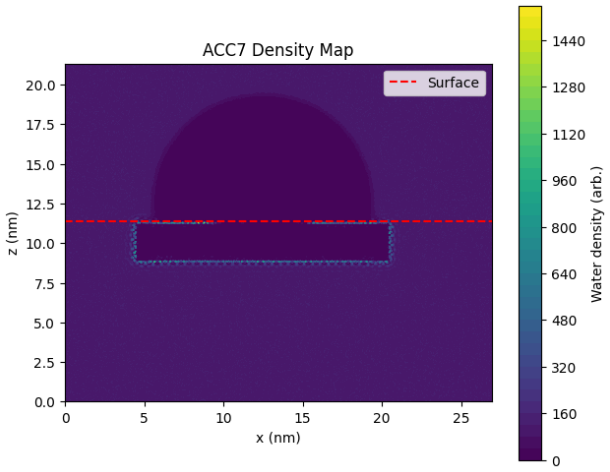

(a) Two-dimensional water density map used to determine the liquid-vapor interface. The dashed line indicates the solid surface position.

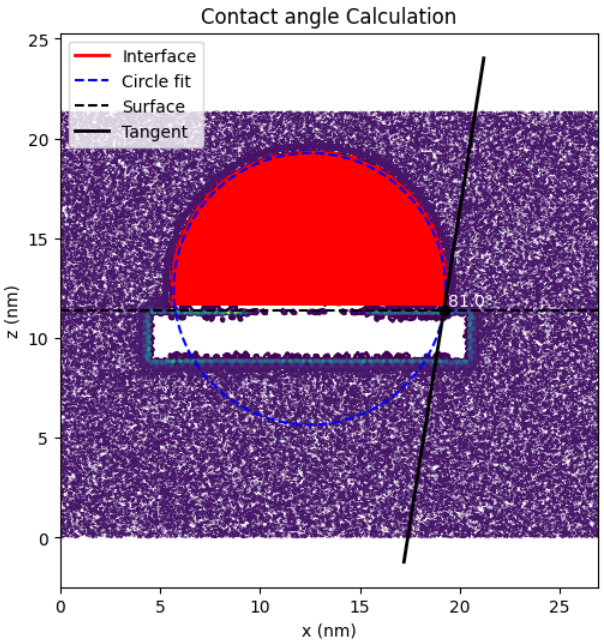

(b) Construction of the contact angle. A circular fit is applied to the detected interface points, and the tangent at the three phase contact line is used to compute the contact angle.

Figure B.34: Illustration of the contact angle determination procedure. (a) The liquid-vapor interface is extracted from the time-averaged density field using a threshold criterion. (b) A circle is fitted to the interface contour, and the contact angle is obtained from the tangent at the intersection between the fitted circle and the solid surface.

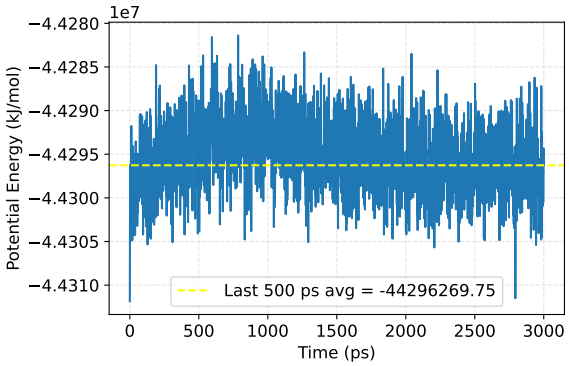

(a) Potential energy

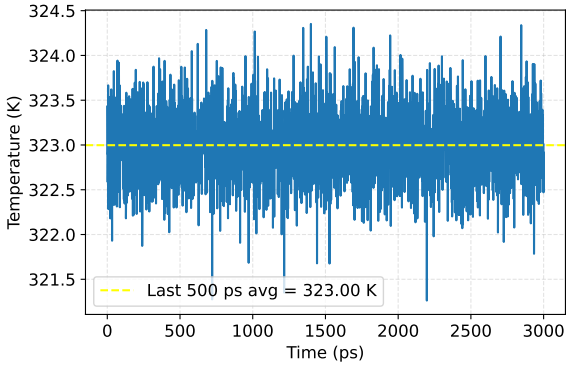

(b) Temperature

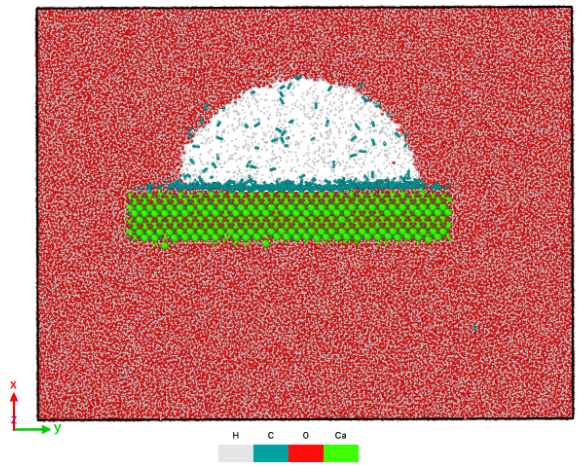

(c) System snapshot (.gro)

Figure B.35: Validation of the equilibrated ACC8 system. The potential energy (left) and temperature (right) are shown as a function of time; the dashed horizontal lines indicate the mean value over the final 500 ps of the trajectory, used as an equilibrium indicator. The bottom panel shows a representative configuration of the system rendered from the corresponding .gro structure file.

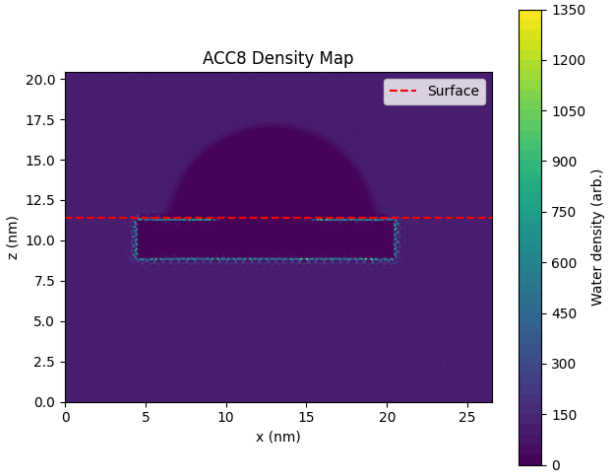

(a) Two-dimensional water density map used to determine the liquid-vapor interface. The dashed line indicates the solid surface position.

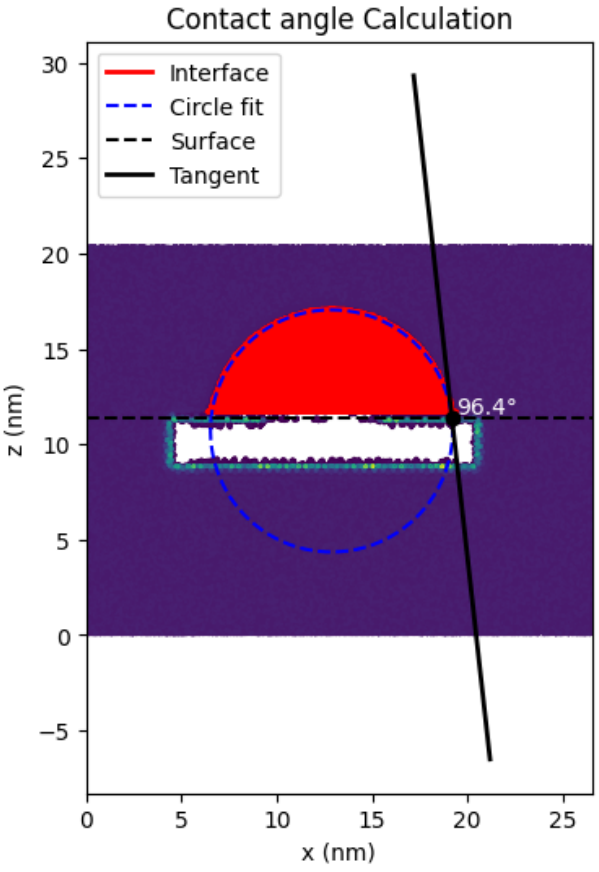

(b) Construction of the contact angle. A circular fit is applied to the detected interface points, and the tangent at the three phase contact line is used to compute the contact angle.

Figure B.36: Illustration of the contact angle determination procedure. (a) The liquid-vapor interface is extracted from the time-averaged density field using a threshold criterion. (b) A circle is fitted to the interface contour, and the contact angle is obtained from the tangent at the intersection between the fitted circle and the solid surface.

scaled H_2

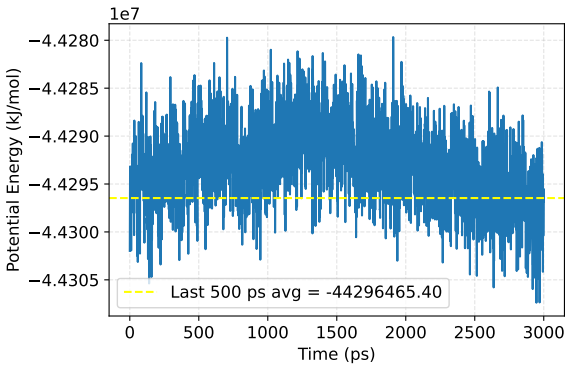

(a) Potential energy

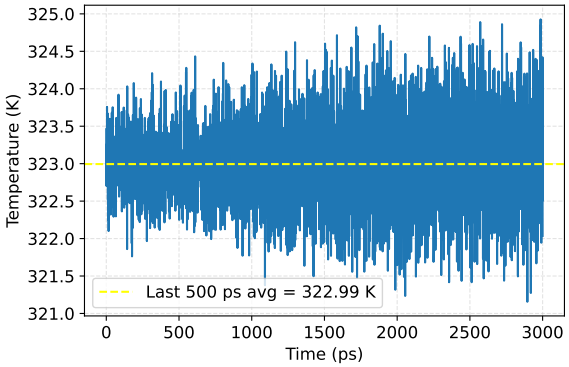

(b) Temperature

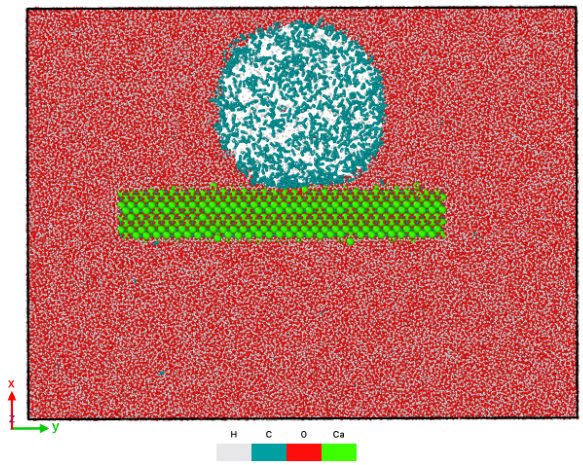

(c) System snapshot (.gro)

Figure B.37: Validation of the equilibrated ACH2 system. The potential energy (left) and temperature (right) are shown as a function of time; the dashed horizontal lines indicate the mean value over the final 500 ps of the trajectory, used as an equilibrium indicator. The bottom panel shows a representative configuration of the system rendered from the corresponding .gro structure file.

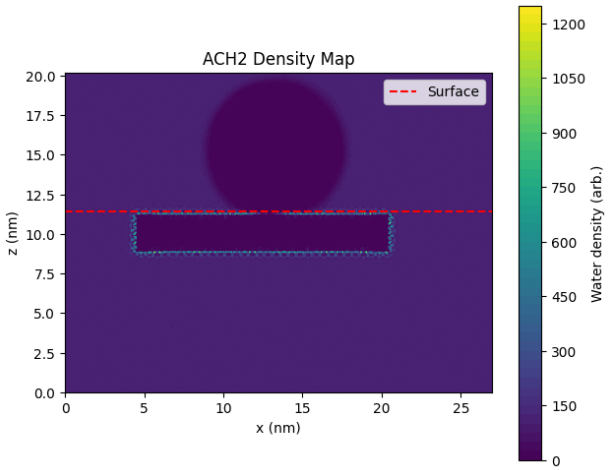

(a) Two-dimensional water density map used to determine the liquid-vapor interface. The dashed line indicates the solid surface position.

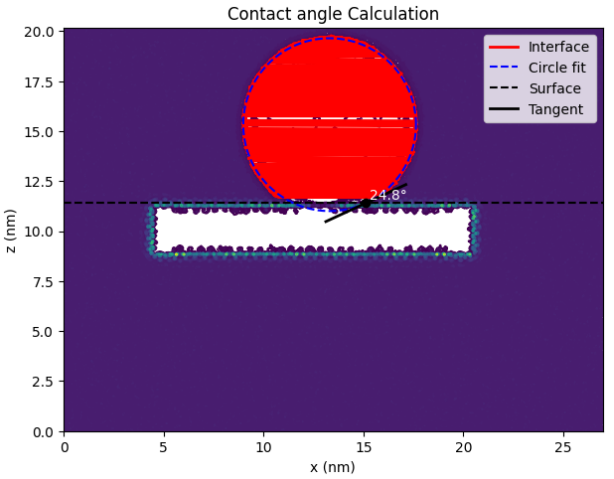

(b) Construction of the contact angle. A circular fit is applied to the detected interface points, and the tangent at the three phase contact line is used to compute the contact angle.

Figure B.38: Illustration of the contact angle determination procedure. (a) The liquid-vapor interface is extracted from the time-averaged density field using a threshold criterion. (b) A circle is fitted to the interface contour, and the contact angle is obtained from the tangent at the intersection between the fitted circle and the solid surface.

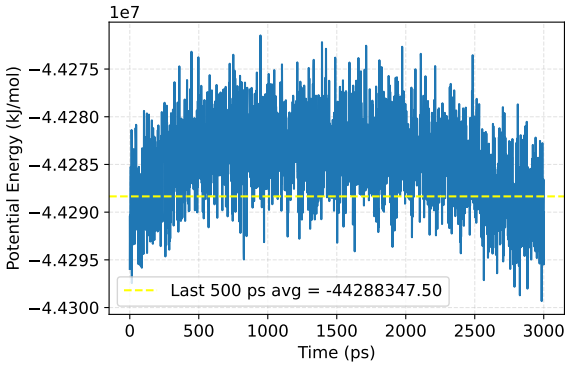

(a) Potential energy

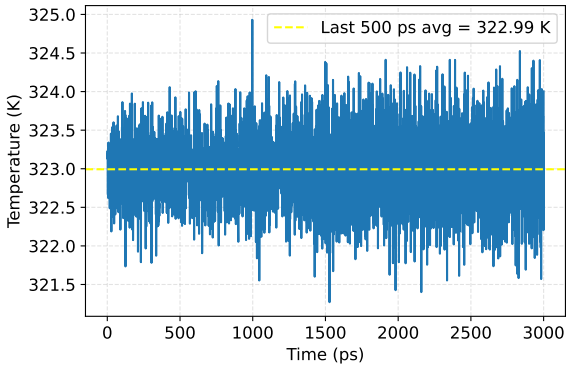

(b) Temperature

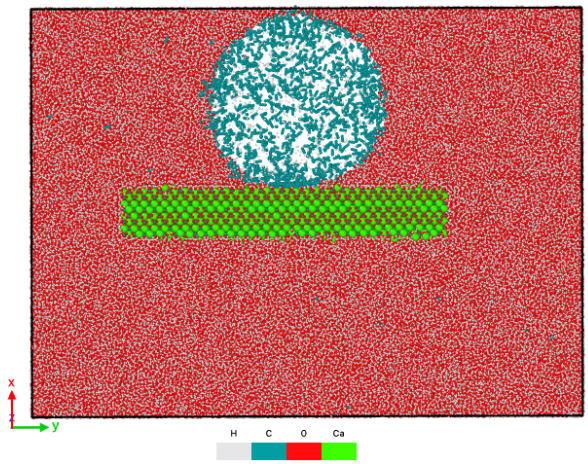

(c) System snapshot (.gro)

Figure B.39: Validation of the equilibrated ACH3 system. The potential energy (left) and temperature (right) are shown as a function of time; the dashed horizontal lines indicate the mean value over the final 500 ps of the trajectory, used as an equilibrium indicator. The bottom panel shows a representative configuration of the system rendered from the corresponding .gro structure file.

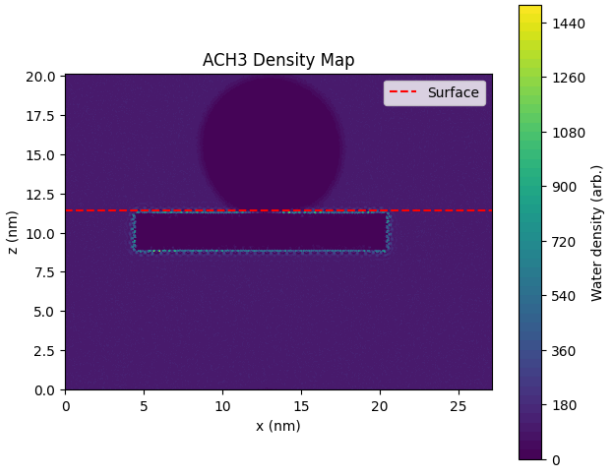

(a) Two-dimensional water density map used to determine the liquid-vapor interface. The dashed line indicates the solid surface position.

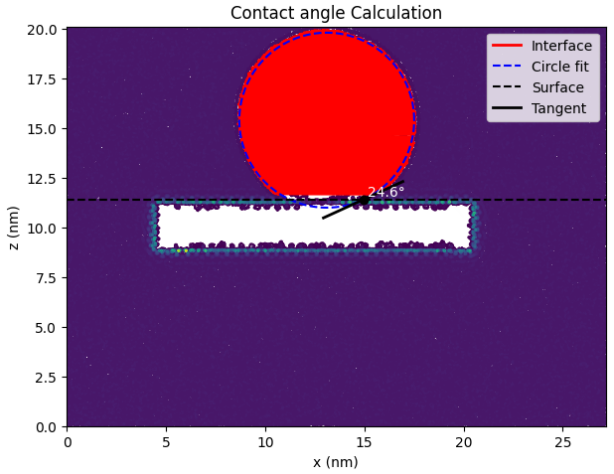

(b) Construction of the contact angle. A circular fit is applied to the detected interface points, and the tangent at the three phase contact line is used to compute the contact angle.

Figure B.40: Illustration of the contact angle determination procedure. (a) The liquid-vapor interface is extracted from the time-averaged density field using a threshold criterion. (b) A circle is fitted to the interface contour, and the contact angle is obtained from the tangent at the intersection between the fitted circle and the solid surface.

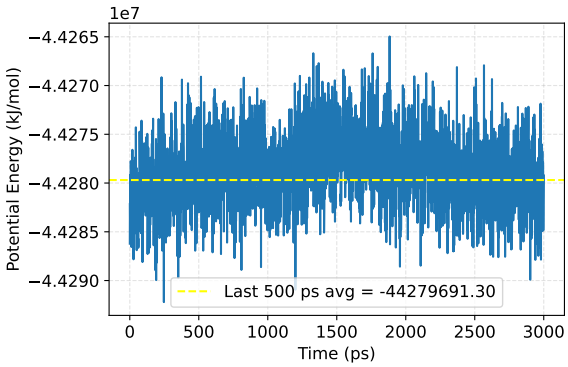

(a) Potential energy

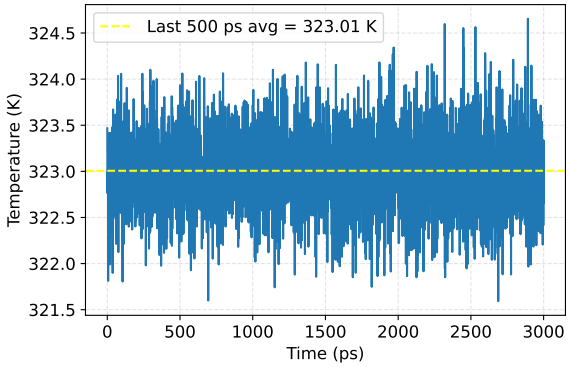

(b) Temperature

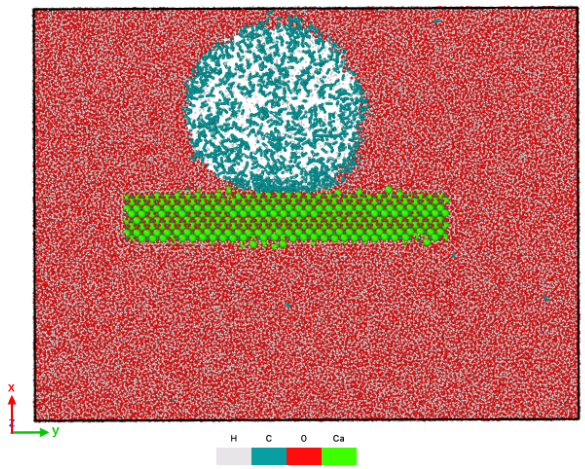

(c) System snapshot (.gro)

Figure B.41: Validation of the equilibrated ACH4 system. The potential energy (left) and temperature (right) are shown as a function of time; the dashed horizontal lines indicate the mean value over the final 500 ps of the trajectory, used as an equilibrium indicator. The bottom panel shows a representative configuration of the system rendered from the corresponding .gro structure file.

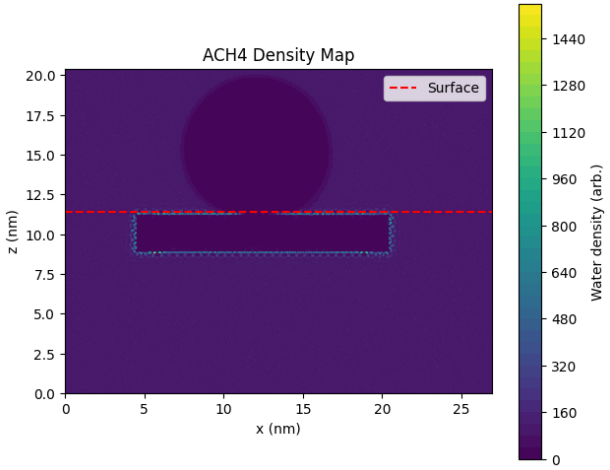

(a) Two-dimensional water density map used to determine the liquid-vapor interface. The dashed line indicates the solid surface position.

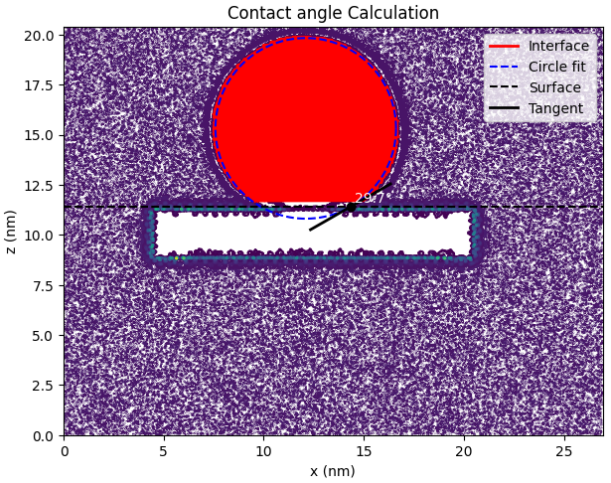

(b) Construction of the contact angle. A circular fit is applied to the detected interface points, and the tangent at the three phase contact line is used to compute the contact angle.

Figure B.42: Illustration of the contact angle determination procedure. (a) The liquid-vapor interface is extracted from the time-averaged density field using a threshold criterion. (b) A circle is fitted to the interface contour, and the contact angle is obtained from the tangent at the intersection between the fitted circle and the solid surface.

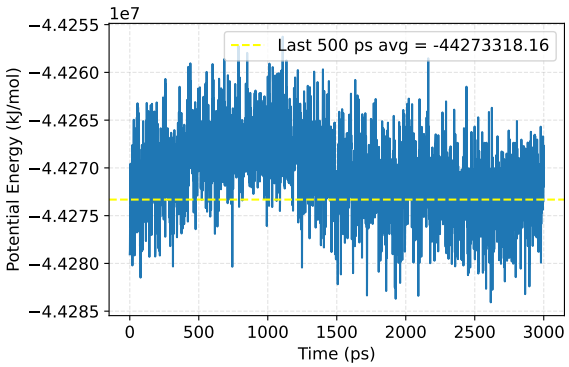

(a) Potential energy

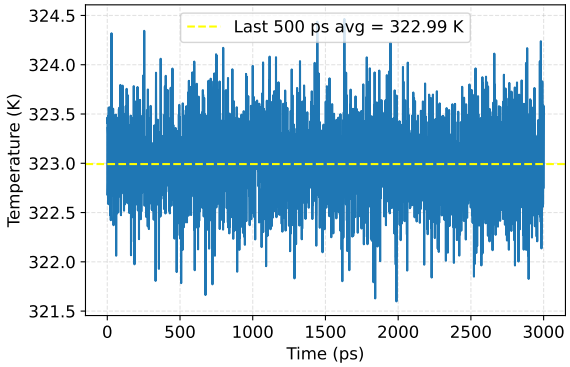

(b) Temperature

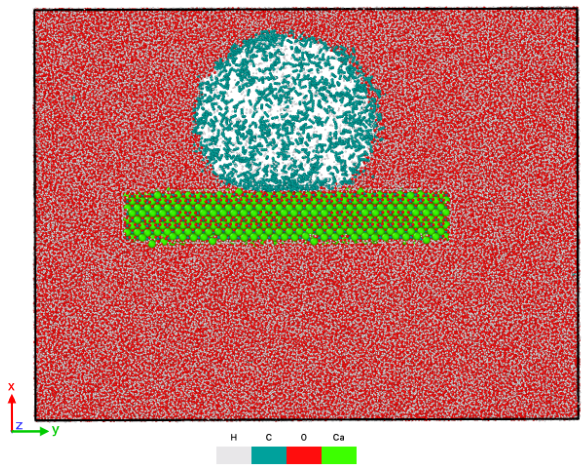

(c) System snapshot (.gro)

Figure B.43: Validation of the equilibrated ACH5 system. The potential energy (left) and temperature (right) are shown as a function of time; the dashed horizontal lines indicate the mean value over the final 500 ps of the trajectory, used as an equilibrium indicator. The bottom panel shows a representative configuration of the system rendered from the corresponding .gro structure file.

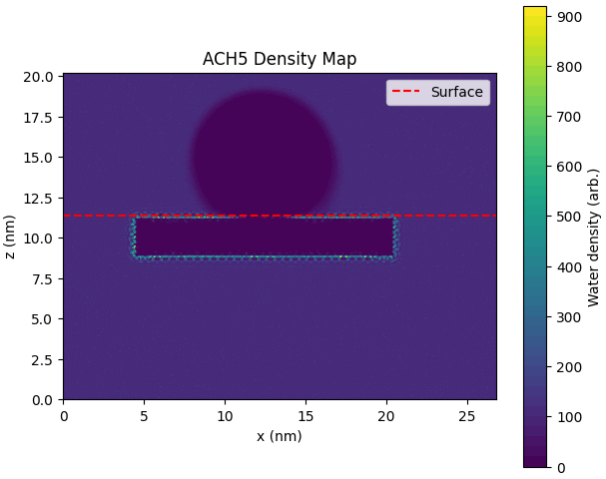

(a) Two-dimensional water density map used to determine the liquid-vapor interface. The dashed line indicates the solid surface position.

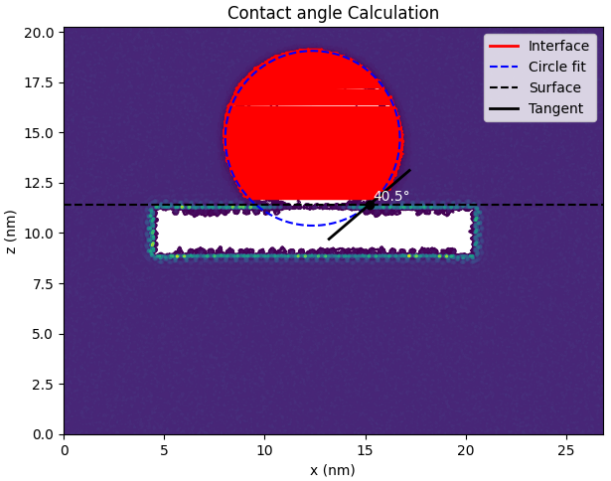

(b) Construction of the contact angle. A circular fit is applied to the detected interface points, and the tangent at the three phase contact line is used to compute the contact angle.

Figure B.44: Illustration of the contact angle determination procedure. (a) The liquid-vapor interface is extracted from the time-averaged density field using a threshold criterion. (b) A circle is fitted to the interface contour, and the contact angle is obtained from the tangent at the intersection between the fitted circle and the solid surface.

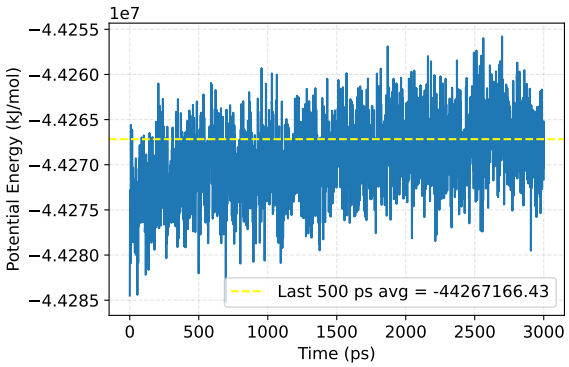

(a) Potential energy

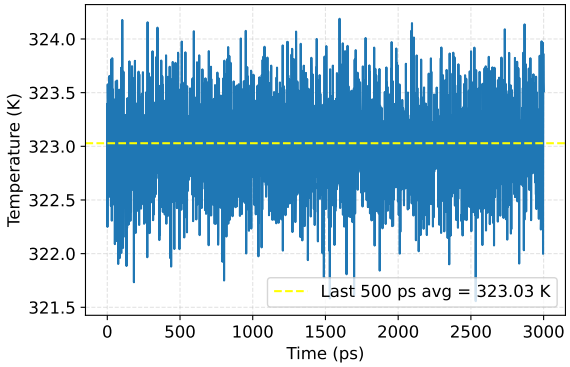

(b) Temperature

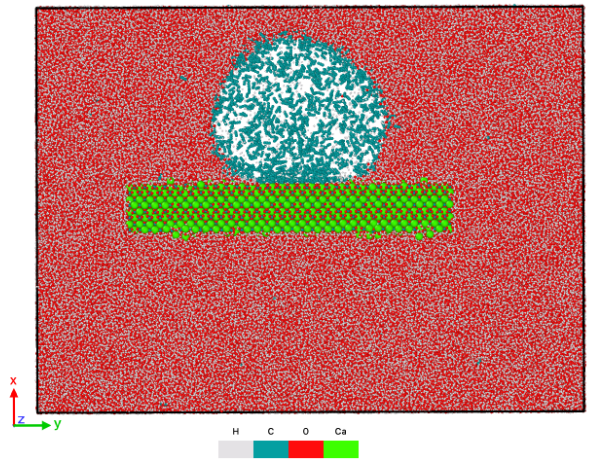

(c) System snapshot (.gro)

Figure B.45: Validation of the equilibrated ACH6 system. The potential energy (left) and temperature (right) are shown as a function of time; the dashed horizontal lines indicate the mean value over the final 500 ps of the trajectory, used as an equilibrium indicator. The bottom panel shows a representative configuration of the system rendered from the corresponding .gro structure file.

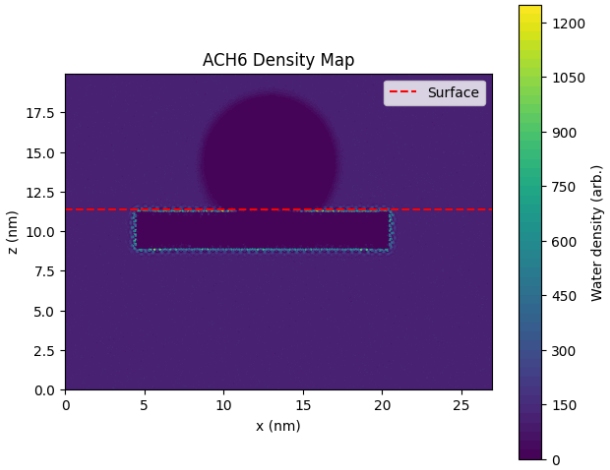

(a) Two-dimensional water density map used to determine the liquid-vapor interface. The dashed line indicates the solid surface position.

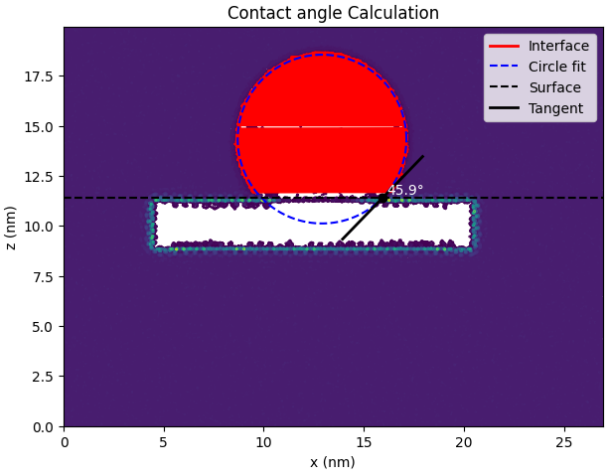

(b) Construction of the contact angle. A circular fit is applied to the detected interface points, and the tangent at the three phase contact line is used to compute the contact angle.

Figure B.46: Illustration of the contact angle determination procedure. (a) The liquid-vapor interface is extracted from the time-averaged density field using a threshold criterion. (b) A circle is fitted to the interface contour, and the contact angle is obtained from the tangent at the intersection between the fitted circle and the solid surface.

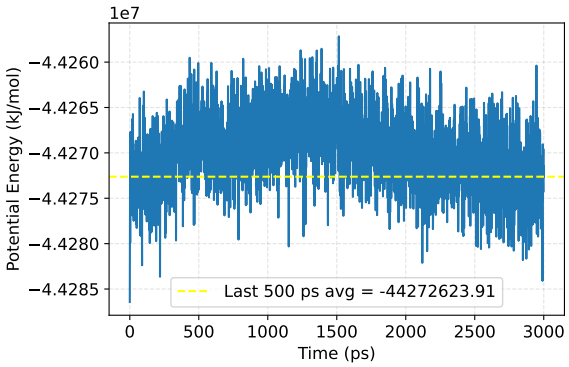

(a) Potential energy

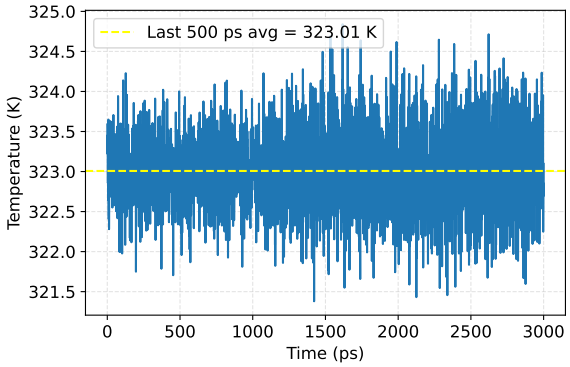

(b) Temperature

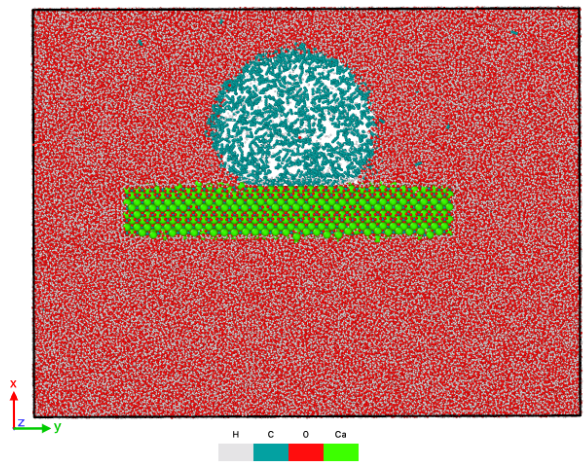

(c) System snapshot (.gro)

Figure B.47: Validation of the equilibrated ACH7 system. The potential energy (left) and temperature (right) are shown as a function of time; the dashed horizontal lines indicate the mean value over the final 500 ps of the trajectory, used as an equilibrium indicator. The bottom panel shows a representative configuration of the system rendered from the corresponding .gro structure file.

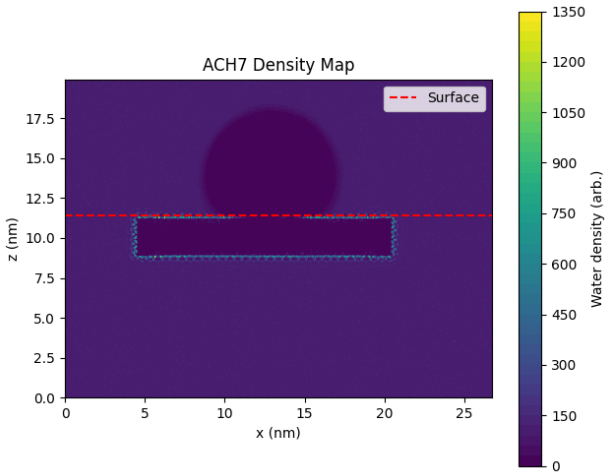

(a) Two-dimensional water density map used to determine the liquid-vapor interface. The dashed line indicates the solid surface position.

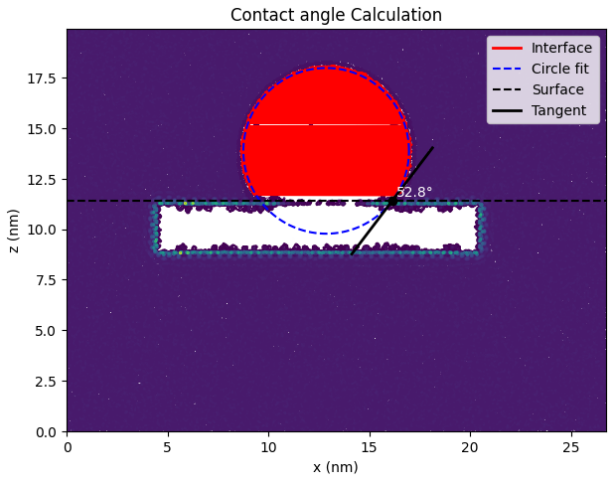

(b) Construction of the contact angle. A circular fit is applied to the detected interface points, and the tangent at the three phase contact line is used to compute the contact angle.

Figure B.48: Illustration of the contact angle determination procedure. (a) The liquid-vapor interface is extracted from the time-averaged density field using a threshold criterion. (b) A circle is fitted to the interface contour, and the contact angle is obtained from the tangent at the intersection between the fitted circle and the solid surface.

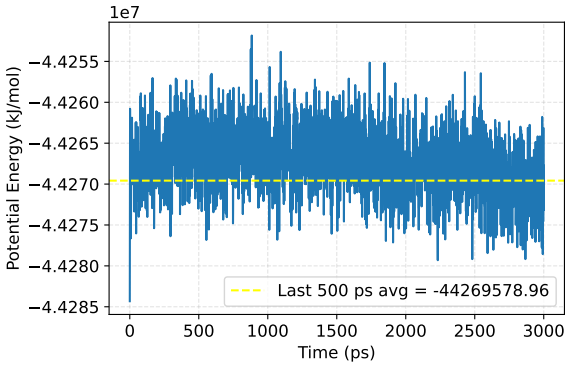

(a) Potential energy

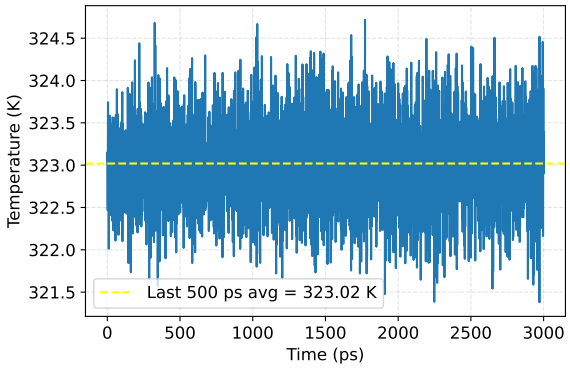

(b) Temperature

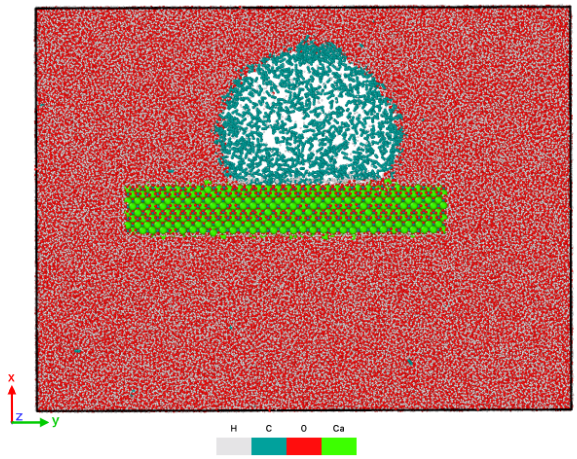

(c) System snapshot (.gro)

Figure B.49: Validation of the equilibrated ACH8 system. The potential energy (left) and temperature (right) are shown as a function of time; the dashed horizontal lines indicate the mean value over the final 500 ps of the trajectory, used as an equilibrium indicator. The bottom panel shows a representative configuration of the system rendered from the corresponding .gro structure file.

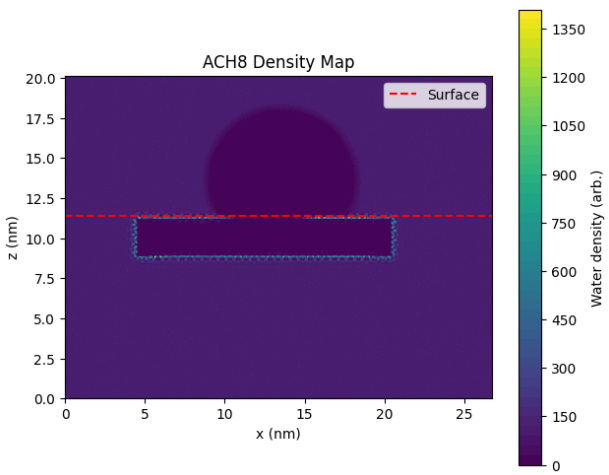

(a) Two-dimensional water density map used to determine the liquid-vapor interface. The dashed line indicates the solid surface position.

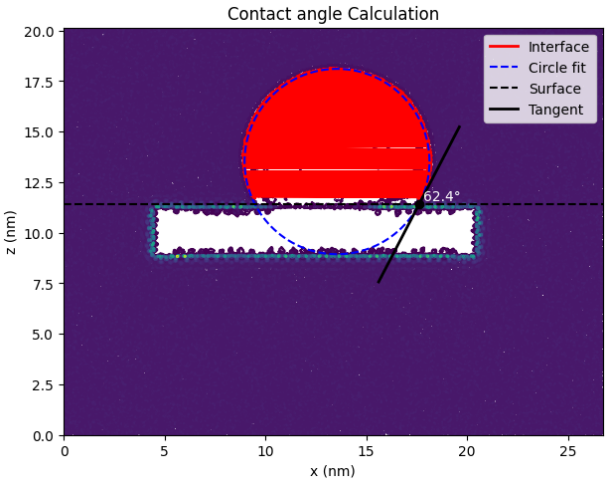

(b) Construction of the contact angle. A circular fit is applied to the detected interface points, and the tangent at the three phase contact line is used to compute the contact angle.

Figure B.50: Illustration of the contact angle determination procedure. (a) The liquid-vapor interface is extracted from the time-averaged density field using a threshold criterion. (b) A circle is fitted to the interface contour, and the contact angle is obtained from the tangent at the intersection between the fitted circle and the solid surface.

B.1.3. AF Systems

CO_2 adsorbed layer

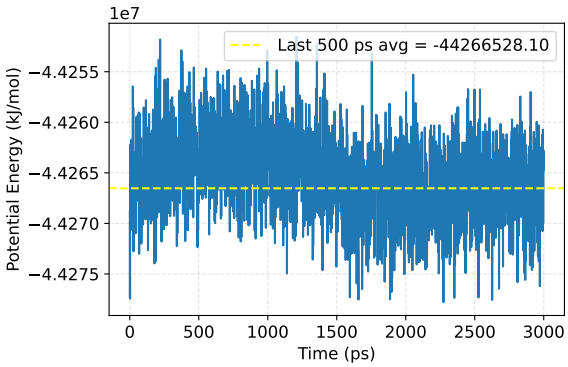

(a) Potential energy

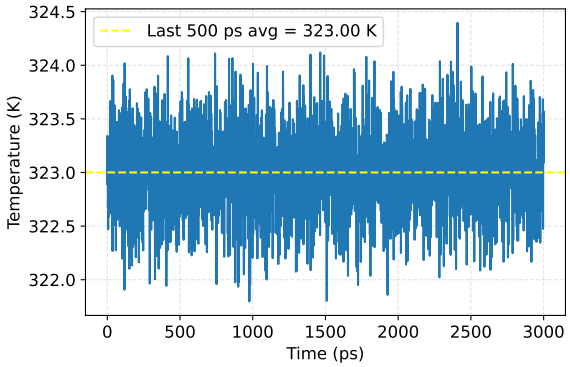

(b) Temperature

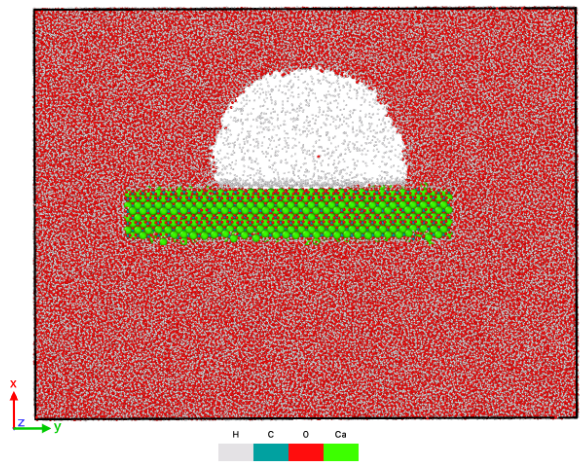

(c) System snapshot (.gro)

Figure B.51: Validation of the equilibrated AFC0 system. The potential energy (left) and temperature (right) are shown as a function of time; the dashed horizontal lines indicate the mean value over the final 500 ps of the trajectory, used as an equilibrium indicator. The bottom panel shows a representative configuration of the system rendered from the corresponding .gro structure file.

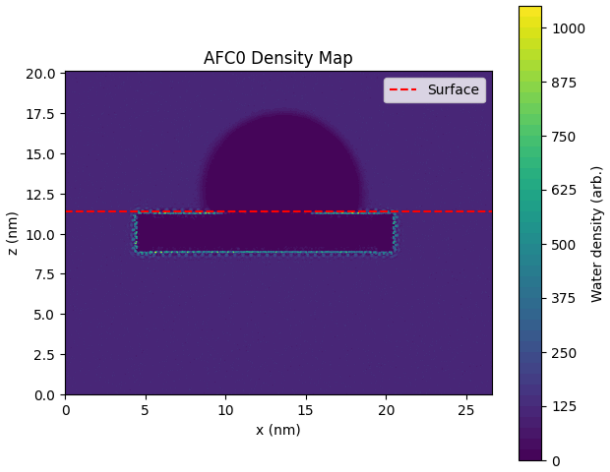

(a) Two-dimensional water density map used to determine the liquid-vapor interface. The dashed line indicates the solid surface position.

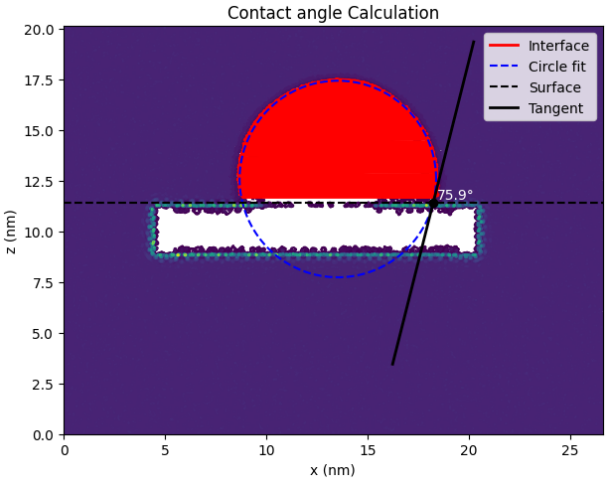

(b) Construction of the contact angle. A circular fit is applied to the detected interface points, and the tangent at the three phase contact line is used to compute the contact angle.

Figure B.52: Illustration of the contact angle determination procedure. (a) The liquid-vapor interface is extracted from the time-averaged density field using a threshold criterion. (b) A circle is fitted to the interface contour, and the contact angle is obtained from the tangent at the intersection between the fitted circle and the solid surface.

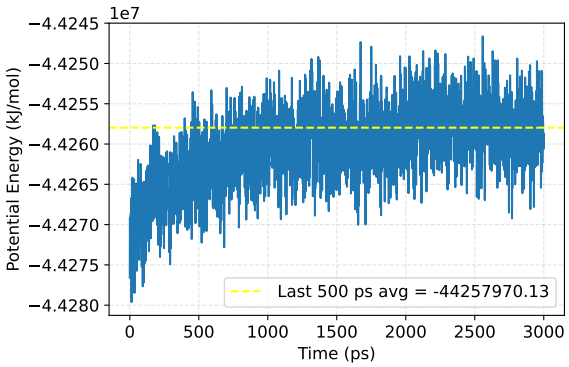

(a) Potential energy

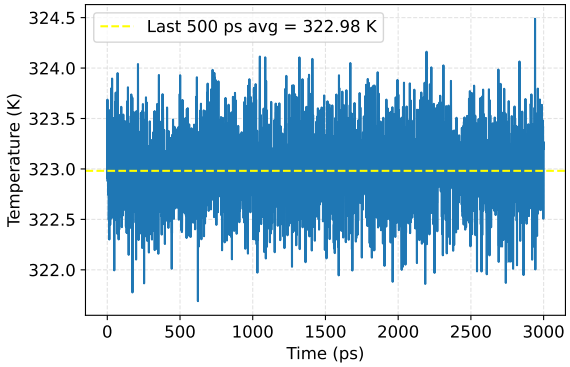

(b) Temperature

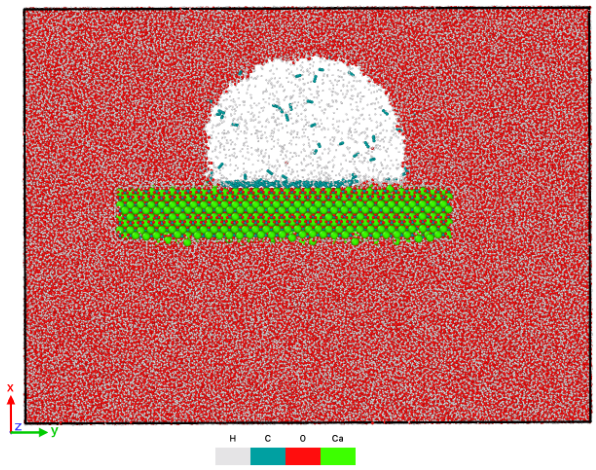

(c) System snapshot (.gro)

Figure B.53: Validation of the equilibrated AFC10 system. The potential energy (left) and temperature (right) are shown as a function of time; the dashed horizontal lines indicate the mean value over the final 500 ps of the trajectory, used as an equilibrium indicator. The bottom panel shows a representative configuration of the system rendered from the corresponding .gro structure file.

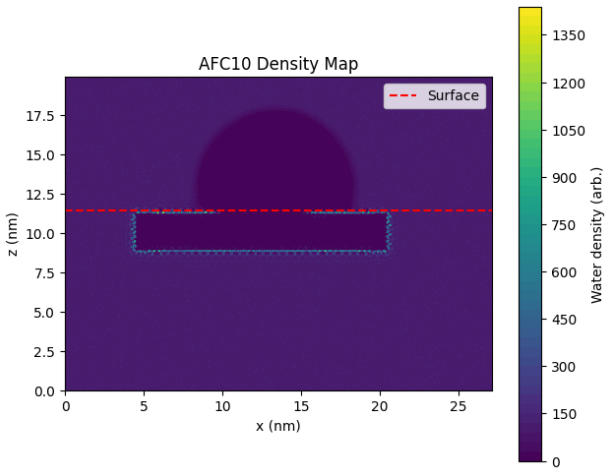

(a) Two-dimensional water density map used to determine the liquid-vapor interface. The dashed line indicates the solid surface position.

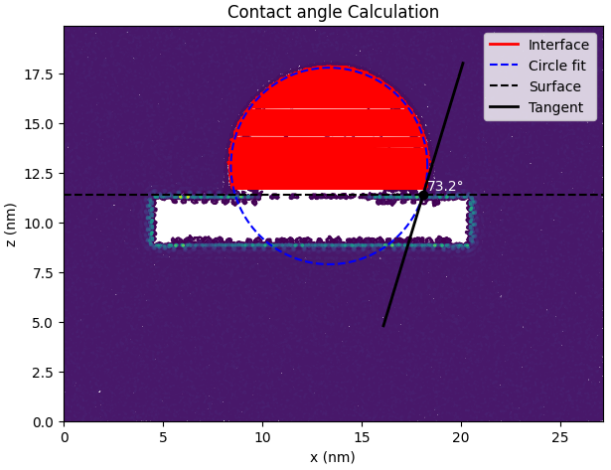

(b) Construction of the contact angle. A circular fit is applied to the detected interface points, and the tangent at the three phase contact line is used to compute the contact angle.

Figure B.54: Illustration of the contact angle determination procedure. (a) The liquid-vapor interface is extracted from the time-averaged density field using a threshold criterion. (b) A circle is fitted to the interface contour, and the contact angle is obtained from the tangent at the intersection between the fitted circle and the solid surface.

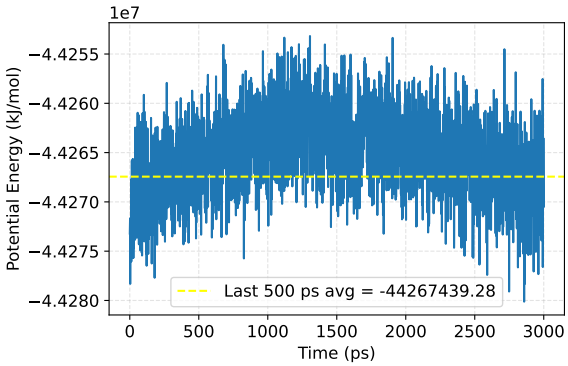

(a) Potential energy

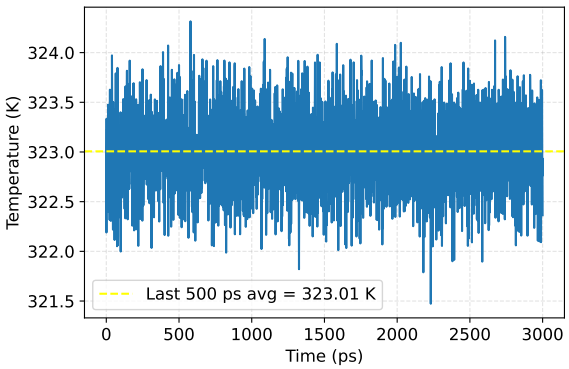

(b) Temperature

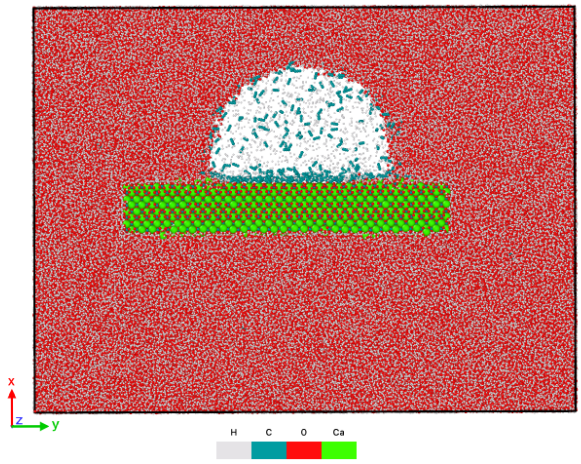

(c) System snapshot (.gro)

Figure B.55: Validation of the equilibrated AFC20 system. The potential energy (left) and temperature (right) are shown as a function of time; the dashed horizontal lines indicate the mean value over the final 500 ps of the trajectory, used as an equilibrium indicator. The bottom panel shows a representative configuration of the system rendered from the corresponding .gro structure file.

H_2 adsorbed layer

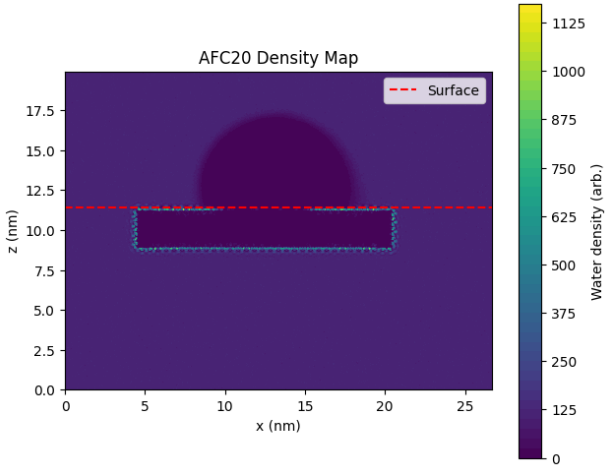

(a) Two-dimensional water density map used to determine the liquid-vapor interface. The dashed line indicates the solid surface position.

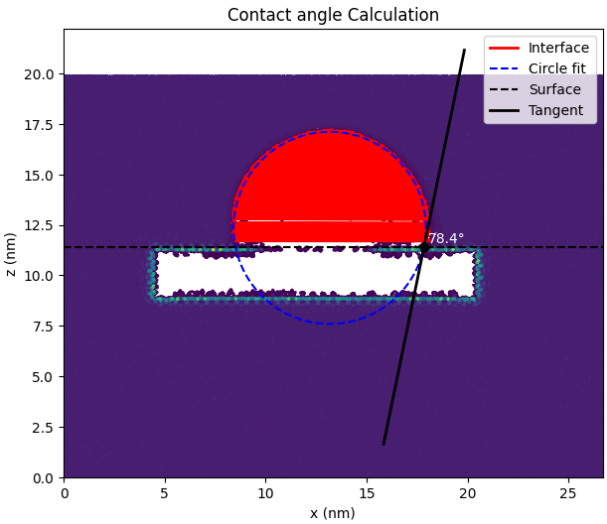

(b) Construction of the contact angle. A circular fit is applied to the detected interface points, and the tangent at the three phase contact line is used to compute the contact angle.

Figure B.56: Illustration of the contact angle determination procedure. (a) The liquid-vapor interface is extracted from the time-averaged density field using a threshold criterion. (b) A circle is fitted to the interface contour, and the contact angle is obtained from the tangent at the intersection between the fitted circle and the solid surface.

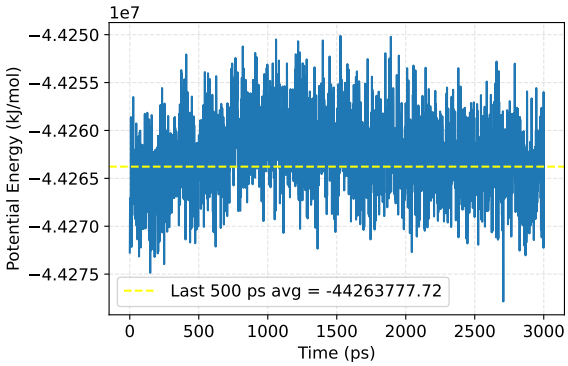

(a) Potential energy

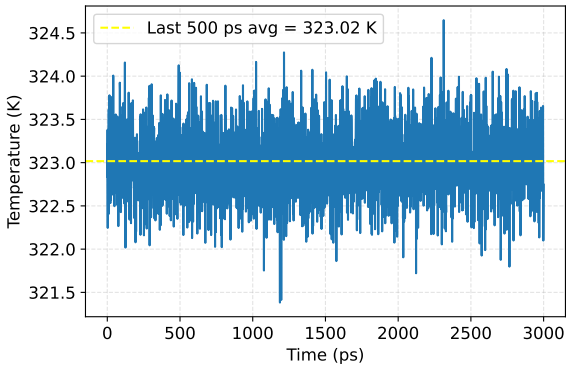

(b) Temperature

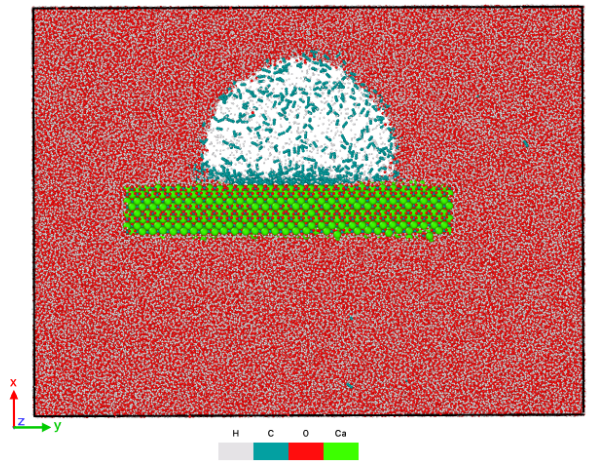

(c) System snapshot (.gro)

Figure B.57: Validation of the equilibrated AFC30 system. The potential energy (left) and temperature (right) are shown as a function of time; the dashed horizontal lines indicate the mean value over the final 500 ps of the trajectory, used as an equilibrium indicator. The bottom panel shows a representative configuration of the system rendered from the corresponding .gro structure file.

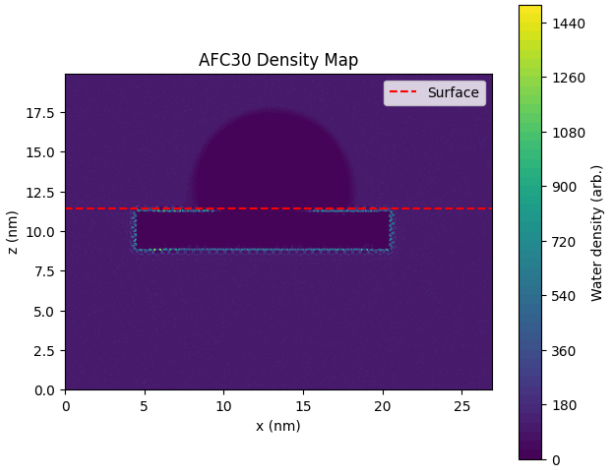

(a) Two-dimensional water density map used to determine the liquid-vapor interface. The dashed line indicates the solid surface position.

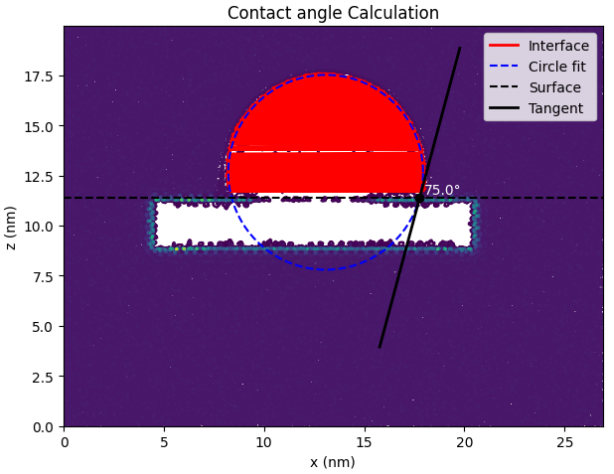

(b) Construction of the contact angle. A circular fit is applied to the detected interface points, and the tangent at the three phase contact line is used to compute the contact angle.

Figure B.58: Illustration of the contact angle determination procedure. (a) The liquid-vapor interface is extracted from the time-averaged density field using a threshold criterion. (b) A circle is fitted to the interface contour, and the contact angle is obtained from the tangent at the intersection between the fitted circle and the solid surface.

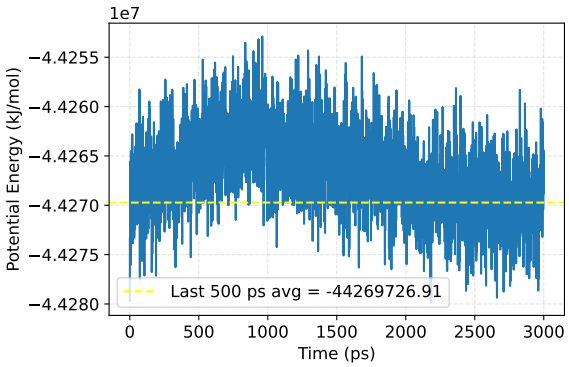

(a) Potential energy

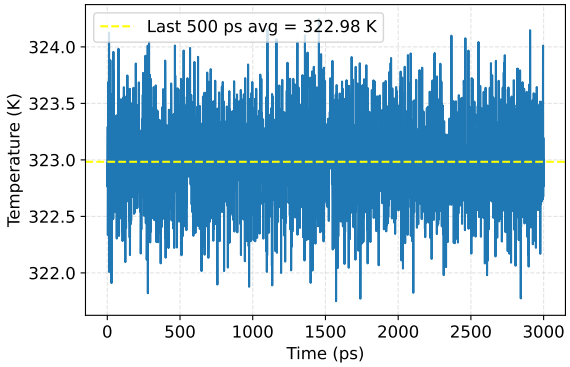

(b) Temperature

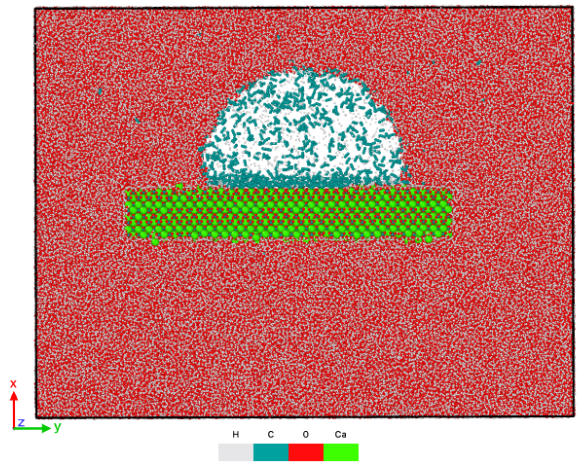

(c) System snapshot (.gro)

Figure B.59: Validation of the equilibrated AFC40 system. The potential energy (left) and temperature (right) are shown as a function of time; the dashed horizontal lines indicate the mean value over the final 500 ps of the trajectory, used as an equilibrium indicator. The bottom panel shows a representative configuration of the system rendered from the corresponding .gro structure file.

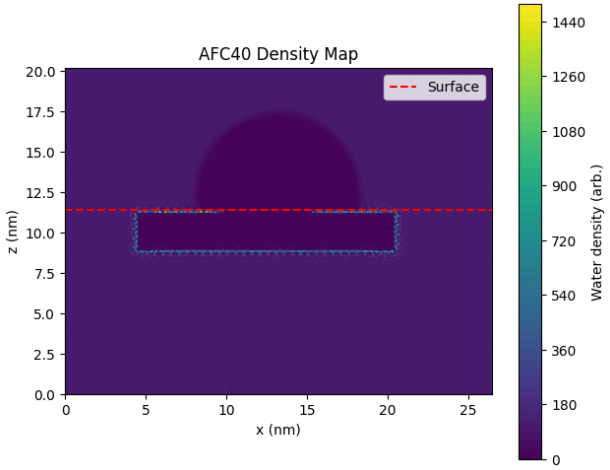

(a) Two-dimensional water density map used to determine the liquid-vapor interface. The dashed line indicates the solid surface position.

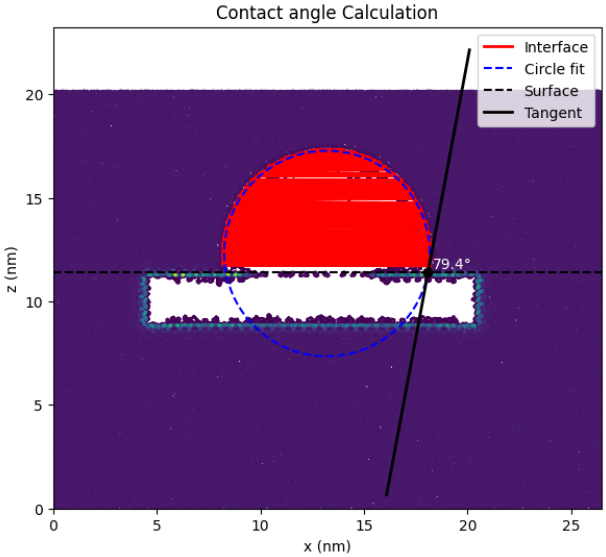

(b) Construction of the contact angle. A circular fit is applied to the detected interface points, and the tangent at the three phase contact line is used to compute the contact angle.

Figure B.60: Illustration of the contact angle determination procedure. (a) The liquid-vapor interface is extracted from the time-averaged density field using a threshold criterion. (b) A circle is fitted to the interface contour, and the contact angle is obtained from the tangent at the intersection between the fitted circle and the solid surface.

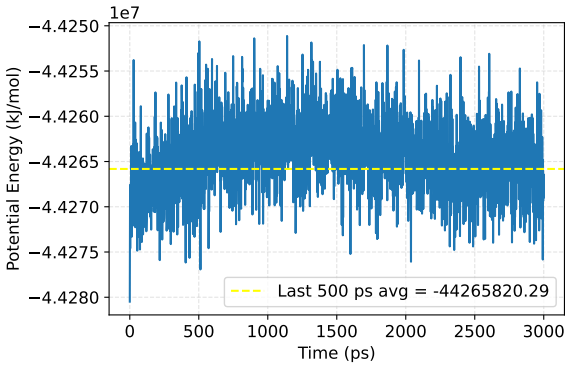

(a) Potential energy

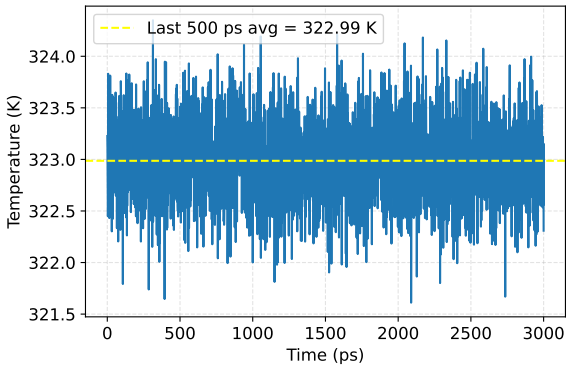

(b) Temperature

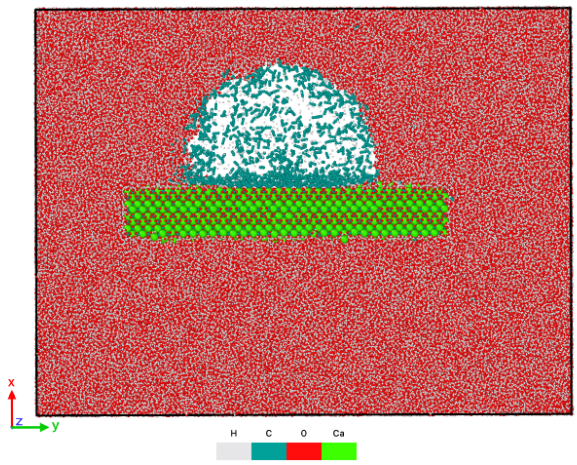

(c) System snapshot (.gro)

Figure B.61: Validation of the equilibrated AFC50 system. The potential energy (left) and temperature (right) are shown as a function of time; the dashed horizontal lines indicate the mean value over the final 500 ps of the trajectory, used as an equilibrium indicator. The bottom panel shows a representative configuration of the system rendered from the corresponding .gro structure file.

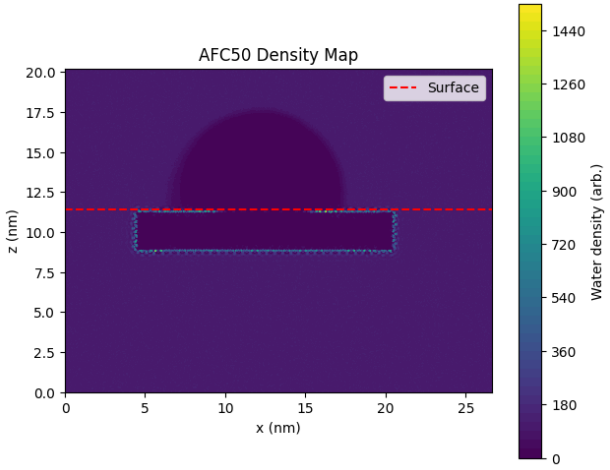

(a) Two-dimensional water density map used to determine the liquid-vapor interface. The dashed line indicates the solid surface position.

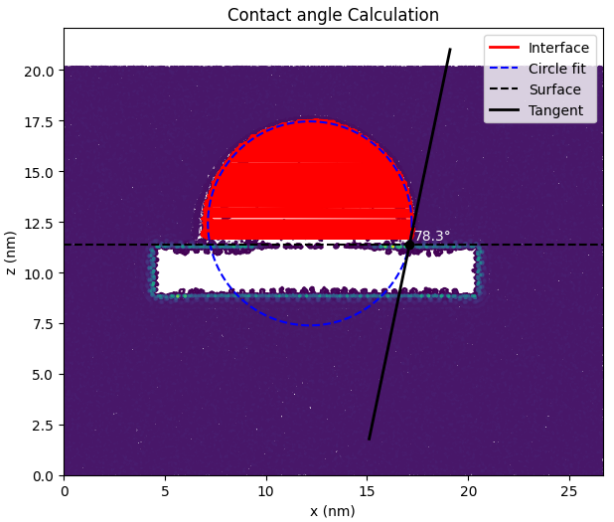

(b) Construction of the contact angle. A circular fit is applied to the detected interface points, and the tangent at the three phase contact line is used to compute the contact angle.

Figure B.62: Illustration of the contact angle determination procedure. (a) The liquid-vapor interface is extracted from the time-averaged density field using a threshold criterion. (b) A circle is fitted to the interface contour, and the contact angle is obtained from the tangent at the intersection between the fitted circle and the solid surface.

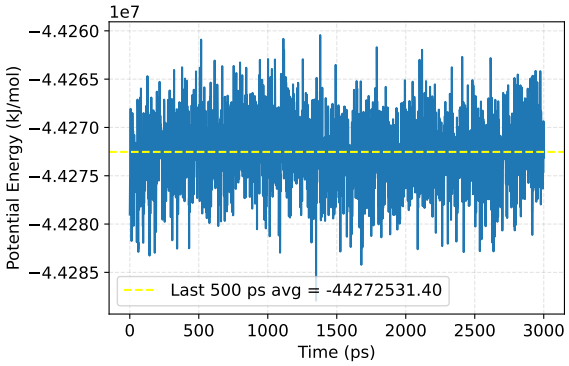

(a) Potential energy

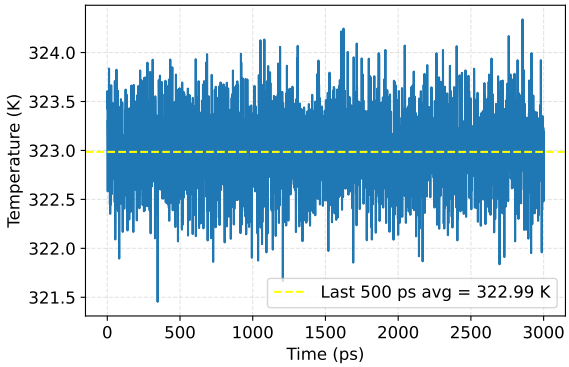

(b) Temperature

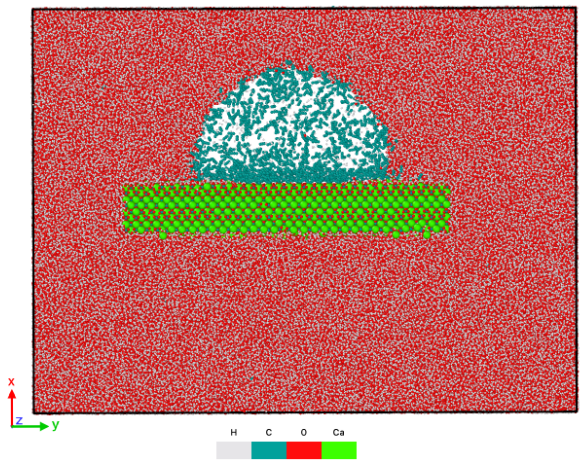

(c) System snapshot (.gro)

Figure B.63: Validation of the equilibrated AFC60 system. The potential energy (left) and temperature (right) are shown as a function of time; the dashed horizontal lines indicate the mean value over the final 500 ps of the trajectory, used as an equilibrium indicator. The bottom panel shows a representative configuration of the system rendered from the corresponding .gro structure file.

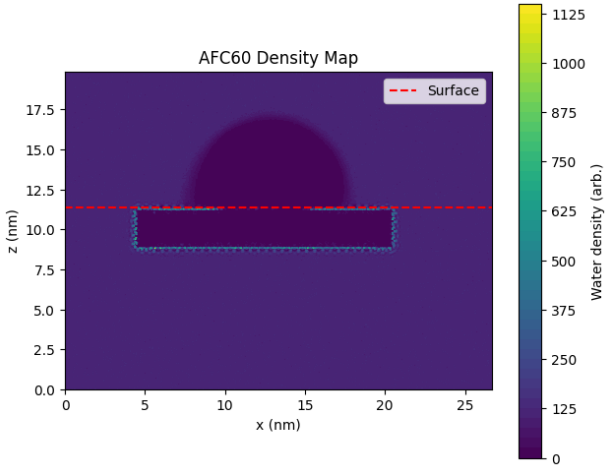

(a) Two-dimensional water density map used to determine the liquid-vapor interface. The dashed line indicates the solid surface position.

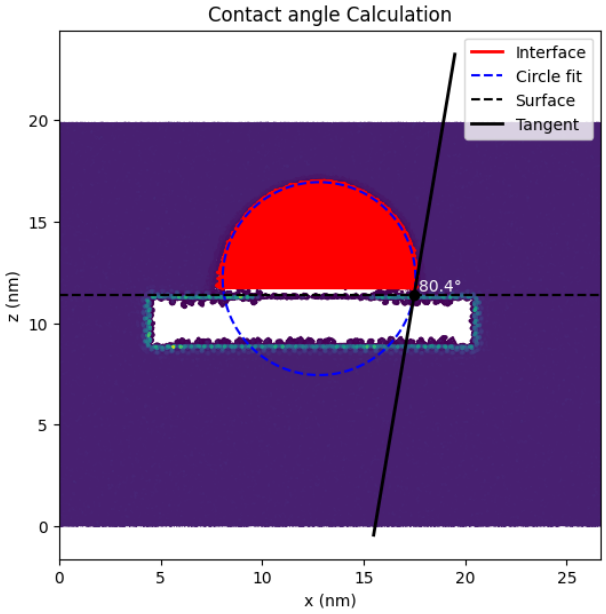

(b) Construction of the contact angle. A circular fit is applied to the detected interface points, and the tangent at the three phase contact line is used to compute the contact angle.

Figure B.64: Illustration of the contact angle determination procedure. (a) The liquid-vapor interface is extracted from the time-averaged density field using a threshold criterion. (b) A circle is fitted to the interface contour, and the contact angle is obtained from the tangent at the intersection between the fitted circle and the solid surface.

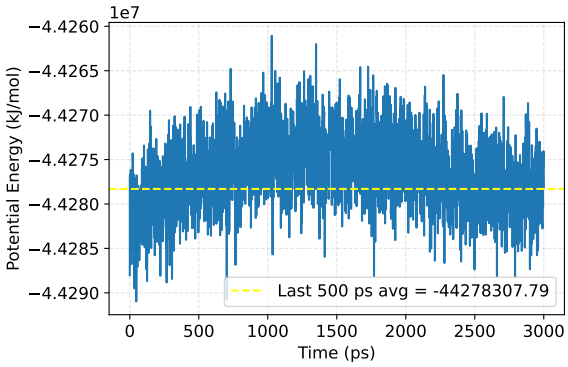

(a) Potential energy

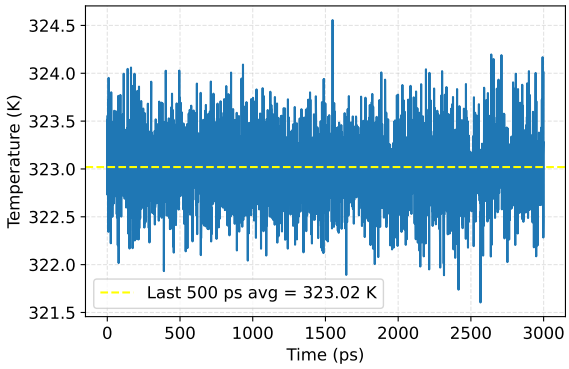

(b) Temperature

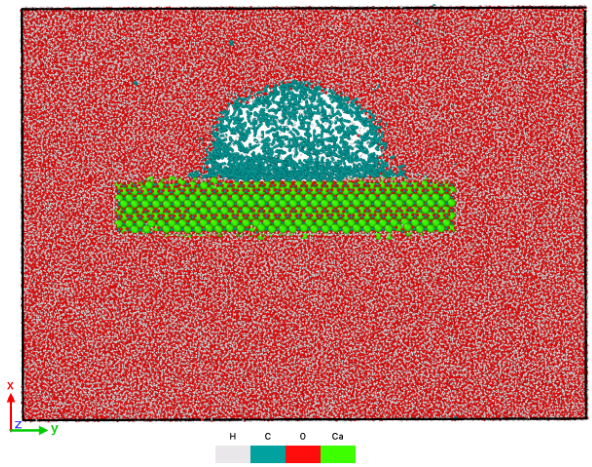

(c) System snapshot (.gro)

Figure B.65: Validation of the equilibrated AFC70 system. The potential energy (left) and temperature (right) are shown as a function of time; the dashed horizontal lines indicate the mean value over the final 500 ps of the trajectory, used as an equilibrium indicator. The bottom panel shows a representative configuration of the system rendered from the corresponding .gro structure file.

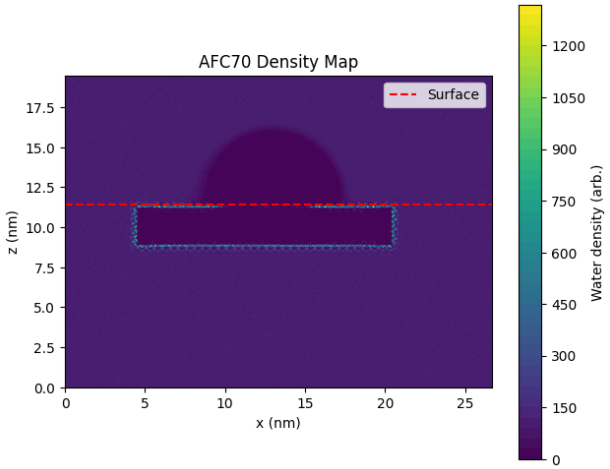

(a) Two-dimensional water density map used to determine the liquid-vapor interface. The dashed line indicates the solid surface position.

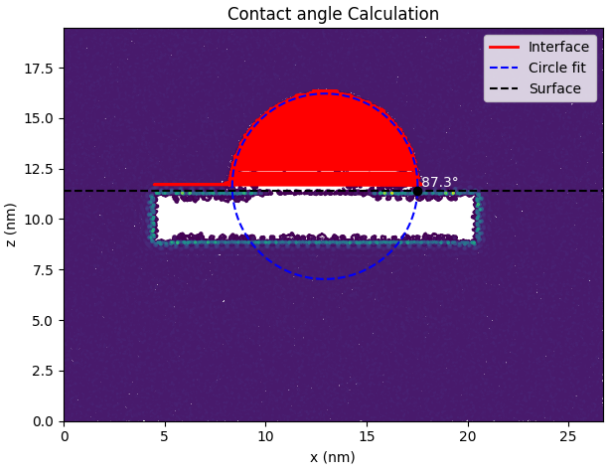

(b) Construction of the contact angle. A circular fit is applied to the detected interface points, and the tangent at the three phase contact line is used to compute the contact angle.

Figure B.66: Illustration of the contact angle determination procedure. (a) The liquid-vapor interface is extracted from the time-averaged density field using a threshold criterion. (b) A circle is fitted to the interface contour, and the contact angle is obtained from the tangent at the intersection between the fitted circle and the solid surface.

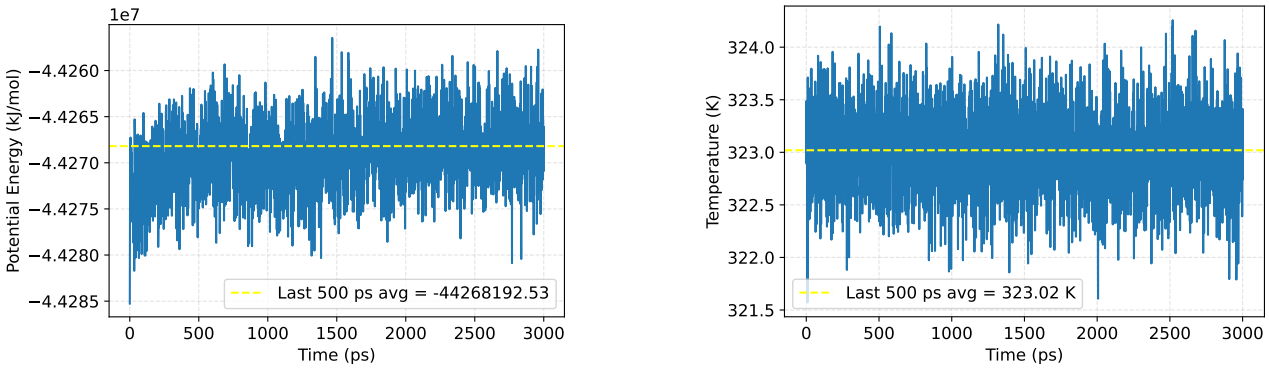

(a) Temperature

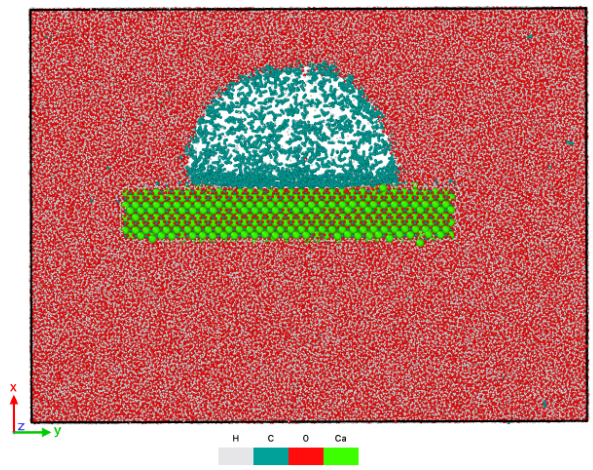

(b) System snapshot (.gro)

Figure B.67: Validation of the equilibrated AFC80 system. The potential energy (left) and temperature (right) are shown as a function of time; the dashed horizontal lines indicate the mean value over the final 500 ps of the trajectory, used as an equilibrium indicator. The bottom panel shows a representative configuration of the system rendered from the corresponding .gro structure file.

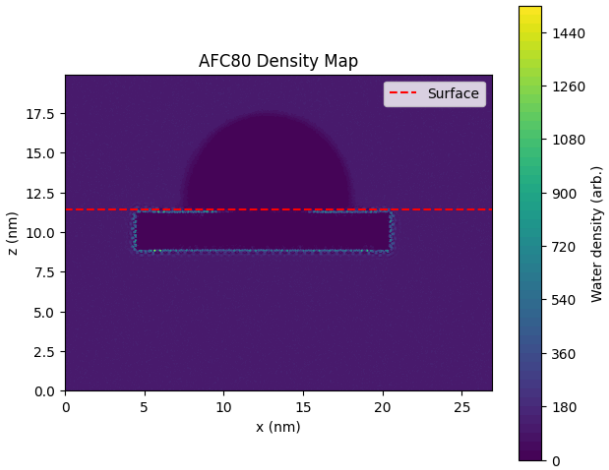

(a) Two-dimensional water density map used to determine the liquid-vapor interface. The dashed line indicates the solid surface position.

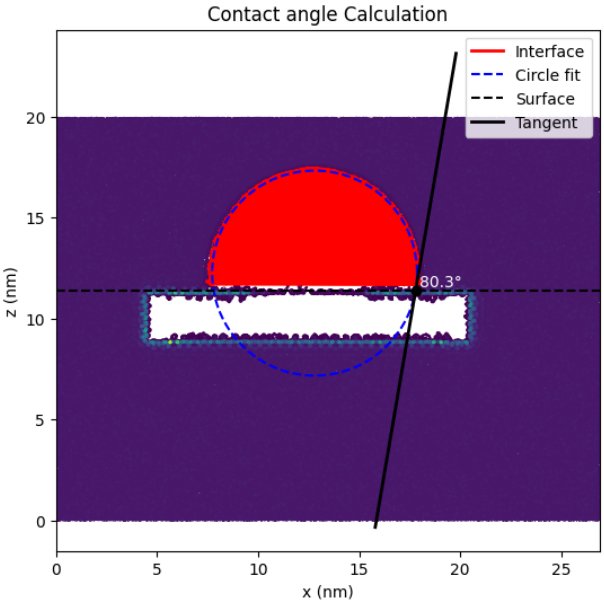

(b) Construction of the contact angle. A circular fit is applied to the detected interface points, and the tangent at the three phase contact line is used to compute the contact angle.

Figure B.68: Illustration of the contact angle determination procedure. (a) The liquid-vapor interface is extracted from the time-averaged density field using a threshold criterion. (b) A circle is fitted to the interface contour, and the contact angle is obtained from the tangent at the intersection between the fitted circle and the solid surface.

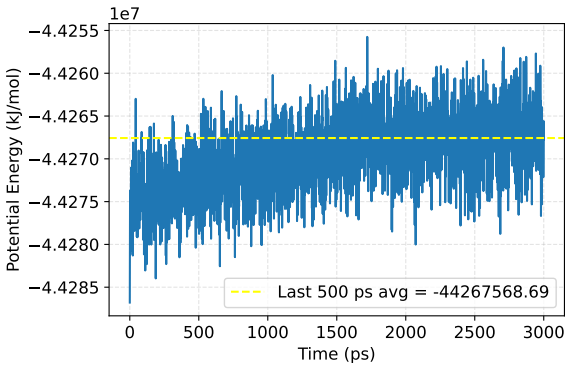

(a) Potential energy

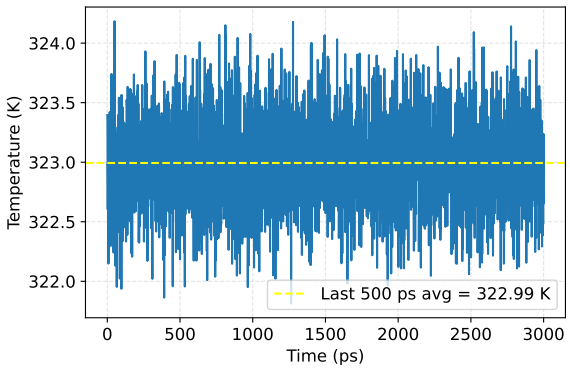

(b) Temperature

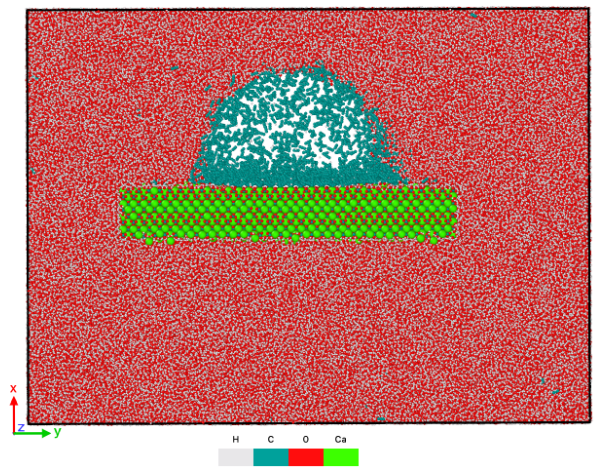

(c) System snapshot (.gro)

Figure B.69: Validation of the equilibrated AFC90 system. The potential energy (left) and temperature (right) are shown as a function of time; the dashed horizontal lines indicate the mean value over the final 500 ps of the trajectory, used as an equilibrium indicator. The bottom panel shows a representative configuration of the system rendered from the corresponding .gro structure file.

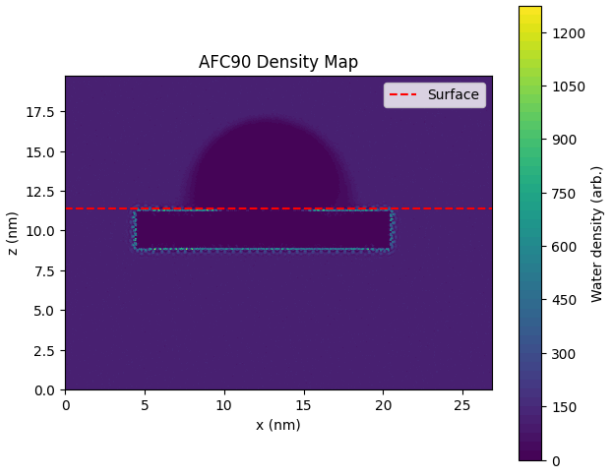

(a) Two-dimensional water density map used to determine the liquid-vapor interface. The dashed line indicates the solid surface position.

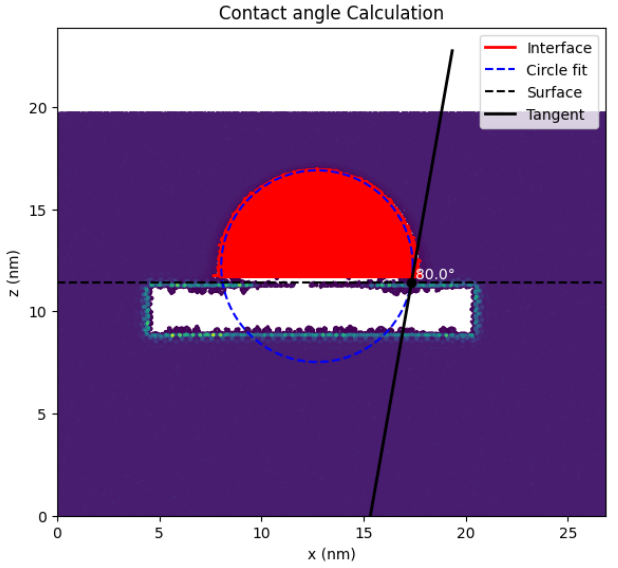

(b) Construction of the contact angle. A circular fit is applied to the detected interface points, and the tangent at the three phase contact line is used to compute the contact angle.

Figure B.70: Illustration of the contact angle determination procedure. (a) The liquid-vapor interface is extracted from the time-averaged density field using a threshold criterion. (b) A circle is fitted to the interface contour, and the contact angle is obtained from the tangent at the intersection between the fitted circle and the solid surface.

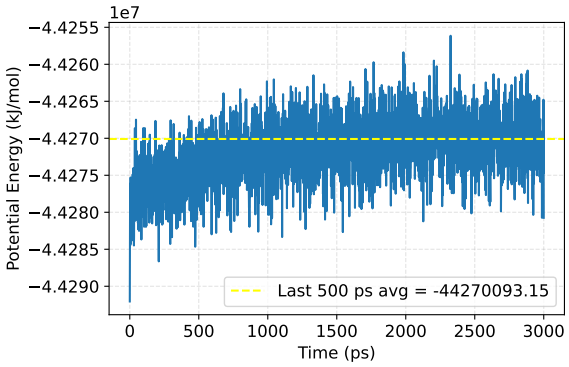

(a) Potential energy

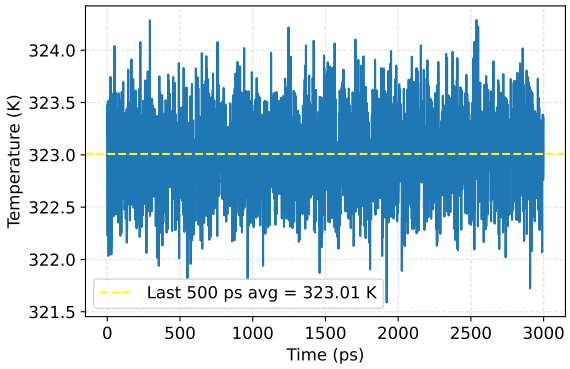

(b) Temperature

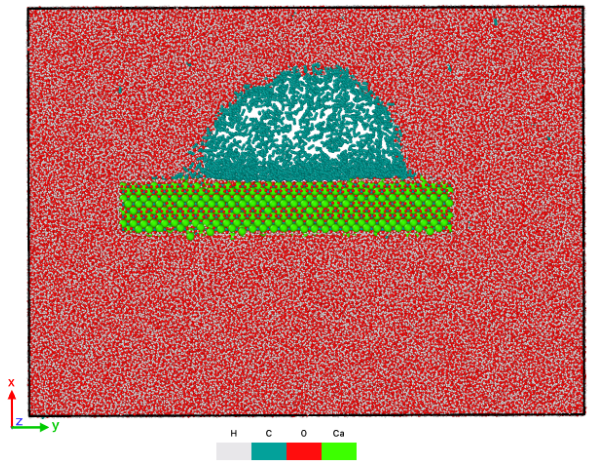

(c) System snapshot (.gro)

Figure B.71: Validation of the equilibrated AFC100 system. The potential energy (left) and temperature (right) are shown as a function of time; the dashed horizontal lines indicate the mean value over the final 500 ps of the trajectory, used as an equilibrium indicator. The bottom panel shows a representative configuration of the system rendered from the corresponding .gro structure file.

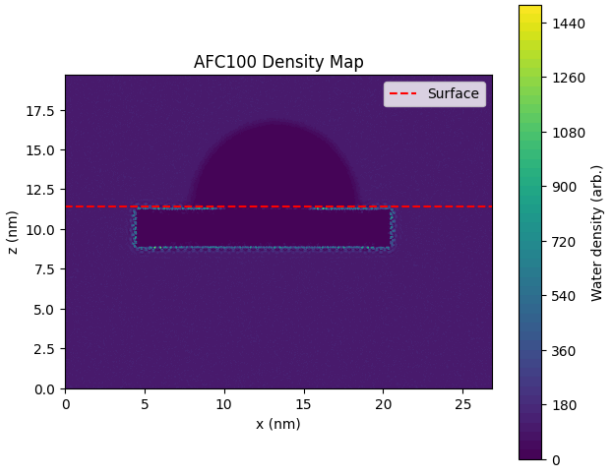

(a) Two-dimensional water density map used to determine the liquid-vapor interface. The dashed line indicates the solid surface position.

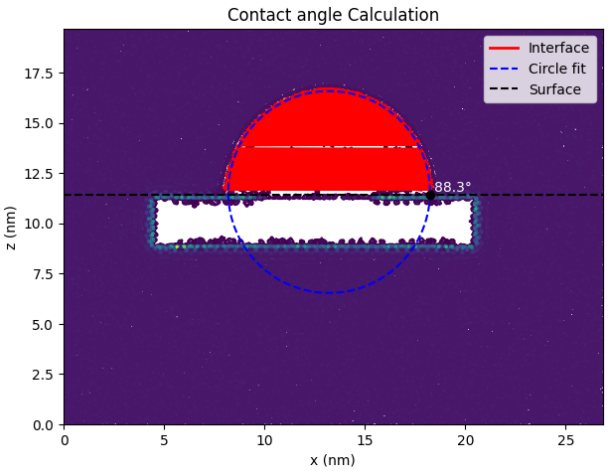

(b) Construction of the contact angle. A circular fit is applied to the detected interface points, and the tangent at the three phase contact line is used to compute the contact angle.

Figure B.72: Illustration of the contact angle determination procedure. (a) The liquid-vapor interface is extracted from the time-averaged density field using a threshold criterion. (b) A circle is fitted to the interface contour, and the contact angle is obtained from the tangent at the intersection between the fitted circle and the solid surface.

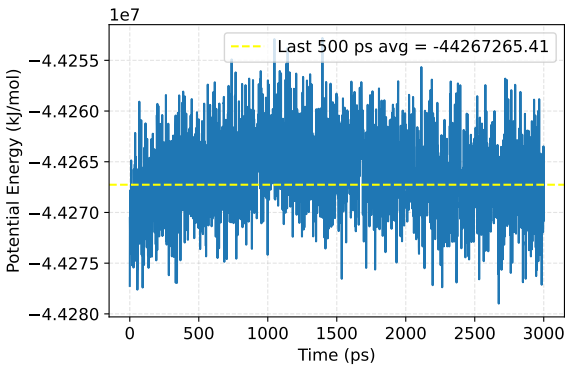

(a) Potential energy

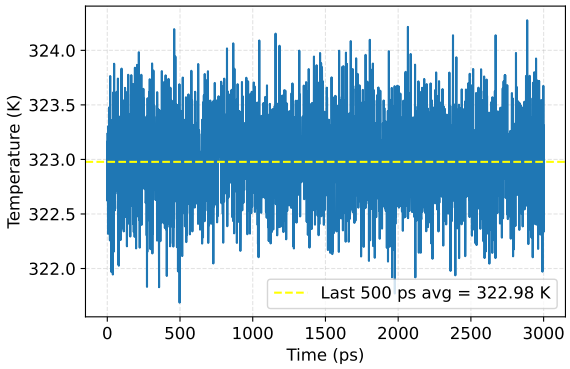

(b) Temperature

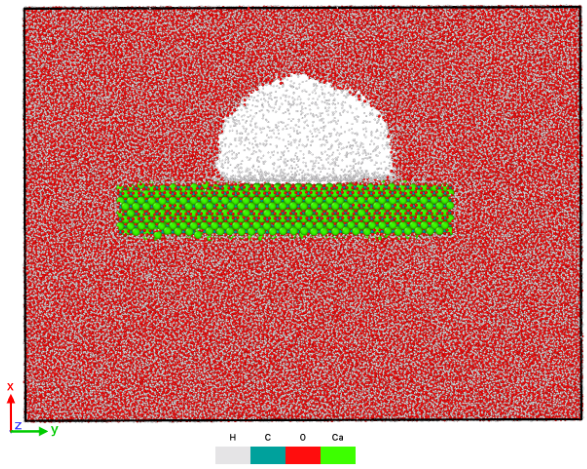

(c) System snapshot (.gro)

Figure B.73: Validation of the equilibrated AFH0 system. The potential energy (left) and temperature (right) are shown as a function of time; the dashed horizontal lines indicate the mean value over the final 500 ps of the trajectory, used as an equilibrium indicator. The bottom panel shows a representative configuration of the system rendered from the corresponding .gro structure file.

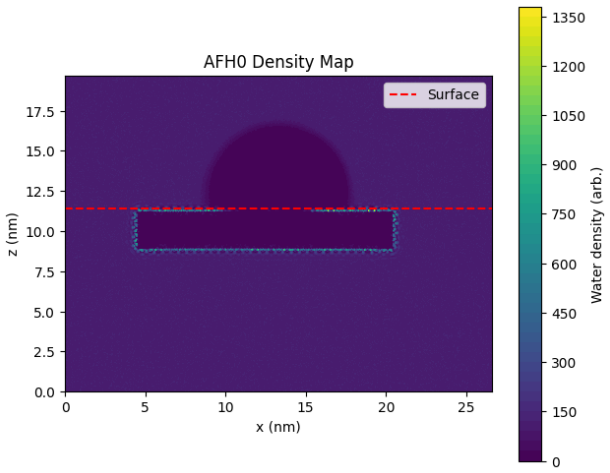

(a) Two-dimensional water density map used to determine the liquid-vapor interface. The dashed line indicates the solid surface position.

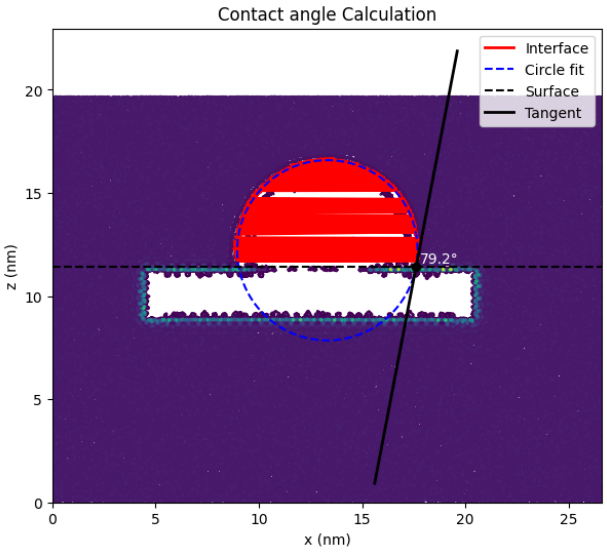

(b) Construction of the contact angle. A circular fit is applied to the detected interface points, and the tangent at the three phase contact line is used to compute the contact angle.

Figure B.74: Illustration of the contact angle determination procedure. (a) The liquid-vapor interface is extracted from the time-averaged density field using a threshold criterion. (b) A circle is fitted to the interface contour, and the contact angle is obtained from the tangent at the intersection between the fitted circle and the solid surface.

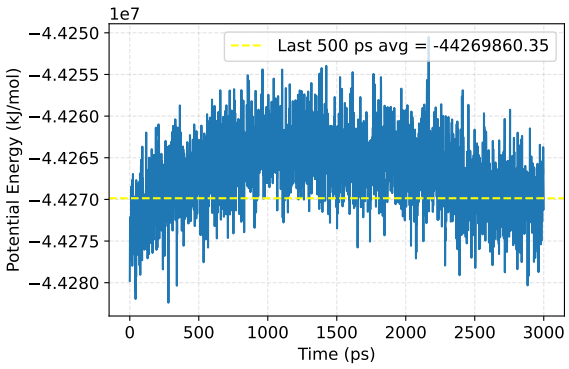

(a) Potential energy

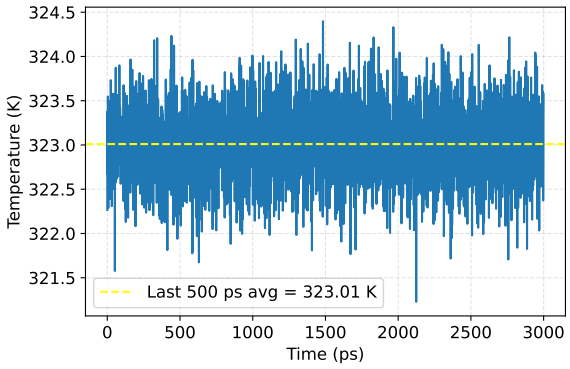

(b) Temperature

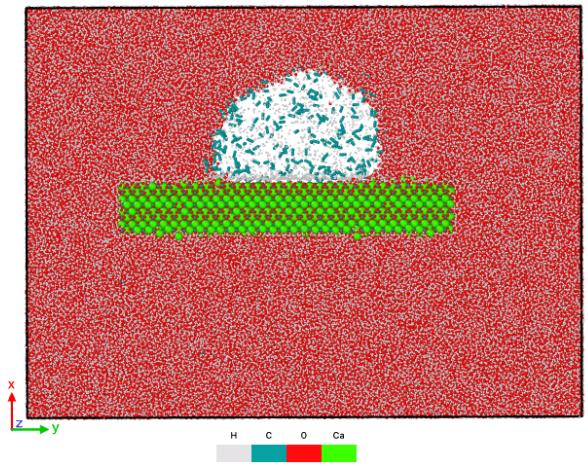

(c) System snapshot (.gro)

Figure B.75: Validation of the equilibrated AFH10 system. The potential energy (left) and temperature (right) are shown as a function of time; the dashed horizontal lines indicate the mean value over the final 500 ps of the trajectory, used as an equilibrium indicator. The bottom panel shows a representative configuration of the system rendered from the corresponding .gro structure file.

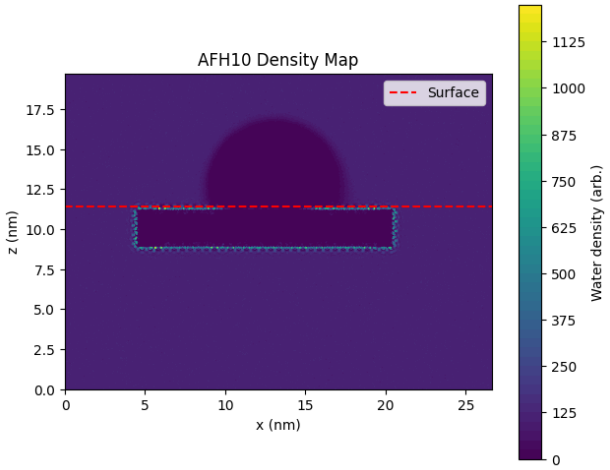

(a) Two-dimensional water density map used to determine the liquid-vapor interface. The dashed line indicates the solid surface position.

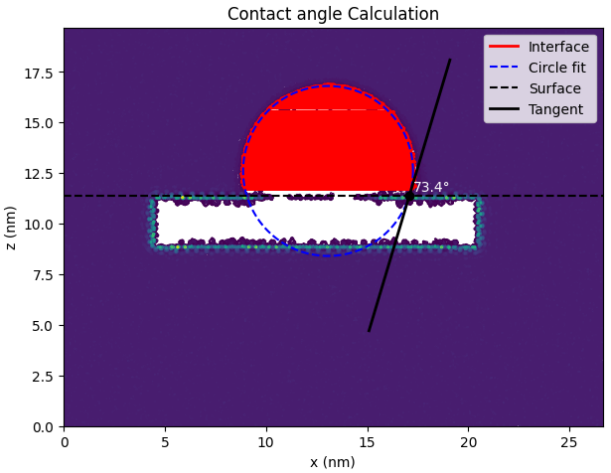

(b) Construction of the contact angle. A circular fit is applied to the detected interface points, and the tangent at the three phase contact line is used to compute the contact angle.

Figure B.76: Illustration of the contact angle determination procedure. (a) The liquid-vapor interface is extracted from the time-averaged density field using a threshold criterion. (b) A circle is fitted to the interface contour, and the contact angle is obtained from the tangent at the intersection between the fitted circle and the solid surface.

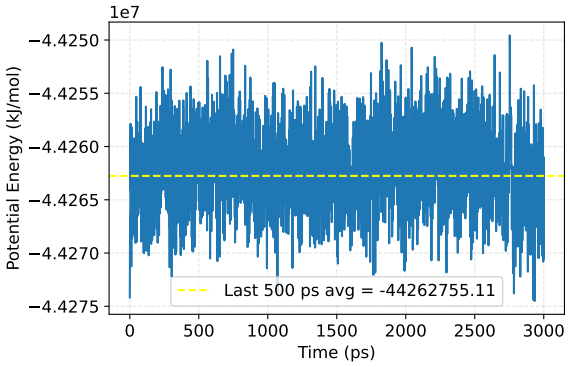

(a) Potential energy

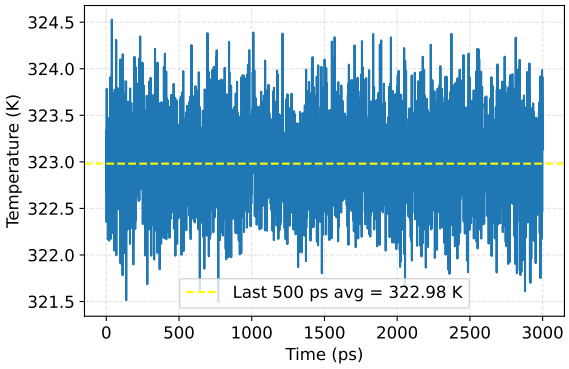

(b) Temperature

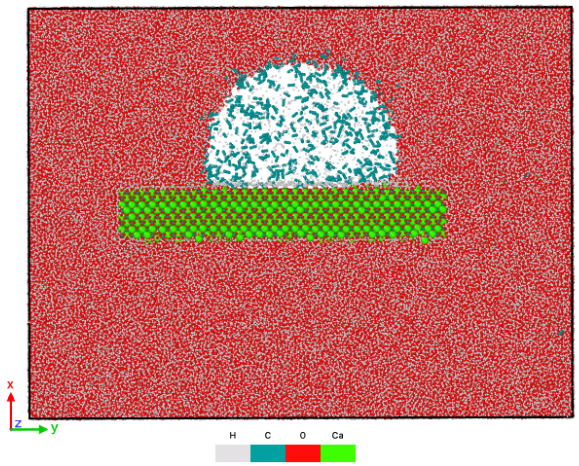

(c) System snapshot (.gro)

Figure B.77: Validation of the equilibrated AFH20 system. The potential energy (left) and temperature (right) are shown as a function of time; the dashed horizontal lines indicate the mean value over the final 500 ps of the trajectory, used as an equilibrium indicator. The bottom panel shows a representative configuration of the system rendered from the corresponding .gro structure file.

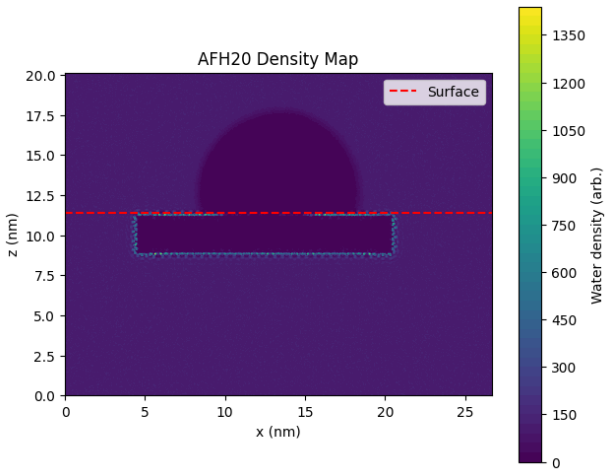

(a) Two-dimensional water density map used to determine the liquid-vapor interface. The dashed line indicates the solid surface position.

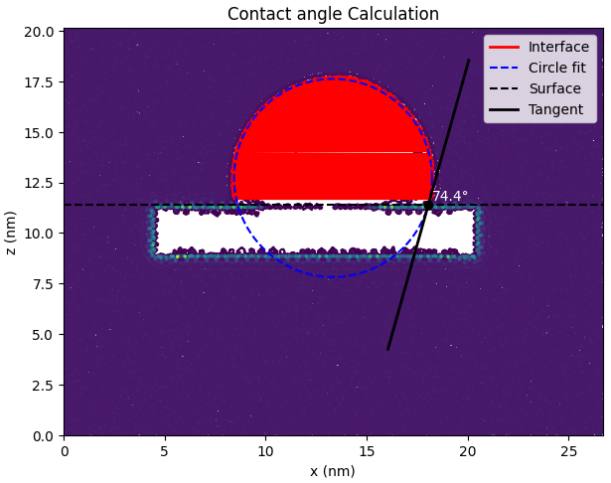

(b) Construction of the contact angle. A circular fit is applied to the detected interface points, and the tangent at the three phase contact line is used to compute the contact angle.

Figure B.78: Illustration of the contact angle determination procedure. (a) The liquid-vapor interface is extracted from the time-averaged density field using a threshold criterion. (b) A circle is fitted to the interface contour, and the contact angle is obtained from the tangent at the intersection between the fitted circle and the solid surface.

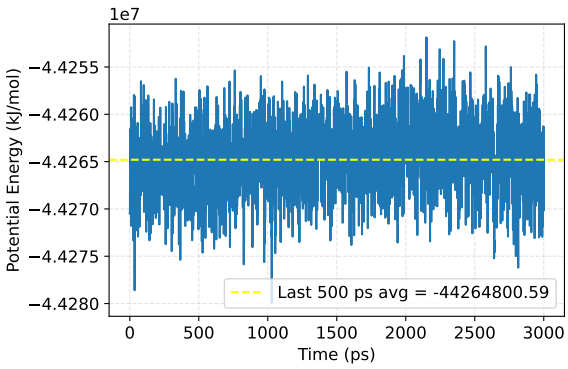

(a) Potential energy

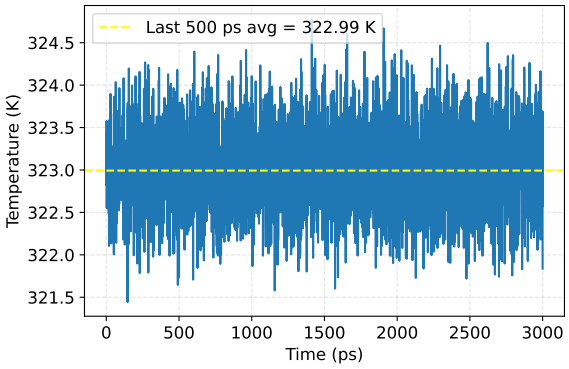

(b) Temperature

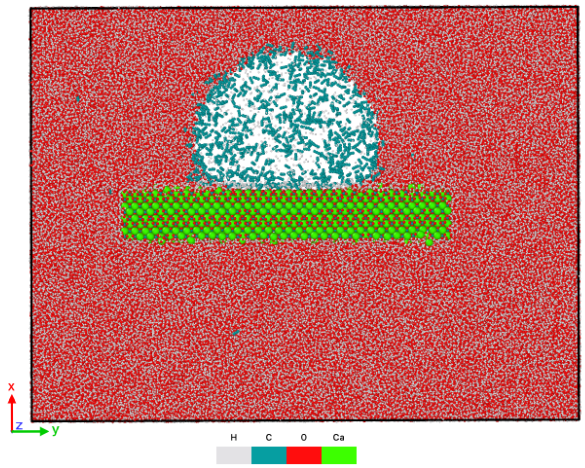

(c) System snapshot (.gro)

Figure B.79: Validation of the equilibrated AFH30 system. The potential energy (left) and temperature (right) are shown as a function of time; the dashed horizontal lines indicate the mean value over the final 500 ps of the trajectory, used as an equilibrium indicator. The bottom panel shows a representative configuration of the system rendered from the corresponding .gro structure file.

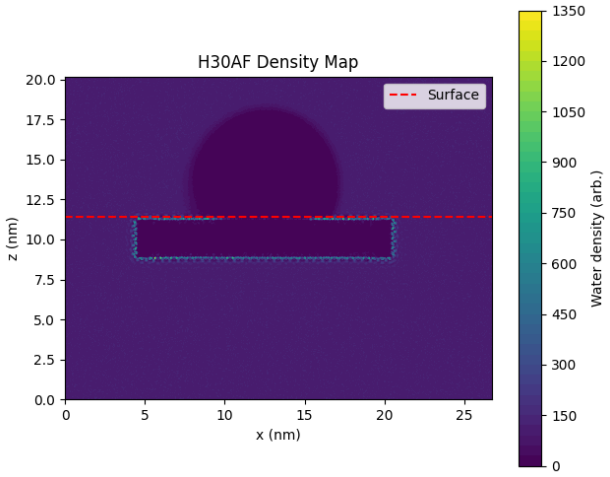

(a) Two-dimensional water density map used to determine the liquid-vapor interface. The dashed line indicates the solid surface position.

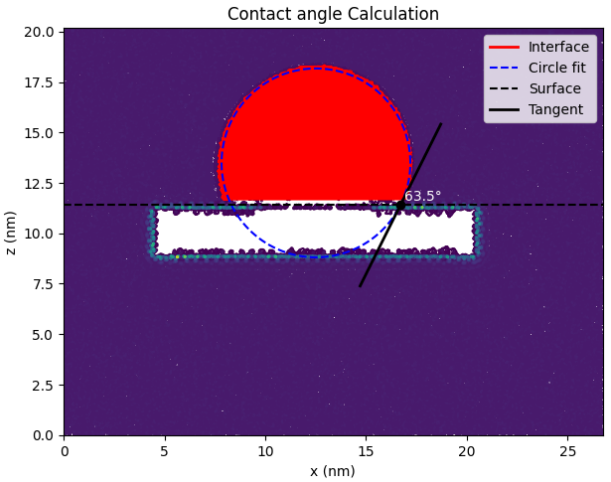

(b) Construction of the contact angle. A circular fit is applied to the detected interface points, and the tangent at the three phase contact line is used to compute the contact angle.

Figure B.80: Illustration of the contact angle determination procedure. (a) The liquid-vapor interface is extracted from the time-averaged density field using a threshold criterion. (b) A circle is fitted to the interface contour, and the contact angle is obtained from the tangent at the intersection between the fitted circle and the solid surface.

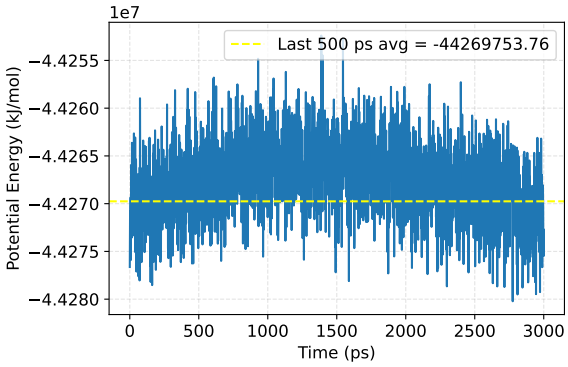

(a) Potential energy

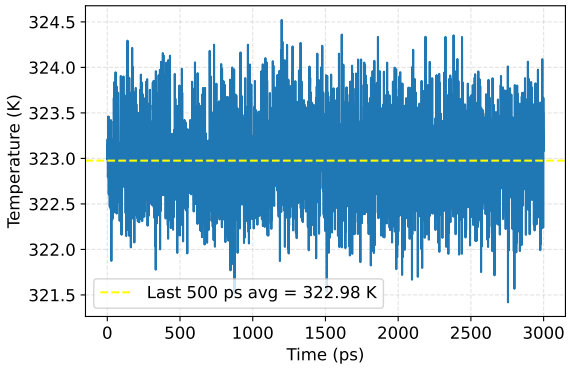

(b) Temperature

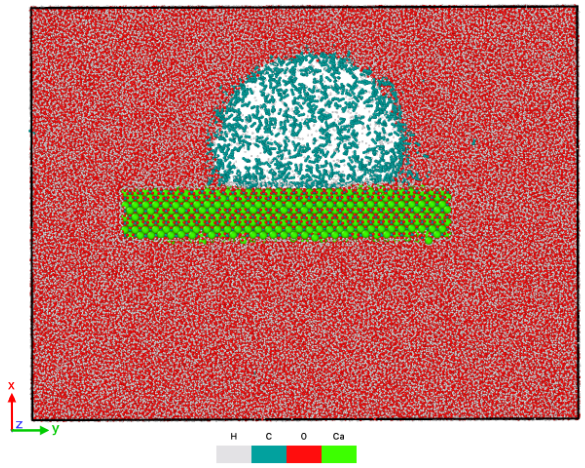

(c) System snapshot (.gro)

Figure B.81: Validation of the equilibrated AFH40 system. The potential energy (left) and temperature (right) are shown as a function of time; the dashed horizontal lines indicate the mean value over the final 500 ps of the trajectory, used as an equilibrium indicator. The bottom panel shows a representative configuration of the system rendered from the corresponding .gro structure file.

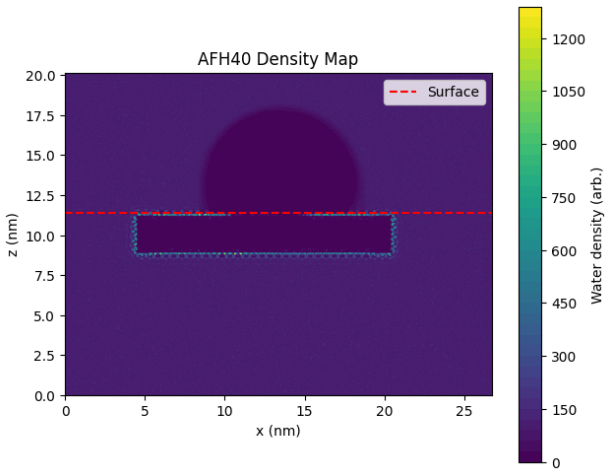

(a) Two-dimensional water density map used to determine the liquid-vapor interface. The dashed line indicates the solid surface position.

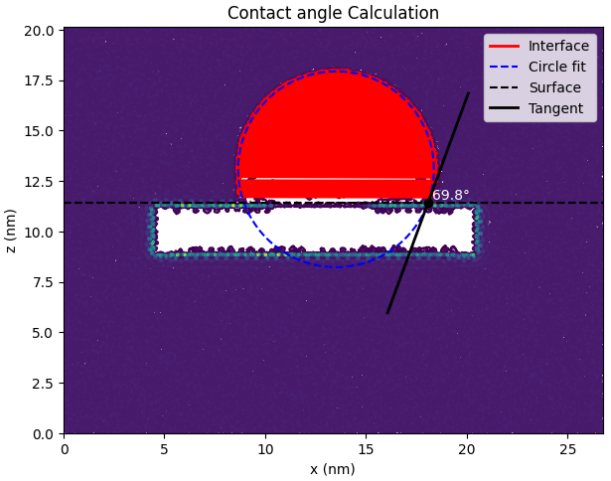

(b) Construction of the contact angle. A circular fit is applied to the detected interface points, and the tangent at the three phase contact line is used to compute the contact angle.

Figure B.82: Illustration of the contact angle determination procedure. (a) The liquid-vapor interface is extracted from the time-averaged density field using a threshold criterion. (b) A circle is fitted to the interface contour, and the contact angle is obtained from the tangent at the intersection between the fitted circle and the solid surface.

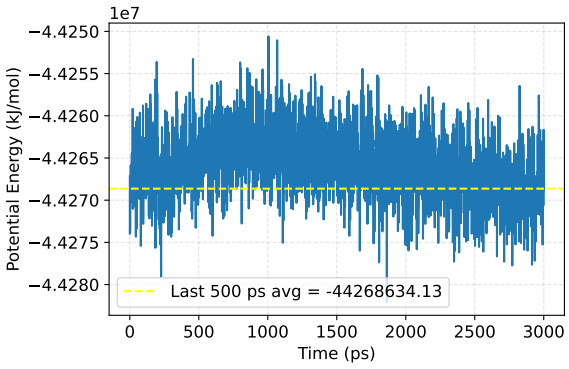

(a) Potential energy

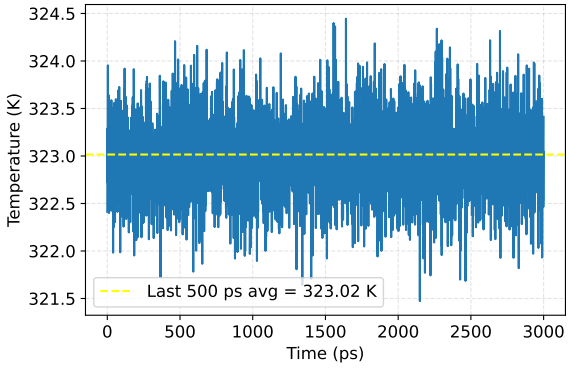

(b) Temperature

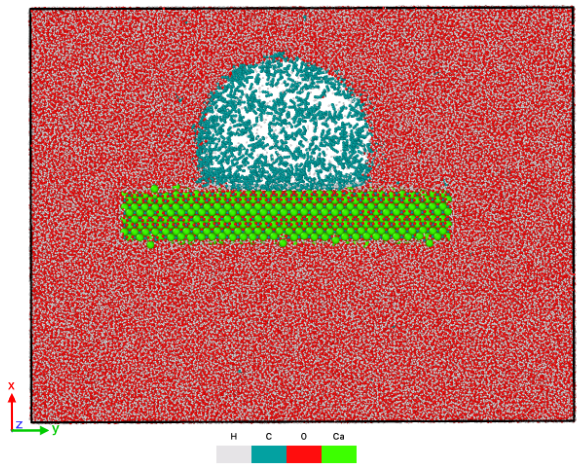

(c) System snapshot (.gro)

Figure B.83: Validation of the equilibrated AFH50 system. The potential energy (left) and temperature (right) are shown as a function of time; the dashed horizontal lines indicate the mean value over the final 500 ps of the trajectory, used as an equilibrium indicator. The bottom panel shows a representative configuration of the system rendered from the corresponding .gro structure file.

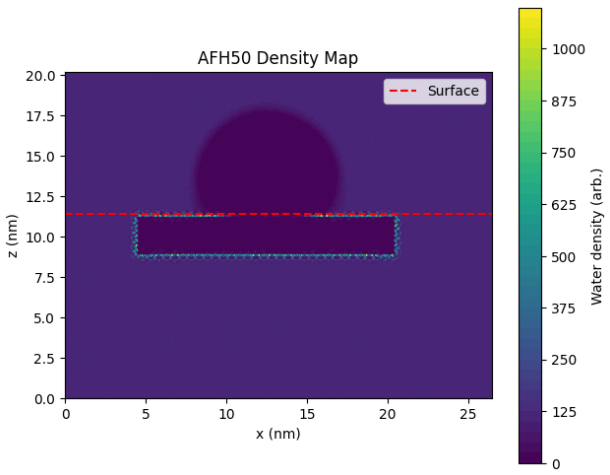

(a) Two-dimensional water density map used to determine the liquid-vapor interface. The dashed line indicates the solid surface position.

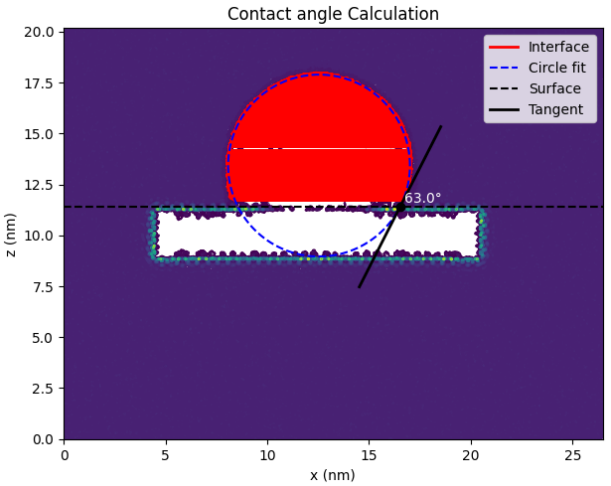

(b) Construction of the contact angle. A circular fit is applied to the detected interface points, and the tangent at the three phase contact line is used to compute the contact angle.

Figure B.84: Illustration of the contact angle determination procedure. (a) The liquid-vapor interface is extracted from the time-averaged density field using a threshold criterion. (b) A circle is fitted to the interface contour, and the contact angle is obtained from the tangent at the intersection between the fitted circle and the solid surface.

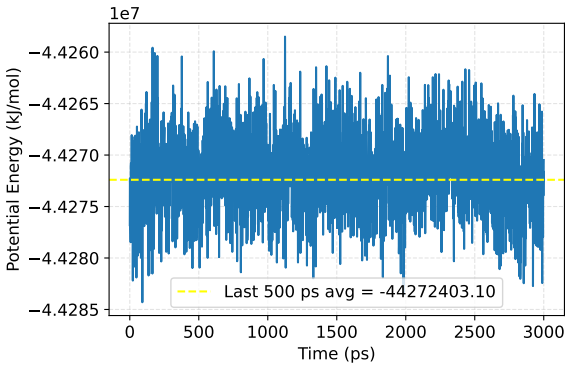

(a) Potential energy

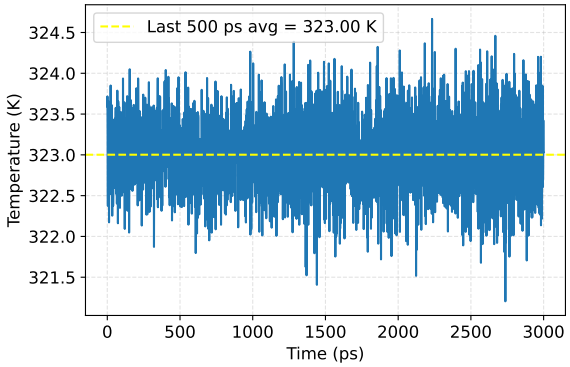

(b) Temperature

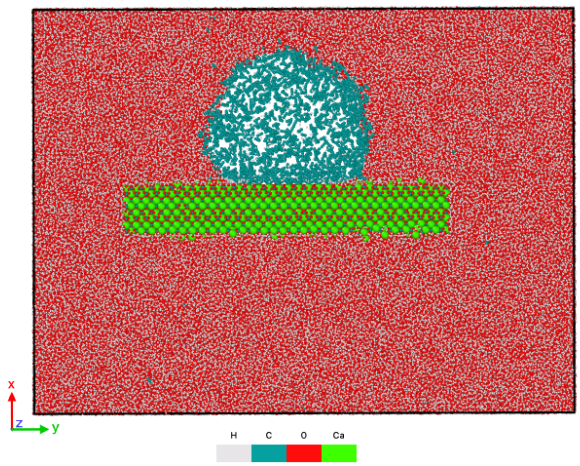

(c) System snapshot (.gro)

Figure B.85: Validation of the equilibrated AFH60 system. The potential energy (left) and temperature (right) are shown as a function of time; the dashed horizontal lines indicate the mean value over the final 500 ps of the trajectory, used as an equilibrium indicator. The bottom panel shows a representative configuration of the system rendered from the corresponding .gro structure file.

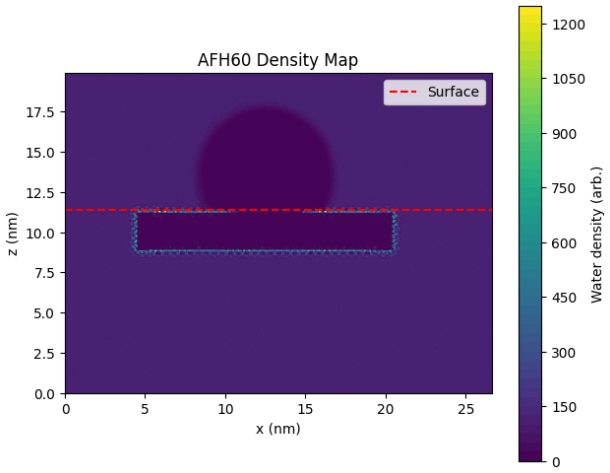

(a) Two-dimensional water density map used to determine the liquid-vapor interface. The dashed line indicates the solid surface position.

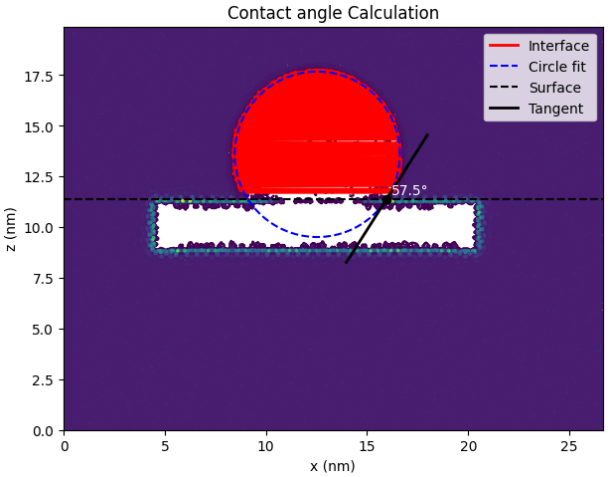

(b) Construction of the contact angle. A circular fit is applied to the detected interface points, and the tangent at the three phase contact line is used to compute the contact angle.

Figure B.86: Illustration of the contact angle determination procedure. (a) The liquid-vapor interface is extracted from the time-averaged density field using a threshold criterion. (b) A circle is fitted to the interface contour, and the contact angle is obtained from the tangent at the intersection between the fitted circle and the solid surface.

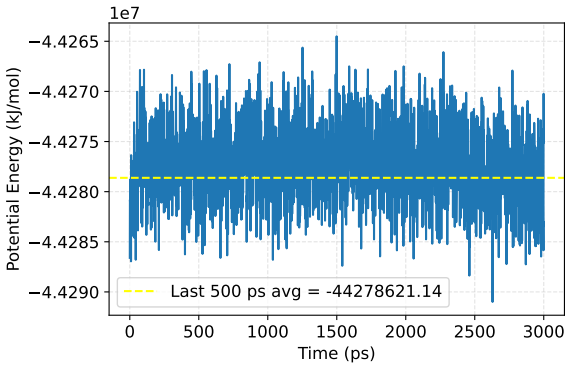

(a) Potential energy

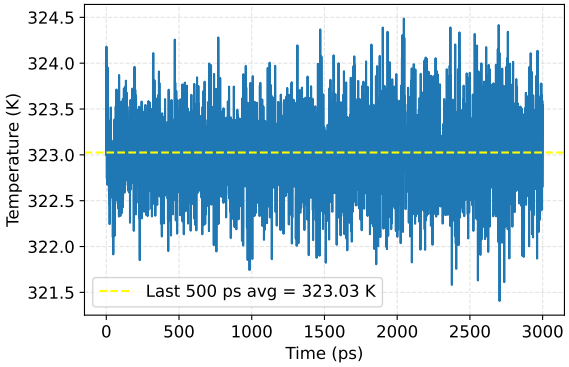

(b) Temperature

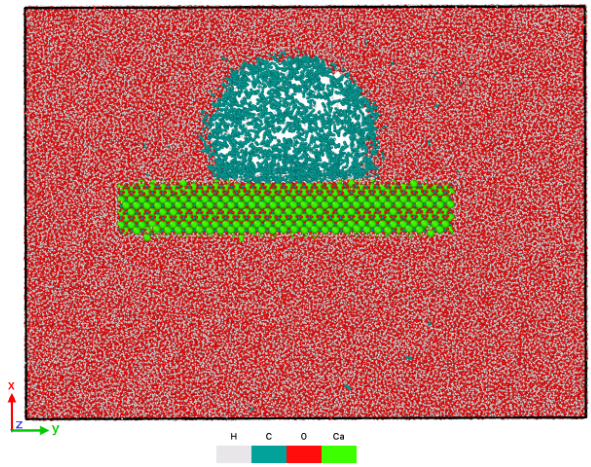

(c) System snapshot (.gro)

Figure B.87: Validation of the equilibrated AFH70 system. The potential energy (left) and temperature (right) are shown as a function of time; the dashed horizontal lines indicate the mean value over the final 500 ps of the trajectory, used as an equilibrium indicator. The bottom panel shows a representative configuration of the system rendered from the corresponding .gro structure file.

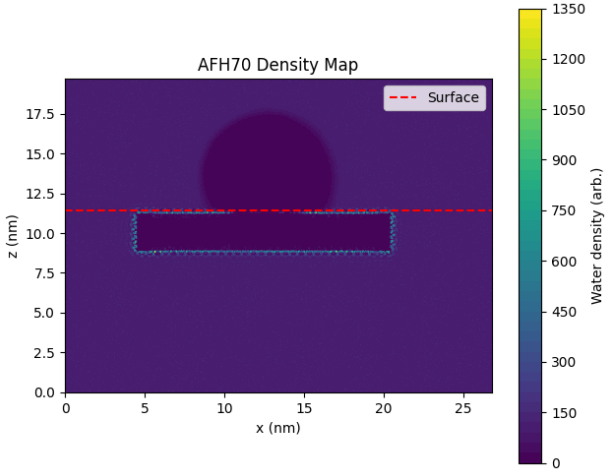

(a) Two-dimensional water density map used to determine the liquid-vapor interface. The dashed line indicates the solid surface position.

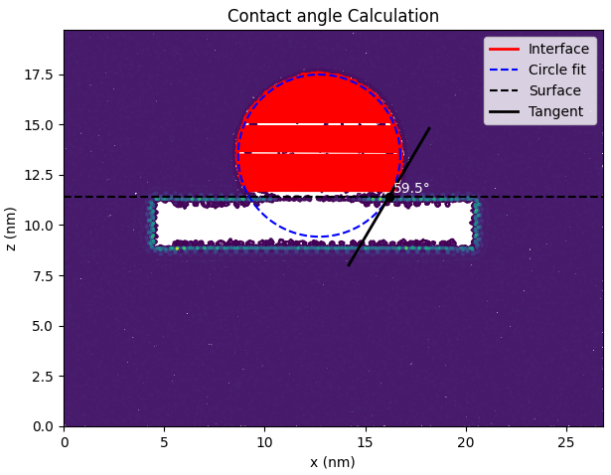

(b) Construction of the contact angle. A circular fit is applied to the detected interface points, and the tangent at the three phase contact line is used to compute the contact angle.

Figure B.88: Illustration of the contact angle determination procedure. (a) The liquid-vapor interface is extracted from the time-averaged density field using a threshold criterion. (b) A circle is fitted to the interface contour, and the contact angle is obtained from the tangent at the intersection between the fitted circle and the solid surface.

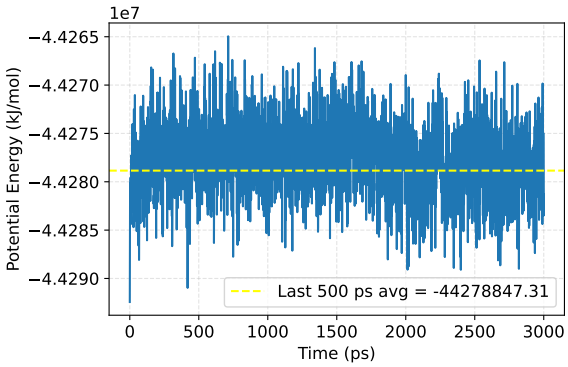

(a) Potential energy

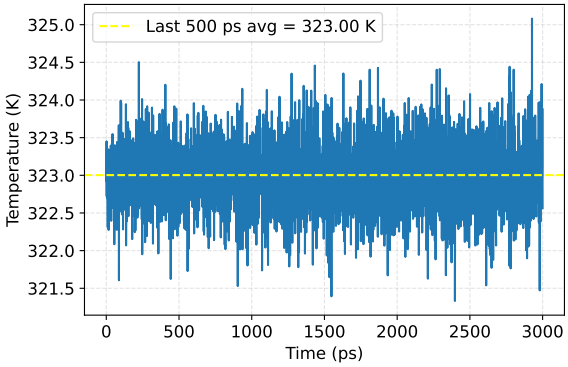

(b) Temperature

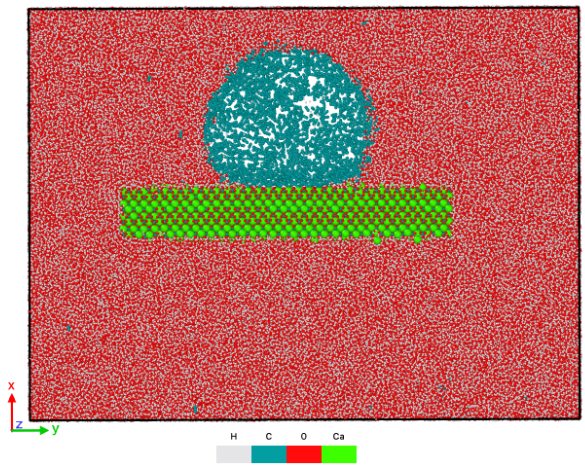

(c) System snapshot (.gro)

Figure B.89: Validation of the equilibrated AFH80 system. The potential energy (left) and temperature (right) are shown as a function of time; the dashed horizontal lines indicate the mean value over the final 500 ps of the trajectory, used as an equilibrium indicator. The bottom panel shows a representative configuration of the system rendered from the corresponding .gro structure file.

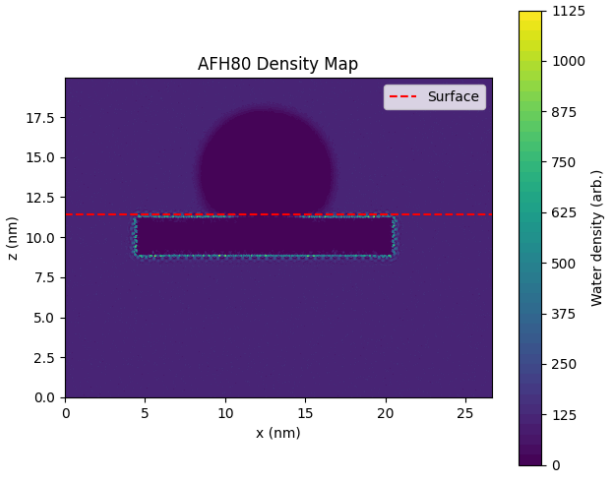

(a) Two-dimensional water density map used to determine the liquid-vapor interface. The dashed line indicates the solid surface position.

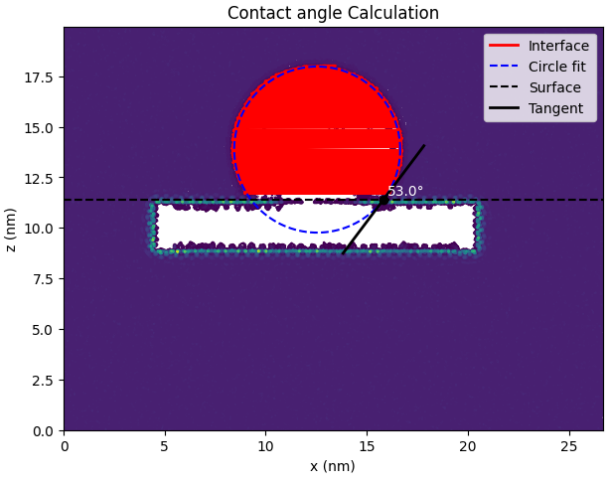

(b) Construction of the contact angle. A circular fit is applied to the detected interface points, and the tangent at the three phase contact line is used to compute the contact angle.

Figure B.90: Illustration of the contact angle determination procedure. (a) The liquid-vapor interface is extracted from the time-averaged density field using a threshold criterion. (b) A circle is fitted to the interface contour, and the contact angle is obtained from the tangent at the intersection between the fitted circle and the solid surface.

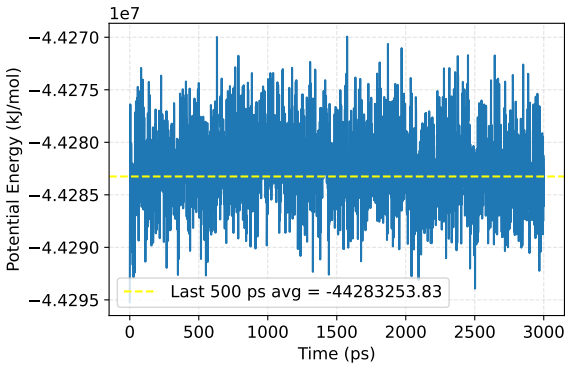

(a) Potential energy

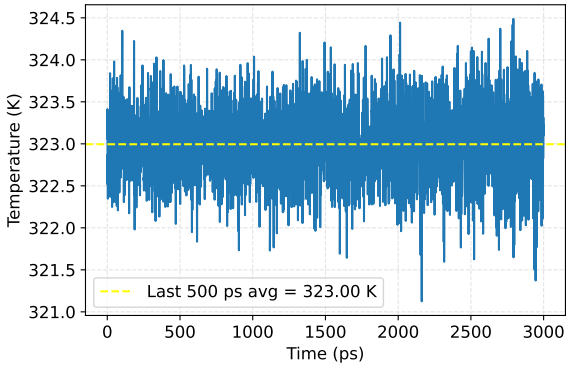

(b) Temperature

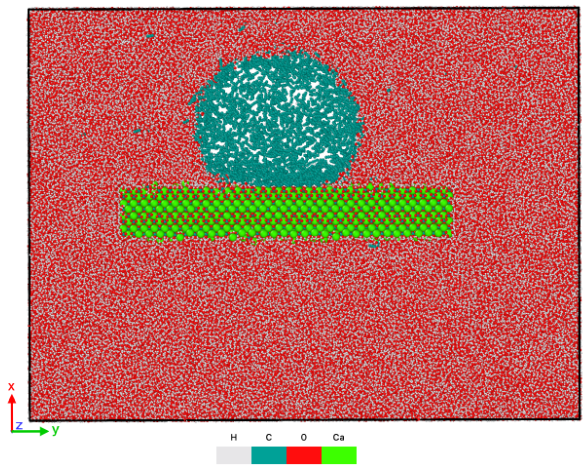

(c) System snapshot (.gro)

Figure B.91: Validation of the equilibrated AFH90 system. The potential energy (left) and temperature (right) are shown as a function of time; the dashed horizontal lines indicate the mean value over the final 500 ps of the trajectory, used as an equilibrium indicator. The bottom panel shows a representative configuration of the system rendered from the corresponding .gro structure file.

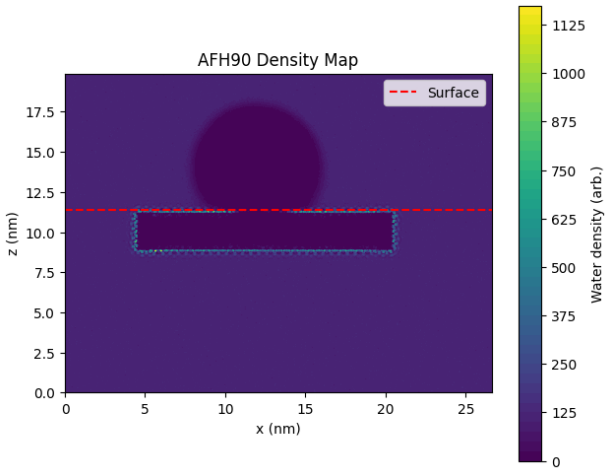

(a) Two-dimensional water density map used to determine the liquid-vapor interface. The dashed line indicates the solid surface position.

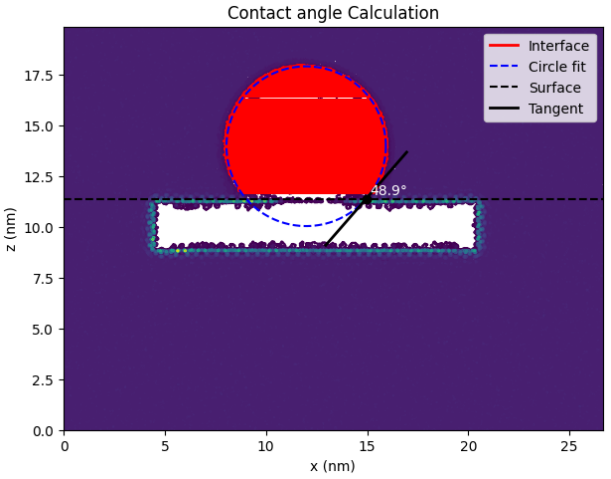

(b) Construction of the contact angle. A circular fit is applied to the detected interface points, and the tangent at the three phase contact line is used to compute the contact angle.

Figure B.92: Illustration of the contact angle determination procedure. (a) The liquid-vapor interface is extracted from the time-averaged density field using a threshold criterion. (b) A circle is fitted to the interface contour, and the contact angle is obtained from the tangent at the intersection between the fitted circle and the solid surface.

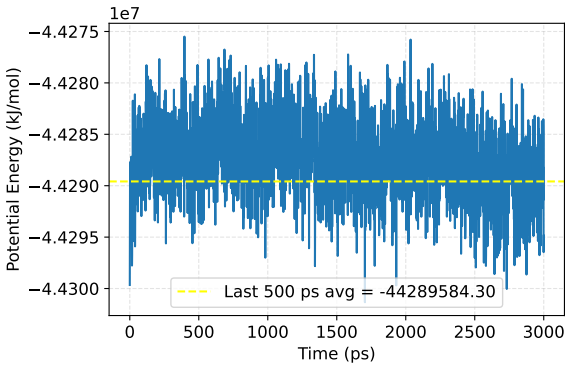

(a) Potential energy

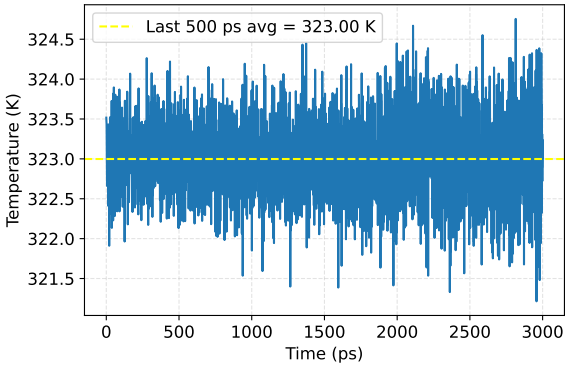

(b) Temperature

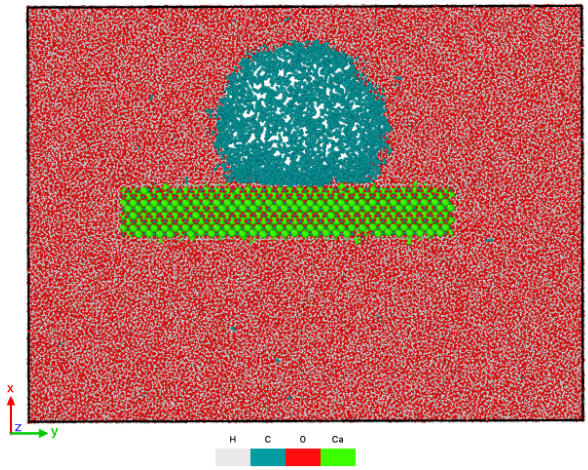

(c) System snapshot (.gro)

Figure B.93: Validation of the equilibrated AFH100 system. The potential energy (left) and temperature (right) are shown as a function of time; the dashed horizontal lines indicate the mean value over the final 500 ps of the trajectory, used as an equilibrium indicator. The bottom panel shows a representative configuration of the system rendered from the corresponding .gro structure file.

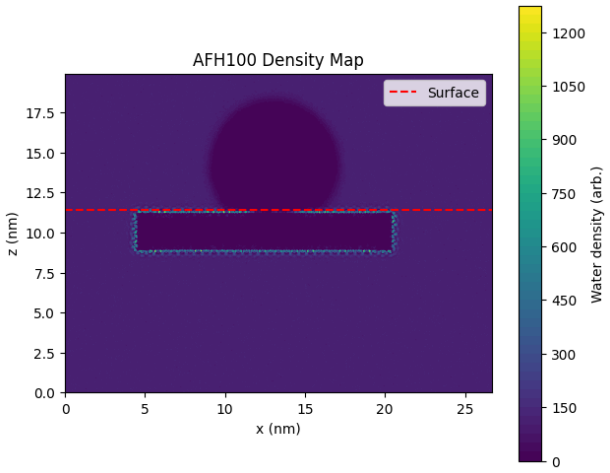

(a) Two-dimensional water density map used to determine the liquid-vapor interface. The dashed line indicates the solid surface position.

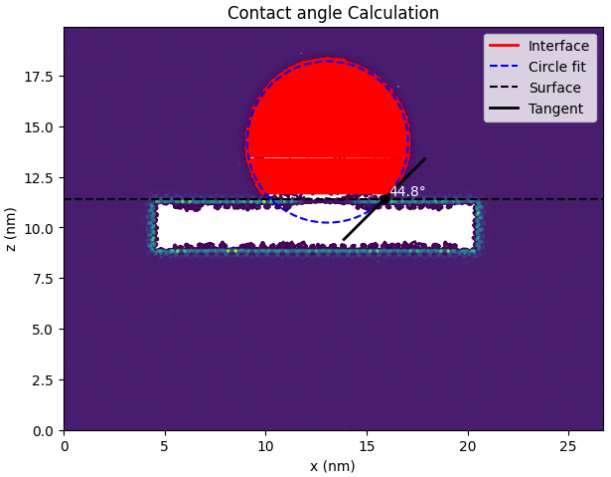

(b) Construction of the contact angle. A circular fit is applied to the detected interface points, and the tangent at the three phase contact line is used to compute the contact angle.

Figure B.94: Illustration of the contact angle determination procedure. (a) The liquid-vapor interface is extracted from the time-averaged density field using a threshold criterion. (b) A circle is fitted to the interface contour, and the contact angle is obtained from the tangent at the intersection between the fitted circle and the solid surface.

C

Appendix-C

C.1. Code for Contact Angle Calculation

contactanglepdf.py

```python
import numpy as np
import matplotlib.pyplot as plt
from scipy.optimize import least_squares

densmap_file = "densmap-H30AF.dat"

densmap = np.loadtxt(densmap_file)

z = densmap[1:, 0]
x = densmap[0, 1:]
rho = densmap[1:, 1:]

plt.figure(figsize=(7,6))
plt.contourf(x, z, rho, levels=50, cmap="viridis")
plt.colorbar(label="Water density (arb.)")
plt.axhline(h, color='r', ls='--', label="Surface")
plt.xlabel("x (nm)")
plt.ylabel("z (nm)")
plt.title("H30AF Density Map")
plt.legend()
plt.gca().set_aspect("equal")
plt.show()

rho_liq = np.percentile(rho, 95)
rho_gas = np.percentile(rho, 5)
rho_interface = 0.4 * (rho_liq + rho_gas)
print(rho_liq, rho_gas, rho_interface)

cs = plt.contour(x, z, rho, levels=[rho_interface])
plt.close()

paths = cs.collections[0].get_paths()
interface = max((p.vertices for p in paths), key=len)
interface = interface[interface[:,1] >= (h + buffer)]

def circle_residuals(p, x, z):
    xc, zc, R = p
    return np.sqrt((x-xc)**2 + (z-zc)**2) - R

x_i, z_i = interface[:,0], interface[:,1]
x0 = np.mean(x_i)
z0 = np.mean(z_i)
R0 = np.mean(np.sqrt((x_i-x0)**2 + (z_i-z0)**2))

res = least_squares(circle_residuals, x0=[x0, z0, R0], args=(x_i, z_i))
xc, zc, R = res.x
```

```
print(xc,zc,R)

dz = h - zc
dx = np.sqrt(R**2 - dz**2)
x_contact = xc + dx

slope = -(x_contact - xc) / (h - zc)
theta_liquid = np.degrees(np.arctan(abs(slope)))
theta_bubble = 180 - theta_liquid

print(f"Liquid-side angle: {theta_liquid:.2f}°")
print(f"Bubble contact angle: {theta_bubble:.2f}°")

plt.figure(figsize=(7,6))
plt.contour(x, z, rho, levels=50, cmap="viridis")
plt.plot(interface[:,0], interface[:,1], 'r', lw=2, label="Interface")

t = np.linspace(0, 2*np.pi, 400)
plt.plot(xc + R*np.cos(t), zc + R*np.sin(t), 'b--', label="Circle fit")

plt.axhline(h, color='k', ls='--', label="Surface")

xline = np.linspace(x_contact-2, x_contact+2, 100)
zline = slope*(xline-x_contact) + h
plt.plot(xline, zline, 'k-', lw=2, label="Tangent")

plt.plot(x_contact, h, 'ko')
plt.text(x_contact+0.2, h+0.2, f"{theta_liquid:.1f}°", color='white')

#plt.plot(xc, zc, 'wo', ms=8, mec='k', mew=1.5, label="Circle center")
#plt.text(xc + 0.2, zc + 0.2, f"({xc:.2f}, {zc:.2f})", color='w',
 #        bbox=dict(facecolor='black', alpha=0.5, edgecolor='none', pad=2))

plt.xlabel("x (nm)")
plt.ylabel("z (nm)")
plt.legend()
plt.gca().set_aspect("equal")
plt.title("Contact angle Calculation")
plt.show()
```

Bibliography

[1] Abdelateef M. Adam et al. “Molecular dynamics simulations of the interfacial tension and the solubility of brine/H2/CO2 systems: Implications for underground hydrogen storage”. en. In: *International Journal of Hydrogen Energy* 78 (Aug. 2024), pp. 1344–1354. ISSN: 03603199. DOI: 10.1016/j.ijhydene.2024.06.319.

[2] Sajjad Ahmadi Goltapeh et al. “Drivers of Low Salinity Effect in Carbonate Reservoirs Using Molecular Dynamic Simulation”. en. In: *Journal of Molecular Liquids* 360 (Aug. 2022), p. 119490. ISSN: 01677322. DOI: 10.1016/j.molliq.2022.119490.

[3] Saman Alavi, J. A. Ripmeester, and D. D. Klug. “Molecular-dynamics study of structure II hydrogen clathrates”. en. In: *The Journal of Chemical Physics* 123.2 (2005), p. 024507. ISSN: 0021-9606, 1089-7690. DOI: 10.1063/1.1953577.

[4] Azeezat Ali, David R. Cole, and Alberto Striolo. “Cushion gas effects on clay-hydrogen-brine wettability at conditions relevant to underground gas storage”. In: *International Journal of Hydrogen Energy* 58 (2024), pp. 668–677. ISSN: 0360-3199. DOI: https://doi.org/10.1016/j.ijhydene.2024.01.151. URL: https://www.sciencedirect.com/science/article/pii/S0360319924001733.

[5] Azeezat Ali, David R. Cole, and Alberto Striolo. “Cushion gas effects on clay-hydrogen-brine wettability at conditions relevant to underground gas storage”. en. In: *International Journal of Hydrogen Energy* 58 (Mar. 2024), pp. 668–677. ISSN: 03603199. DOI: 10.1016/j.ijhydene.2024.01.151.

[6] Azeezat Ali, David R. Cole, and Alberto Striolo. “Cushion gas effects on clay-hydrogen-brine wettability at conditions relevant to underground gas storage”. en. In: *International Journal of Hydrogen Energy* 58 (Mar. 2024), pp. 668–677. ISSN: 03603199. DOI: 10.1016/j.ijhydene.2024.01.151.

[7] Michael P. Allen and Dominic J. Tildesley. *Computer Simulation of Liquids*. 2nd. Practical approaches to statistical mechanics, molecular dynamics, ensemble sampling, and measurable observables. London, England: Oxford University Press, 2017. ISBN: 9780198803195. URL: https://academic.oup.com/book/27866.

[8] None Available. *Materials Data on CaCO3 by Materials Project*. en. 2020. DOI: 10.17188/1207669. URL: https://www.osti.gov/servlets/purl/1207669/.

[9] Lars Banenburg. *Crystallography I and II*. PowerPoint slides, CH3175: Solid State Materials, TU Delft. Unpublished lecture slides. 2025.

[10] Gabriel D. Barbosa et al. “Wettability of Chemically Heterogeneous Clay Surfaces: Correlation between Surface Defects and Contact Angles as Revealed by Machine Learning”. en. In: *ACS Applied Materials & Interfaces* 17.14 (Apr. 2025), pp. 21916–21928. ISSN: 1944-8244, 1944-8252. DOI: 10.1021/acsami.4c20587.

[11] Edgar M. Blokhuis and Joris Kuipers. “Thermodynamic expressions for the Tolman length”. en. In: *The Journal of Chemical Physics* 124.7 (Feb. 2006), p. 074701. ISSN: 0021-9606, 1089-7690. DOI: 10.1063/1.2167642.

[12] Maartje Boon and Hadi Hajibeygi. “Experimental characterization of H2/water multiphase flow in heterogeneous sandstone rock at the core scale relevant for underground hydrogen storage (UHS)”. en. In: *Scientific Reports* 12.1 (Aug. 2022), p. 14604. ISSN: 2045-2322. DOI: 10.1038/s41598-022-18759-8.

[13] Maartje Boon et al. “Microbial induced wettability alteration with implications for Underground Hydrogen Storage”. en. In: *Scientific Reports* 14.1 (Apr. 2024), p. 8248. ISSN: 2045-2322. DOI: 10.1038/s41598-024-58951-6.

[14] Maartje Boon et al. “Multiscale experimental study of H2/brine multiphase flow in porous rock characterizing relative permeability hysteresis, hydrogen dissolution, and Ostwald ripening”. en. In: *Scientific Reports* 14.1 (Dec. 2024), p. 30170. ISSN: 2045-2322. DOI: 10.1038/s41598-024-81720-4.

[15] Edward Bormashenko. “Progress in understanding wetting transitions on rough surfaces”. en. In: *Advances in Colloid and Interface Science* 222 (Aug. 2015), pp. 92–103. ISSN: 00018686. DOI: 10.1016/j.cis.2014.02.009.

[16] British Geological Survey. *Making the case for underground hydrogen storage in the UK*. https://www.bgs.ac.uk/news/making-the-case-for-underground-hydrogen-storage-in-the-uk/. Accessed: 2026-02-19. 2025.

[17] V. Buch. “Path integral simulations of mixed para -D2 and ortho -D2 clusters: The orientational effects”. en. In: *The Journal of Chemical Physics* 100.10 (May 1994), pp. 7610–7629. ISSN: 0021-9606, 1089-7690. DOI: 10.1063/1.466854.

[18] Weiwei Cai et al. “Semiquantitative Detection of Hydrogen-Associated or Hydrogen-Free Electron Transfer within Methanogenic Biofilm of Microbial Electrosynthesis”. In: *Applied and Environmental Microbiology* 86.17 (2020), e01056–20. DOI: 10.1128/AEM.01056-20.

[19] Nisha Chandramoorthy and Nicolas G. Hadjiconstantinou. “Solving lubrication problems at the nanometer scale”. en. In: *Microfluidics and Nanofluidics* 22.4 (Apr. 2018), p. 48. ISSN: 1613-4982, 1613-4990. DOI: 10.1007/s10404-018-2067-z.

[20] Cheng Chen and Jun Xia. “A comparative study on transport and interfacial physics of H2/CO2/CH4 interacting with H2O and/or silica by molecular dynamics simulation”. en. In: *Physics of Fluids* 36.1 (Jan. 2024), p. 016606. ISSN: 1070-6631, 1089-7666. DOI: 10.1063/5.0184754.

[21] Cheng Chen, Jun Xia, and Hamid Bahai. “Effect of the Temperature on Interfacial Properties of CO2 /H2 Mixtures Contacting with Brine and Hydrophilic Silica by Molecular Dynamics Simulations”. en. In: *Energy Fuels* 37.23 (Dec. 2023), pp. 18986–18995. ISSN: 0887-0624, 1520-5029. DOI: 10.1021/acs.energyfuels.3c03164.

[22] Y.T. Florence Chow, Geoffrey C. Maitland, and J.P. Martin Trusler. “Interfacial tensions of (H2O + H2) and (H2O + CO2 + H2) systems at temperatures of (298–448) K and pressures up to 45 MPa”. en. In: *Fluid Phase Equilibria* 475 (Nov. 2018), pp. 37–44. ISSN: 03783812. DOI: 10.1016/j.fluid.2018.07.022.

[23] Randall T. Cygan, Jian-Jie Liang, and Andrey G. Kalinichev. “Molecular Models of Hydroxide, Oxyhydroxide, and Clay Phases and the Development of a General Force Field”. en. In: *The Journal of Physical Chemistry B* 108.4 (Jan. 2004), pp. 1255–1266. ISSN: 1520-6106, 1520-5207. DOI: 10.1021/jp0363287.

[24] Xuguang Dai et al. “Understanding CO2 mineralization and associated storage space changes in illite using molecular dynamics simulation and experiments”. en. In: *Energy* 283 (Nov. 2023), p. 128467. ISSN: 03605442. DOI: 10.1016/j.energy.2023.128467.

[25] Jaroslaw Drelich, Jan D. Miller, and Robert J. Good. “The Effect of Drop (Bubble) Size on Advancing and Receding Contact Angles for Heterogeneous and Rough Solid Surfaces as Observed with Sessile-Drop and Captive-Bubble Techniques”. en. In: *Journal of Colloid and Interface Science* 179.1 (Apr. 1996), pp. 37–50. ISSN: 00219797. DOI: 10.1006/jcis.1996.0186.

[26] D. Nicolas Espinoza and J. Carlos Santamarina. “CO2 breakthrough—Caprock sealing efficiency and integrity for carbon geological storage”. en. In: *International Journal of Greenhouse Gas Control* 66 (Nov. 2017), pp. 218–229. ISSN: 17505836. DOI: 10.1016/j.ijggc.2017.09.019.

[27] Joseph C. Fogarty et al. “A reactive molecular dynamics simulation of the silica-water interface”. en. In: *The Journal of Chemical Physics* 132.17 (May 2010), p. 174704. ISSN: 0021-9606, 1089-7690. DOI: 10.1063/1.3407433.

[28] Daan Frenkel and Berend Smit. *Understanding Molecular Simulation: From Algorithms to Applications*. 2nd. Foundations of statistical mechanics and molecular dynamics algorithms, phase space sampling, ensembles, thermodynamic observables. San Diego, CA, USA: Academic Press, 2002. ISBN: 9780122673511. URL: https://www.sciencedirect.com/book/9780122673511/understanding-molecular-simulation.

[29] Mohamad Ali Ghafari et al. “Wetting Preference of Silica Surfaces in the Context of Underground Hydrogen Storage: A Molecular Dynamics Perspective”. en. In: *Langmuir* 40.39 (Oct. 2024), pp. 20559–20575. ISSN: 0743-7463, 1520-5827. DOI: 10.1021/acs.langmuir.4c02311.

[30] Kenji Hagiya et al. “The crystal data and stability of calcite III at high pressures based on single-crystal X-ray experiments”. en. In: *Journal of Mineralogical and Petrological Sciences* 100.1 (2005), pp. 31–36. ISSN: 1345-6296, 1349-3825. DOI: 10.2465/jmps.100.31.

[31] Frank Heberling et al. “Structure and reactivity of the calcite–water interface”. In: *Journal of Colloid and Interface Science* 354.2 (2011), pp. 843–857. DOI: 10.1016/j.jcis.2010.10.047.

[32] Hendrik Heinz et al. “Thermodynamically Consistent Force Fields for the Assembly of Inorganic, Organic, and Biological Nanostructures: The INTERFACE Force Field”. en. In: *Langmuir* 29.6 (Feb. 2013), pp. 1754–1765. ISSN: 0743-7463, 1520-5827. DOI: 10.1021/la3038846.

[33] Yasaman Hosseinzadeh Dehaghani, Mehdi Assareh, and Farzaneh Feyzi. “Simultaneous Prediction of Equilibrium, Interfacial, and Transport Properties of CO 2 -Brine Systems Using Molecular Dynamics Simulation: Applications to CO 2 Storage”. In: *Industrial Engineering Chemistry Research* 61 (Sept. 2022). DOI: 10.1021/acs.iecr.2c02249.

[34] Feifei Huang et al. “Microscopic insights into water wetting behaviors and physical origin on α-quartz exposed to varying underground gas species”. en. In: *Chemical Engineering Journal* 498 (Oct. 2024), p. 155128. ISSN: 13858947. DOI: 10.1016/j.cej.2024.155128.

[35] Nobuo Ishizawa, Hayato Setoguchi, and Kazumichi Yanagisawa. “Structural evolution of calcite at high temperatures: Phase V unveiled”. In: *Scientific Reports* 3 (2013), p. 2832. DOI: 10.1038/srep02832.

[36] Masao Iwamatsu. “A generalized Young’s equation to bridge a gap between the experimentally measured and the theoretically calculated line tensions”. In: *Journal of Adhesion Science and Technology* (2018). DOI: 10.48550/ARXIV.1805.02837. URL: https://arxiv.org/abs/1805.02837.

[37] Bernadeta Jasiok et al. “Thermophysical properties of the SPC/E model of water between 250 and 400 K at pressures up to 1000 MPa”. In: *Fluid Phase Equilibria* 584 (2024), p. 114118. ISSN: 0378-3812. DOI: https://doi.org/10.1016/j.fluid.2024.114118.

[38] Cliff T. Johnston. “Clay mineral–water interactions”. en. In: *Developments in Clay Science*. Vol. 9. Elsevier, 2018, pp. 89–124. ISBN: 978-0-08-102432-4. DOI: 10.1016/B978-0-08-102432-4.00004-4. URL: https://linkinghub.elsevier.com/retrieve/pii/B9780081024324000044.

[39] Sachini P. Kadaoluwa Pathirannahalage et al. “Systematic Comparison of the Structural and Dynamic Properties of Commonly Used Water Models for Molecular Dynamics Simulations”. en. In: *Journal of Chemical Information and Modeling* 61.9 (2021), pp. 4521–4536. ISSN: 1549-9596, 1549-960X. DOI: 10.1021/acs.jcim.1c00794.

[40] Keren Kles. *Contact Angles*. https://chem.libretexts.org/@go/page/1501. Chemistry LibreTexts, accessed 11 Feb 2026. July 2024.

[41] Przemyslaw Kowalczuk et al. “Water contact angle on corresponding surfaces of freshly fractured fluorite, calcite and mica”. In: *Fizykochemiczne Problemy Mineralurgii - Physicochemical Problems of Mineral Processing* 53 (Jan. 2017), pp. 192–201. DOI: 10.5277/ppmp170116.

[42] Huifang Li et al. “Mechanism of wettability alteration of the calcite 1014 surface”. en. In: *Physical Chemistry Chemical Physics* 22.27 (2020), pp. 15365–15372. ISSN: 1463-9076, 1463-9084. DOI: 10.1039/D0CP01715A.

[43] Kejiang Li et al. “Thermal behaviour, kinetics and mechanisms of CO2 interactions with graphene: An atomic scale reactive molecular dynamic study”. en. In: *Chemical Engineering Journal* 425 (Dec. 2021), p. 131529. ISSN: 13858947. DOI: 10.1016/j.cej.2021.131529.

[44] Wenchuan Liu et al. “Understanding the adsorption properties of CO2 and N2 by a typical MOF structure: Molecular dynamics and weak interaction visualization”. In: *Chemical Engineering Science* 296 (2024), p. 120233. ISSN: 0009-2509. DOI: https://doi.org/10.1016/j.ces.2024.120233.

[45] Qian Mao et al. “Classical and reactive molecular dynamics: Principles and applications in combustion and energy systems”. en. In: *Progress in Energy and Combustion Science* 97 (2023), p. 101084. ISSN: 03601285. DOI: 10.1016/j.pecs.2023.101084.

[46] Antonin Marchand et al. “Why is surface tension a force parallel to the interface?” en. In: *Am. J. Phys.* 79.10 (Oct. 2011), pp. 999–1008.

[47] Grant Charles Mwakipunda et al. “Underground hydrogen storage in geological formations: A review”. en. In: *Journal of Rock Mechanics and Geotechnical Engineering* 17.10 (Oct. 2025), pp. 6704–6741. ISSN: 16747755. DOI: 10.1016/j.jrmge.2025.02.014.

[48] Chinedu J. Okere, James J. Sheng, and Chinedu Ejike. “Evaluating reservoir suitability for large-scale hydrogen storage: A preliminary assessment considering reservoir properties”. en. In: *Energy Geoscience* 5.4 (Oct. 2024), p. 100318. ISSN: 26667592. DOI: 10.1016/j.engeos.2024.100318.

[49] Sina Omrani et al. “Interfacial Tension–Temperature–Pressure–Salinity Relationship for the Hydrogen–Brine System under Reservoir Conditions: Integration of Molecular Dynamics and Machine Learning”. en. In: *Langmuir* 39.36 (2023), pp. 12680–12691. ISSN: 0743-7463, 1520-5827. DOI: 10.1021/acs.langmuir.3c01424.

[50] Le Nhan Pham and Tiffany R. Walsh. “Force fields for water–surface interaction: is reproduction of the experimental water contact angle enough?” en. In: *Chemical Communications* 57.27 (2021), pp. 3355–3358. ISSN: 1359-7345, 1364-548X. DOI: 10.1039/D1CC00426C.

[51] Anh Phan et al. “Simulation insights into wetting properties of hydrogen-brine-clay for hydrogen geo-storage”. en. In: *Journal of Energy Storage* 112 (Mar. 2025), p. 115477. ISSN: 2352152X. DOI: 10.1016/j.est.2025.115477.

[52] Hannah Pollak, Matteo T. Degiacomi, and Valentina Erastova. “Modeling Realistic Clay Systems with ClayCode”. en. In: *Journal of Chemical Theory and Computation* 20.21 (Nov. 2024), pp. 9606–9617. ISSN: 1549-9618, 1549-9626. DOI: 10.1021/acs.jctc.4c00987.

[53] Jeffrey J. Potoff and J. Ilja Siepmann. “Vapor–liquid equilibria of mixtures containing alkanes, carbon dioxide, and nitrogen”. In: *AIChE Journal* 47.7 (2001), pp. 1676–1682. DOI: https://doi.org/10.1002/aic.690470719. eprint: https://aiche.onlinelibrary.wiley.com/doi/pdf/10.1002/aic.690470719. URL: https://aiche.onlinelibrary.wiley.com/doi/abs/10.1002/aic.690470719.

[54] Ahmadreza Rahbari et al. “Molecular Simulation of Hydrogen Systems: From Properties and Methods to Applications and Future Directions”. en. In: *Chemical Reviews* 125.24 (Dec. 2025), pp. 11878–12029. ISSN: 0009-2665, 1520-6890. DOI: 10.1021/acs.chemrev.5c00617.

[55] Mohammad Salehpour et al. “Ostwald Ripening in Underground Gas Storage”. In: (2025). DOI: 10.48550/ARXIV.2509.00044. URL: https://arxiv.org/abs/2509.00044.

[56] Ernest Solomon. “Molecular theory of gases and liquids. Joseph O. Hirschfelder, Charles F. Curtiss, and R. Byron Bird. John Wiley Sons, Inc., New York (1954). 1219 pages. 20”. en. In: *AIChE Journal* 1.2 (1955), pp. 272–272. ISSN: 0001-1541, 1547-5905. DOI: 10.1002/aic.690010225.

[57] Rui Song et al. “Visualized experiments on the hydrogen transports and bubble ripening mechanism in porous reservoir of underground hydrogen storage”. en. In: *International Journal of Hydrogen Energy* 105 (Mar. 2025), pp. 326–344. ISSN: 03603199. DOI: 10.1016/j.ijhydene.2025.01.194.

[58] Catherine Spurin et al. “The Importance and Challenges Associated with Multi-scale Heterogeneity for Geological Storage”. In: *InterPore Journal* 2.1 (Feb. 2025), IPJ260225–2. ISSN: 3007-410X. DOI: 10.69631/ipj.v2i1nr76.

[59] C. Vega and E. De Miguel. “Surface tension of the most popular models of water by using the test-area simulation method”. en. In: *The Journal of Chemical Physics* 126.15 (Apr. 2007), p. 154707. ISSN: 0021-9606, 1089-7690. DOI: 10.1063/1.2715577.

[60] Carlos Vega and Jose L. F. Abascal. “Simulating water with rigid non-polarizable models: a general perspective”. en. In: *Physical Chemistry Chemical Physics* 13.44 (2011), p. 19663. ISSN: 1463-9076, 1463-9084. DOI: 10.1039/c1cp22168j.

[61] Xiao Wang et al. “A Comprehensive Review of Wetting Transition Mechanism on the Surfaces of Microstructures from Theory and Testing Methods”. en. In: *Materials* 15.14 (2022), p. 4747. ISSN: 1996-1944. DOI: 10.3390/ma15144747.

[62] R. H. Worden et al. “Petroleum reservoir quality prediction: overview and contrasting approaches from sandstone and carbonate communities”. en. In: *Geological Society, London, Special Publications* 435.1 (Jan. 2018), pp. 1–31. ISSN: 0305-8719, 2041-4927. DOI: 10.1144/SP435.21.

[63] Shijun Xiao, Scott A. Edwards, and Frauke Gräter. “A New Transferable Forcefield for Simulating the Mechanics of CaCO3 Crystals”. en. In: *The Journal of Physical Chemistry C* 115.41 (Oct. 2011), pp. 20067–20075. ISSN: 1932-7447, 1932-7455. DOI: 10.1021/jp202743v.

[64] Yafan Yang et al. “Molecular perspectives of interfacial properties of the hydrogen+water mixture in contact with silica or kerogen”. en. In: *Journal of Molecular Liquids* 385 (2023), p. 122337. ISSN: 01677322. DOI: 10.1016/j.molliq.2023.122337.

[65] Yafan Yang et al. “Molecular perspectives of interfacial properties of the hydrogen+water mixture in contact with silica or kerogen”. en. In: *Journal of Molecular Liquids* 385 (2023), p. 122337. ISSN: 01677322. DOI: 10.1016/j.molliq.2023.122337.

[66] Xinyu Yao et al. “Interfacial properties of the hydrogen+brine system in the presence of hydrophilic silica”. en. In: *International Journal of Hydrogen Energy* 101 (Feb. 2025), pp. 741–749. ISSN: 03603199. DOI: 10.1016/j.ijhydene.2024.12.417.

[67] Ahmed Al-Yaseri, Safwat Abdel-Azeim, and Jafar Al-Hamad. “Wettability of water-H2-quartz and water-H2-calcite experiment and molecular dynamics simulations: Critical assessment”. en. In: *International Journal of Hydrogen Energy* 48.89 (Nov. 2023), pp. 34897–34905. ISSN: 03603199. DOI: 10.1016/j.ijhydene.2023.05.294.

[68] Ahmed Al-Yaseri et al. “Impact of wettability on storage and recovery of hydrogen gas in the lesueur sandstone formation (Southwest hub project, Western Australia)”. en. In: *International Journal of Hydrogen Energy* 48.61 (2023), pp. 23581–23593. ISSN: 03603199. DOI: 10.1016/j.ijhydene.2023.03.131.

[69] Siqin Yu et al. “Unraveling residual trapping for geologic hydrogen storage and production using pore-scale modeling”. en. In: *Advances in Water Resources* 185 (Mar. 2024), p. 104659. ISSN: 03091708. DOI: 10.1016/j.advwatres.2024.104659.

[70] Xinran Yu et al. “In-situ wettability alteration of organic-rich shale caprock in hydrogen with cushion gas: Implications for hydrogen geo-storage”. en. In: *International Journal of Hydrogen Energy* 103 (Feb. 2025), pp. 75–86. ISSN: 03603199. DOI: 10.1016/j.ijhydene.2025.01.062.

[71] Leila Zargarzadeh and Janet A. W. Elliott. “Thermodynamics of Surface Nanobubbles”. en. In: *Langmuir* 32.43 (Nov. 2016), pp. 11309–11320. ISSN: 0743-7463, 1520-5827. DOI: 10.1021/acs.langmuir.6b01561.

[72] Hongguang Zhang and Xianren Zhang. “Size dependence of bubble wetting on surfaces: breakdown of contact angle match between small sized bubbles and droplets”. en. In: *Nanoscale* 11.6 (2019), pp. 2823–2828. ISSN: 2040-3364, 2040-3372. DOI: 10.1039/C8NR08929A.

[73] Jun Zhang et al. “A critical assessment of the line tension determined by the modified Young’s equation”. en. In: *Physics of Fluids* 30.8 (Aug. 2018), p. 082003. ISSN: 1070-6631, 1089-7666. DOI: 10.1063/1.5040574.

[74] Siqi Zhang et al. “Molecular dynamic simulations on the hydrogen wettability of caprock: Considering effects of mineralogy, pressure, temperature and salinity”. en. In: *International Journal of Hydrogen Energy* 109 (Mar. 2025), pp. 367–382. ISSN: 03603199. DOI: 10.1016/j.ijhydene.2025.01.467.

[75] Zhe Zhang and Xiaoyu Song. “NEMD modeling of nanoscale hydrodynamics of clay-water system at elevated temperature”. In: (2021). DOI: 10.48550/ARXIV.2112.14654. URL: https://arxiv.org/abs/2112.14654.

[76] Jin Zhao et al. “Molecular dynamics investigation of substrate wettability alteration and oil transport in a calcite nanopore”. en. In: *Fuel* 239 (Mar. 2019), pp. 1149–1161. ISSN: 00162361. DOI: 10.1016/j.fuel.2018.11.089.

[77] Lingru Zheng et al. “Surrogate Models for Studying the Wettability of Nanoscale Natural Rough Surfaces Using Molecular Dynamics”. en. In: *Energies* 13.11 (2020), p. 2770. ISSN: 1996-1073. DOI: 10.3390/en13112770.

[78] Ruyi Zheng et al. “Driving mechanisms of quartz wettability alteration under in-situ H2 geo-storage conditions: Role of organic ligands and surface morphology”. en. In: *International Journal of Hydrogen Energy* 59 (Mar. 2024), pp. 1388–1398. ISSN: 03603199. DOI: 10.1016/j.ijhydene.2024.02.158.

[79] Ruyi Zheng et al. “Driving mechanisms of quartz wettability alteration under in-situ H2 geo-storage conditions: Role of organic ligands and surface morphology”. en. In: *International Journal of Hydrogen Energy* 59 (Mar. 2024), pp. 1388–1398. ISSN: 03603199. DOI: 10.1016/j.ijhydene.2024.02.158.

[80] Ruyi Zheng et al. “Molecular Insights into the Impact of Surface Chemistry and Pressure on Quartz Wettability: Resolving Discrepancies for Hydrogen Geo-storage”. en. In: *ACS Sustainable Chemistry Engineering* 12.14 (Apr. 2024), pp. 5555–5563. ISSN: 2168-0485, 2168-0485. DOI: 10.1021/acssuschemeng.3c08241.

[81] Zhiyan Zhou et al. “Occurrence Characteristics of Water in Nano-Slit Pores under Different Solution Conditions: A Case Study on Kaolinite”. en. In: *ACS Omega* 8.21 (May 2023), pp. 18990–19001. ISSN: 2470-1343, 2470-1343. DOI: 10.1021/acsomega.3c01640.